DISS. ETH NO. 29182

APPLICATIONS OF BISTATIC KU-BAND RADAR IN SNOW-COVERED ENVIRONMENTS

A thesis submitted to attain the degree of

DOCTOR OF SCIENCES

(Dr. sc. ETH Zurich)

presented by

MARCEL ŠTEFKO

ing. phys. dipl. EPF
École Polytechnique Fédérale de Lausanne

born on 17.12.1993

accepted on the recommendation of

Prof. Dr. Irena Hajnsek
Dr. Othmar Frey
Prof. Dr. Jordi J. Mallorqui
Prof. Dr. Keith Morrison
Dr. Marc Rodriguez-Cassola

2023

ETH zürich

Chair of Earth Observation and Remote Sensing, ETH Zurich, Switzerland.

To my family.

ABSTRACT

Bistatic radar imaging is a remote sensing method which employs a spatially separated radio wave transmitter and receiver, in order to construct a two-dimensional image of the reflective properties of objects within a certain area. Compared to the more common monostatic radar systems (which use a co-located transmitter and receiver), bistatic radar systems are considered to be specialized tools which are more suitable for certain specific purposes, at cost of higher complexity. The special-purpose character and higher complexity of bistatic systems cause a low availability of such systems, and thus also of bistatic radar datasets. This is an obstacle for performing studies which require the use of bistatic systems. In the Earth Observation domain, such studies may be aiming, e.g., to explore non-reciprocal scattering processes which do not occur in the monostatic regime, or to investigate phenomena with specific bistatic signatures.

This dissertation makes use of KAPRI, a ground-based Ku-band polarimetric radar interferometer based on the Gamma Portable Radar Interferometer (GPRI). KAPRI was specifically modified by the manufacturer to allow full-polarimetric bistatic radar acquisitions, and can thus be used for studies of the bistatic scattering processes occurring at Ku-band in a variety of environments. The Ku-band frequency of KAPRI makes the study of glacial and snow-covered environments particularly attractive, due to the relatively short but non-zero penetration depth into snow and ice, and due to high interferometric sensitivity to small displacements. In the first part of this thesis, the bistatic operation mode of KAPRI is developed and validated. In the latter two parts, bistatic KAPRI is used to investigate the bistatic scattering properties of snow and ice-covered environments, using two different approaches.

The first part of this thesis focuses on development of the bistatic operation mode of KAPRI, and the associated data processing and polarimetric calibration procedures. A bistatic signal model was developed, which accounts for the offset between the internal oscillators of the two devices forming the bistatic configuration. This offset was compensated through the use of a synchronization link which transmits part of the pulse directly between the two devices. Processing procedures which allow coregistration of bistatic and monostatic datasets were developed through analysis of the elliptical acquisition geometry. The challenge of bistatic polarimetric calibration was resolved through development of a custom

active calibration device usable in arbitrary geometries. The associated novel calibration method was compared with the established monostatic procedure, thus validating the novel method for bistatic use.

The second investigation employs KAPRI to study the bistatic scattering properties of snow cover on top of the Great Aletsch Glacier in Switzerland. Two multi-modal time series datasets encompassing full-polarimetric, interferometric, monostatic and bistatic acquisitions were acquired, one in August 2021, and one in March 2022. Analysis of the data revealed considerable differences in polarimetric scattering between the two seasons, caused by the yearly cycle of changing structure of the snow cover. Particular attention was given to polarimetric phase differences, which exhibit a diametrally different response between the two seasons. The results indicate that the co-polar phase difference (CPD) exhibits a smooth, predictable spatial behaviour in summer when the snow cover is firn-like. In winter it exhibits rapid variation and phase-wrapping, thus complicating the use of CPD inversion methods to retrieve snow property information. Analysis of bistatic polarimetric data also revealed the presence of non-reciprocal scattering processes, which manifested itself in the non-zero value of the phase difference between the two cross-polarized polarimetric channels, HV and VH. The temporal coherence of the scene was analyzed and revealed the decorrelation timescale of the snow cover to be between 4-12 hours. This constrains the maximal allowable revisit time for repeat-pass radar methods at Ku-band.

The third investigation of this theses focuses on a specific phenomenon, the coherent backscatter opposition effect (CBOE). We performed the first full bistatic characterization of this effect in the Earth's cryosphere with a terrestrial sensor (KAPRI) at Ku-band, and with a spaceborne sensor (TanDEM-X) at X-band. The results revealed that the CBOE occurs in terrestrial snow at radio wavelengths, and is detectable at Ku-band in relatively thin seasonal snow layers with thickness of several meters. At X-band the effect was detected in deep firn areas of the Great Aletsch Glacier, indicating the need for a thicker snow layer in order to detect the effect at X-band. Through application of a CBOE scattering model, we were able to relate the angular width and height of the observed enhancement peaks to the scattering and absorption mean free paths of the radio waves within the snow layer. This showcased a possible pathway towards snow parameter estimation through bistatic radar observations of the CBOE.

ZUSAMMENFASSUNG

Bistatische Radarbildgebung ist eine Fernerkundungsmethode, bei der räumlich getrennte Radiowellensender und -empfänger verwendet werden, wodurch ein zweidimensionales Bild der Reflexionseigenschaften von Objekten eines bestimmten Bereiches erzeugt werden kann. Im Vergleich zu den gebräuchlicheren monostatischen Radarsystemen (bei welchen sowohl Transmitter auch Empfänger am selben Ort positioniert sind), eignen sich bistatische Radarsysteme als hochspezialisierte Geräte für ausgewählte Untersuchungen. Die spezifischen Eigenschaften sowie die Komplexität der bistatischen Radarsysteme führen dazu, dass sowohl bistatische Geräte als auch die damit verbundenen Datensätze nur schlecht verfügbar sind. Dies ist ein Hindernis, um Studien durchzuführen, welche ein solches bistatisches System voraussetzen. Im Bereich der Erdbeobachtung können solche Studien mit dem Ziel der Erforschung nicht-reziproker Streuprozesse, welche in der monostatischen Variante nicht ersichtlich sind, durchgeführt werden. Es können ebenfalls Phänomene mit spezifisch bistatischen Eigenschaften erforscht werden.

Diese Dissertation verwendet KAPRI, ein bodengestütztes, polarimetrisches Radarinterferometer im Ku-Band, welches auf dem Gamma Portable Radar Interferometer (GPRI) basiert. KAPRI wurde vom Hersteller spezifisch modifiziert um voll-polarimetrische bistatische Radaraufnahmen durchzuführen. So kann es für Studien verwendet werden, die bistatischen Streuprozesse untersuchen, welche im Ku-Band in verschiedensten Umgebungen auftreten können. Die Ku-Band Frequenz von KAPRI ist für Studien von gletscher- und schneebedeckten Umgebungen aufgrund der relativ kurzen, aber nicht vernachlässigbaren Penetrationstiefe in Schnee und Eis, sowie der hohen interferometrischen Sensitivität von kleinen Verschiebungen der Oberfläche besonders attraktiv. Im ersten Teil dieser Dissertation wird der bistatische Operationsmodus von KAPRI entwickelt und validiert. In den folgenden zwei Teilen wird KAPRI verwendet, um bistatische Streuprozesse auf schnee- und eisbedeckten Umgebungen mittels zweier Ansätze zu analysieren.

Der erste Teil dieser Arbeit befasst sich mit der Entwicklung des bistatischen Operationsmodus von KAPRI und den damit verbundenen Verfahren zur Datenverarbeitung und der polarimetrischen Kalibrierung. Es wurde ein bistatisches Signalmodell entwickelt, welches den Versatz zwischen den internen Oszillatoren der beiden Geräte, die die bistatische Konfiguration bilden, berücksichtigt. Dieser Versatz wurde durch die Verwendung einer

Synchronisierungsverbindung kompensiert, welche Teile des Radarsignals direkt zwischen den zwei Geräten überträgt. Durch die Analyse der elliptischen Aufnahmegeometrie wurden Verarbeitungsverfahren entwickelt, die eine Koregistrierung von bistatischen und monostatischen Datensätzen ermöglichen. Die Herausforderung der bistatischen, polarimetrischen Kalibrierung wurde mit der Entwicklung eines aktiven Kalibrierungsgerätes, das in unterschiedlichsten Anordnungen verwendet werden kann, gelöst. Die damit verbundene neue Kalibrierungsmethode wurde mit dem etablierten Verfahren für monostatische Messungen verglichen, wodurch die neue Methode für den bistatischen Einsatz validiert werden konnte.

Im zweiten Teil der Arbeit wird KAPRI verwendet, um die bistatischen Streueigenschaften der Schneedecke auf dem grossen Aletschgletscher in der Schweiz zu untersuchen. Zwei multimodale Zeitreihendatensätze, die aus voll-polarimetrischen, interferometrischen, monostatischen und bistatischen Daten bestehen, wurden aufgezeichnet; der erste im August 2021, und der zweite im März 2022. Die Datenanalyse zeigte nicht zu vernachlässigende Unterschiede in der polarimetrischen Streuung zwischen den zwei Jahreszeiten, ausgelöst durch den jährlichen Zyklus der sich verändernden Schneedecke. Ein besonderer Fokus wurde auf die polarimetrischen Phasendifferenzen gelegt, die ebenfalls einen grossen Unterschied zwischen den beiden Jahreszeiten aufwiesen. Die Ergebnisse zeigen, dass die co-polare Phasendifferenz (CPD) im Sommer, wenn die Schneedecke firnartig ist, ein gleichmäßiges, räumlich vorhersehbares Verhalten aufweist. Im Winter zeigt sie rasche Schwankungen und Phasenverschiebungen, was den Einsatz von CPD-Inversionsmethoden zur Ermittlung von Informationen über Schneeeigenschaften erschwert. Die Analyse bistatischer polarimetrischer Daten zeigte auch das Vorhandensein nicht-reziproker Streuprozesse, welches sich in einem von Null verschiedenen Wert der Phasendifferenz zwischen den beiden kreuzpolarisierten polarimetrischen Kanälen HV und VH manifestierte. Zusätzlich wurde die zeitliche Kohärenz der Szene analysiert und gezeigt, dass die Dekorrelationszeitzeit der Schneedecke zwischen 4 und 12 Stunden liegt. Dies schränkt die maximal zulässige Wiederholungszeit für Repeat-Pass-Radarmethoden im Ku-Band ein.

Der dritte Teil dieser Arbeit legt den Fokus auf ein spezifisches Phänomen mit dem Namen "coherent backscatter opposition effect"(CBOE). Hierbei wurde die erste vollständige bistatische Charakterisierung dieses Effektes in der Kryosphäre der Erde mit dem terrestrischen Sensor KAPRI im Ku-Band und mit dem Weltraumsensor TanDEM-X im X-Band durchgeführt. Die Resultate zeigten, dass der CBOE in Schnee bei Radiowellen auftritt, und im Ku-Band auch bei relativ dünnen saisonalen Schneeschichten (mit der Dicke von einigen Metern) messbar ist. Im X-Band wurde der Effekt in tiefen Firnbereichen des Aletschgletschers gemessen, was darauf hindeutet, dass eine dickere Schneeschicht erforderlich ist,

um den Effekt im X-Band zu erkennen. Durch die Anwendung eines CBOE-Streumodells war es uns möglich, die Winkelbreite und -höhe der beobachteten Ausschläge mit den durchschnittlichen Streu- und Absorptionslängen der Radiowellen in Relation zu setzen. Dies zeigte einen möglichen Weg in Richtung einer Schneeparameterschätzung anhand von bistatischen radargestützten Beobachtungen des CBOE.

ACKNOWLEDGEMENTS

The achievements of this thesis wouldn't have been possible without the support, guidance, and encouragement of my supervisor Prof. Dr. Irena Hajnsek, and my co-supervisor Dr. Othmar Frey. I would also like to acknowledge Dr. Silvan Leinss and Dr. Charles Werner, who both provided invaluable inputs and suggestions leading to very exciting avenues of research which would not have been discovered without them, and Michael Arnold whose technical and mountaineering skills enabled this research to go to places I would not be capable of going myself. I would also like to give recognition to my former supervisors Dr. Christian Erd, Dr. Kyle Douglass, and Dr. Dalibor Šulc, who guided me in earlier work and research endeavours which ultimately brought me to the ETH.

At the ETH I had the pleasure of working with wonderful people – Simone, Adnan, Roberto, Rafael, Ani, Philipp, Lanqing, Shiyi, Pol, Yuta, Tingting, Manuel, Giulia, Clotilde, Magnus, Kathrin, and Esther – who made also the working hours and lunch breaks enjoyable with sometimes productive and sometimes less productive but nevertheless entertaining discussions.

I am thankful for all the friends I made along my (at this point quite extensive) academic journey – Lukáš, Michal, Tomáš, Gleb, Zoey, Alena, Igor, Peter, Beta, Jan, Gleb, Tamanna, Kieran, Maria, Niccolò, Peter, Denisa, Csaba, Laylan, and many others. While with many of them we are often separated by distance, I always look forward to our next reunion, which I wish there will be many of in the future.

My gratitude goes to Catrina, whose support helped me overcome the challenges of the PhD study, and to her welcoming and kind family. I would also like to thank everyone else who made Zurich feel familiar during my studies – Fabian, Mariana, Alina, Fiona, Vladimír, Lydie, Aleš, Adam, Peter, Bára, and all others.

Finally, my utmost thank you belongs to my family and especially my parents, Alena and Patrik, who always provided me and my brothers, Peter and Pavol, with every kind of support we could wish for.

CONTENTS

1

INTRODUCTION

1.1 MOTIVATION AND RELEVANCE

Radar (an acronym for "RAdio Detection And Ranging") is an all-encompassing term for methods which use the radio frequency part of the electromagnetic spectrum to detect and study objects at a distance. Its roots reach into the early 20-th century when it was used as a tool for rudimentary detection of objects in shipping and aviation, but it has since then developed into a highly-advanced industry which influences virtually all aspects of our daily life. In this time, radar had also become an invaluable tool for study of the environment, offering multiple standalone benefits as well as complementary properties to other remote sensing or in-situ measurement methods.

The vast majority of today's radar sensors used for environmental applications operate in a so-called monostatic regime, i.e. a mode of operation where the transmitter and the receiver are placed in the same location (or the distance between them is negligible). This is due to the simpler nature of monostatic measurements, since both components can be operated from one platform, and the challenges of their synchronization and simultaneous operation are simplified. However, monostatic radar sensors can only observe a small part of the overall scattering processes, since they can by definition only detect radio waves which are scattered directly back in the direction they arrived from (i.e. back towards the radar system). If one wants to detect radio waves scattered in a different direction, the transmitter and the receiver need to be spatially separated – this configuration is referred to as bistatic radar.

Operation of bistatic radar systems introduces challenges of separate operation of the transmitter and the receiver, and of their synchronization. Furthermore, due to their spatial separation, the two components usually need to be operated on separate platforms, which increases developmental and operational costs. The processing of bistatic data also usually requires additional steps due to a more complicated geometrical configuration of the observations. All these factors limit the proliferation of bistatic radar systems. Nevertheless, there is persistent interest in applications of bistatic radar systems for Earth observation, as they are better-suited for observation of particular scattering phenomena (such as opposition effects or specular reflection) and application of certain acquisition methods (such as long-baseline single-pass interferometry).

A large benefit of radar Earth observation methods is that they are scalable – spaceborne radar sensors are capable of imaging a large part of the Earth's surface in a relatively short amount of time. Current radar satellite systems are capable of providing virtually worldwide observation coverage with revisit times on the order of days to weeks. However, novel observation concepts require extensive investigation and validation before they can be deployed as a spaceborne mission. These exploratory investigations are usually carried out with airborne or ground-based sensors, which are more flexible in terms of their configuration, and less costly to develop and operate. For investigation of bistatic concepts, these exploratory systems need to have bistatic capabilities. Systems with bistatic capabilities are currently relatively rare, which reduces the availability of validation data, acting as a further obstacle towards development of bistatic radar observation concepts. Development and use of ground-based bistatic radar systems can help overcome this obstacle and can facilitate investigation, development and validation of novel radar observation concepts. The knowledge gained from these ground-based systems can also enable more efficient scaling of these concepts to airborne and spaceborne systems.

Snow and ice-covered environments can particularly benefit from radar remote sensing observations. The Earth's cryosphere provides some of the most useful indcators of climate variability and change, yet is considered one of the most under-sampled domains of the Earth system [1]. This is due to their remoteness and inhospitability, which make long-term in-situ monitoring challenging. Spaceborne radar remote sensing can provide large-scale and long-term access to these environments, and for this reason there is a large interest in development of novel radar remote sensing methods for estimation of parameters of terrestrial snow and ice. Radio waves can penetrate relatively deep into dry snow and ice, which offers the possibility of probing of deeper layers, however it also reduces sensitivity to snow layers of limited thickness, such as seasonal snow cover. For this reason short radio wavelengths (such as X-, Ku-, and Ka-band) are of particular interest, since their penetration depth is shorter as opposed to e.g. P- or L-band, and thus they can retrieve information about snow properties even if the snow layer's thickness is too limited for application of longer wavelengths.

Observation of snow-covered environments with a ground-based bistatic Ku-band radar system, which is the central theme of this dissertation, occurs at the intersection of the above-mentioned motivating factors. It allows investigation of previously unexplored radar measurement configurations in a relatively low-cost and flexible manner, and observation of snow scattering phenomena which are not possible to characterize in the conventional monostatic regime. This can yield useful information for better understanding and modeling

of scattering behaviour of snow and ice at Ku-band, thus improving our understanding of snow as an Essential Climate Variable [2]. The lessons learned from ground-based observations can also open pathways towards development of novel spaceborne Earth observation mission concepts incorporating bistatic and/or Ku-band radar observations.

1.2 BACKGROUND

This section aims to provide a brief introduction into radar Earth observation, with focus on the topics relevant to the scope of this dissertation, namely radar imaging, frequency modulated signals, real-aperture radar, bistatic radar, radar interferometry and polarimetry, and radar monitoring of snow and ice. Ample references are provided for a more in-depth introduction of each topic.

1.2.1 *Radar imaging*

An imaging radar is a device which, through the use of radio waves, constructs a two-dimensional image of a particular area. While the output often resembles an aerial photograph taken with an optical camera, the principle of operation and data reconstruction is diametrally different, and the data has to be interpreted accordingly. One notable difference of radar imaging sensors as opposed to optical sensors is that radar imaging sensors are active sensors, i.e. they provide their own source of illumination. This has the benefit that they can operate irrespective of time and day. Furthermore, since radio waves can penetrate through fog and clouds relatively unobstructed, radar imaging sensors can also operate in poor weather and low visibility conditions. The topic of imaging radar, its acquisition principles, and geometric effects is the subject of a large number of research articles and textbooks [3–13]. This introduction thus only outlines selected basic concepts that distinguish it from other imaging methods.

1.2.1.1 *Real vs. synthetic aperture radar*

Every active radar sensor is based on the principle of transmitting a known radar signal, and then measuring the travel time of the signal's echoes which were reflected from the observed objects. Each individual transmit-receive sequence forms a single line of the image, called a range line. Through a process referred to as range compression, the range distance of individual targets within this range line can be determined. This is done by

quantifying the travel time of each signal T, and relating it to total distance traveled p through the speed-of-light formula $p = cT$. This value is then in turn usually transformed to range r, the distance between the radar and the reflecting object. Assuming a simple sensor with co-located transmitter and receiver (a monostatic sensor), and a straight-line path between the radar and the scattering object, the range is calculated trivially as $r = p/2$. This calculation provides information about the object's distance from the radar, however it does not provide information about the left-right direction, since a basic radar system does not have the ability to detect from which direction (within the beam of its antennas) the scattered signal came from. This directional ambiguity can be addressed using different approaches. It can be resolved by either physically reducing the width of the radar beam through use of a large antenna (real-aperture radar, RAR), or by coherently acquiring several range lines with a moving sensor and then applying an azimuth compression algorithm to identify the closest-approach point of each target (synthetic aperture radar, SAR). A two-dimensional image containing the information about the scattering amplitude and phase, called a single-look complex (SLC) image is produced. Each SLC image has a range and an azimuth direction, which are intrinsically tied to the acquisition geometry. Figure 1.1 illustrates the difference between the RAR and SAR image forming procedures.

Real-aperture radar reduces the directional ambiguity of the received signal by reducing the physical angular size of the transmitting and/or receiving antennas' beam. The angular width of an antenna's beam θ_{ant} can be approximated as

$$\theta_{\text{ant}} = \frac{\lambda}{L_{\text{ant}}} \tag{1.1}$$

where λ is the wavelength of the radio signal, and L_{ant} is the physical size of the antenna. This equation shows that the angular width of the beam can be reduced by increasing the physical size of the antenna. Thus, by making the antenna larger, the width of the beam along that direction can be reduced, which increases the resolving capability of the system, since the span of possible directions from which the signal reflections can be received is reduced. The radar's azimuth resolution (i.e., the minimal separation distance for two objects to be separately resolvable) at range r can then be approximated as the width of the beam at the particular range distance

$$\delta_{\text{RAR}} = \theta_{\text{ant}} r = \frac{\lambda r}{L_{\text{ant}}} \tag{1.2}$$

By physically moving or rotating the antenna, the beam can be consecutively pointed at different parts of the scene, and a complete image of the observed scene can be reconstructed.

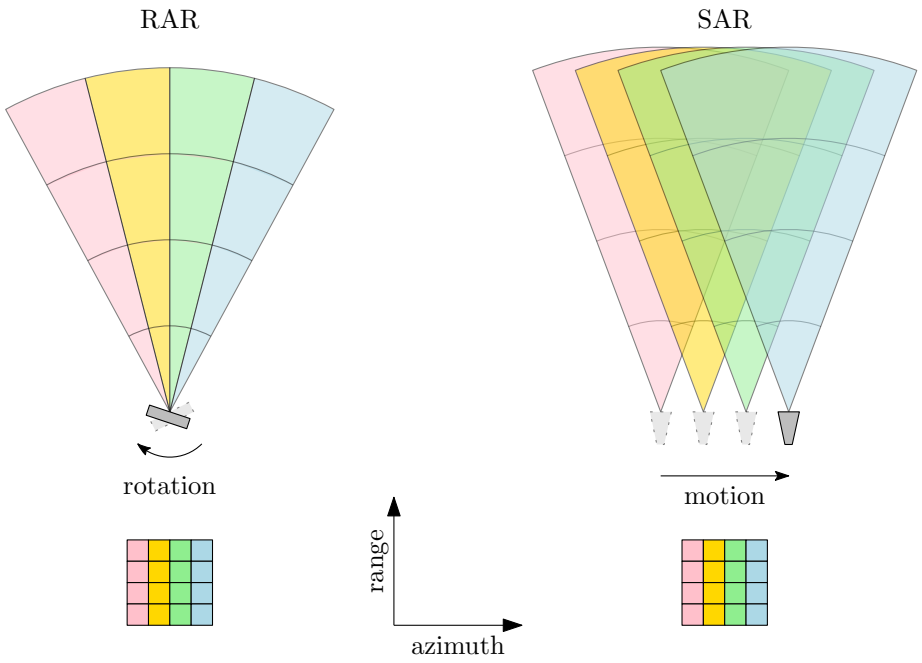

FIGURE 1.1: Comparison of (typical) image forming methods of real aperture radar (RAR), and synthetic aperture radar (SAR). Each color represents the acquisition of one range line, i.e. one Tx-Rx sequence. RAR uses a rotating platform with a narrow beam. To avoid left-right ambiguity, each target is only present within the beam for one range line, and thus RAR does not need to perform azimuth compression. SAR uses a moving platform and each target is usually present within the beam for several range lines. An additional processing step, called azimuth compression, eliminates this left-right ambiguity by identifying the target's nearest approach point using the target's Doppler phase.

The physical size of the antenna can be adjusted along two different dimensions; the antenna's horizontal width w and vertical height h can be adjusted separately. These dimensions then respectively translate to the beam's angular width along the left-right direction (also known as the "azimuth" direction), and along the up-down direction (the "elevation" direction). Some systems have both a large antenna width and a large antenna height, resulting in narrow beam widths along both azimuth and elevation. This setup is called a "pencil-beam" setup. This provides excellent directional resolving capability, however due to the beam's small size the area that can be covered at any time is small. To increase the covered area, pencil-beam systems need to perform a scan in both the azimuth and elevation direction, increasing the needed acquisition time. An alternative real-aperture approach (used by KAPRI) is a so-called "fan-beam" setup, where the antenna's width is large, but the height is reduced. This results in a beam that is narrow in azimuth, but wide in elevation. This increases the elevation coverage of the beam, and thus only an azimuthal scan is needed to cover the whole scene. The elevation ambiguity of the received echoes is then usually resolved in post-processing. For example, if a digital elevation model (DEM) of

the observed scene is available, the target's elevation can be determined from its range by assuming that the target is placed at ground level. A comparison of pencil beam and fan beam concepts is shown in Figure 1.2.

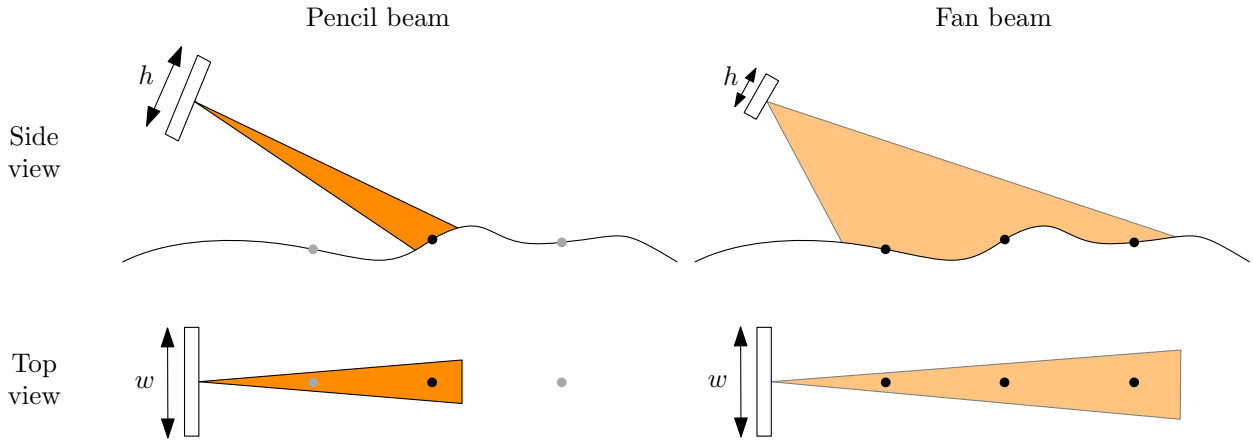

FIGURE 1.2: Comparison of pencil beam and fan beam real-aperture radar concepts. The pencil beam setup (left) has a large antenna width w and a large antenna height h, forming a narrow beam in both dimensions. This ensures strong signal intensity, however it also reduces coverage – only one of the three points of the scene is covered by the beam; the other two are not covered. The fan beam setup (right) has a reduced antenna height h, which results in a larger beam spread in the vertical direction. This increases coverage at cost of reduced signal intensity. The azimuthal angular resolution is unchanged between the two concepts, since the antenna width w is identical.

Since the resolving capability of real-aperture radar systems is tied to the width of their beam, their azimuth resolution quickly degrades as range increases. Furthermore, at longer wavelengths the antenna sizes necessary to achieve a good resolving capability are prohibitively large for most applications. Nevertheless, they are compact and robust, and at short wavelengths and relatively short distances they can provide excellent resolution and coverage, making them well-suited for ground-based applications.

Synthetic aperture radar sensors use a moving platform to overcome the resolution limit imposed by the antenna beam's width. By moving the sensor along the azimuth direction, SAR sensors record several echoes from different positions and coherently combine them to *synthesize* a virtual antenna with a much larger size than the actual physical size of the antenna used to transmit/receive the signal.

The length of the synthetic aperture L_{SAR} can be determined as the spatial separation between the points where the target enters and leaves the antenna's beam (see Figure 1.3):

$$L_{\mathrm{SAR}} = \lambda r / L_{\mathrm{ant}}. \tag{1.3}$$

SAR systems use the Doppler frequency shift – caused by the relative motion of the sensor with respect to the target – to identify the target's azimuthal position. A target at range

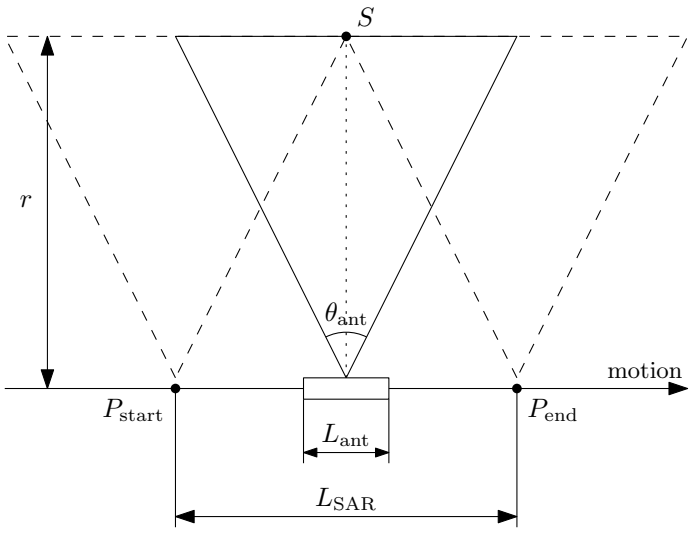

FIGURE 1.3: Principle of synthetic aperture radar (SAR). A relatively small antenna of size L_{ant} (with corresponding real-aperture azimuth resolution $\delta_{\text{RAR}} = \lambda r / L_{\text{ant}}$) is placed on a moving platform. A scatterer S placed at range r enters the beam when the radar is at position P_{start}, and leaves the beam at position P_{end}. Radar echoes acquired between these two points can be coherently combined to synthesize an aperture with length L_{SAR}. The resulting azimuth resolution is $\delta_{\text{SAR}} = L_{\text{ant}}/2$. A smaller antenna thus results in better resolution, at cost of increased aperture length.

r which is offset by distance x from the central axis of the antenna's beam will exhibit a Doppler shift f_{d}:

$$f_{\text{d}} = \frac{2v}{\lambda r} x \tag{1.4}$$

where v is the relative velocity of the system and the target [6, 13]. The azimuthal resolution of the system (i.e. the precision of the azimuth position measurement δx) is thus linearly related to the capability to resolve the Doppler frequency δf_{d}:

$$\delta_{\text{SAR}} = \delta x = \frac{\lambda r}{2v} \delta f_{\text{d}} \tag{1.5}$$

The Doppler frequency resolution δf_{d} depends on the duration that the target spent within the beam – i.e., the longer the target's Doppler phase history can be measured, the more precisely can its Doppler frequency shift be determined. The frequency resolving capability can thus be approximated as the inverse of the total time duration which the target spent inside the beam $\tau = \frac{L_{\text{SAR}}}{v}$ [13]:

$$\delta f_{\text{d}} \approx \frac{1}{\tau} = \frac{v}{L_{\text{SAR}}}. \tag{1.6}$$

The SAR azimuth resolution can then be determined by combining eqs. (1.3), (1.5), and (1.6):

$$\delta_{\text{SAR}} = \frac{\lambda r}{2v} \frac{v}{L_{\text{SAR}}} = \frac{\lambda r}{2v} \frac{v L_{\text{ant}}}{\lambda r} = \frac{L_{\text{ant}}}{2}. \tag{1.7}$$

Comparing eq. (1.7) to (1.2) shows that reducing the antenna size of a SAR sensor actually increases the resolving capability (as opposed to reducing it for a RAR sensor), and the resolution is no longer tied to the range distance of the target. For this reason, virtually all spaceborne radar sensors and a large fraction of airborne and ground-based sensors utilize aperture synthesis, since the platform can be much more compact. However, the moving-platform nature of SAR measurements makes their operation more costly, and their trajectory stability requirements are sometimes difficult to satisfy with ground-based sensors for long aperture lengths. For this reason, real-aperture sensors retain their use cases, especially when operation on long time scales and/or short revisit times is required.

1.2.1.2 *Topographic effects*

Active radar imaging sensors for Earth observation in the side-looking geometry are susceptible to geometrical distortions which are caused by the relation of the local topography to the incidence angle of the side-looking system. The three common types of distortions are shadowing, foreshortening, and layover.

Shadowing occurs when tall topographic features in the near range obstruct the line of sight to the features behind them. The transmitted pulses thus cannot reach the shadowed areas, and no information from these areas can be retrieved. Foreshortening occurs on positive slopes of mountains (i.e. slopes facing toward the radar sensor), where the local topography causes a large area of the slope to fall within one range cell, thus reducing the ground-range resolution. Layover is an extreme case of foreshortening where the local slope of the topographic features exceeds the incidence angle of the sensor, and thus peaks of mountains appear closer in range to the sensor than the base, even though the ground range distance of the base of the mountain is shorter than the ground-range distance of the peak. The three effects are visualized in Figure 1.4.

The magnitude of all three effects is related to the incidence angle of the sensor. At low incidence angles (i.e. steep incidence of the signal), shadowing is mitigated while the scene is prone to foreshortening and layover even in relatively smooth topography. At high incidence angles (i.e. shallow incidence of the signal), the opposite scenario occurs and thus foreshortening and layover occur only in the steepest topographies, while shadowing occurs frequently even in smooth topography. The choice of a particular incidence angle is thus a partial trade-off between shadowing on one side, and foreshortening and layover on the other.

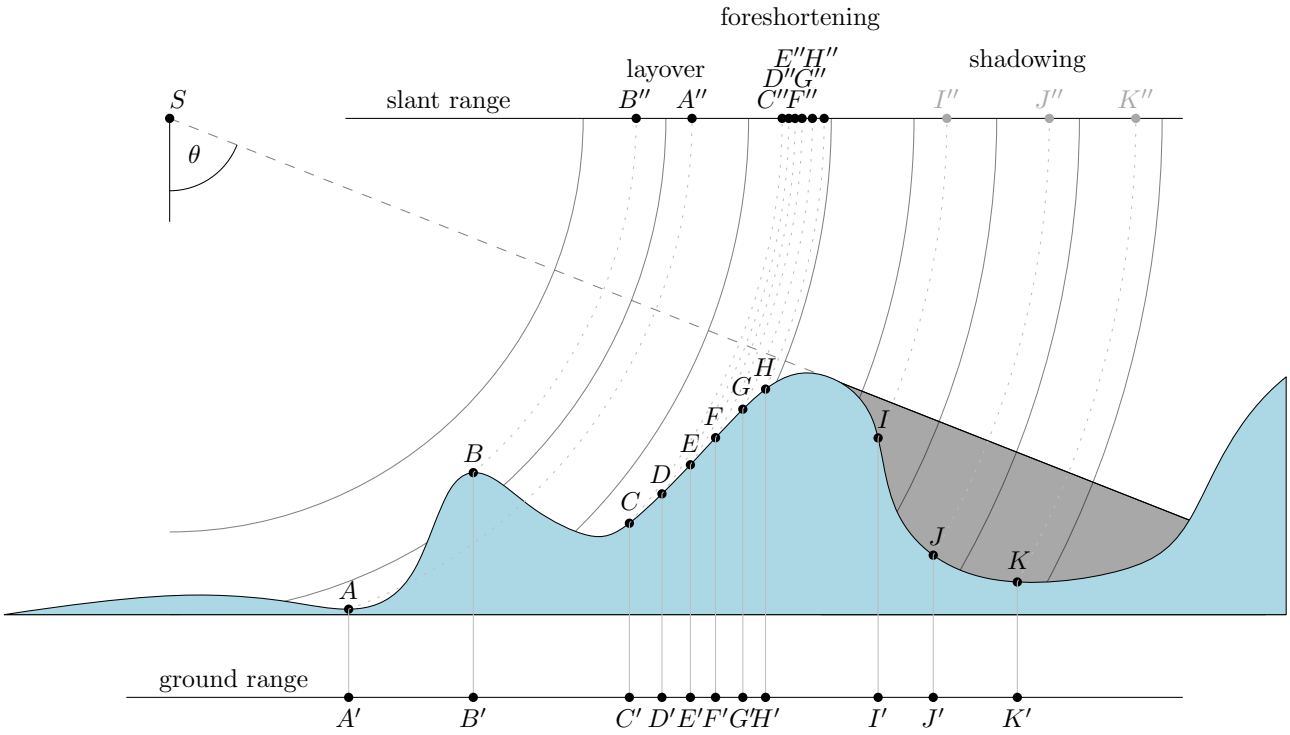

FIGURE 1.4: Visualization of the three geometric effects affecting the radar acquisition geometry. Points A, B are affected by layover, as their relative order with respect to the sensor S is flipped in the slant range geometry as opposed to the ground range geometry. Points $C - H$ are affected by foreshortening, as their relative distance in slant range is much shorter than their ground range distance. Points $I - K$ are affected by shadowing, since they are not visible to the radar due to topography. The magnitude (or likelihood) of layover and foreshortening increases with decreasing incidence angle θ, while the magnitude of shadowing increases as θ increases.

1.2.2 *Radar signal processing*

Since this thesis is centered around use of real-aperture radar systems, in this section only the properties of individual radar pulses are discussed. Aperture synthesis and azimuth processing, which form the basis of synthetic aperture radar, are considered out of scope of this introduction.

1.2.2.1 *Pulses and frequency modulation*

In terms of the properties of the transmission-reception procedure and signal model, the most commonly known type of radar is a "pulsed radar" system. This system involves transmitting a (relatively) short EM pulse (also known as "chirp") towards the observed scene and then switching to reception mode and "listening" for the returning echoes. Echoes from targets at different ranges will arrive back at the sensor at different times, and thus these echoes can be separated from one another by performing a "matched filter" operation,

i.e. a convolution of the received signal with the transmitted chirp. This process is referred to as range compression. The resolving capability (i.e. the smallest range difference between two targets that can still be distinguished) is given by the bandwidth of the chirp W:

$$\delta_r = \frac{c}{2W}. \tag{1.8}$$

The pulse energy is the total amount of energy delivered over the duration of one pulse, and affects the sensitivity of the system. It can be defined (in a simplified form) as:

$$E = \int_0^\tau P(t)\mathrm{d}t. \tag{1.9}$$

where $P(t)$ is the instantaneous power output of the transmitter.

The chirp itself can have an arbitrary waveform. One of the most simple chirp waveforms is a rectangular chirp

$$s_{\text{rect}}(t) = \begin{cases} e^{i2\pi f_c t} & -\tau/2 \leq t \leq \tau/2, \\ 0 & \text{otherwise.} \end{cases} \tag{1.10}$$

where f_c is the carrier frequency of the signal. The bandwidth of the rectangular chirp is the inverse of its pulse length τ:

$$W_{\text{rect}} = \frac{1}{\tau}, \tag{1.11}$$

and thus the shorter the chirp, the better is the resolving capability. However, the rectangular pulse suffers from a trade-off between its bandwidth W and its pulse energy E. For the rectangular pulse, the instantaneous power output is constant and equal to the peak power output P_{peak}:

$$E = P_{\text{peak}}\tau. \tag{1.12}$$

The drawback of the rectangular pulse thus is that the delivered pulse energy E is (through the pulse length τ) inversely related to the bandwidth and thus also inversely related to the resolving capability. Therefore there will always be a trade-off between the signal-to-noise ratio (which requires a long pulse) and the range resolution (which requires a short pulse).

The linear frequency-modulated chirp overcomes this limitation by transmitting a different waveform:

$$s_t(t) = \begin{cases} e^{i2\pi\left[f_c t + \frac{\gamma}{2}t^2\right]} & -\tau/2 \leq t \leq \tau/2, \\ 0 & \text{otherwise.} \end{cases} \tag{1.13}$$

where $\gamma = W_{\mathrm{FM}}/\tau$ is referred to as the chirp rate. The bandwidth of the FM chirp W_{FM} becomes decoupled from the pulse length τ, and thus both the pulse energy defined by eq. (1.12) and the resolving capability defined by eq. (1.8) can be adjusted independently. This reduces the demand on the power electronics of the radar system, since the SNR can now be increased by increasing the pulse length, without needing to increase the peak power output P_{peak} or sacrificing resolving capability. However, in case the same antenna is used for transmission and reception, then the need to receive echoes from a particular set of range distances precludes the radar from transmitting at the corresponding times, imposing a scheduling constraint on the Tx-Rx sequence.

The frequency-modulated continuous-wave (FMCW) radar concept overcomes this scheduling constraint by employing a separate set of transmit and receive antennas. This allows the radar to transmit continuously and achieve very high signal-to-noise ratios with comparatively very low peak power output P_{peak}. The transmitted signal has the same form as the FM pulse shown in eq. (1.13), with the distinction that the individual chirps of length τ immediately follow one after another with no delay, thus maximizing the value of τ.

The continuous signal echo received from any particular scatterer (barring transitional phenomena at chirp edges) can then be expressed as a time-delayed version of the transmitted chirp:

$$s_{\mathrm{r}}(t) = e^{i2\pi\left[f_{\mathrm{c}}(t-T)+\frac{\gamma}{2}(t-T)^2\right]} \tag{1.14}$$

where the travel delay time T is related to the range distance of the scatterer r:

$$T = 2r/c \tag{1.15}$$

The necessary sampling frequency of the receiver's analog-to-digital converter (ADC) can also be dramatically reduced through the use of the deramp-on-receive architecture, where the received signal s_{r} is immediately multiplied by the complex conjugate of the transmitted signal s_{t}^*, before digitization:

$$s_{\mathrm{d}}(t) = s_{\mathrm{r}} s_{\mathrm{t}}(t)^* = e^{-i2\pi f_{\mathrm{c}} T} e^{-i\pi\gamma T^2} e^{i2\pi\gamma T t}. \tag{1.16}$$

It is important to note that the time delay T is constant for any scatterer, and thus the deramped signal $s_{\mathrm{d}}(t)$ contains only one oscillating term with a range-dependent beat frequency f_{b}:

$$f_{\mathrm{b}}(r) = \gamma T = \frac{2\gamma r}{c}, \tag{1.17}$$

and two constant phase terms, the interferometric phase term

$$\phi_{\text{int}} = -2\pi f_c T = -4\pi r/\lambda, \tag{1.18}$$

and the "residual video phase" term

$$\phi_{\text{rvp}} = -\pi\gamma T^2 = -4\pi r^2\gamma/c^2. \tag{1.19}$$

The deramped signal can thus be rewritten as

$$s_d(t) = e^{i(2\pi f_b t + \phi_{\text{int}} + \phi_{\text{rvp}})}. \tag{1.20}$$

Figure 1.5 visualizes the relationship of time-dependent frequencies of the transmitted and the received chirp.

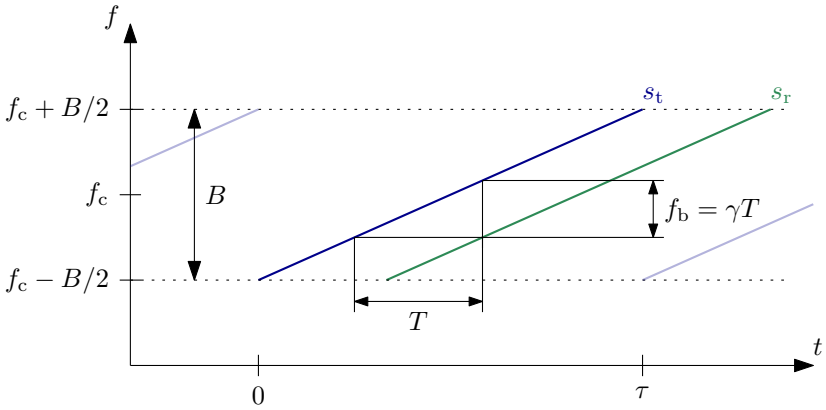

FIGURE 1.5: Time-frequency diagram of an FMCW chirp. The received chirp s_r is delayed by travel time T with respect to the transmitted chirp s_t. The slope of the lines describing both chirps is equal to $\gamma = B/\tau$. Complex conjugate multiplication of the two chirps within the receiver $s_r s_t^*$ yields a beat signal with oscillating frequency f_b. The travel time T can thus be computed as f_b/γ, and from the travel time the range can be computed as $r = c/T$. Transitional phenomena occur near $t = 0$ and $t = \tau$, and thus samples from these areas are usually excluded in processing.

Usually the received signal contains echoes from a large number of scatterers. The received signal is then a coherent superposition of these individual echoes. Since the scatterers are placed at different range distances, each echo will have a different beat frequency $f_b(r)$. The range compression is performed by applying the Fourier transform on the deramped signal. This process separates the echoes from individual targets into their corresponding frequency bins and the range-dependent complex reflectivity profile of the scene can thus be retrieved.

1.2.2.2 *Signal to noise ratio*

Every radar system is affected by noise, i.e. an unwanted random component of the received signal which by definition provides no information about the observed target. While its behaviour can be usually statistically quantified, its random nature makes it impossible to remove from the received signal. In order to mitigate its influence on the resulting data, the energy delivered by the true signal E_{signal} has to be sufficiently strong so that the noise-related energy E_{noise} can be neglected. The signal-to-noise ratio (SNR) quantifies the influence of noise on the received data. The SNR for a particular radar system, geometry, and a point-like target can be calculated using the radar equation [5, 13]:

$$\text{SNR} = \frac{E_{\text{signal}}}{E_{\text{noise}}} = \frac{P_t \tau G_T G_R \lambda^2 \sigma}{(4\pi)^3 r_T^2 r_R^2 k_B T_s L}, \tag{1.21}$$

where P_t is the transmitter output power, τ is the pulse duration, G_T, G_R are the transmitting and receiving antenna's gain respectively, λ is the wavelength, σ is the target's radar cross-section, r_T, r_R are the target's respective distances to the transmitter and the receiver, k_B is the Boltzmann constant, T_s is the system noise temperature, and L are the system losses. The system noise temperature T_s depends on the setup of the signal processing chain, and is not equal to the actual temperature of the radar system, although it is usually affected by it. Similarly, the target's radar cross section σ, which is expressed in units of area, does partly depend on the target's size, but two targets of similar size can have dramatically different cross sections, depending on their shape, material, and orientation with respect to the radar system.

For distributed targets, the radar cross-section term in eq. (1.21) can be expanded as

$$\sigma = A\beta_0 = A\sigma_0 / \sin\theta \tag{1.22}$$

where A is the physical size of the radar range cell (in slant-range geometry) and β_0 is the dimensionless *radar brightness*. β_0 can be further expanded as $\sigma_0 / \sin\theta$ where the denominator accounts for the change of the range cell size due to the local incidence angle θ, and thus the dimensionless numerator term σ_0 is purely dependent on the reflective properties of the distributed target and does not depend on the acquisition geometry. σ_0 is thus an important value for characterization of natural targets.

It should be noted that the radar equation can be expressed in a multitude of ways, using e.g. the system noise figure F_n instead of noise temperature T_s, or the system bandwidth B instead of pulse duration τ. However, use of the bandwidth term B in the radar equation is

discouraged, since the system bandwidth is not necessarily equal to the chirp bandwidth, or bandwidth of any other signal within the radar signal processing chain [13]. This can easily lead to misinterpretations and incorrect SNR calculations. The energy-based approach in eq. (1.21) is less ambiguous and thus preferred.

Eq. (1.21) indicates that the SNR is inversely proportional to the fourth power of the range scale factor (SNR $\sim r^{-4}$). This is true for point-like targets whose radar cross section σ is range-independent. However, in some applications such as Earth Observation, the cross section σ can depend on range. In case of a real-aperture fan beam radar observing the ground clutter, σ is linearly dependent on range (since the size of the radar footprint on the ground scales linearly with range), and the SNR for a particular type of ground cover scales with the inverse third power of range distance (SNR $\sim r^{-3}$). Similarly, the gain of the transmitting antenna can also affect the size of the footprint, correlating the σ and G_T terms. The individual terms of eq. (1.21) are thus not independent and the equation always needs to be solved for the system as a whole.

1.2.3 *Bistatic radar*

The term *bistatic radar* [14–16] refers to a radar measurement concept where the transmitter and the receiver of the radar system are in separate locations. It is the counterpart of the *monostatic radar* concept, where the spatial separation between the transmitter and receiver is assumed to be negligible. The vast majority of currently operating imaging radar systems – regardless if they are spaceborne, airborne, or terrestrial – are monostatic. Some radar scientists go as far as to say that "bistatic radars are special-purpose devices and must be treated as such" [15].

While bistatic radar systems may be special-purpose devices, the bistatic radar concept is actually a generalization of monostatic radar. A monostatic geometry is a special case of the bistatic geometry where the separation between the transmitter and receiver, referred to as the *bistatic baseline*, is zero (or negligible). The equations of bistatic geometry are thus always a generalized form of the corresponding monostatic equations [15], and the monostatic equations can be retrieved from bistatic equations by setting the value of the bistatic baseline b to zero. This fact makes the bistatic geometry and the corresponding equations more complicated. Figure 1.6 shows a comparison between the monostatic and bistatic real-aperture geometries, where it can be seen that the bistatic geometry requires introduction of additional parameters needed to describe it.

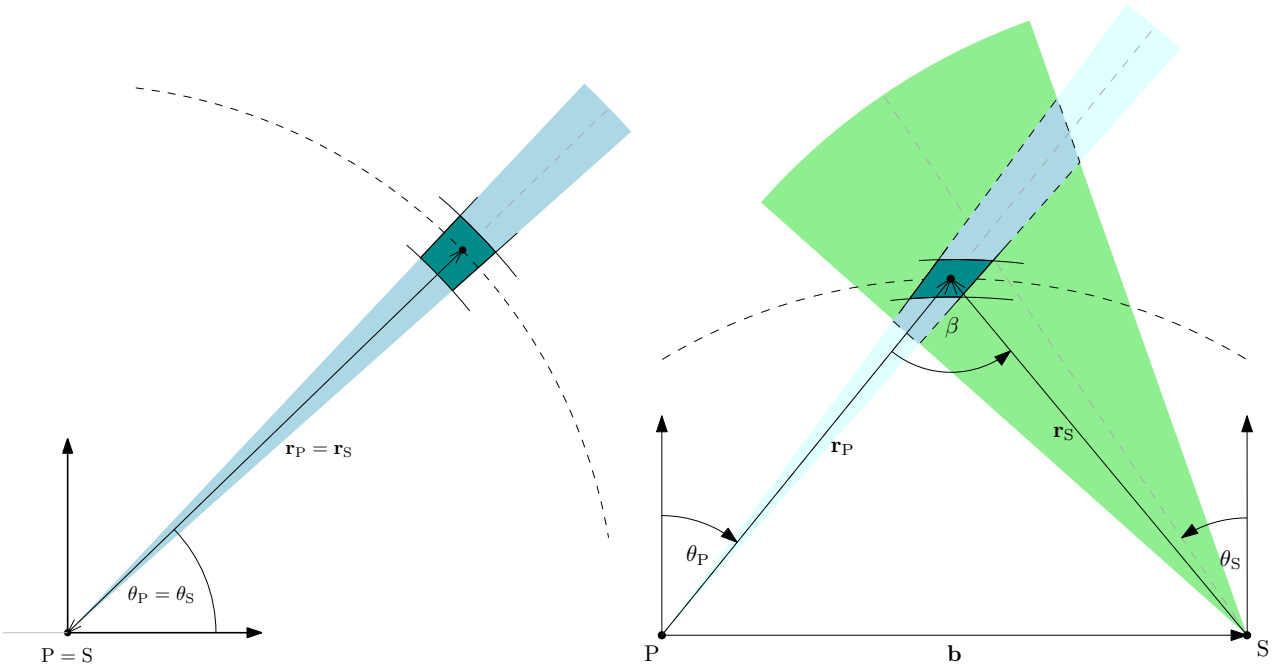

FIGURE 1.6: Comparison between a monostatic fan beam real-aperture radar setup (left), and a bistatic setup (right). The diagram is a top-down view of the geometry. In both diagrams, the transmitter's position is designated as P (primary), and the receiver's position as S (secondary). The azimuthal coordinates of the target from these positions are denoted as θ_P, θ_S respectively, and the range distances are denoted r_P, r_S. In the bistatic case, the bistatic angle (i.e. the angle between the transmitter and the receiver from the point of view of the target) is denoted as β, in the monostatic case this angle is zero by definition. $\mathbf{b}$ denotes the bistatic baseline between the transmitter and the receiver, which is also zero by defition in the monostatic case. The lines of constant range are marked as dashed lines, and have circular shape in the monostatic case, and an elliptical shape in the generalized bistatic case. The teal-colored area represents one range cell.

The line between monostatic and bistatic systems, i.e. the definition of "negligible separation" between the transmitter and receiver, is blurred and application-specific. In the strictest sense of the word "separation", any radar operating a distinct transmitting and receiving antenna would be bistatic, which is not a practical definition. As pointed out in [15], various publications attempted to define this separation as "a considerable distance" [3], "separation [...] comparable with the target distance" [14], "[angular separation] comparable or greater than either beamwidth" [17], and similar. Over the course of this dissertation, all these definitions will end up being broken at some point. The most suitable definition for the goals of this dissertation focuses instead on the technical aspects, and can be phrased as follows: *A bistatic radar system uses two spatially separated and independently operating platforms for the transmission and the reception of the signal.* This definition also highlights some of the major technical challenges faced by bistatic systems, which also limit their proliferation.

The first challenge is synchronization of the two radar platforms – to acquire a coherent radar image, a precise phase reference for the signal, that relates the phase of the transmitted

signal to the phase of the received signal, is required. This is trivial in monostatic systems (i.e., single-platform systems according to our definition), since usually both the transmitter and the receiver use the same oscillator as a time/phase reference, and thus no offsets between their phase reference signals arise. In case of a bistatic system, since the two components are separated, one either needs to find separate oscillators which are sufficiently stable to drive both components in a synchronized manner, or the two devices need to be synchronized externally, e.g. through use of a phase reference signal transmission.

The second challenge is antenna beam overlap – in monostatic systems either the same antenna is used for both transmission and reception, or two antennas pointed in the same direction are used. This achieves an optimal overlap of the transmit and receive beam patterns – i.e., at any time, every point of the scene which is covered by the transmitting antenna beam is also covered by the receiving antenna beam, and vice versa. This guarantees the maximization of coverage and of received signal strength. When the transmitting and the receiving antennas are not co-located, it becomes much more challenging to maximize the overlap of the two beam patterns, and achieving complete overlap becomes often impossible. This has the adverse effect of reducing the coverage of the scene, as well as reducing the signal-to-noise ratio. This issue usually becomes more pronounced as the bistatic angle increases. The antenna beam overlap is visualized in Figure 1.6 as the blue-colored area.

Despite the above-mentioned challenges and special-purpose character, bistatic radar certainly has its use cases due to advantageous properties – its ability to receive signal scattered at a non-zero bistatic angle, and the receiver's ability to remain "silent" (i.e., the receiver does not need to transmit any signal of its own and can remain hidden from adverse actors) make it attractive for military detection and counter-stealth applications [14, 18, 19]. In the Earth Observation domain, the ability to extend the baseline between the transmitter and the receiver can greatly increase the single-pass interferometric phase-to-height sensitivity, which is very useful for applications such as digital elevation model generation [20–22]. Differential interferometric applications include the retrieval of 3-dimensional displacement vectors [23, 24]. The fact that scattering at a different angle is observed can also be exploited by radar polarimetry to retrieve additional information about the scattering properties of the observed scene [25, 26], and possibly give access to biophysical parameters [27–30]. Finally, some scattering phenomena have an intrinsic bistatic signature, and thus bistatic observations are necessary to fully characterize them [31, 32].

Only one spaceborne radar sensor in current (or past) operation can be labeled as bistatic according to the given definition – TanDEM-X [33], operated by the German Aerospace Center. It operates with a relatively low value of bistatic angle $\beta < 1°$ which can be

considered negligible for some applications. However – in alignment with this dissertation's definition – it uses two completely separate platforms for transmission and reception, with a synchronization link in-between [34]. Several other concepts are under current evaluation, such as Harmony [35] or Tandem-L [23]. A large number of spaceborne bistatic concepts were also previously proposed [36–40]. This indicates the ongoing interest of the scientific community in bistatic radar applications.

1.2.4 *Radar interferometry*

Most current radar imaging sensors acquire a *coherent* radar signal, i.e. they record not only the received signal amplitude, but also its phase. The phase of the signal is a measure of the time (or distance) traveled by the signal from its transition until its reception. Radar interferometry makes use of the phase information of the signal in order to retrieve information about the positions of the observed targets [41–43]. Due to the periodic nature of electromagnetic wave oscillation, the signal phase can only take values between 0 and 2π, and all points along the signal's path that are separated by an integer multiple of the wavelength λ share the same phase (barring any changes in the wave's propagation velocity). This property of the phase causes interferometric methods to be very effective at detecting and quantifying small, sub-wavelength-length-scale changes in a signal's propagation path length, however if the magnitude of the changes reaches or exceeds the wavelength, the path delay retrieval will become ambiguous since the phase will periodically revisit the entire $(0; 2\pi)$ interval several times. This phenomenon is referred to as phase wrapping, and procedures which aim to compensate for this phenomenon and retrieve the true path delay are referred to as phase unwrapping [44, 45]. Two most common interferometric methods are differential interferometry and single-pass interferometry.

1.2.4.1 *Differential interferometry*

Differential interferometry performs repeated measurements of the phase of the signal scattered from a scene. By comparing the phase of two measurements, any displacement of scatterers between the two measurements will be detected as a change in phase and can be quantified. Assuming that the displacement is small compared to the wavelength, and that no other phenomena affected the phase, the displacement of the scatterer can be computed from the differential phase $\Delta\phi$:

$$\Delta r = \frac{\lambda}{4\pi}\Delta\phi, \tag{1.23}$$

where Δr is the displacement along the radar's line of sight (i.e. along the slant range direction). The 4π factor in the denominator is caused by the two-way propagation of the signal. Note that only the displacement component that occurs along the line of sight can be detected, displacement in the plane perpendicular to the line of sight does not affect the differential interferometric phase. Furthermore, in practice there are usually several other factors that affect the path delay. Since the signal usually propagates not through a vacuum but through the atmosphere, which can impose a path delay due to tropospheric effects. Furthermore, the magnitude of this path delay often evolves over time, and thus affects the differential interferometric measurements [46, 47]. Noise also affects these measurements, as well as possible changes in the scattering properties of the scene that are not related to displacement. If the temporal baseline between the two measurements is too long, a phase wrapping factor $\frac{\lambda}{2}n$ where $n \in \mathrm{Z}$ needs to be added to the right hand side of eq. (1.23). In order to successfully retrieve the true displacement using differential interferometry, one needs to properly account for all these aspects.

1.2.4.2 *Single-pass interferometry*

Single-pass interferometry employs two receivers placed in two (relatively close) locations in order to track the phase difference between the signals received by these two receivers (also known as the interferometric phase). Since the locations of the two receivers are precisely known, the measured interferometric phase (and the inferred path delay) of the signal can provide information about the position of the scattering target. One use case of single-pass interferometry is construction of digital elevation models (DEMs). It is possible to determine a scatterer's height h from its observed phase ϕ and slant range r by use of the formula [48]

$$h = r \sin\left(\cos^{-1}\frac{\phi\lambda}{2\pi B} - \theta\right) \tag{1.24}$$

where B is the interferometric baseline of the sensor, θ is the elevation angle of the bistatic baseline with respect to the horizontal plane, and λ is the wavelength. This equation can thus be used to construct the digital elevation model of the area from single-pass interferometric observations, although care has to be taken in order to properly account for phase-wrapping effects. DEM reconstruction can also be performed by carrying out two consecutive acquisitions with a single receiver in different locations, however, introduction of a temporal baseline can introduce other phase delay terms (such as the ones mentioned in Section 1.2.4.1). Single-pass interferometry is thus best performed using two receivers acquiring at the same time, which eliminates the influence of temporal effects.

1.2.4.3 *Interferometric coherence*

All interferometric methods rely in some way on measuring the phase difference between 2 (or more) measurements. In order to successfully perform interferometric measurements, the two datasets/signals s_1 and s_2 need to have a high degree of *coherence*, i.e. their phase information needs to be correlated to a certain extent so that the relevant phase term can be identified and extracted. Interferometric coherence $\tilde{\gamma}$ is a measure of the correlation of the two signals. Given two 2-dimensional SLC images s_1 and s_2, their interferometric coherence can be estimated as:

$$\tilde{\gamma} = \frac{\sum_W s_1 s_2^*}{\sqrt{\sum_W s_1^2}\sqrt{\sum_W s_2^2}}, \tag{1.25}$$

where W is a boxcar moving window. The coherence estimate is thus also a 2-dimensional complex image, and is a measure of the local similarity between the two SLC images. Its final absolute value γ is for each pixel constrained between 0 (no coherence) and 1 (full coherence). The phase of $\tilde{\gamma}$ is an intensity-weighted average phase offset between all s_1 and s_2 pixels within the averaging window, and thus the phase of the interferometric coherence between two images is equal to the phase difference of the two images. A low value of coherence magnitude γ indicates a large influence of noise or other decorrelation phenomena and limits the precision of information that can be extracted using interferometric methods [49]. Many effects can cause the reduction of coherence [33], such as low signal-to-noise ratio [49, 50], information loss during signal quantization [51], range and azimuth ambiguities, baseline decorrelation [52], relative shift of the Doppler spectra [50], volume decorrelation [53, 54] or temporal decorrelation [55–57]. Influence of each factor is modeled as a separate coherence term with value between 0 and 1, and the total coherence is then computed as a product of all these individual sub-terms, e.g. for the effects mentioned above:

$$\gamma = \gamma_{\text{SNR}}\gamma_{\text{Quant}}\gamma_{\text{Amb}}\gamma_{\text{Rg}}\gamma_{\text{Az}}\gamma_{\text{Vol}}\gamma_{\text{Temp}}. \tag{1.26}$$

In order to successfully apply interferometric methods, the influence of all these effects thus needs to be quantified and accounted for.

1.2.5 *Radar polarimetry*

1.2.5.1 *Polarimetric theory*

Electromagnetic waves exhibit a property called polarization, which describes the orientation and temporal behavior of the waves' electric and magnetic field vectors in the plane normal to the direction of propagation of the wave. Differently polarized radio waves can exhibit different scattering characteristics, depending on the properties of the media they scatter in. Radar polarimetry measures these differences in order to extract information about the physical properties of the scattering environment. [25, 26, 58, 59]

The particular polarization state of a polarized radio wave can be described by a two-component complex vector called the Jones vector $\mathbf{E}$. The Jones vector requires a choice of a particular polarization basis, which describes the two principal polarization states from which all other states are derived by linear combination. Popular polarization bases are, for example, the horizontal-vertical (HV) basis where the two principal vectors represent a fully vertically and a fully horizontally polarized wave, or the left-right (LR) circularly polarized basis. It is worth noting that all polarization bases contain the same information, and they can be freely transformed between each other using a mathematical operation called the basis transform [25, 60]. For KAPRI, the use of the HV basis is the natural choice, as these are also the principal polarizations of KAPRI's antennas [61].

A polarimetric system thus transmits a particularly polarized wave described by vector $\mathbf{E}^{\mathrm{i}}$ and receives a scattered wave described by a (possibly different) Jones vector $\mathbf{E}^{\mathrm{s}}$. These two vectors are related to each other through a 2x2 matrix called the scattering matrix $\mathbf{S}$

$$\mathbf{E}^{\mathrm{s}} = \mathbf{S}\mathbf{E}^{\mathrm{i}} \tag{1.27}$$

$$\begin{bmatrix} E^{\mathrm{s}}_{\mathrm{H}} \\ E^{\mathrm{s}}_{\mathrm{V}} \end{bmatrix} = \frac{e^{-ikr}}{r} \begin{bmatrix} S_{\mathrm{HH}} & S_{\mathrm{HV}} \\ S_{\mathrm{VH}} & S_{\mathrm{VV}} \end{bmatrix} \begin{bmatrix} E^{\mathrm{i}}_{\mathrm{H}} \\ E^{\mathrm{i}}_{\mathrm{V}} \end{bmatrix} \tag{1.28}$$

where $k = 2\pi/\lambda$ is the wavenumber of the wave, i is the imaginary unit, and r is the range of the scattering target. Each term of the $\mathbf{S}$ matrix is complex-valued, and thus can be split into the real-valued amplitude $|S|$ and real-valued phase ϕ, i.e. for the HH term:

$$S_{\mathrm{HH}} = |S_{\mathrm{HH}}| e^{i\phi_{\mathrm{HH}}} \tag{1.29}$$

and equivalently for the other three channels. The term $\frac{e^{-jkr}}{r}$ in eq. (1.28) describes the phase modulation and intensity decay of the signal caused by the propagation path length, and is

not directly tied to the scattering properties of the target. For this reason it is often omitted in polarimetric equations. Furthermore, the phase modulation term is coupled to all four phase terms of the **S** matrix, which means that all four phase terms of the **S** matrix can be offset by an arbitrary phase factor by correspondingly adjusting the range distance r. What remains constant are the relative phase terms with respect to one "reference" polarimetric channel; usually the HH or VV channel is chosen as the reference. A simplified version of eq. (1.28) which still preserves all polarimetric information about the target can thus be written by neglecting the propagation path term and modulating the phase of the **S** matrix so that the phase of the HH term is zero:

$$\begin{bmatrix} E_{\mathrm{H}}^{\mathrm{s}} \\ E_{\mathrm{V}}^{\mathrm{s}} \end{bmatrix} = \begin{bmatrix} |S_{\mathrm{HH}}| & |S_{\mathrm{HV}}|e^{i\phi_{\mathrm{HV}}} \\ |S_{\mathrm{VH}}|e^{i\phi_{\mathrm{VH}}} & |S_{\mathrm{VV}}|e^{i\phi_{\mathrm{VV}}} \end{bmatrix} \begin{bmatrix} E_{\mathrm{H}}^{\mathrm{i}} \\ E_{\mathrm{V}}^{\mathrm{i}} \end{bmatrix}. \tag{1.30}$$

In this equation remain the four amplitudes $|S_{\mathrm{HH}}|, |S_{\mathrm{HV}}|, |S_{\mathrm{VH}}|, |S_{\mathrm{VV}}|$ and three relative phase offsets $\phi_{\mathrm{HV}}, \phi_{\mathrm{VH}}, \phi_{\mathrm{VV}}$. These are the seven real-valued measurable free parameters in a polarimetric bistatic measurement. In the monostatic case, due to the physical principle of reciprocity, the cross-polarized phase and amplitude terms can be assumed to be equal, i.e. $S_{\mathrm{HV}} = S_{\mathrm{VH}}$, which further eliminates one amplitude and one phase parameter, bringing the total amount of free polarimetric parameters down to five [25]. The reciprocity principle however cannot be assumed in the generalized bistatic case [26].

A system that can measure all components (i.e. all free parameters) of the **S** matrix is called a fully-polarimetric system. The scattering matrix in case of distributed targets (which is the case for many natural targets) varies stochastically over neighboring pixels, and over time. Repeated observations over time, and possibly also from a variety of directions, are thus desirable in order to achieve a complete overview of the polarimetric scattering behaviour of the observed scene.

Once a sensor has acquired a polarimetric dataset of the scene, this can be interpreted in a multitude of ways [25, 58, 62]. Scattering vector representations, such as the lexicographic vector $\mathbf{k}_{\mathrm{L}}$

$$\mathbf{k}_{\mathrm{L}} = \begin{bmatrix} S_{\mathrm{HH}} & S_{\mathrm{HV}} & S_{\mathrm{VH}} & S_{\mathrm{VV}} \end{bmatrix}^{\mathrm{T}}, \tag{1.31}$$

where the $^{\mathrm{T}}$ symbol indicates a matrix transpose, can be used to compare the scattering intensities of individual polarimetric channels. This is often done by creating a color map of

the observed scene and assigning each principal RGB color to the amplitude of one of the vector components. Similarly, the Pauli scattering vector representation

$$\mathbf{k}_{\mathrm{P}} = \frac{1}{\sqrt{2}} \begin{bmatrix} S_{\mathrm{HH}} + S_{\mathrm{VV}} & S_{\mathrm{HH}} - S_{\mathrm{VV}} & S_{\mathrm{HV}} + S_{\mathrm{VH}} & j(S_{\mathrm{HV}} - S_{\mathrm{VH}}) \end{bmatrix}^{\mathrm{T}}, \tag{1.32}$$

is popular since it can be used to distinguish between elementary scattering processes, since each of the four components respectively captures surface, dihedral, volume, and non-reciprocal scattering types.

This vector representation is sufficient to describe fully polarized, deterministic scatterers. However, when observing natural targets, a typical resolution cell often contains a large amount of distributed scatterers which can also exhibit depolarizing behaviour. In order to capture this stochastic behaviour, spatial ensemble averaging of scattering vectors is often employed to calculate the covariance matrix $\mathbf{C}$ and coherency matrix $\mathbf{T}$ from the scattering vectors:

$$\mathbf{C} = \left\langle \mathbf{k}_{\mathrm{L}} \cdot \mathbf{k}_{\mathrm{L}}^{\dagger} \right\rangle, \tag{1.33}$$

$$\mathbf{T} = \left\langle \mathbf{k}_{\mathrm{P}} \cdot \mathbf{k}_{\mathrm{P}}^{\dagger} \right\rangle, \tag{1.34}$$

where the symbol † indicates a hermitian conjugate transpose, and the brackets $\langle \cdot \rangle$ indicate spatial averaging. From these matrices, second-order polarimetric parameters can be computed. First, the $\mathbf{T}$ matrix is decomposed into its eigenvectors:

$$\mathbf{T} = \sum_{k=1}^{4} \lambda_k \mathbf{u}_k \cdot \mathbf{u}_k^{\dagger}, \tag{1.35}$$

where λ_k and $\mathbf{u}_k$ are the matrix's k-th eigenvalue and the corresponding eigenvector. It is often useful to normalize each eigenvalue to the sum of all eigenvalues:

$$P_k = \frac{\lambda_k}{\sum_{l=1}^{4} \lambda_l} \tag{1.36}$$

Then the scattering entropy H is defined as [25, 26, 63]

$$H = -\sum_{k=1}^{4} P_k \log_4 P_k \tag{1.37}$$

and it quantifies the diversity of scattering processes occurring within the observed scene, with the value 0 representing minimal diversity (i.e. presence of only one scattering process),

and value 1 representing maximal diversity (i.e. four equally dominant scattering processes). Each of the eigenvectors $\mathbf{u}_k$ can be expressed in the unitary vector representation as:

$$\mathbf{u}_k = e^{j\phi_k} \begin{bmatrix} \cos\alpha_k \\ \sin\alpha_k \cos\beta_k e^{j\chi_k} \\ \sin\alpha_k \sin\beta_k \cos\gamma_k e^{j\psi_k} \\ \sin\alpha_k \sin\beta_k \sin\gamma_k e^{j\xi_k} \end{bmatrix}, \tag{1.38}$$

where α_k is the roll-invariant polarimetric scattering parameter describing the type of scattering process, β_k is the parameter tied to the orientation around the line of sight, γ_k is a parameter capturing cross-polar reciprocity, and $\phi_k, \chi_k, \psi_k, \xi_k$ are phase angles [25, 26, 64]. Then the mean alpha angle $\bar{\alpha}$ can be computed as an eigenvalue-weighted average of the alpha angles of the four eigenvectors

$$\bar{\alpha} = \sum_{k=1}^{4} P_k \alpha_k \tag{1.39}$$

and it quantifies the "average" type of scattering process. Its value is constrained between 0 and 90°, where surface-type scattering has value of 0°, dipole scattering 45°, and dihedral scattering 90°. The mean alpha angle is thus a useful quantity to identify the dominant type of scattering present within the scene. The relative values of the eigenvalues can provide information as well – in the monostatic case, reciprocal symmetry of the HV and VH channels reduces the dimensionality of the **T** matrix into a 3×3 matrix, and thus the fourth (i.e. the smallest) eigenvalue λ_4 should have a value of zero if no noise is present. Its value can thus be considered a measure of the noise level, which usually distributes itself evenly between all eigenvalues [65]. Alternatively, in the bistatic case a relatively high value of the fourth eigenvalue λ_4 can be used as an indicator of non-reciprocal scattering occurring within the scene.

1.2.5.2 *Calibration of polarimetric systems*

No polarimetric radar sensor is perfect – construction imperfections, varying ambient conditions, material wear and other similar effects can have a significant effect on the observed scattering matrix **O**, which can differ from the actual scattering matrix of the target **S**. This has to be corrected through a process called polarimetric calibration [66]. The particular method varies depending on application and the instrument used. The

popular linear distortion matrix model describes the relation between the observed and real scattering matrices as [67]

$$\mathbf{O} = \mathbf{RST} + \mathbf{N}, \tag{1.40}$$

where **R**,**T**, and **N** are matrices that describe the distortions caused by the receiver apparatus, the transmitter apparatus, and noise respectively. The exact form of these matrices is instrument-specific, and is often determined by comparing the observed polarimetric signature of a known target to its expected signature predicted by scattering theory. Once the distortion matrices are determined, the real scattering matrix **S** can be estimated from the observed matrix **O** by inverting eq. (1.40). Popular calibration targets are trihedral or dihedral corner reflectors [61, 66, 68, 69], active transponder devices [20, 70–72], or other specialized objects such as cylinders [73, 74]. Each of these have their own benefits and drawbacks – for example, trihedral corner reflectors are extremely robust and relatively cheap to manufacture, but can only be used in the monostatic regime and cannot be used to calibrate the cross-polarized channels (HV and VH), unless specially modified. In contrast, active calibration devices are usually more flexible towards geometrical and polarization configuration, however they are more expensive to manufacture and more complex to operate in field conditions.

1.2.6 *Radar investigations of snow and ice*

Synthetic and real-aperture radar has been used for exploration and monitoring of the Earth's cryosphere for several decades. The Earth's cryosphere is a vital part of its ecosystem and it provides some of the most useful indicators of climate variability and change, yet is considered one the most under-sampled domains of the Earth System [1]. Radar imaging not only provides year-round monitoring capabilities (which is especially useful in polar regions which experience polar night, and in regions with high rates of cloud coverage), but the specifics of the interaction of radio waves with snow and ice also offer unique opportunities for remote monitoring of various processes and phenomena. Interferometric methods are capable of monitoring the dynamics of processes such as glacier drift and detachments, changes in land/sea ice thickness, or processes associated with melting of permafrost. Polarimetric methods allow insights into properties such as snow anisotropy (direction-specific orientation of ice grains), and can provide insights into snow microstructure. Advanced methods such as Pol-InSAR [75] or SAR tomography [76] can provide further insights into the layer structure of snow and ice-covered areas.

Scattering characteristics of snow are strongly dependent not only on the properties of the incident radiation (frequency, polarization), but also on physical parameters of the snow medium (grain size, water content, layer parameters), as well as observation geometry (incidence, scattering angle). Extensive review literature is available on the topic of radar investigations of snow, e.g., [77–81]. Occurrence of snow melt has a strong influence on scattering characteristics of snow and ice, as liquid water has a very high dielectric constant and is a strong radio wave absorbent, particularly at high frequencies such as Ku-band. Snow melt thus dramatically reduces backscatter intensity and penetration depth, and precludes the possibility of probing of deeper layers. While Ku-band radio waves can penetrate several meters deep into dry snow, in wet snow this depth is reduced to only a few centimeters [82]. The orientation, size and shape of the ice grains evolves as the snow pack ages and possibly partially melts and refreezes. This often results in an anisotropic orientation of ice grains, which can impose a propagation velocity differential on differently polarized radio waves. This fact can be used by polarimetric methods to infer properties of snow cover from measurements of the phase difference between horizontally and vertically polarized radio waves [83, 84]. Large research focus is present also on methods aiming to retrieve snow water equivalent (SWE) – the potential amount of water stored in the snowpack – from radar observations [77]. SWE is one of the key observable parameters of snow as an Essential Climate Variable, together with snow extent and snow depth [2].

One particular scattering phenomenon of interest for *bistatic* radar investigations of snow and ice is the coherent backscatter opposition effect (CBOE) [31, 32, 85]. The CBOE causes an enhancement of backscatter intensity by up to a factor of two in the direct return direction, thus forming a very sharp and narrow intensity peak around the monostatic direction. It only occurs when coherent radiation scatters in a disordered, weakly absorbing and strongly scattering medium. These conditions should be satisfied when (coherent) radio waves scatter in layers of snow and ice. Despite the fact that it could affect the intensity of monostatic backscatter from snow and ice by up to 3 dB, the effect has so far received relatively little attention in radar research of terrestrial snow.

1.3 RESEARCH OBJECTIVES AND QUESTIONS

This dissertation is centered around exploration of applications of bistatic Ku-band radar to snow-covered environments using an terrestrial real-aperture radar KAPRI [46, 47, 61, 86]. KAPRI is based on and has a rich heritage in the terrestrial interferometer Gamma Portable Radar Interferometer (GPRI) [87–90]. Compared to the GPRI, KAPRI is additionaly

capable of full-polarimetric and bistatic acquisitions. Its polarimetric operation mode had been previously developed and tested [61], however the bistatic operation mode is an experimental feature for which the operational and data processing procedures had not been previously developed. The first objective of this dissertation is thus development and validation of the bistatic operational mode and the associated calibration and processing methods. Afterwards, this new bistatic operation mode is applied to observations of snow and ice-covered environments in two different approaches, with the objective to explore the bistatic scattering properties of seasonal snow at Ku-band. The first approach makes use of the multi-modal capabilities of KAPRI to acquire a diverse multi-seasonal dataset in order to explore the temporal and spatial behaviour of scattering properties of snow cover. The second approach leverages KAPRI's portability and flexibility in terms of bistatic geometrical setup, in order to investigate the occurrence and properties of a particular bistatic phenomenon – the coherent backscatter opposition effect (CBOE) – in seasonal snow.

1.3.1 *Calibration and operation of a bistatic real-aperture polarimetric-interferometric Ku-band radar*

This study focuses on development of the bistatic operation mode of KAPRI. The processing procedures originally developed for the monostatic version of KAPRI needed to be revised to account for the spatial separation of the transmitter and the receiver, and the associated transition from polar to elliptical acquisition geometry. Furthermore, several new processing steps needed to be added to compensate for offsets between the two devices' internal oscillators. Finally, a novel polarimetric calibration procedure needed to be developed, since the monostatic procedure relied on principles and targets which are not applicable in the generalized bistatic case. This required development of a novel active calibration target (VSPARC) which enabled polarimetric calibration in arbitrary bistatic geometries. This study can be concisely summarized with the following research questions:

RQ1.1 *How to model and compensate the offset between the transmitter's and the receiver's internal oscillators in a bistatic frequency-modulated continuous-wave radar system, so that accurate range and phase information can still be retrieved?*

RQ1.2 *How to modify the polarimetric processing pipeline of a monostatic real-aperture fan-beam radar system in order to enable processing of acquisitions in an arbitrary bistatic geometry?*

RQ1.3 *How can one efficiently estimate the polarimetric calibration parameters of KAPRI in the bistatic regime, which precludes the application of the reciprocity principle and use of trihedral corner reflectors?*

1.3.2 *Polarimetric analysis of multi-seasonal monostatic and bistatic radar observations of a glacier accumulation zone at Ku-band*

This study employs the developed bistatic operation mode to study the snow-covered environment of the Great Aletsch Glacier in Switzerland. Two acquisition campaigns were carried out, one in late August, and one in late March, observing the snow cover in two significantly different states. Furthermore, all modalities of KAPRI were employed, thus creating a combined monostatic/bistatic, full-polarimetric and interferometric dataset. KAPRI's fast repetition time was employed to create day-long time series with a very short time step on the order of minutes, which enabled the study of changing scattering properties, glacier flow, and decorrelation phenomena. The following research questions are addressed in this study:

RQ2.1 *What is the timescale on which snow cover on top of a glacier maintains/loses its interferometric coherence at Ku-band in summer and in winter?*

RQ2.2 *What are the similarities and the differences of polarimetric scattering characteristics of snow cover between the monostatic and the bistatic regime, and between summer and winter observations?*

RQ2.3 *Does the reciprocity principle remain valid, or do non-reciprocal scattering processes arise in the bistatic regime in snow at Ku-band?*

1.3.3 *Coherent backscatter enhancement in bistatic Ku- and X-band radar observations of dry snow*

This study investigates the occurrence and properties of one specific scattering phenomenon snow and ice at radio frequencies, the coherent backscatter opposition effect (CBOE). This electromagnetic scattering phenomenon has been known in the field of optics and planetary science for several decades, but until now has received comparably little attention amongst radar scientists studying and modeling snow and ice backscatter. This is despite the fact that the condition for its existence (scattering of coherent radiation in a disordered medium) is generally considered to be satisfied. One possible reason for the lack of attention is that

the effect is difficult to study with most radar sensors, since bistatic measurements are required to fully characterize it. In this study we carried out bistatic KAPRI measurements and analyzed data from observations with a spaceborne bistatic radar sensor TanDEM-X to answer the following research questions:

RQ3.1 *Does the coherent backscatter opposition effect (CBOE) occur in terrestrial snow cover at radio frequencies?*

RQ3.2 *What are the characteristics of the CBOE enhancement peak in snow cover at X-/Ku-band, and where does it occur?*

RQ3.3 *Can bistatic radar observations of the CBOE enhancement peak be used to infer properties of the scattering medium?*

1.4 STRUCTURE OF THIS DISSERTATION

The three above-mentioned studies, i.e. the development and implementation of the bistatic calibration and the bistatic operation mode and the two separate cryospheric investigations, form the three following chapters of this dissertation. Each of these chapters is published or is currently submitted for publication in a peer-reviewed journal. The final Chapter 5 summarizes the results and conclusions of these investigations and provides an outlook.

REFERENCES

1. *Global Cryosphere Watch (GCW) Implementation Plan, Version 1.6* tech. rep. (World Meteorological Organization, 2015).
2. *The 2022 GCOS Implementation Plan (GCOS-245)* tech. rep. (World Meteorological Organization, 2022).
3. Skolnik, M. I. *Introduction to radar systems* 2nd ed. (McGraw-Hill, New York, 1980).
4. Meyer, F. in *SAR Handbook: Comprehensive Methodologies for Forest Monitoring and Biomass Estimation* chap. Spaceborne (2019). doi:10.25966/ez4f-mg98.
5. NAWCWD Avionics Department. Electronic Warfare and Radar Systems Engineering Handbook. *Published in association with MTTS & IEEE*, 455 (1997).
6. Fitch, J. P. *Synthetic Aperture Radar* doi:10.1007/978-1-4612-3822-5 (Springer New York, New York, NY, 1988).

7. Curlander, J. C. & McDonough, R. N. *Synthetic aperture radar : systems and signal processing* (Wiley, New York [etc, 1991).

8. Bamler, R. Principles of synthetic aperture radar. *Surveys in Geophysics* **21**, 147. doi:10.1023/A:1006790026612 (2000).

9. Oliver, C. & Quegan, S. *Understanding synthetic aperture radar images* (Scitech Publishing, Raleigh, NC, 2004).

10. Richards, J. A. *Remote Sensing with Imaging Radar* doi:10.1007/978-3-642-02020-9 (Springer Berlin Heidelberg, Berlin, Heidelberg, 2009).

11. Curry, G. R. *Radar Essentials: A concise handbook for radar design and performance analysis* doi:10.1049/SBRA029E (Institution of Engineering and Technology, 2012).

12. Rees, W. G. *Physical Principles of Remote Sensing* doi:10.1017/CBO9781139017411 (Cambridge University Press, 2012).

13. Budge, M. C. & German, S. R. *Basic radar analysis* (Artech house, 2015).

14. Skolnik, M. I. An analysis of bistatic radar. *IRE Transactions on Aerospace and Navigational Electronics*, 19. doi:10.1109/TANE3.1961.4201772 (1961).

15. Willis, N. J. *Bistatic Radar* (eds Willis & Griffiths) doi:10.1049/SBRA003E (Institution of Engineering and Technology, 2005).

16. Cherniakov, M. *Bistatic Radar* (ed Cherniakov, M.) 1. doi:10.1002/9780470985755 (John Wiley & Sons, Ltd, Chichester, UK, 2008).

17. Blake, L. *Radar range-performance analysis* Lexington, Mass., D. C. Heath and Co., 1980. 464 p. 1980.

18. Griffiths, H. D. *From a Different Perspective : Principles, Practice and Potential of Bistatic Radar* in *2003 Proceedings of the International Conference on Radar (IEEE Cat. No. 03EX695)* (2003), 1. doi:10.1109/RADAR.2003.1278701.

19. Gierull, C. H. *Bistatic Synthetic Aperture Radar, TIF-Report (Phase I)* tech. rep. (Defence Research and Development Canada, Ottawa, Ontario, Canada, 2004).

20. Dubois-Fernandez, P., Cantalloube, H., Vaizan, B., Krieger, G., Horn, R., Wendler, M. & Giroux, V. ONERA-DLR bistatic SAR campaign: Planning, data acquisition, and first analysis of bistatic scattering behavior of natural and urban targets. *Radar, Sonar and Navigation, IEE Proceedings* - **153**, 214. doi:10.1049/ip-rsn:20045117 (2006).

21. Krieger, G. & Moreira, A. Spaceborne bi-and multistatic SAR: potential and challenges. *IEE Proceedings-Radar, Sonar and Navigation* **153**, 184. doi:https://doi.org/10.1049/ip-rsn:20045111 (2006).

22. Krieger, G., Fiedler, H., Houman, D. & Moreira, A. *Analysis of system concepts for bi-and multi-static SAR missions* in *IGARSS 2003. 2003 IEEE International Geoscience and Remote Sensing Symposium. Proceedings (IEEE Cat. No. 03CH37477)* **2** (2003), 770. doi:10.1109/IGARSS.2003.1293912.

23. Moreira, A., Krieger, G., Hajnsek, I., Papathanassiou, K., Younis, M., Lopez-Dekker, P., Huber, S., Villano, M., Pardini, M., Eineder, M., De Zan, F. & Parizzi, A. Tandem-L: A Highly Innovative Bistatic SAR Mission for Global Observation of Dynamic Processes on the Earth's Surface. *IEEE Geoscience and Remote Sensing Magazine* **3**, 8. doi:10.1109/MGRS.2015.2437353 (2015).

24. Pieraccini, M. & Miccinesi, L. *Bistatic GBSAR for detecting target elevation* in *2017 IEEE International Conference on Microwaves, Antennas, Communications and Electronic Systems (COMCAS)* (2017), 1. doi:10.1109/COMCAS.2017.8244728.

25. Lee, J.-S. & Pottier, E. *Polarimetric radar imaging: from basics to applications* (CRC press, 2009).

26. Everaere, E. *Polarimetry in bistatic configuration for ultra high frequency radar measurements on forest environment* PhD thesis (Ecole Polytechnique, 2015).

27. Villard, L., Hajnsek, I., Borderies, P. & Papathanassiou, K. Pol-InSAR Simulations in Forest Bistatic Scattering. *7th European Conference on Synthetic Aperture Radar*, 3 (2008).

28. Khadhra, K. B., Boerner, T., Hounam, D. & Chandra, M. Surface Parameter Estimation Using Bistatic Polarimetric X-Band Measurements. *Progress In Electromagnetics Research B* **39**, 197. doi:10.2528/PIERB12020112 (2012).

29. Erten, E., Lopez-Sanchez, J. M., Yuzugullu, O. & Hajnsek, I. Retrieval of agricultural crop height from space: A comparison of SAR techniques. *Remote Sensing of Environment* **187**, 130. doi:10.1016/j.rse.2016.10.007 (2016).

30. Erten, E., Rossi, C. & Yüzügüllü, O. Polarization impact in TanDEM-X data over vertical-oriented vegetation: The paddy-rice case study. *IEEE Geoscience and Remote Sensing Letters* **12**, 1501. doi:10.1109/LGRS.2015.2410339 (2015).

31. Akkermans, E., Wolf, P. E. & Maynard, R. Coherent backscattering of light by disordered media: Analysis of the peak line shape. *Physical review letters* **56**, 1471. doi:10.1103/PhysRevLett.56.1471 (1986).

32. Hapke, B. *Theory of reflectance and emittance spectroscopy, second edition* 1. doi:10.1017/CBO9781139025683 (Cambridge University Press, Cambridge, 2012).

33. Krieger, G., Moreira, A., Fiedler, H., Hajnsek, I., Werner, M., Younis, M. & Zink, M. TanDEM-X: A satellite formation for high-resolution SAR interferometry. *IEEE Transactions on Geoscience and Remote Sensing* **45**, 3317. doi:10.1109/TGRS.2007.900693 (2007).

34. Rodriguez-Cassola, M., Prats, P., Schulze, D., Tous-Ramon, N., Steinbrecher, U., Marotti, L., Nannini, M., Younis, M., López-Dekker, P., Zink, M., Reigber, A., Krieger, G. & Moreira, A. First bistatic spaceborne SAR experiments with TanDEM-X. *IEEE Geoscience and Remote Sensing Letters* **9**, 33. doi:10.1109/LGRS.2011.2158984 (2012).

35. Lopez-Dekker, P., Rott, H., Prats-Iraola, P., Chapron, B., Scipal, K. & Witte, E. D. *Harmony: an Earth Explorer 10 Mission Candidate to Observe Land, Ice, and Ocean Surface Dynamics* in *IGARSS 2019 - 2019 IEEE International Geoscience and Remote Sensing Symposium* (IEEE, 2019), 8381. doi:10.1109/IGARSS.2019.8897983.

36. Moccia, A., Rufino, G., D'Errico, M., Alberti, G. & Salzillo, G. *BISSAT: A bistatic SAR for earth observation* in *International Geoscience and Remote Sensing Symposium (IGARSS)* **5** (IEEE, 2002), 2628. doi:10.1109/igarss.2002.1026723.

37. Massonnet, D. The interferometric cartwheel: A constellation of passive satellites to produce radar images to be coherently combined. *International Journal of Remote Sensing* **22**, 2413. doi:10.1080/01431160118952 (2001).

38. Zebker, H. A., Farr, T. G., Salazar, R. P. & Dixon, T. H. Mapping the World's Topography Using Radar Interferometry: The TOPSAT Mission. *Proceedings of the IEEE* **82**, 1774. doi:10.1109/5.338070 (1994).

39. Gebert, N., Carnicero Dominguez, B., Davidson, M. W. J., Diaz Martin, M. & Silvestrin, P. *SAOCOM-CS - A passive companion to SAOCOM for single-pass L-band SAR interferometry* in *EUSAR 2014; 10th European Conference on Synthetic Aperture Radar* (2014), 1.

40. Davidson, M., Chini, M., Dierking, W., Djavidnia, S., Haarpaintner, J., Hajduch, G., Laurin, G. V., Lavalle, M., López-Martinez, C., Nagler, T., Pierdicca, N. & Su, B. Copernicus L-band SAR Mission Requirements Document. *European Space Agency, ESA-EOPSM-CLIS-MRD-3371* (2019).

41. Rosen, P., Hensley, S., Joughin, I., Li, F., Madsen, S., Rodriguez, E. & Goldstein, R. Synthetic aperture radar interferometry. *Proceedings of the IEEE* **88**, 333. doi:10.1109/5.838084 (2000).

42. Hanssen, R. F. *Radar interferometry : data interpretation and error analysis* 1st ed. 20. eng. doi:10.1007/0-306-47633-9 (Kluwer Academic Publishers, New York, 2001).

43. Zebker, H. A. *Radar interferometry* eng, 1 (Wiley-Blackwell, Oxford, 2011).

44. Goldstein, R. M., Zebker, H. A. & Werner, C. L. Satellite radar interferometry: Two-dimensional phase unwrapping. *Radio Science* **23**, 713. doi:10.1029/RS023i004p00713 (1988).

45. Zebker, H. A. & Lu, Y. Phase unwrapping algorithms for radar interferometry: residue-cut, least-squares, and synthesis algorithms. *Journal of the Optical Society of America A* **15**, 586. doi:10.1364/JOSAA.15.000586 (1998).

46. Baffelli, S., Frey, O. & Hajnsek, I. Geostatistical Analysis and Mitigation of the Atmospheric Phase Screens in Ku-Band Terrestrial Radar Interferometric Observations of an Alpine Glacier. *IEEE Transactions on Geoscience and Remote Sensing* **58**, 7533. doi:10.1109/TGRS.2020.2976656 (2020).

47. Izumi, Y., Frey, O., Baffelli, S., Hajnsek, I. & Sato, M. Efficient Approach for Atmospheric Phase Screen Mitigation in Time Series of Terrestrial Radar Interferometry Data Applied to Measure Glacier Velocity. *IEEE Journal of Selected Topics in Applied Earth Observations and Remote Sensing* **14**, 7734. doi:10.1109/JSTARS.2021.3099873 (2021).

48. Zebker, H. A. & Goldstein, R. M. Topographic mapping from interferometric synthetic aperture radar observations. *Journal of Geophysical Research* **91**, 4993. doi:10.1029/JB091iB05p04993 (1986).

49. Rodriguez, E. & Martin, J. M. Theory and design of interferometric synthetic aperture radars. *IEE Proceedings, Part F: Radar and Signal Processing* **139**, 147. doi:10.1049/ip-f-2.1992.0018 (1992).

50. Just, D. & Bamler, R. Phase statistics of interferograms with applications to synthetic aperture radar. *Applied Optics* **33**, 4361. doi:10.1364/AO.33.004361 (1994).

51. McLeod, I., Cumming, I. G. & Seymour, M. ENVISAT ASAR data reduction: impact on SAR interferometry. *IEEE Transactions on Geoscience and Remote Sensing* **36**, 589. doi:10.1109/36.662741 (1998).

52. Li, F. K. & Goldstein, R. M. Studies of Multibaseline Spaceborne Interferometric Synthetic Aperture Radars. *IEEE Transactions on Geoscience and Remote Sensing* **28**, 88. doi:10.1109/36.45749 (1990).

53. Treuhaft, R. N. & Siqueira, P. R. Vertical structure of vegetated land surfaces from interferometric and polarimetric radar. *Radio Science* **35**, 141. doi:10.1029/1999RS900108 (2000).

54. Zebker, H. & Weber Hoen, E. Penetration depths inferred from interferometric volume decorrelation observed over the Greenland Ice Sheet. *IEEE Transactions on Geoscience and Remote Sensing* **38**, 2571. doi:10.1109/36.885204 (2000).

55. Zebker, H. A., Villasenor, J., *et al.* Decorrelation in interferometric radar echoes. *IEEE Transactions on geoscience and remote sensing* **30**, 950. doi:10.1109/36.175330 (1992).

56. Narayanan, R. M., Doerr, D. W. & Rundquist, D. C. Temporal Decorrelation of X-Band Backscatter from Wind-Influenced Vegetation. *IEEE Transactions on Aerospace and Electronic Systems* **28**, 404. doi:10.1109/7.144566 (1992).

57. Leinss, S., Wiesmann, A., Lemmetyinen, J. & Hajnsek, I. Snow Water Equivalent of Dry Snow Measured by Differential Interferometry. *IEEE Journal of Selected Topics in Applied Earth Observations and Remote Sensing* **8**, 3773. doi:10.1109/JSTARS.2015.2432031 (2015).

58. Hajnsek, I. *Inversion of Surface Parameters Using Polarimetric SAR* PhD thesis (2001).

59. Cloude, S. *Polarisation: Applications in Remote Sensing* doi:10.1093/acprof:oso/9780199569731.001.0001 (Oxford University Press, 2009).

60. Van Zyl, J. J., Zebker, H. A. & Elachi, C. Imaging radar polarization signatures: Theory and observation. *Radio Science* **22**, 529. doi:10.1029/RS022i004p00529 (1987).

61. Baffelli, S., Frey, O., Werner, C. & Hajnsek, I. Polarimetric Calibration of the Ku-Band Advanced Polarimetric Radar Interferometer. *IEEE Transactions on Geoscience and Remote Sensing* **56**, 2295. doi:10.1109/TGRS.2017.2778049 (4 2018).

62. Cloude, S. & Pottier, E. A review of target decomposition theorems in radar polarimetry. *IEEE Transactions on Geoscience and Remote Sensing* **34**, 498. doi:10.1109/36.485127 (1996).

63. Cloude, S. & Pottier, E. An entropy based classification scheme for land applications of polarimetric SAR. *IEEE Transactions on Geoscience and Remote Sensing* **35**, 68. doi:10.1109/36.551935 (1997).

64. Touzi, R. Target Scattering Decomposition in Terms of Roll-Invariant Target Parameters. *IEEE Transactions on Geoscience and Remote Sensing* **45**, 73. doi:10.1109/TGRS.2006.886176 (2007).

65. Hajnsek, I., Papathanassiou, K. P. & Cloude, S. R. *Removal of additive noise in polarimetric eigenvalue processing* in *IGARSS 2001. Scanning the Present and Resolving the Future. Proceedings. IEEE 2001 International Geoscience and Remote Sensing Symposium (Cat. No.01CH37217)* **6** (2001), 2778. doi:10.1109/IGARSS.2001.978160.

66. Van Zyl, J. J. & Kim, Y. in *Synthetic Aperture Radar Polarimetry* 145 (John Wiley & Sons, Inc., Hoboken, NJ, USA, 2011). doi:10.1002/9781118116104.ch4.

67. Sarabandi, K. & Ulaby, F. T. *A convenient technique for polarimetric calibration of radar systems* in *Digest - International Geoscience and Remote Sensing Symposium (IGARSS)* **28** (IEEE, 1990), 803. doi:10.1109/igarss.1990.688611.

68. Beaudoin, C., Horgan, T., Demartinis, G., Coulombe, M. J., Gatesman, A. J. & Nixon, W. E. Fully polarimetric bistatic radar calibration with modified dihedral objects. *IEEE Transactions on Antennas and Propagation* **66**, 937. doi:10.1109/TAP.2017.2783191 (2017).

69. Kahny, D., Schmitt, K. & Wiesbeck, W. Calibration of bistatic polarimetric radar systems. *IEEE transactions on geoscience and remote sensing* **30**, 847. doi:10.1109/36.175318 (1992).

70. Brunfeldt, D. R. & Ulaby, F. T. Active reflector for radar calibration. *IEEE Transactions on Geoscience and Remote Sensing*, 165. doi:10.1109/TGRS.1984.350610 (1984).

71. Pienaar, M., Odendaal, J. W., Joubert, J., Cilliers, J. E. & Smit, J. C. Active calibration target for bistatic radar cross-section measurements. *Radio Science* **51**, 515. doi:10.1002/2015RS005931 (2016).

72. Fujita, M., Masuda, T., Fujino, Y. & Satake, M. Polarimetric calibration of the SIR-C C-band channel using active radar calibrators and polarization selective dihedrals. *IEEE transactions on geoscience and remote sensing* **36**, 1872. doi:10.1109/36.729358 (1998).

73. Sarabandi, K., Ulaby, F. T. & Tassoudji, M. A. Calibration of Polarimetric Radar Systems With Good Polarization Isolation. *IEEE Transactions on Geoscience and Remote Sensing* **28**, 70. doi:10.1109/36.45747 (1990).

74. Monzon, C. A cross-polarized bistatic calibration device for RCS measurements. *IEEE Transactions on Antennas and Propagation* **51**, 833. doi:10.1109/TAP.2003.811071 (2003).

75. Fischer, G., Papathanassiou, K. P. & Hajnsek, I. Modeling Multifrequency Pol-InSAR Data From the Percolation Zone of the Greenland Ice Sheet. *IEEE Transactions on Geoscience and Remote Sensing* **57**, 1963. doi:10.1109/TGRS.2018.2870301 (2019).

76. Fischer, G., Jager, M., Papathanassiou, K. P. & Hajnsek, I. Modeling the Vertical Backscattering Distribution in the Percolation Zone of the Greenland Ice Sheet With SAR Tomography. *IEEE Journal of Selected Topics in Applied Earth Observations and Remote Sensing* **12**, 4389. doi:10.1109/JSTARS.2019.2951026 (2019).

77. Tsai, Y. L. S., Dietz, A., Oppelt, N. & Kuenzer, C. Remote sensing of snow cover using spaceborne SAR: A review. *Remote Sensing* **11**. doi:10.3390/rs11121456 (2019).

78. Snehmani, Singh, M. K., Gupta, R. D., Bhardwaj, A. & Joshi, P. K. Remote sensing of mountain snow using active microwave sensors: a review. *Geocarto International* **30**, 1. doi:10.1080/10106049.2014.883434 (2015).

79. Awasthi, S. & Varade, D. Recent advances in the remote sensing of alpine snow: a review. *GIScience & Remote Sensing* **58**, 852. doi:10.1080/15481603.2021.1946938 (2021).

80. Tsang, L., Durand, M., Derksen, C., Barros, A. P., Kang, D.-H., Lievens, H., Marshall, H.-P., Zhu, J., Johnson, J., King, J., Lemmetyinen, J., Sandells, M., Rutter, N., Siqueira, P., Nolin, A., Osmanoglu, B., Vuyovich, C., Kim, E. J., Taylor, D., Merkouriadi, I., Brucker, L., Navari, M., Dumont, M., Kelly, R., Kim, R. S., Liao, T.-H. & Xu, X. Review Article: Global Monitoring of Snow Water Equivalent using High Frequency Radar Remote Sensing. *The Cryosphere Discussions* **2021**, 1. doi:10.5194/tc-2021-295 (2021).

81. Dietz, A. J., Kuenzer, C., Gessner, U. & Dech, S. Remote sensing of snow – a review of available methods. *International Journal of Remote Sensing* **33**, 4094. doi:10.1080/01431161.2011.640964 (2012).

82. Mätzler, C. Applications of the interaction of microwaves with the natural snow cover. *Remote Sensing Reviews* **2**, 259. doi:10.1080/02757258709532086 (1987).

83. Leinss, S., Löwe, H., Proksch, M., Lemmetyinen, J., Wiesmann, A. & Hajnsek, I. Anisotropy of seasonal snow measured by polarimetric phase differences in radar time series. *Cryosphere* **10**, 1771. doi:10.5194/tc-10-1771-2016 (2016).

84. Parrella, G., Hajnsek, I. & Papathanassiou, K. P. Retrieval of Firn Thickness by Means of Polarisation Phase Differences in L-Band SAR Data. *Remote Sensing* **13**. doi:10.3390/rs13214448 (2021).

85. Tsang, L. & Ishimaru, A. Backscattering enhancement of random discrete scatterers. *Journal of the Optical Society of America A* **1**, 836. doi:10.1364/josaa.1.000836 (1984).

86. Baffelli, S., Frey, O. & Hajnsek, I. Polarimetric Analysis of Natural Terrain Observed With a Ku -Band Terrestrial Radar. *IEEE Journal of Selected Topics in Applied Earth Observations and Remote Sensing* **12**, 5268. doi:10.1109/JSTARS.2019.2953206 (2019).

87. Werner, C., Wiesmann, A., Strozzi, T., Kos, A., Caduff, R. & Wegmiüler, U. *The GPRI multi-mode differential interferometric radar for ground-based observations* in *EUSAR 2012; 9th European Conference on Synthetic Aperture Radar* (2012), 304.

88. Strozzi, T., Werner, C., Wiesmann, A. & Wegmuller, U. Topography mapping with a portable real-aperture radar interferometer. *IEEE Geoscience and Remote Sensing Letters* **9**, 277. doi:10.1109/LGRS.2011.2166751 (2011).

89. Caduff, R., Kos, A., Schlunegger, F., McArdell, B. W. & Wiesmann, A. Terrestrial radar interferometric measurement of hillslope deformation and atmospheric disturbances in the Illgraben debris-flow catchment, Switzerland. *IEEE Geoscience and Remote Sensing Letters* **11**, 434. doi:10.1109/LGRS.2013.2264564 (2014).

90. Wiesmann, A., Caduff, R. & Mätzler, C. Terrestrial radar observations of dynamic changes in alpine snow. *IEEE Journal of Selected Topics in Applied Earth Observations and Remote Sensing* **8**, 3665. doi:10.1109/JSTARS.2015.2400972 (2015).

2

CALIBRATION AND OPERATION OF A BISTATIC REAL-APERTURE POLARIMETRIC-INTERFEROMETRIC KU-BAND RADAR

Marcel Stefko[1], Othmar Frey[1,2], Charles Werner[2], and Irena Hajnsek[1,3]

[1] Chair of Earth Observation and Remote Sensing, ETH Zurich, Switzerland

[2] GAMMA Remote Sensing AG, Switzerland

[3] Microwaves and Radar Institute, German Aerospace Center DLR, Germany

Article published in

IEEE Transactions on Geoscience and Remote Sensing

Citation: M. Stefko, O. Frey, C. Werner and I. Hajnsek, "Calibration and Operation of a Bistatic Real-Aperture Polarimetric-Interferometric Ku-Band Radar," in *IEEE Transactions on Geoscience and Remote Sensing*, vol. 60, pp. 1-19, 2022, Art no. 5106719, doi: 10.1109/TGRS.2021.3121466.

Key findings/developments:

- The bistatic FMCW signal model, synchronization method, and data processing pipeline were developed.
- A novel active radar calibration device VSPARC, which allows bistatic polarimetric calibration, was developed.
- A novel calibration method using VSPARC for calibration of radar system KAPRI was developed and validated.

The author's contributions:

- developed and implemented the presented bistatic processing methodology,
- developed the bistatic calibration method and the associated hardware,
- coordinated and performed the data acquisition campaigns,
- interpreted the results and wrote the manuscript.

The co-authors' contributions:

- Othmar Frey contributed to methodology development, data evaluation, and writing of the manuscript.
- Charles Werner was responsible for the radar instrument design, development, and implementation, provided feedback during calibration method development, and provided feedback on the manuscript.
- Irena Hajnsek contributed to the study design, experiment coordination, data evaluation, and writing of the manuscript.

This article presents the bistatic operation mode and the performance analysis of KAPRI, a terrestrial frequency-modulated continuous-wave (FMCW) Ku-band polarimetric radar interferometer capable of acquiring bistatic full-polarimetric datasets with high spatial and temporal resolution. In the bistatic configuration, the system is composed of two independently operating KAPRI devices, one serving as a primary transmitter and receiver and the other as a secondary receiver. The secondary bistatic dataset is affected by possible offsets between the two devices' reference clocks, as well as distortions arising from the bistatic geometry. To correct for this, we present a two-chirp bistatic FMCW signal model, which accounts for the distortions, and a reference chirp transmission procedure, which allows correcting the clock offsets in the deramped signal time domain. The second challenge of operation of a bistatic polarimetric system is polarimetric calibration since it is not possible to employ purely monostatic targets such as corner reflectors. For this purpose, we developed a novel active calibration device Variable-Signature Polarimetric Active Radar Calibrator (VSPARC), designed for monostatic and bistatic calibration of all polarimetric channels. VSPARC and its associated novel polarimetric calibration method were then used to achieve full calibration of both KAPRI devices with polarimetric phase calibration accuracy of 20° and 30-dB polarization purity in field conditions. This article thus presents a complete measurement configuration and data processing pipeline necessary for synchronization, coregistration, and polarimetric calibration of bistatic and monostatic datasets acquired by a real-aperture FMCW radar.

2.1 INTRODUCTION

Bistatic radar refers to a configuration of radar systems where the transmitter (Tx) and receiver (Rx) are spatially separated. It is of research interest because of its complementary properties to the monostatic case, such as access to a larger number of polarimetric parameters [1, 2], recovery of 3-D displacement vectors [3, 4], possibility of long-baseline single-pass interferometric measurements [5], increased radar cross section of certain targets such as the sea surface [6], retrieval of biophysical parameters [7–9], and also military surveillance applications [10–12].

Flexibility and lower costs of terrestrial devices make them especially useful for exploratory acquisitions, as well as development and validation of new observation methods and processing algorithms, upon which airborne and spaceborne missions can be designed and implemented. Furthermore, for small-scale applications, terrestrial sensors can offer denser temporal sampling (as opposed to spaceborne sensors) and longer observation periods (as opposed to airborne sensors) while keeping costs low.

2.1.1 *State of the Art*

2.1.1.1 *Bistatic Radar for Earth Observation*

The field of bistatic radar for monitoring of the natural environment has not been as thoroughly explored as its monostatic counterpart since the requirement of physical separation between the transmitter and the receiver introduces additional technical and operational challenges [13]. Continued interest of the scientific community in this area is reflected in past proposals of bistatic satellite mission concepts [14–17], as well as proposals currently in evaluation such as Tandem-L [3], Harmony [18], and ROSE-L [19]. The Shuttle Radar Topography Mission [20] employed a single-pass interferometry configuration, where a considerable bistatic baseline between receiver antennas on a single platform was achieved through deployment of an extensible mast. TanDEM-X [21] is the first and currently only mission to demonstrate spaceborne bistatic synthetic aperture radar (SAR) measurements using two completely separate platforms and has a bistatic angle β on the order of 1° or less in nominal operation.

Several experimental bistatic campaigns using airborne SAR systems had been carried out in the past two decades, such as the ONERA-DLR bistatic SAR experiment [5], MetaSensing's BelSAR campaign [22, 23], and hybrid bistatic experiments between a spaceborne transmitter (TerraSAR-X) and an airborne receiver (F-SAR [24] and PAMIR [25]).

Ground-based measurements offer more flexibility in terms of temporal coverage and system configuration, such as a systematic variation and sampling of different bistatic angles. Several experimental bistatic terrestrial radar devices employing aperture synthesis were built recently [4, 26–28], as well as multiple passive bistatic SAR (PB-SAR) receivers that use orbiting satellites as transmitters of opportunity [29–34].

There is a relative lack of available polarimetric-interferometric bistatic datasets with large bistatic angles since most of the available systems either operate in the small bistatic angle mode for single-pass InSAR purposes [21, 23], are of one-off experimental nature [5, 24, 25], can only operate in very constrained geometry [26, 27, 29–32], or do not have full-polarimetric capabilities [4, 29, 30, 32]. Such datasets are, however, vital for development, testing, and verification of future bistatic spaceborne mission concepts and model-based inversion procedures. Terrestrial radars that are capable of acquiring polarimetric-interferometric datasets at a variety of bistatic angles such as the bistatic KAPRI provide a possibility to perform many of these required measurements.

2.1.1.2 *Bistatic Real-Aperture Radar*

Partly due to its potential surveillance applications, bistatic real-aperture radar geometry and associated parameters, such as signal intensity, range, clutter cell area, and others, have been extensively analyzed in the literature [10, 35, 36].

2.1.1.3 *Polarimetric Calibration*

In the monostatic case, polarimetric calibration of radar systems is usually performed using trihedral corner reflectors, which serve as a robust and passive target with a high radar cross section for radiometric and polarimetric calibration [37]. For cross-polarized channels, usually, a supplemental target with a strong cross-polarizing signature [38, 39] or alternative approaches such as the reciprocity principle are utilized [37, 40].

Neither the trihedral corner reflector nor the reciprocity principle is usable in the bistatic case. Bistatic calibration is thus performed via other approaches, such as a modified dihedral with a varying opening angle [41, 42], a cross-polarizing cylinder [43], or an active calibrator [5, 44, 45].

2.1.2 *KAPRI: A Real-Aperture Polarimetric-Interferometric FMCW Radar with Bistatic Capabilities*

Monostatic operation mode and the polarimetric calibration of KAPRI (Ku-band Advanced Polarimetric Radar Interferometer)—a real-aperture, frequency-modulated continuous-wave (FMCW) radar—have been introduced in [40], with application to observation of natural environments in [46] and [47]. It was built by Gamma Remote Sensing and is an extension of the GPRI [48–51] with fully polarimetric capabilities and a custom hardware extension that allows chirp synchronization. By employing two KAPRI devices, one as a transmitter and the other as a receiver, and increasing the beamwidth of the receiver device's antennas, it is possible to perform bistatic acquisitions while preserving the high flexibility of the acquisition geometry. To the best of our knowledge, KAPRI is the first real-aperture, full-polarimetric, interferometric, and bistatic radar system capable of monitoring areas kilometers in size with meter-scale resolution.

2.1.3 *Contributions of This Article*

The following procedures, which are necessary in order to fully allow bistatic operation and acquisition of calibrated bistatic single look complex (SLC) datasets, are described in this article:

1. synchronizing the acquisition start times and frequency sweeps of both radars using a synchronization link;
2. compensating for relative drift of local oscillators (LOs) and resulting frequency / bandwidth / phase offsets;
3. modeling the bistatic geometry in order to consider the elliptical shape of bistatic iso-range lines, and the antenna gain of the bistatic transmit and receive antennas;
4. calibrating individual polarimetric channels of both devices—this required development of a novel calibration target capable of calibration of both co- and cross-polarized channels in both monostatic and bistatic acquisition modes, as well as application of an appropriate calibration method.

These procedures are then validated via analysis of the following:

1. the synchronization signal behavior in terms of its phase and frequency;
2. polarization purity and phase retrieval accuracy of both devices;
3. the polarimetric signature of the novel active calibration device;
4. polarimetric calibration coefficients retrieved for both devices using the novel active calibration method and their comparison to coefficients retrieved using the previously validated calibration procedure using passive corner reflectors described in [40].

2.1.4 *Outline*

Section 2.2.1 presents the geometrical configuration employed for bistatic KAPRI acquisitions and the additional instrumentation required for bistatic operation. In Sections 2.2.2 and 2.2.3, a signal model that considers the two-chirp nature of the bistatic measurements is developed, and Section 2.2.4 shows how these time-related oscillator distortions are compensated by a synchronization link. Section 2.2.5 analyzes the effect of the synchronization link and lower antenna gain on phase retrieval accuracy of the bistatic receiver. Section 2.2.6 describes

a procedure that aligns the bistatic dataset acquired in an elliptical geometry with the polar geometry of the monostatic dataset and compensates for varying resolution cell size. Possible off-center gain corrections in case of uneven horn antenna patterns are described in Section 2.2.7. Section 2.2.8 describes a novel calibration target well-suited for calibration of bistatic polarimetric-interferometric systems, and Section 2.2.9 describes the polarimetric calibration method, which makes use of this novel target. Finally, the processing pipeline is summarized in Section 2.2.10.

Several experiments were carried out to demonstrate certain features of bistatic KAPRI operation. Section 2.3.1 verifies the signal model by analyzing the predicted connection between the slow time behavior of the reference signal's range position and phase. Section 2.3.2 analyzes the polarimetric signature of the novel calibration target. Section 2.3.3 analyzes polarization purity with respect to the requirements of the chosen polarimetric calibration method, as well as effects of antenna gain on phase retrieval accuracy. Section 2.3.4 verifies the polarimetric calibration method by comparing the resulting calibration parameters with the parameters returned from the monostatic calibration method introduced in [40]. Finally, Section 2.3.5 provides a visualization of key steps of the bistatic processing pipeline.

Section 2.4 discusses the geometric features of bistatic KAPRI datasets, properties of the reference signal, validity of the novel calibration method and its advantages, as well as possible applications of bistatic KAPRI within the framework of Earth observation. A conclusion is given in Section 2.5.

2.2 METHODS

2.2.1 *Bistatic KAPRI Configuration*

The bistatic configuration of KAPRI consists of two devices—the monostatic transmitter–receiver P (primary) and a bistatic receiver S (secondary). The antennas of the primary monostatic KAPRI device are mounted on a single rotating tower with two alternating transmitting and four receiving slotted-waveguide antennas with a half-power beamwidth (HPBW) of approximately 0.5° in azimuth. To obtain a bistatic configuration, the secondary tower employing a set of four receiving antennas with a gain pattern HPBW of 12° in azimuth is set up. The addition of the passive bistatic receiver has the benefit that two datasets—one monostatic and one bistatic—are acquired during each acquisition. This creates possibilities to naturally combine and extend the well-known monostatic polarimetric imaging mode into the bistatic mode.

Key system parameters of the bistatic KAPRI configuration are summarized in Table 2.1. The wider antenna beamwidth of the bistatic receiver was chosen for practical reasons—at any given time, only the targets that are located in the intersection of the Tx and Rx antenna beams can be imaged (see Fig. 2.1). In the bistatic geometry, narrow-beam receiver antennas would provide higher gain, but the beam intersection—and thus the imaged area size—would be prohibitively small. A beamwidth of 12° for the bistatic receiver is a compromise between coverage and signal strength. Table 2.2 shows the range and azimuth resolutions of both devices in multiple example geometric configurations.

Table 2.1: Main system parameters of KAPRI.

Parameter	Symbol	Value
Start frequency	f_c	17.1 GHz
Chirp bandwidth	B	up to 200 MHz
Output power	P_t	21.5 dBm
Receiver noise figure	F_n	3.1 dB at 290 K
FMCW chirp duration	τ	between 250 µs and 16 ms
Range sample spacing	δ^{rs}	0.75 m
Primary (P) azimuth beamwidth	δ_P^θ	0.5°
Primary (P) elevation beamwidth	δ_P^ε	>31°
Secondary (S) azimuth beamwidth	δ_S^θ	12°
Secondary (S) elevation beamwidth	δ_S^ε	24°
Clock frequency	f_{clock}	100 MHz GPS-disciplined

Note: Beamwidth values correspond to one-way HPBW.

Table 2.2: Examples of range (δ^{RNG}) and azimuth (δ^{AZM}) resolutions of monostatic primary (P) and bistatic secondary (S) KAPRI with varying values of range from primary device (r_P) and bistatic angle (β). Resolution values correspond to −3 dB peak width.

r_P	β	δ_P^{RNG}	δ_S^{RNG}	δ_P^{AZM}	δ_S^{AZM}
400 m	0°	0.95 m	0.95 m	2.69 m	3.49 m
400 m	30°	0.95 m	1.02 m	2.69 m	3.49 m
400 m	120°	0.95 m	3.80 m	2.69 m	3.49 m
6000 m	0°	0.95 m	0.95 m	40.3 m	52.4 m
6000 m	30°	0.95 m	1.02 m	40.3 m	52.4 m
6000 m	120°	0.95 m	3.80 m	40.3 m	52.4 m

In general, bistatic experiments require a synchronization procedure, preferably using a dedicated built-in link (such as in case of TanDEM-X [52]). KAPRI also employs such a

link—Fig. 2.2 shows the reference chirp transmission method: a directional coupler is used to transmit approximately 10% of chirp power directly from the primary to the secondary device. This directly transmitted signal is used to correct phase and frequency offsets, as described in Section 2.2.3.

2.2.2 *Bistatic KAPRI FMCW Signal Model*

KAPRI is using a deramp-on-receive FMCW radar architecture [53]. The monostatic signal model is described in [40], and this section describes the bistatic signal model and acquisition mode. The measurement geometry is shown in Fig. 2.1, and the device configuration depicting the antennas used and the reference chirp transmission is shown in Fig. 2.2. Photographs of the deployed devices are shown in Fig. 2.3.

The two devices are not perfectly synchronized—varying conditions at operation locations, as well as unavoidable manufacturing differences in parameters such as exact oscillator base frequency, cause differences between their frequency-modulated chirps. This can be addressed by modeling each device's linear FM chirp with its own start frequency, bandwidth, and sweep start time.

The primary device transmits a linearly modulated signal $s_{\mathrm{pt}}(t)$ of duration τ with bandwidth B and start frequency f_{c}

$$s_{\mathrm{pt}}(t) = e^{j2\pi(f_{\mathrm{c}}t+\frac{\gamma}{2}t^2)} \tag{2.1}$$

where $\gamma = \frac{B}{\tau}$ is the chirp rate. The signal is then scattered by a scatterer with complex reflectivity σ and delayed by $\frac{p}{c}$, where

$$p = r_{\mathrm{P}} + r_{\mathrm{S}} \tag{2.2}$$

is the bistatic path length. The signal received at the secondary receiver $s_{\mathrm{sr}}(t)$ is then:

$$s_{\mathrm{sr}}(t) = \sigma e^{j2\pi\left(f_{\mathrm{c}}\left[t-\frac{p}{c}\right]+\frac{\gamma}{2}\left[t-\frac{p}{c}\right]^2\right)} \tag{2.3}$$

The secondary device (i.e., bistatic receiver) generates its own linearly modulated chirp $s_{\mathrm{st}}(t)$ with bandwidth B' and start frequency f_{c}'

$$s_{\mathrm{st}}(t) = e^{j2\pi\left(f_{\mathrm{c}}'[t-\Delta t]+\frac{\gamma'}{2}[t-\Delta t]^2\right)} \tag{2.4}$$

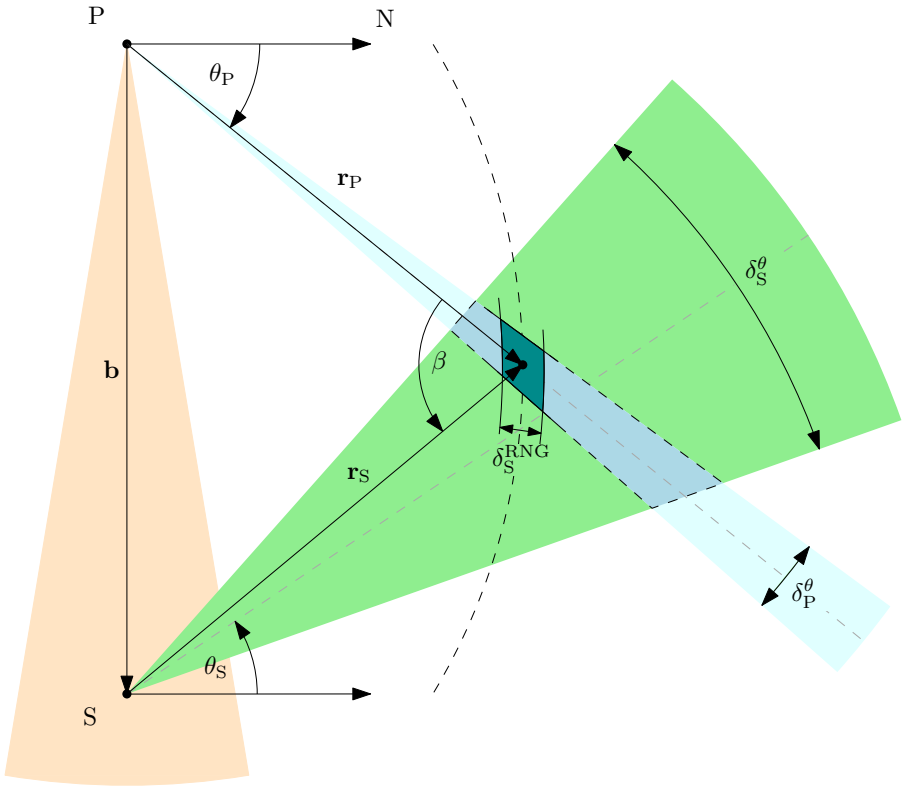

FIGURE 2.1: Bistatic KAPRI configuration. In the bistatic north-referenced coordinate system, the secondary device (S) is at the 90° azimuth coordinate with respect to the primary device (P). The dashed curve marks the elliptical isorange line. Azimuth resolution is provided by the narrow aperture of the rotating primary antennas (blue), while the pattern of static wide-aperture secondary receiver horn antennas (green) defines the total covered area. The teal-colored area defines one resolution cell. The light-brown colored synchronization beam transmits the bistatic reference signal directly from the primary to the secondary device.

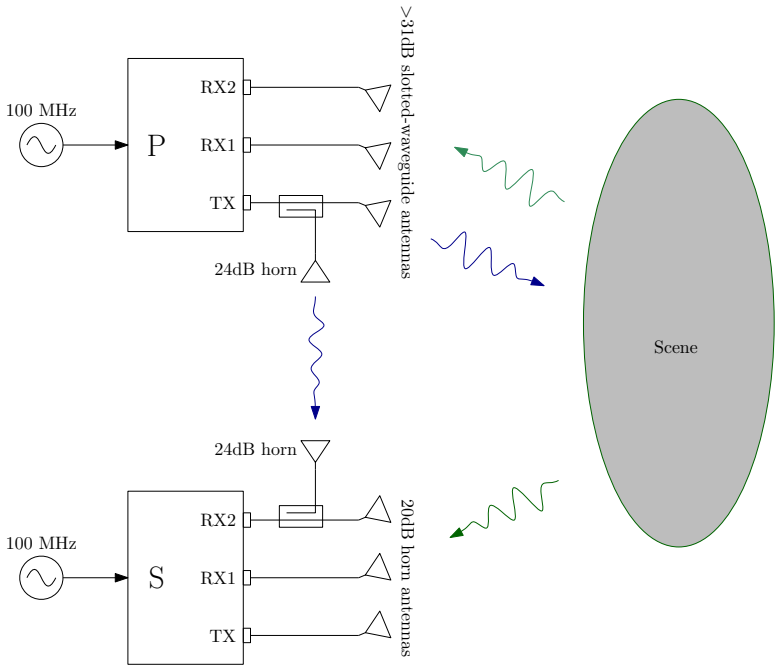

FIGURE 2.2: Simplified antenna configuration. Each device is driven by its own local oscillator (LO), and these two LOs drift with respect to one another. In order to correct this phase drift, directional couplers are used to transmit a part of the signal directly from the primary to the secondary. This signal then serves as a reference for phase drift correction. The nominal gain and type of each antenna are marked in the figure.

FIGURE 2.3: Bistatic KAPRI device configuration (left: primary device (P) equipped with narrow-beam slotted-waveguide antennas and right: secondary receiver device (S) equipped with horn antennas). Reference link horn antennas are placed on tripods on the right side of the two images, together with long-range Wi-Fi antennas for remote device control.

where Δt describes the starting time offset between the two devices' chirps and $\gamma' = \frac{B'}{\tau}$. The time–frequency diagram of this signal model is shown in Fig. 2.4.

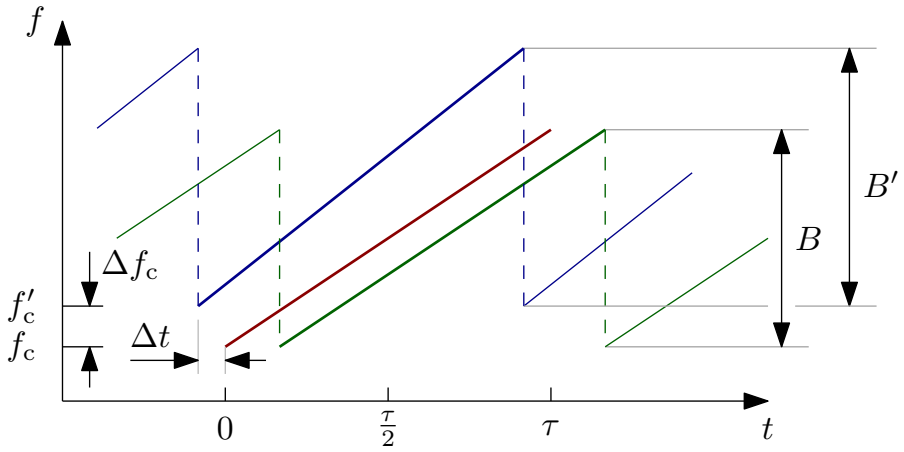

FIGURE 2.4: Time-frequency diagram of the transmitted s_{pt} (dark red), received s_{sr} (green), and receiver reference s_{st} (blue) chirps. Start frequency offset Δf_{c} and bandwidth offset ΔB between transmitter and receiver chirps cause range offset and peak smearing within the range-compressed data, respectively. While the start times of chirps are synchronized via GPS PPS signals at acquisition start, due to clock speed offsets, a chirp start time offset Δt accumulates over the course of the acquisition, causing additional range and phase drift of the deramped signal.

In the secondary device's receiver, the received bistatic signal s_{sr} is mixed with its own reference chirp s_{st}, which removes the linear modulation and results in a deramped signal s_{d}

$$s_{\mathrm{d}}(t) = s_{\mathrm{sr}}(t)^* s_{\mathrm{st}}(t) \tag{2.5a}$$

$$= \sigma^* e^{j2\pi\left(\left[\frac{p\gamma}{c}+\Delta f_{\mathrm{c}}-\gamma'\Delta t\right]t+\frac{p}{\lambda}-\frac{p^2\gamma}{2c^2}+\frac{\Delta\gamma}{2}t^2-f'_{\mathrm{c}}\Delta t+\frac{\gamma'}{2}\Delta t^2\right)} \tag{2.5b}$$

where $\lambda = c/f_{\mathrm{c}}$ is the wavelength, $\Delta f_{\mathrm{c}} = f'_{\mathrm{c}} - f_{\mathrm{c}}$ is the start frequency offset between the two radars, $\Delta\gamma = \gamma' - \gamma$ is chirp rate offset between the two radars, and the * symbol represents the complex conjugate.

The six phase terms in the complex exponent in eq. (2.5b) are as follows:

1. $2\pi\left[\frac{p\gamma}{c} + \Delta f_{\mathrm{c}} - \gamma'\Delta t\right] t$—beat signal with beat frequency proportional to the signal travel path p, shifted by Δf_{c} and $-\gamma'\Delta t$ due to offset between the two radars' start frequencies and chirp start times, respectively;

2. $2\pi\frac{p}{\lambda}$—two-way propagation phase;

3. $-\pi\frac{p^2\gamma}{c^2}$—"residual video phase" (RVP) present also in the monostatic deramped signal [40];
4. $\pi\Delta\gamma t^2$—residual frequency ramp caused by chirp rate offset $\Delta\gamma$;
5. $-2\pi f_c'\Delta t$—dominant phase drift term caused by start time offset Δt;
6. $\pi\gamma'\Delta t^2$—second-order time offset term.

These terms are analyzed in more detail in Section 2.2.3.

2.2.3 *Deramped Signal Analysis*

By noting the time dependence of the first term in the exponential of eq. (2.5b), one can estimate the profile of the complex reflectivity of the observed scene $\hat{\sigma}(p,\theta)$ by taking the Fourier transform of $s_d(t)^*$. Several corrections are, however, needed in order to achieve data coregistration, and polarimetric and interferometric calibration since $s_d(t)$ contains additional terms as a result of possible mismatching chirp rate, start frequency, and LO frequency between transmitter and receiver devices.

2.2.3.1 *Beat Signal*

The beat signal term of eq. (2.5b) has three components: the signal travel path component $\frac{p\gamma}{c}$ (the term of interest for ranging using FMCW radar), the frequency offset Δf_c, and start time offset $-\gamma'\Delta t$. We define the total observed frequency offset Δf

$$\Delta f = \Delta f_c - \gamma'\Delta t \tag{2.6}$$

This offset causes incorrect range determination for the observed scene. Furthermore, the value of this offset possibly changes on both short time scales of individual pulses (due to accumulation of start time offset Δt), as well as longer time scales (due to changes in Δf_c and γ' due to variations in environmental conditions).

2.2.3.2 *Two-Way Propagation Phase*

The phase term

$$\phi_{\text{prop}} = 2\pi\frac{p}{\lambda} \tag{2.7}$$

is the quantity of interest for interferometric measurements since wavelength-scale changes in signal travel path p cause considerable changes in the value of this term.

2.2.3.3 *Residual Video Phase*

The term

$$\phi_{\text{rvp}} = -\pi \frac{p^2 \gamma}{c^2} \tag{2.8}$$

is assumed to be constant for each target over the antenna aperture for the KAPRI configuration [40]. The value of this term varies with the signal travel path length, similar to the propagation phase term. We can define changes in signal phase $\Delta\phi$ due to a small change in signal path Δp at total path p as

$$\Delta\phi_{\text{prop}}(p, \Delta p) = \frac{2\pi(p + \Delta p)}{\lambda} - \frac{2\pi p}{\lambda} = \frac{2\pi \Delta p}{\lambda} \tag{2.9a}$$

$$\Delta\phi_{\text{rvp}}(p, \Delta p) = ... = -\frac{\pi\gamma}{c^2}(2p\Delta p + \Delta p^2) \tag{2.9b}$$

The ratio of magnitudes of these changes is then

$$\left| \frac{\Delta\phi_{\text{rvp}}}{\Delta\phi_{\text{prop}}}(p, \Delta p) \right| = \frac{\lambda\gamma}{2c^2} \frac{2p\Delta p + \Delta p^2}{\Delta p} \approx \frac{\lambda\gamma p}{c^2} = \frac{\gamma p}{f_c c} \tag{2.10}$$

For KAPRI parameters, the worst case estimate of this ratio is $\sim 10^{-4}$, and thus, the propagation phase term varies with p orders of magnitude faster than the RVP term. Because of this, for most interferometric and polarimetric purposes, the effects of RVP can be neglected. If necessary, the RVP contribution can be trivially corrected by phase-shifting each range cell by the corresponding value of eq. (2.8).

2.2.3.4 *Residual Frequency Ramp*

Reflected in term $\pi\Delta\gamma t^2$, bandwidth mismatch results in a residual low-frequency chirp component in the deramped signal, with peak frequency $\Delta\gamma\tau$. This residual chirp defocuses the compressed signal over a range of neighboring frequencies and thus degrades the spatial resolution.

2.2.3.5 *Phase Drift Term*

The fifth phase term in eq. (2.5b)

$$\phi_{\text{d}} = -2\pi f_c' \Delta t \tag{2.11}$$

is caused by the changing value of start time offset Δt. . This offset accumulates in-between synchronizations via GPS PPS pulses, which resets Δt back to 0. We can compute the current value of Δt at time T since the last synchronization as

$$\Delta t(T) = \int_0^T \frac{\Delta\tau(T')}{\tau} \mathrm{d}T' \tag{2.12}$$

where $\Delta\tau(T')$ is the difference between the two devices' chirp lengths τ and τ' at slow time T'. The phase drift rate can then be calculated by taking the slow-time derivative of eq. (2.11):

$$\frac{\mathrm{d}\phi_\mathrm{d}(T)}{\mathrm{d}T} = -2\pi f_\mathrm{c}' \frac{\mathrm{d}\Delta t(T)}{\mathrm{d}T} = -2\pi f_\mathrm{c}' \frac{\Delta\tau(T)}{\tau} \tag{2.13}$$

The phase drift rate at any given moment is thus linearly proportional to the value of $\Delta\tau$. This phase drift can compromise interferometric measurements, since within $s_\mathrm{d}(t)$, the phase drift ϕ_d is indistinguishable from changes in the geometric phase term ϕ_prop and needs to be corrected via the synchronization link.

2.2.3.6 *Second-Order Phase Drift Term*

Similar to the RVP term, the effects of second-order phase drift term

$$\phi_{\mathrm{d},2} = \pi\gamma'\Delta t^2 \tag{2.14}$$

are negligible compared to the previous term

$$\frac{\phi_{\mathrm{d},2}}{\phi_\mathrm{d}} = -\frac{\gamma'\Delta t}{2f_\mathrm{c}'} \tag{2.15}$$

Experiments show that value of Δt in nominal operation is at most 100 ns at any time, corresponding to a worst case ratio of $\sim 10^{-5}$.

2.2.4 *Correction via Reference Signal Transmission*

Offset effects described in the previous section can be corrected in the data by transmitting a reference signal directly from primary transmitter to secondary receiver (see Fig. 2.2). This reference signal does not scatter off the scene and, at the receiver, has the form

$$s_\text{sr-ref}(t) = e^{j2\pi\left(f_\mathrm{c}\left[t-\frac{b}{c}\right]+\frac{\gamma}{2}\left[t-\frac{b}{c}\right]^2\right)} \tag{2.16}$$

where b is the length of the bistatic baseline. The corresponding deramped reference signal is

$$s_{\text{d-ref}}(t) = s_{\text{sr-ref}}(t)^* s_{\text{st}}(t) \tag{2.17a}$$

$$= e^{j2\pi\left(\left[\frac{b\gamma}{c}+\Delta f\right]t+\frac{b}{\lambda}-\frac{b^2\gamma}{2c^2}+\frac{\Delta\gamma}{2}t^2-f_c'\Delta t+\frac{\gamma'}{2}\Delta t^2\right)}. \tag{2.17b}$$

By multiplying the deramped signal s_{d} by the complex conjugate of the deramped reference signal $s_{\text{d-ref}}$, one can compensate for the drift effects

$$s_{\text{d}}(t)s_{\text{d-ref}}(t)^* = \sigma^* e^{j2\pi\left(\frac{(p-b)\gamma}{c}t+\frac{p-b}{\lambda}-\frac{(p^2-b^2)\gamma}{2c^2}\right)} \tag{2.18}$$

and by mutiplying the expression in (2.18) by an additional oscillating term with frequency $\frac{b\gamma}{c}$, the corrected deramped signal $s_{\text{d-corr}}$ is recovered

$$s_{\text{d-corr}}(t) = s_{\text{d}}(t)s_{\text{d-ref}}(t)^* e^{j2\pi\frac{b\gamma}{c}t} \tag{2.19a}$$

$$= \sigma^* e^{j2\pi\left(\frac{p\gamma}{c}t+\frac{p-b}{\lambda}-\frac{(p^2-b^2)\gamma}{2c^2}\right)} \tag{2.19b}$$

Analysis of this signal then enables interferometric, polarimetric, and bistatic radar cross section (RCS) measurements. In order to recover it, it is necessary to be able to isolate the reference signal $s_{\text{d-ref}}(t)$ from the total deramped signal $s_{\text{d}}(t)$.

The reference signal can be either transmitted using its own channel or superimposed on the signal from the scene (e.g., by use of a directional coupler as in Fig. 2.2). Due to triangle inequality, any signals scattered from the scene will have a path delay longer than the directly transmitted reference chirp, i.e., $p > b$. This means that even when the reference chirp is not transmitted via a dedicated channel, the reference signal can be identified within the SLC as the peak with the shortest range distance. Provided that the scene area in the region where $p \approx b$ is relatively clutter-free, the deramped observed reference signal $\hat{s}_{\text{d-ref}}$ can be isolated by applying a window around the range-compressed signal $\mathcal{F}[\hat{s}_{\text{d}}]$

$$\hat{s}_{\text{d-ref}}(t) = \mathcal{F}^{-1}\left[\mathcal{F}[\hat{s}_{\text{d}}]\, W\right] \tag{2.20}$$

where $\mathcal{F}$ denotes the Fourier transform and W is a window (e.g., a Hanning window) in the range-compressed signal domain centered around the range distance b and wide enough to

capture the reference signal even when it is offset in frequency by Δf and spread out by bandwidth offset $\Delta\gamma$.

Having isolated $\hat{s}_{\text{d-ref}}$, it is now possible to correct for the offset effects in the scene signal $\hat{s}_{\text{d}}$ via multiplication in the deramped signal domain

$$\hat{s}_{\text{d-corr}}(t) = \hat{s}_{\text{d}}(t)\hat{s}_{\text{d-ref}}(t)^* e^{j2\pi\frac{b\gamma}{c}t} \tag{2.21}$$

where the final term with beat frequency $\frac{b\gamma}{c}$ ensures correct range positioning of the corrected signal. Finally, $\mathcal{F}\left[\hat{s}_{\text{d-corr}}(t)\right]$ yields the corrected range-compressed bistatic signal.

2.2.5 *Phase Retrieval Accuracy*

The bistatic acquisition configuration has an effect on phase retrieval accuracy of $\hat{s}_{\text{d-corr}}$ in two ways

1. The reduced gain of the secondary device's antennas (necessary to increase the beam pattern width) causes a reduction of signal-to-noise ratio (SNR) of scene signal $\hat{s}_{\text{d}}$.
2. Any phase noise along the directly transmitted reference signal link affects $\hat{s}_{\text{d-ref}}$.

The final phase variance can then be expressed as a sum of the variances of the two effects

$$\sigma_\phi^2 = \sigma_{\phi,\text{scene}}^2 + \sigma_{\phi,\text{ref}}^2 \tag{2.22}$$

where $\sigma_{\phi,\text{scene}}$ is the phase noise contribution of the scene signal $\hat{s}_{\text{d}}$ and $\sigma_{\phi,\text{ref}}$ is the phase noise contribution of the reference signal $\hat{s}_{\text{d-ref}}$.

We now investigate the contribution of the reference signal $\sigma_{\phi,\text{ref}}$. The variance of the phase noise of a signal is related to the SNR of the signal and in case of high SNR can be estimated as [54–56]

$$\sigma_{\phi,\text{ref}}^2 = \frac{1}{\text{SNR}_{\text{ref}}} \tag{2.23}$$

The exact requirement for value of $\sigma_{\phi,\text{ref}}$ depends on the particular application. For example, in order to achieve the value of phase noise standard deviation of the reference signal below 2°, we can determine the necessary SNR

$$\sigma_{\phi,\text{ref}} \leq 2^\circ \implies \text{SNR}_{\text{ref}} \geq 29.1\,\text{dB} \tag{2.24}$$

The reference signal's SNR can be computed using the nominal parameters of the KAPRI system and applying the one-way radar equation [57, 58]

$$\mathrm{SNR}_{\mathrm{ref}} = \frac{P_{\mathrm{t}}\tau G_{\mathrm{t}} G_{\mathrm{r}} \lambda^2}{(4\pi b)^2 k T_0 F_{\mathrm{n}} L} \tag{2.25}$$

where P_{t} is the transmitter output power, τ is the transmitted pulse length, $G_{\mathrm{t}}, G_{\mathrm{r}}$ are the gains of corresponding transmit and receive antennas, respectively, L are the line losses, b is the bistatic baseline, k is Boltzmann's constant, T_0 is the system temperature, and F_{n} is the system noise figure.

Taking the logarithmic form of eq. (2.25), we can write

$$\mathrm{SNR}_{\mathrm{ref}}^{\mathrm{dB}} = 10\left[\log\frac{P_{\mathrm{t}}\tau G_{\mathrm{t}} G_{\mathrm{r}}}{k T_0 F_{\mathrm{n}} L} + 2\log\frac{\lambda}{4\pi b}\right] \tag{2.26}$$

The SNR value thus reduces/increases by 6 dB for each doubling/halving of the baseline length b, and increases/reduces by 3 dB for each doubling/halving of the chirp length τ.

To account for all system losses and noise sources along the signal path, we determined a reference SNR value for KAPRI experimentally by determining the intensity of the reference signal peak during an acquisition I_{ref}, and comparing it to the noise floor I_{noise}[1]

$$\mathrm{SNR}_{\mathrm{ref}} = \frac{I_{\mathrm{ref}}}{I_{\mathrm{noise}}} \approx 50\,\mathrm{dB} \text{ at } b = 950\,\mathrm{m}, \tau = 4\,\mathrm{ms}. \tag{2.27}$$

The reference signal thus has sufficient SNR in this configuration to satisfy the 2° phase noise requirement for a bistatic baseline value of up to ~ 8000 m at 4 ms chirp length.

For the scene signal contribution $\sigma_{\phi,\mathrm{scene}}$, the main differentiating factor between the primary (P) and secondary (S) devices is the reduction of receiver antenna gain. This 12-dB reduction directly translates to reduction of scene SNR for the secondary device and will cause the standard deviation of interferogram phase noise (and the corresponding distance measurement precision) to degrade [48]

$$\frac{\sigma_{\phi,\mathrm{scene,S}}}{\sigma_{\phi,\mathrm{scene,P}}} = \frac{1}{\sqrt{10^{-1.2}}} \approx 4. \tag{2.28}$$

1 The noise floor of the receiver I_{noise} can be determined by measuring the intensity of the noise within the secondary receiver's SLC dataset, acquired while the primary transmitter is turned off.

2.2.6 *Bistatic Geometry Corrections*

For the purpose of correctly geocoding data within the bistatic acquisition geometry with elliptical iso-range lines, it is important to be able to reference the internal azimuth coordinate of each tower's rotational positioner to the bistatic north-referenced coordinate system shown in Fig. 2.1, and afterward to real-world geographic coordinates. This can be done by carrying out a monostatic acquisition by each device and referencing a target with known geographic coordinates with its position within the SLC. One narrow-beam transmitter antenna is placed on the secondary device for the purpose of this initial referencing acquisition, the principle of which is shown in Fig. 2.5.

The bistatic geometry also has specific implications for recovery of the scatterers' range and intensity values.

2.2.6.1 *Range*

The total signal travel distance p for each scatterer can by recovered by taking the Fourier transform of the deramped corrected signal $s_{\text{d-corr}}(t)$. In the monostatic case, this travel distance has a trivial connection to range

$$r_{\text{P}} = r_{\text{S}} = \frac{p}{2}. \tag{2.29}$$

In the bistatic case, the scatterer's distance to the primary device r_{P} is calculated as [35]

$$r_{\text{P}} = \frac{p^2 - b^2}{2(p - b\sin\theta_{\text{P}})} \tag{2.30}$$

where b is the length of the bistatic baseline, and the scatterer's azimuth coordinate θ_{P} is defined by the current rotational position of the narrow-aperture antennas.[2] After range compression of the acquired signal is performed, the bistatic dataset thus needs to be shifted in range according to eq. (2.30). This aligns the bistatic SLC with the simultaneously acquired monostatic SLC.[3] Visualization of this range shift in different parts of the scene is shown in Fig. 2.6a.

2 Eq. (2.30) reduces to eq. (2.29) in the monostatic case $b = 0$.

3 Range resolution will, in general, be worse in the bistatic dataset, especially at bistatic angles $\beta > 90°$. Length (along range direction) of a range-limited bistatic resolution cell is scaled by a factor of approximately $\cos(\beta/2)^{-2}$ as opposed to monostatic resolution cell length [35].

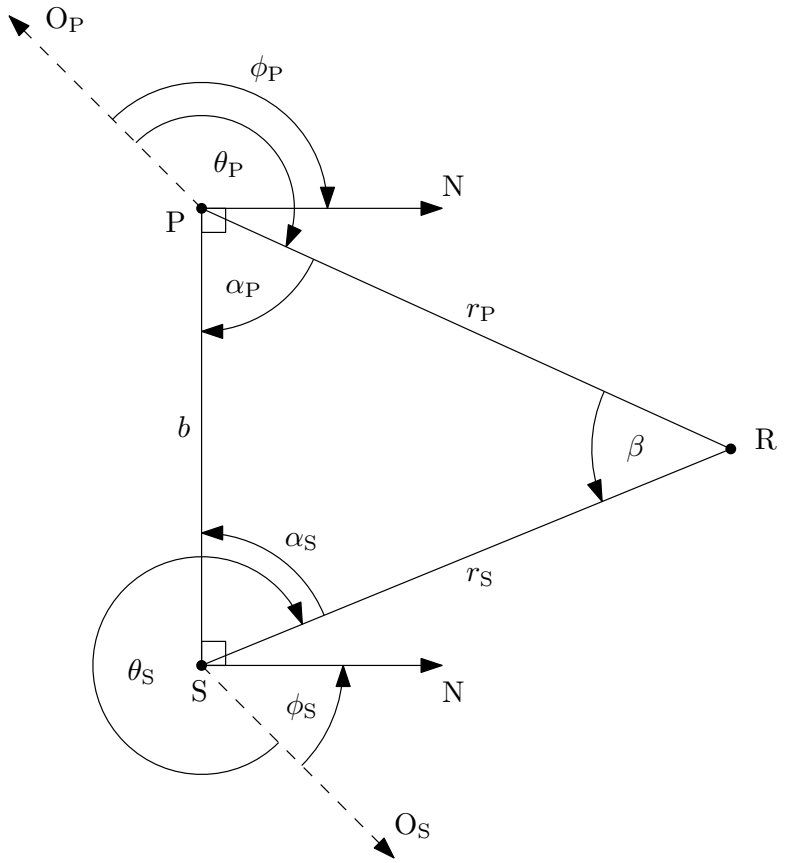

FIGURE 2.5: Bistatic north coordinate system derivation procedure. For all angles, a positive angle value represents a clockwise rotation from the direction marked by the start of the arrow, to the direction marked by the endpoint of the arrow. If the arrow points counterclockwise, the corresponding angle's value is negative. The initial directions of zero-azimuth coordinates O_P, O_S are dependent on particular orientation of the devices' tripods. The objective is then to establish a relation between these directions and the north direction N of the bistatic coordinate system. This is achieved by using a reference point P within the scene. Positions of devices P and S, as well as reference scene point P are determined by GPS measurements. From their coordinates, angles α_P, α_S are calculated. Monostatic acquisitions of point P are then performed by both devices, acquiring the value of P's azimuth coordinates θ_P, θ_S. From this, the azimuth direction of bistatic North can be determined, as $\phi_P = \theta_P + \alpha_P - (\pi/2)$, and $\phi_S = \theta_S + \alpha_S + (\pi/2)$.

2.2.6.2 *Intensity*

It is desired that the intensity of the SLC data is directly proportional to radar brightness β_0. In the monostatic case, this is achieved by scaling each range line of the SLC by $\sqrt{r^3}$ to compensate for varying resolution cell size and power spreading loss [40]. In the bistatic case

$$\beta_0 \sim P r_{\mathrm{P}}^2 r_{\mathrm{S}}^2 \frac{\cos^2 \frac{\beta}{2}}{r_{\mathrm{P}}} \tag{2.31}$$

where β is the bistatic angle, P is the received power, $r_{\mathrm{P}}^2 r_{\mathrm{S}}^2$ is the power spreading term, and $r_{\mathrm{P}}^{-1} \cos^2 \frac{\beta}{2}$ accounts for varying resolution cell area [35, 59]. Thus, the final SLC scaling factor varies in both range and azimuth and is equal to $\sqrt{r_{\mathrm{P}} r_{\mathrm{S}}^2} \cos \frac{\beta}{2}$. Visualization of the ratio of bistatic to monostatic intensity in different areas of the scene is shown in Fig. 2.6b.

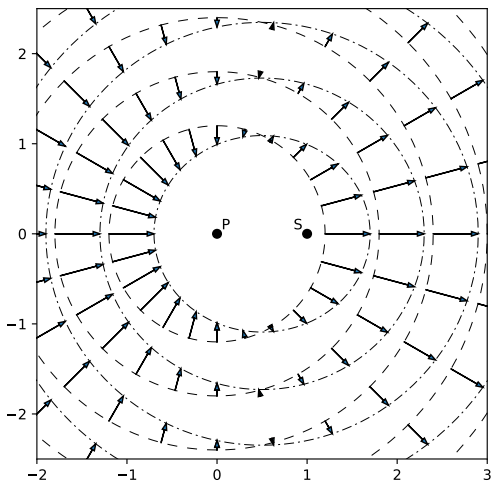

(a) Correction of observed range according to eq. (2.30). The start points of the arrows (and the dashed lines) mark the perceived location if monostatic range equation (2.29) were used, whereas the end points of the arrows (and the corresponding dashed-dotted lines) mark the real location of the target. Targets near the primary device appear further away than they actually are, while targets near the secondary receiver appear closer.

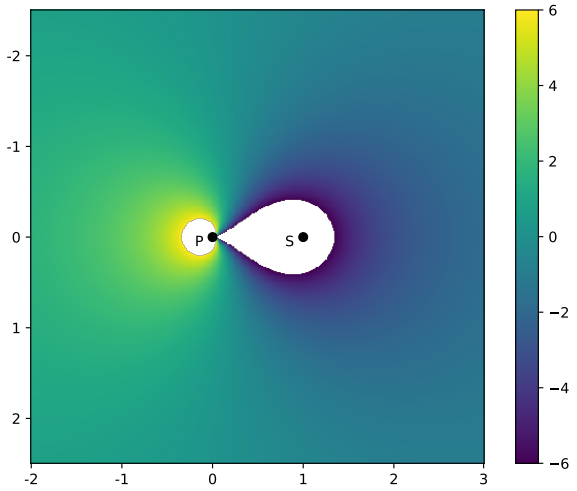

(b) Correction of intensity due to varying resolution cell area according to eq. (2.31). The shown value is the difference in dB between real β_0 for the bistatic receiver, and β_0 observed using monostatic intensity scaling. An uncorrected bistatic dataset would overestimate β_0 of targets in the vicinity of the secondary receiver while underestimating β_0 of targets close to the primary transmitter. The difference vanishes for large range distances.

FIGURE 2.6: Bistatic geometry corrections necessary to align the data acquired by the secondary bistatic receiver with the primary monostatic dataset. The P and S points mark the location of the primary and secondary device, respectively, and axis labels are in units of bistatic baseline.

2.2.7 *Antenna Pattern*

The radar equation for a bistatic real-aperture radar system for a single point scatterer is [10]

$$P_r(r_P, r_S, \theta'_P, \theta'_S, \varepsilon'_P, \varepsilon'_S) = \frac{P_t G_t(\theta'_P, \varepsilon'_P) G_r(\theta'_S, \varepsilon'_S) \lambda^2 \sigma}{(4\pi)^3 r_P^2 r_S^2 L_s} \tag{2.32}$$

where P_t is the transmitted power, r_P, r_S are distances from the primary and secondary devices, respectively, σ is the bistatic radar cross section, L_s is the system losses, and $G_t(\theta'_P, \varepsilon'_P), G_r(\theta'_S, \varepsilon'_S)$ is the antenna gain at the azimuth and elevation offset angle from the respective antenna pointing directions.

For polarimetry, the G_t, G_r terms become important in case that differently polarized antennas have different off-center gain patterns.[4] In that case, intensities of individual polarization channels measured in these off-center pointing directions (but still within the antenna aperture) would be distorted, and as a result, an incorrect polarimetric scattering matrix S would be reconstructed.

The solution is to measure the corresponding antenna gain pattern $G(\theta', \varepsilon')$ and scale each SLC value by the factor $G(\theta', \varepsilon')^{-0.5}$. This, of course, comes at a cost of reduced SNR, so a minimal gain threshold has to be specified, and SLC pixels for which the gain is below this threshold must be discarded.

However, this step is not necessary for the polarimetric analysis, in case the antennas have equal patterns within the cutoff angle, which is the case for the KAPRI radar. Fig. 2.7 shows the calculated antenna patterns for the H- and V-polarized horn antennas of the secondary bistatic receiver.

The fact that only the intersection of the two devices' antenna patterns can be imaged has the following implications for bistatic acquisitions.

- Area coverage of a bistatic acquisition is always lower than in the monostatic case, since while a monostatic acquisition only requires line of sight from one device, a bistatic acquisition requires direct line of sight from every observed point to both transmitter and receiver.

- The need for mosaicking of multiple acquisitions increases the time and data volume necessary to acquire a complete dataset by a factor of $n \approx \frac{\Omega}{\delta_S^\theta}$, where Ω is the desired total azimuth coverage of the secondary device and δ_S^θ is the azimuth beamwidth of the secondary device's antennas.

4 Different antenna gains along the central pointing direction are compensated by polarimetric calibration.

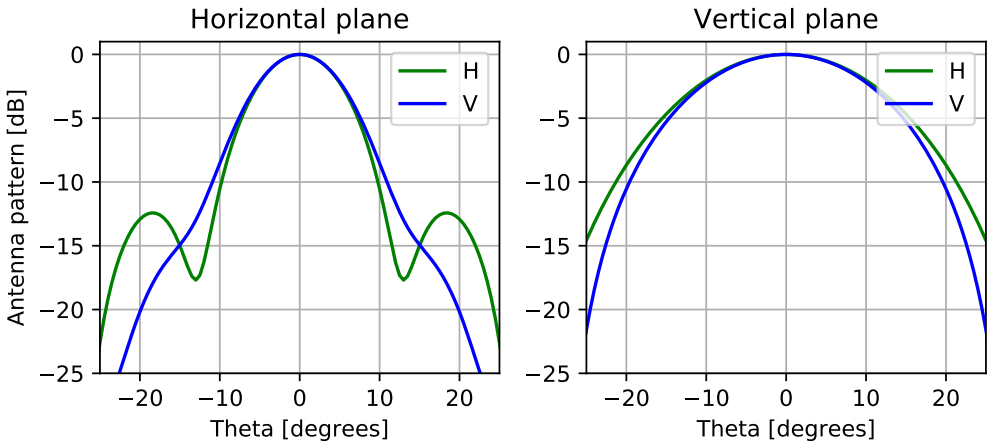

FIGURE 2.7: Calculated co-polarized gain patterns in the horizontal and vertical measurement planes for bistatic Ku-band horn antennas employed by KAPRI.

2.2.8 *Polarimetric Calibration Target*

For the purposes of polarimetric calibration of bistatic KAPRI, an ideal calibration target would have the following properties:

1. a high and stable RCS;
2. capable of returning signal in the desired direction under a variety of bistatic angles;
3. low size and weight for portability in natural environments;
4. ease of alignment under field conditions;
5. capability of calibrating both co- and cross-polarized channels while maintaining identical phase center position for all of these channels.

The first requirement disqualifies targets such as a sphere—wide aperture of the receiver antennas already causes a reduction in SNR and resolution, and thus, a sphere would have too low of a radar cross section compared to clutter within the same range cell. Other passive targets such as a modified dihedral proposed in [41] would likely have sufficient RCS but fail requirements 2–4 since they require precise alignment relative to position of the radar devices. For these reasons, an active calibration device was selected, similar to other bistatic campaigns [5, 45, 60].

Our proposed design Variable-Signature Polarimetric Active Radar Calibrator (VSPARC) employs two horn antennas with a Ku-band amplifier in-between.[5] This ensures sufficient

5 An example of a similar approach can be found in [45] where such a device is used for RCS calibration, as well as [4] where the device was used as a transponder in order to create a bistatic baseline.

RCS for calibration even in presence of background clutter and low weight. Directional flexibility and ease of alignment are provided by custom-made mounting adapters for the antennas—a manually operated camera mount is used for pointing the antennas in the direction toward the transmitting and receiving radars. Afterward, polarization of the antennas can be adjusted by physical rotation around their line of sight, provided by a rotation stage. The mounting adapter is designed in a way such that the phase center of the antenna lies on the central axis of the rotation stage—changing the polarization of the antenna can be thus done without introducing any additional mechanical phase offsets. A schematic of the device is shown in Fig. 2.8, and a prototype of the device deployed in the field is shown in Fig. 2.9.

For both the antenna pointed at the transmitter and the antenna pointed at the receiver, the rotation angle around the pointing axis of the antenna (φ_T and φ_R, respectively) affects the resulting scattering matrix of the calibration target. Sensitivity of the antennas to horizontally and vertically polarized waves can be characterized by a two-component vector

$$\mathbf{t} = \sqrt{G_\mathrm{T}} e^{j\phi_\mathrm{abs,T}(\varphi_\mathrm{T})} \begin{bmatrix} \sin\varphi_\mathrm{T} \\ \cos\varphi_\mathrm{T} \end{bmatrix} \tag{2.33a}$$

$$\mathbf{r} = \sqrt{G_\mathrm{R}} e^{j\phi_\mathrm{abs,R}(\varphi_\mathrm{R})} \begin{bmatrix} \sin\varphi_\mathrm{R} \\ \cos\varphi_\mathrm{R} \end{bmatrix} \tag{2.33b}$$

where $G_\mathrm{T}, G_\mathrm{R}$ are the gain of the respective antenna and ϕ_abs describes any phase offsets introduced due to change of the antenna's rotational position φ.[6]

The scattering matrix is then computed as the outer product of these two vectors, accounting for line losses L and amplifier gain G_A

$$\mathbf{S}_\mathrm{cal} = \sqrt{G_\mathrm{A} L}\,\mathbf{r} \otimes \mathbf{t} \tag{2.34}$$

The final scattering matrix of the calibration target then is

$$\mathbf{S}_\mathrm{cal} = e^{j\phi_\mathrm{abs}(\varphi_\mathrm{T},\varphi_\mathrm{R})} \sqrt{G} \begin{bmatrix} \sin\varphi_\mathrm{T}\sin\varphi_\mathrm{R} & \cos\varphi_\mathrm{T}\sin\varphi_\mathrm{R} \\ \sin\varphi_\mathrm{T}\cos\varphi_\mathrm{R} & \cos\varphi_\mathrm{T}\cos\varphi_\mathrm{R} \end{bmatrix} \tag{2.35}$$

6 While the rotational mounts of the antennas were designed to minimize the shifting of the phase center's position during rotation, at Ku-band wavelengths, even a positional shift on the order of $\sim$1 mm causes a noticeable phase shift.

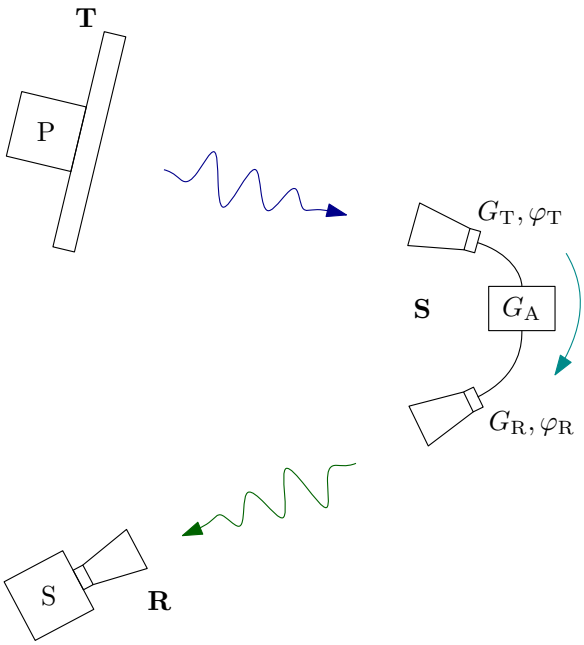

FIGURE 2.8: Schematic of the VSPARC calibration setup. The signal transmitted by the primary device is captured, amplified, and retransmitted by the calibration device toward the secondary. Polarization of the signal is affected by rotation angles $\varphi_\mathrm{T}, \varphi_\mathrm{R}$ of the calibrator's antennas.

where $G = G_\mathrm{T} L G_\mathrm{A} G_\mathrm{R}$, and $\phi_\mathrm{abs}(\varphi_\mathrm{T}, \varphi_\mathrm{R}) = \phi_\mathrm{abs,T}(\varphi_\mathrm{T}) + \phi_\mathrm{abs,R}(\varphi_\mathrm{R})$ is the absolute phase delay term, which depends on cable length and precise position of the antennas. The exact values of individual elements of the scattering matrix can thus be altered by changing the rotational position of the antennas.

2.2.9 *Polarimetric Calibration Method*

The calibration method is based on the linear distortion matrix model [38], which relates the observed scattering matrix $\mathbf{O}$ to the estimated true target scattering matrix $\mathbf{S}$:

$$\mathbf{O} = \mathbf{RST} \tag{2.36}$$

where $\mathbf{R}$ and $\mathbf{T}$ describe phase offsets, amplitude imbalances, and channel crosstalk for the reception and transmission devices, respectively.

KAPRI by design has very good polarization isolation, and thus, crosstalk is negligible [40]. The horn antennas of the bistatic receiver also provide sufficient polarization isolation, as is verified in Section 2.3.3. The distortion matrices then have the form [40]

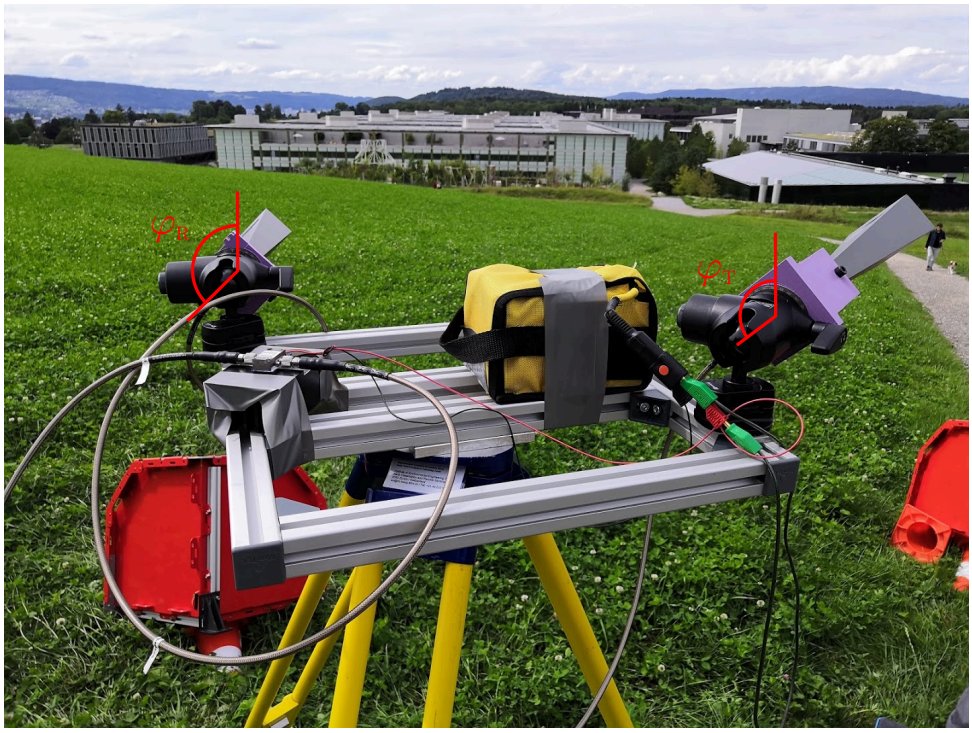

FIGURE 2.9: VSPARC prototype deployed in the field. Antennas are pointed at KAPRI devices and customized 3-D printed adapters enable rotation of antennas around their pointing axis without significantly affecting the position of the phase center. φ_T and φ_R quantify the rotation angle of the corresponding antenna around its pointing axis. A zero value of these angles signifies that the corresponding antenna is in the vertically polarized orientation.

$$\mathbf{R} = \sqrt{A}\begin{bmatrix} 1 & 0 \\ 0 & f/ge^{j\phi_r} \end{bmatrix} \tag{2.37a}$$

$$\mathbf{T} = \sqrt{A}\begin{bmatrix} 1 & 0 \\ 0 & fge^{j\phi_t} \end{bmatrix}. \tag{2.37b}$$

The four real parameters defined in [40] as f (one-way co-polarized amplitude imbalance relative to the H polarization), g (one-way cross-polarized amplitude imbalance), ϕ_t (phase offset between polarizations when transmitting) and ϕ_r (phase offset in reception) can be computed from the covariance matrix C

$$f = \left(\frac{C'_{\mathrm{VVVV}}}{C'_{\mathrm{HHHH}}} \right)^{\frac{1}{4}} \tag{2.38a}$$

$$\phi_r + \phi_t = \arg(C'_{\mathrm{VVHH}}) \tag{2.38b}$$

$$g = \left\langle \frac{C_{\mathrm{HVHV}}}{C_{\mathrm{VHVH}}} \right\rangle^{\frac{1}{4}} \tag{2.38c}$$

$$\phi_t - \phi_r = \arg\left(\langle C_{\mathrm{VVHV}} \rangle \right). \tag{2.38d}$$

where the first two equations are evaluated on the response of a corner reflector C' and the latter two on the whole scene C (due to the reciprocity principle). This method—henceforth referred to as the CR (corner reflector) method—was developed for monostatic KAPRI calibration in [40].

Since, in the generalized bistatic case, neither corner reflectors nor the reciprocity principle can be utilized, a different method has to be developed to compute these four parameters. As a calibration target, we thus use the active calibrator VSPARC described in Section 2.2.8. In order to determine the calibration parameters, we perform acquisitions in five configurations of the calibrator's antennas

$$\varphi_{\mathrm{T}} = 90°, \varphi_{\mathrm{R}} = 90° \implies \mathbf{S}_{\mathrm{cal}}^{\mathrm{HH}} = \sqrt{G} e^{j\phi_{\mathrm{HH}}} \begin{bmatrix} 1 & 0 \\ 0 & 0 \end{bmatrix} \tag{2.39a}$$

$$\varphi_{\mathrm{T}} = 90°, \varphi_{\mathrm{R}} = \ 0° \implies \mathbf{S}_{\mathrm{cal}}^{\mathrm{VH}} = \sqrt{G} e^{j\phi_{\mathrm{VH}}} \begin{bmatrix} 0 & 0 \\ 1 & 0 \end{bmatrix} \tag{2.39b}$$

$$\varphi_{\mathrm{T}} = \ 0°, \varphi_{\mathrm{R}} = 90° \implies \mathbf{S}_{\mathrm{cal}}^{\mathrm{HV}} = \sqrt{G} e^{j\phi_{\mathrm{HV}}} \begin{bmatrix} 0 & 1 \\ 0 & 0 \end{bmatrix} \tag{2.39c}$$

$$\varphi_{\mathrm{T}} = \ 0°, \varphi_{\mathrm{R}} = \ 0° \implies \mathbf{S}_{\mathrm{cal}}^{\mathrm{VV}} = \sqrt{G} e^{j\phi_{\mathrm{VV}}} \begin{bmatrix} 0 & 0 \\ 0 & 1 \end{bmatrix} \tag{2.39d}$$

$$\varphi_{\mathrm{T}} = 45°, \varphi_{\mathrm{R}} = 45° \implies \mathbf{S}_{\mathrm{cal}}^{\mathrm{XX}} = \frac{\sqrt{G}}{2} e^{j\phi_{\mathrm{XX}}} \begin{bmatrix} 1 & 1 \\ 1 & 1 \end{bmatrix} \tag{2.39e}$$

where G is the gain of the calibrator, $\phi_{\mathrm{HH}}, \phi_{\mathrm{VH}} \ldots \phi_{\mathrm{XX}}$ are the absolute phase terms for the corresponding configurations, and the upper index denotes the particular configuration of the antennas.[7]

From measurements of the calibration device's observed scattering matrix $\mathbf{K}$

$$\mathbf{K} = \mathbf{R}\mathbf{S}_{\mathrm{cal}}\mathbf{T} \tag{2.40}$$

the four calibration parameters can be computed as follows:

$$f = \sqrt{\left| \frac{K_{\mathrm{VV}}^{\mathrm{VV}}}{K_{\mathrm{HH}}^{\mathrm{HH}}} \right|} \tag{2.41a}$$

$$g = \sqrt{\left| \frac{K_{\mathrm{HV}}^{\mathrm{HV}}}{K_{\mathrm{VH}}^{\mathrm{VH}}} \right|} \tag{2.41b}$$

$$\phi_r = \arg\left(\frac{K_{\mathrm{VH}}^{\mathrm{XX}}}{K_{\mathrm{HH}}^{\mathrm{XX}}} \right) \tag{2.41c}$$

$$\phi_t = \arg\left(\frac{K_{\mathrm{HV}}^{\mathrm{XX}}}{K_{\mathrm{HH}}^{\mathrm{XX}}} \right) \tag{2.41d}$$

where the upper index denotes the particular configuration of the calibrator as defined in eq. (2.39) and the lower index denotes a particular element of the matrix $\mathbf{K}$ observed in that configuration.[8]

These coefficients can then be used to recover the true scattering matrix $\mathbf{S}$ for any target with observed scattering matrix $\mathbf{O}$

$$\mathbf{S} = \mathbf{R}^{-1}\mathbf{O}\mathbf{T}^{-1} \tag{2.42a}$$

$$= A \begin{bmatrix} O_{\mathrm{HH}} & \frac{e^{-j\phi_t}}{fg} O_{\mathrm{HV}} \\ \frac{g e^{-j\phi_r}}{f} O_{\mathrm{VH}} & \frac{e^{-j(\phi_r+\phi_t)}}{f^2} O_{\mathrm{VV}} \end{bmatrix}. \tag{2.42b}$$

7 For example, in eq. (2.39b), the upper index in notation $\mathbf{S}_{\mathrm{cal}}^{\mathrm{VH}}$ indicates that the calibrator's antenna pointed at the receiver was in the V-sensitive orientation ($\varphi_{\mathrm{R}} = 0°$), while the antenna pointed at the transmitter was in the H-sensitive orientation ($\varphi_{\mathrm{T}} = 90°$). The letter X in eq. (2.39e) denotes equal sensitivity of the antenna to both polarizations ($\varphi = 45°$).

8 For example $K_{\mathrm{VV}}^{\mathrm{HV}}$ indicates the value of the VV element of the calibrator's observed scattering matrix, while it was in a configuration with the T antenna in the V-polarized position and the R antenna in H-polarized position (see Fig. 2.8).

Quantifying the value of A is only necessary for radiometric measurements. It can be performed by observing a target with a bistatic radar cross section σ:

$$A = \frac{\sqrt{\sigma_{\mathrm{HH}}}}{r_{\mathrm{P}} r_{\mathrm{S}}} \frac{1}{|O_{\mathrm{HH}}|} \tag{2.43}$$

where the factor $1/(r_{\mathrm{P}} r_{\mathrm{S}})$ accounts for the power spreading loss. The target can be a well-known target such as a sphere or also the calibrator itself if its gain G is precisely known

$$A = \frac{\sqrt{G}}{r_{\mathrm{P}} r_{\mathrm{S}}} \frac{1}{\left|K_{\mathrm{HH}}^{\mathrm{HH}}\right|}. \tag{2.44}$$

For the purpose of radiometric calibration, this estimation of A should be carried out on SLC values on which range cell area compensation as described in section 2.2.6.2 has not been applied—since these targets can be approximated as point targets, their observed radar brightness is only affected by their range distance and not by the size of the range cell they are contained in.

2.2.10 *Processing Pipeline Summary*

The processing steps necessary in order to align the bistatic dataset acquired by the secondary device with the primary device's monostatic acquired dataset can be summarized as follows:

1. reference signal compensation as per Section 2.2.4;
2. frequency-dependent antenna squint compensation as described in [40];
3. bistatic range and intensity corrections as per Section 2.2.6;
4. azimuth phase ramp correction as described in [40].
5. antenna pattern compensation/cropping as per Section 2.2.7;
6. polarimetric calibration as per Section 2.2.9;
7. mosaicking of multiple acquisitions to achieve larger coverage;
8. geocoding and data analysis.

2.3 DATA & RESULTS

2.3.1 *Phase Drift and Start Time Offset*

Phase drift described in Section 2.2.3.5 can be measured by connecting the primary device's transmitter port with the secondary device's receiver port using a delay line—see Fig. 2.10.

This measurement can then be used to estimate the clock speed offset between the two devices. Via eq. (2.13), we can estimate the offset between the device's clock frequencies

$$\frac{\Delta\tau}{\tau} = -\frac{1}{2\pi f_c'}\frac{\mathrm{d}\phi_d}{\mathrm{d}T}. \tag{2.45}$$

For the measurement shown in Fig. 2.10, the average drift rate is estimated to be $\sim 2.5\,^\circ\,\mathrm{ms}^{-1}$ (ms = millisecond), which corresponds to clock frequency offset of

$$\frac{\Delta\tau}{\tau} = -\frac{2.5\,^\circ\,\mathrm{ms}^{-1}}{2\times\pi\times 17.1\,\mathrm{GHz}} \approx -4\times 10^{-10}. \tag{2.46}$$

The value of the start time offset Δt can also be estimated from the observed range position p_{ref} and the observed phase ϕ_{ref} of the reference signal peak, as shown in equations (2.6) and (2.11). From eq. (2.17)

$$\frac{p_{\mathrm{ref}}\gamma}{c} = \frac{b\gamma}{c} + \Delta f_c - \gamma'\Delta t \tag{2.47a}$$

$$\phi_{\mathrm{ref}} = 2\pi\left[\frac{b}{\lambda} - \frac{b^2\gamma}{2c^2} - f_c'\Delta t + \frac{\gamma'}{2}\Delta t^2\right]. \tag{2.47b}$$

Eq. (2.47a) is derived from the frequency of the oscillating term of eq. (2.17), while eq. (2.47b) is derived from its phase. From these two expressions we can obtain two independent estimates of the current value of $\Delta t(T)$

$$\Delta t_{\mathrm{range}}(T) = \frac{\gamma\left[b - p_{\mathrm{ref}}(T)\right]}{\gamma' c} + \frac{\Delta f_c}{\gamma'} \tag{2.48a}$$

$$\Delta t_{\mathrm{phase}}(T) = -\frac{\phi_{\mathrm{ref}}(T)/2\pi - b/\lambda + b^2\gamma/2c^2}{f_c'} \tag{2.48b}$$

where T represents the slow time, and the second-order phase drift term was neglected in eq. (2.48b). However, the value of $\frac{\Delta f_c}{\gamma'}$ in eq. (2.48a) cannot be isolated given the available

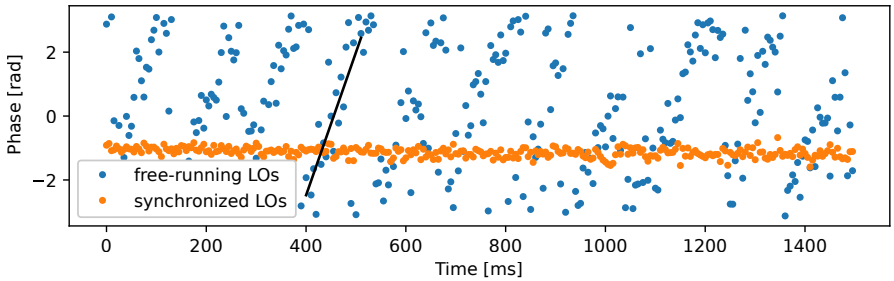

FIGURE 2.10: Measurement of phase drift between the two KAPRI devices. For the orange dataset, both devices were synchronized by a single 100-MHz signal using a cable. In this way, no phase drift between the two devices is observed. The blue dataset corresponds to nominal bistatic operation mode where each device is driven by its own LO, in which case significant phase drift is observed, with an average drift rate of $\sim 2.5°$ per millisecond (slope of black line). The signal was transmitted in both cases using a $-70\,\mathrm{dB}$ delay line.

data, and the estimate in eq. (2.48b) is phase-wrapped, and thus, its starting absolute value is unknown. For both of these estimates, it is simpler to evaluate $\Delta\hat{t}(T) = \Delta t(T) - \Delta t(0)$

$$\Delta\hat{t}_{\mathrm{range}}(T) = \gamma \frac{p_{\mathrm{ref}}(0) - p_{\mathrm{ref}}(T)}{\gamma' c} \tag{2.49a}$$

$$\Delta\hat{t}_{\mathrm{phase}}(T) = \frac{\phi_{\mathrm{ref}}(0) - \phi_{\mathrm{ref}}(T)}{2\pi f_{\mathrm{c}}'} \tag{2.49b}$$

the key being that the absolute offset term in (2.49a) was subtracted, and the phase information in (2.49b) can now be unwrapped since the phase history between 0 and T is known.[9]

Fig. 2.11 shows the geometric configuration for measurement of the reference signal peak range position and phase. Fig. 2.12 shows the deramped and range-compressed signal containing the reference signal in one of the two channels. Fig. 2.13 then shows the phase and range coordinate of the reference signal peak and shows the calculated values of $\Delta\hat{t}$ from the reference signal using eqs. (2.49a) and (2.49b).

2.3.2 *Calibrator's Scattering Matrix*

We performed a series of acquisitions of VSPARC's polarimetric signature while varying the R antenna's rotation angle φ_{R}, while the T antenna's rotation angle was set to a constant

9 Values γ' and f_{c}' can be substituted by their nominal counterparts since the change of their value has orders of magnitude lower effect than the change of value of $p_{\mathrm{ref}}(T)$ and $\phi_{\mathrm{ref}}(T)$, respectively.

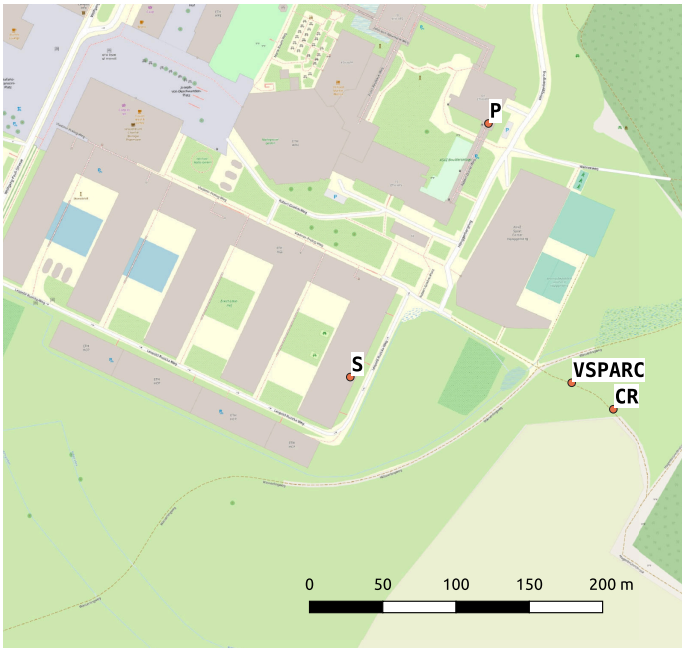

FIGURE 2.11: Synchronization link experimental setup. The bistatic reference signal is transmitted between the primary (P) and secondary (S) devices along a $\sim 200\,\mathrm{m}$ bistatic baseline. Map data © openstreetmap.org contributors.

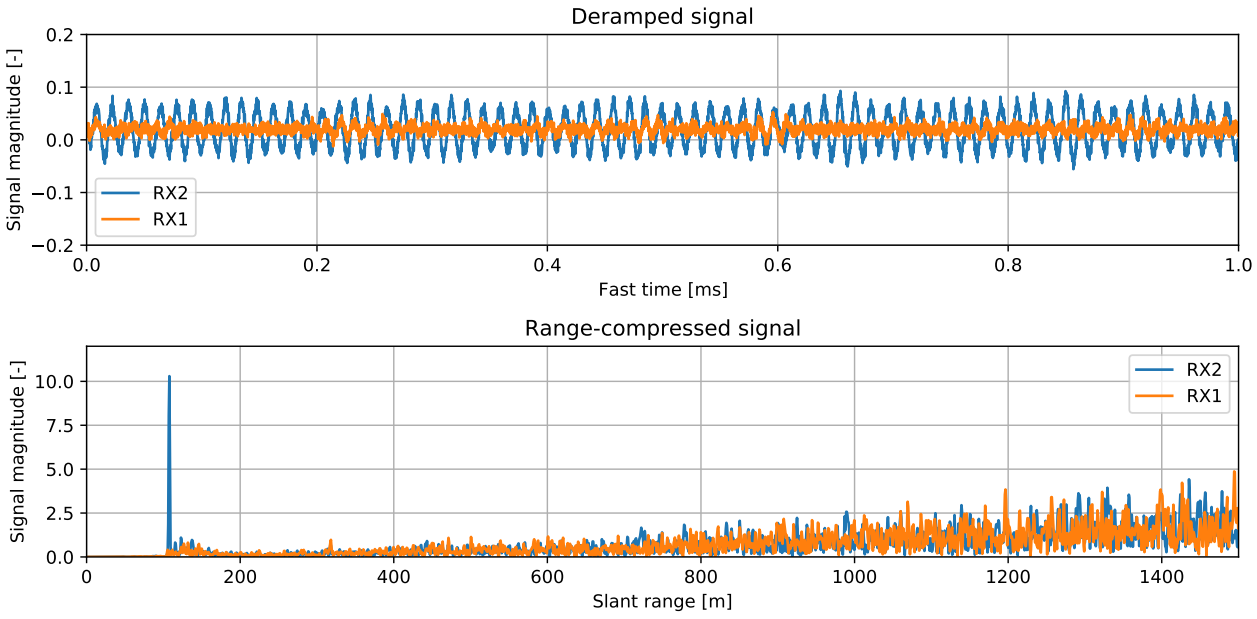

FIGURE 2.12: Deramped and range-compressed signal received by the secondary receiver in the HH polarimetric channel. In channel RX2, strong low-frequency modulation of the deramped signal is caused by the presence of the directly transmitted reference signal (see Figs. 2.2 and 2.11). The reference signal is visible in the range-compressed data as well as the significant peak at range of $\sim 100\,\mathrm{m}$. The range-compressed signal is scaled in range by a factor of $\sqrt{r^3}$.

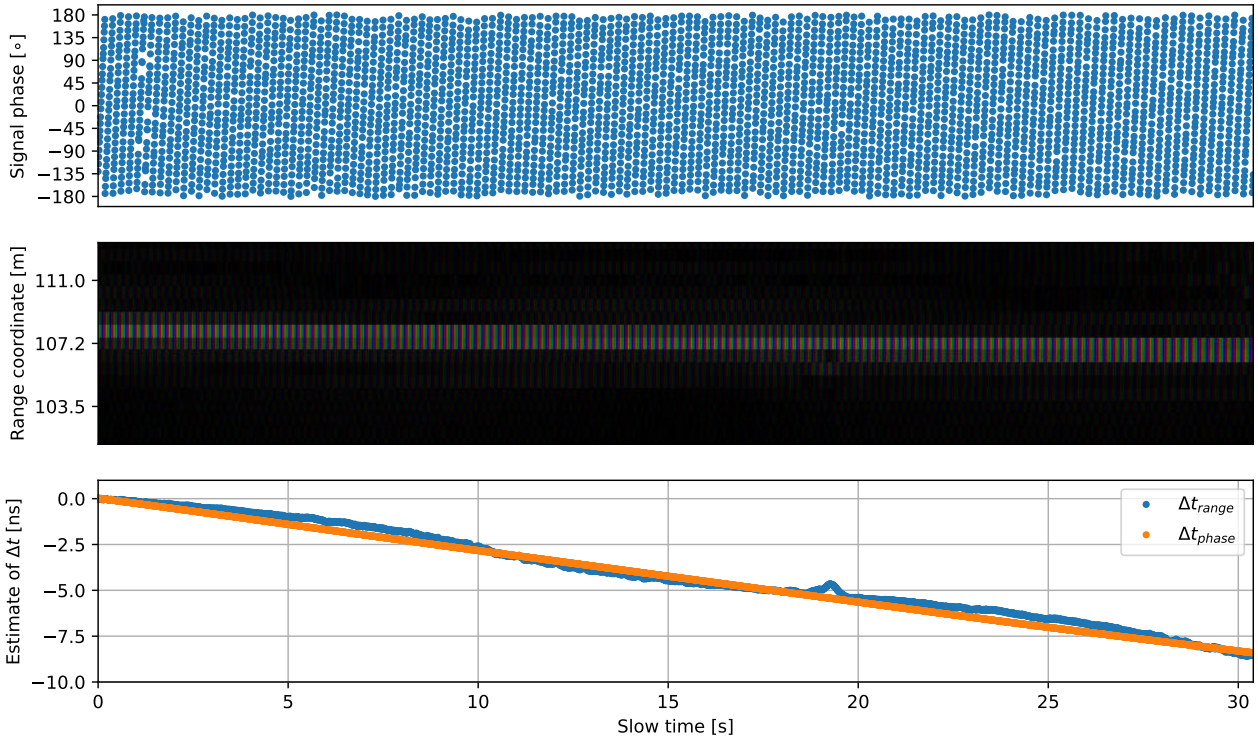

FIGURE 2.13: Estimation of $\Delta\hat{t}(T)$ via analysis of range position and phase of reference signal $s_{\text{d-ref}}$. Top: wrapped phase of reference signal peak–rapid phase drift of the reference signal is observed; however, sampling of phase in time is dense enough to allow error-free phase unwrapping. Middle: magnitude (brightness) and phase (color, i.e., hue) of the reference signal within the SLC dataset. A slow drift of the peak toward smaller range coordinate values can be observed. Bottom: estimates of $\Delta\hat{t}(T)$ via equations (2.49a) (blue) and (2.49b) (orange). Small deviation in the blue line in bottom graph at $T \approx 19\,\text{s}$ is caused by a multipath reflection from the scene interfering with the reference chirp. Small deviations of the two estimates are likely caused by imperfect subpixel peak position estimation. Over the course of the acquisition, $\Delta\hat{t}$ accumulates a value of almost $-10\,\text{ns}$.

value $\varphi_T = 45°$ (geometric configuration shown in Fig. 2.14). The scattering matrix of the calibrator then has the form

$$\mathbf{S}_{cal} = e^{j\phi_{abs}(\varphi_R)} \sqrt{\frac{G}{2}} \begin{bmatrix} \sin\varphi_R & \sin\varphi_R \\ \cos\varphi_R & \cos\varphi_R \end{bmatrix}. \tag{2.50}$$

The observed signal intensities in individual channels are thus expected to follow a $\cos^2$ trend, with a 90° offset between the HH-HV and VH-VV pairs. Furthermore, the observed signal phase in each channel should remain approximately constant (with the exception of a 180° phase flip caused by the changing sign of the respective trigonometric function for each channel) since the antenna mounting adapter was designed to minimize the variation of $\phi_{abs}(\varphi_R)$ over the course of the rotation. Fig. 2.15 shows the measured signal intensity and phase of each channel for a range of φ_R values with a total span of 120°.

FIGURE 2.14: Polarimetric calibration experimental setup. The primary (P) and secondary (S) devices are placed $\sim$ 1.5 m next to each other and thus are both operating with effectively zero bistatic angle. The calibration targets CR1, CR2, and VSPARC are all placed at range distance $\sim$ 400 m (however, at different range and azimuth coordinates). This allows the application of both CR and VSPARC calibration methods for both devices and their comparative validation. Map data © openstreetmap.org contributors.

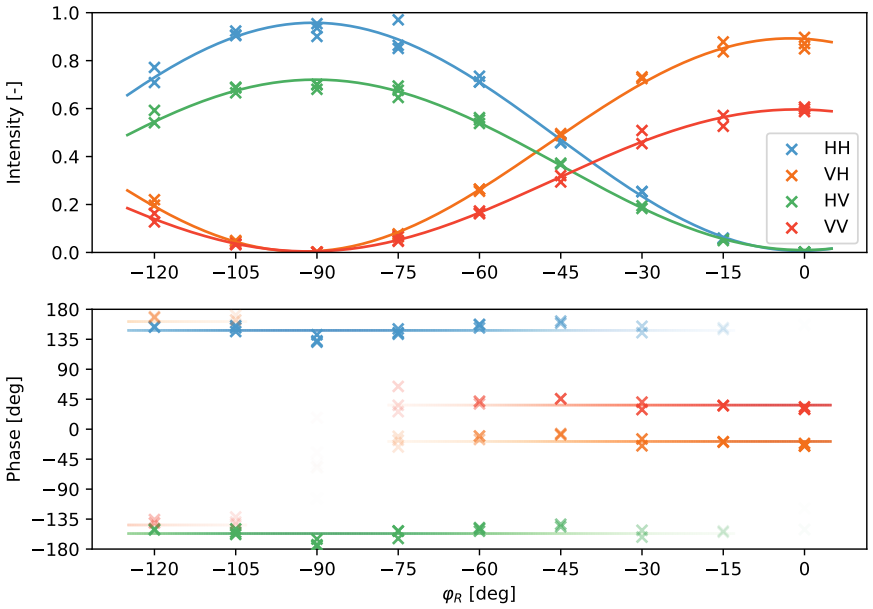

FIGURE 2.15: Measured signal intensity and phase of calibration device VSPARC based on the rotational position of the horn antenna pointed at the receiver φ_R. The color saturation of phase data points and constant fit lines is modulated by signal intensity. The signal intensity follows a $\cos^2$ trend, while the phase for each channel stays constant, just as predicted by eq. (2.50). A small but noticeable variation of phase around the constant line fits is observed. The predicted 180° phase flip can be observed in the VH and VV channels by comparing the phase values for antenna rotation angles $\varphi_R = -60°$ and $\varphi_R = -120°$. Variations in the amplitudes of the $\cos^2$ curves and variations of observed phase between individual channels are caused by the fact that the dataset is uncalibrated.

2.3.3 *Polarization Purity*

Table 2.3 shows the measured polarization purity of the bistatic receiver, obtained from the scattering response of a corner reflector (with the secondary bistatic receiver placed in the monostatic configuration, i.e., at the same position as the primary transmitter, see Fig. 2.14).

TABLE 2.3: Polarization purity p of individual channels and the standard deviation of the co-polar phase difference $\sigma_{\phi,\text{HH-VV}}$ of the primary and secondary devices, measured on ten acquisitions of two corner reflectors in the monostatic regime.

Primary device

	$p_{\text{HH-VH}}$ [dB]	$p_{\text{VV-HV}}$ [dB]	$\sigma_{\phi,\text{HH-VV}}$ [°]
CR1	42.8 ± 1.1	41.8 ± 0.7	1.2
CR2	33.0 ± 0.2	33.5 ± 0.2	2.3

Secondary device

	$p_{\text{HH-VH}}$ [dB]	$p_{\text{VV-HV}}$ [dB]	$\sigma_{\phi,\text{HH-VV}}$ [°]
CR1	29.0 ± 0.4	37.9 ± 0.4	1.1
CR2	25.3 ± 0.1	31.5 ± 0.3	8.1

2.3.4 *Polarimetric Calibration Validation*

The new calibration method presented in Section 2.2.9 (VSPARC method) should yield the same results as the original calibration method described in [40] (CR method). The calibration device VSPARC presented in Section 2.2.8 can be used for monostatic calibration by pointing both antennas in the same direction.

Table 2.4 shows the retrieved calibration coefficients for the primary and secondary device in a monostatic configuration (i.e., both devices placed next to each other, see Fig. 2.14) for two corner reflectors CR1 and CR2 employing the CR method (see eq. (2.38)) and the active calibration device employing the VSPARC method (see eq. (2.41)).

Table 2.5 compares the recovered phase offsets of the two methods in a specific configuration where $\phi_t - \phi_r < -180°$, which triggers a phase-wrapping effect that affects the retrieval of phase coefficients by the calibration method described by eq. (2.38).

TABLE 2.4: Retrieved calibration coefficients for each target and the corresponding method. Coefficients for corner reflectors CR1 and CR2 were computed according to eq. (2.38), and for calibration device VSPARC according to eq. (2.41). Displayed values are mean and standard deviation over three measurements.

Primary device

	f	g	$\phi_t[^\circ]$	$\phi_r[^\circ]$
CR1	0.95 ± 0.01	0.97 ± 0.01	-100.7 ± 0.6	12.9 ± 0.3
CR2	0.95 ± 0.01	0.98 ± 0.01	-90.3 ± 1.0	22.4 ± 0.7
VSPARC	0.92 ± 0.02	0.99 ± 0.01	-90.1 ± 0.8	11.9 ± 1.2

Secondary device

	f	g	$\phi_t[^\circ]$	$\phi_r[^\circ]$
CR1	0.96 ± 0.02	1.02 ± 0.01	-111.3 ± 0.5	25.8 ± 0.7
CR2	0.99 ± 0.07	1.03 ± 0.01	-98.9 ± 9.5	42.1 ± 9.4
VSPARC	0.99 ± 0.04	0.99 ± 0.01	-92.7 ± 2.3	34.3 ± 0.9

TABLE 2.5: Recovered calibration phase offsets for the secondary device in a specific situation where $\phi_t - \phi_r < -180°$, resulting in phase-wrapping. Coefficients for corner reflectors CR1 and CR2 were computed according to eq. (2.38) and for calibration device VSPARC according to eq. (2.41). The displayed values are mean and standard deviation over 3 measurements. A large discrepancy between recovered phase coefficients between the two methods is observed.

	$\phi_t[^\circ]$	$\phi_r[^\circ]$
CR1	65.7 ± 0.4	-81.1 ± 0.1
CR2	86.3 ± 9.2	-65.4 ± 9.8
VSPARC	-101.8 ± 0.6	90.2 ± 2.0

2.3.5 *Bistatic Processing Steps Visualization*

Fig. 2.16 shows the key processing steps outlined in Section 2.2.10.

2.4 DISCUSSION

2.4.1 *Geometric Limitations*

Due to KAPRI's synchronization link and the fact that it consists of two synchronized standalone devices, it is possible to perform acquisitions in a wide range of bistatic geometries, the main limiting factor being the local topography. The requirements for a successful acquisition are as follows.

1. There has to exist a direct line of sight between the two devices and between each of the devices and the observed scene—this is observed in Fig. 2.16, where a "blind spot" is apparent in the center of Fig. 2.16f compared to Fig. 2.16a.
2. Distances of the two devices to the observed scene should be within the same order of magnitude, in order to limit the magnitude of the range and intensity shift effects visualized in Fig. 2.6.
3. The bistatic angle β should not exceed 120°, in order to prevent leakage of the synchronization signal into the observed scene and excessive degradation of range resolution.

2.4.2 *Signal Model and Phase Retrieval*

As shown in Fig. 2.10, a clock drift between the two devices (which can accumulate to a value of several tens of nanoseconds) would have a considerable effect on the recovered signal phase in the bistatic configuration (which in the measurement shown exhibits a phase drift of approximately $2.5\,^\circ\,\mathrm{ms}^{-1}$, but is not constant between individual acquisitions), and thus must be corrected. The dual-chirp signal model introduced and described in Sections 2.2.2 through 2.2.4 is used to apply a correction via a transmitted reference chirp, and Fig. 2.13 shows that the model accurately establishes the relation between clock offset and reference signal phase and range offsets. It can be seen that indeed, the phase and range drift of the reference signal are connected and are dominantly caused by the accumulation of a chirp start time offset Δt. Furthermore, the measurement quantifies that over the course

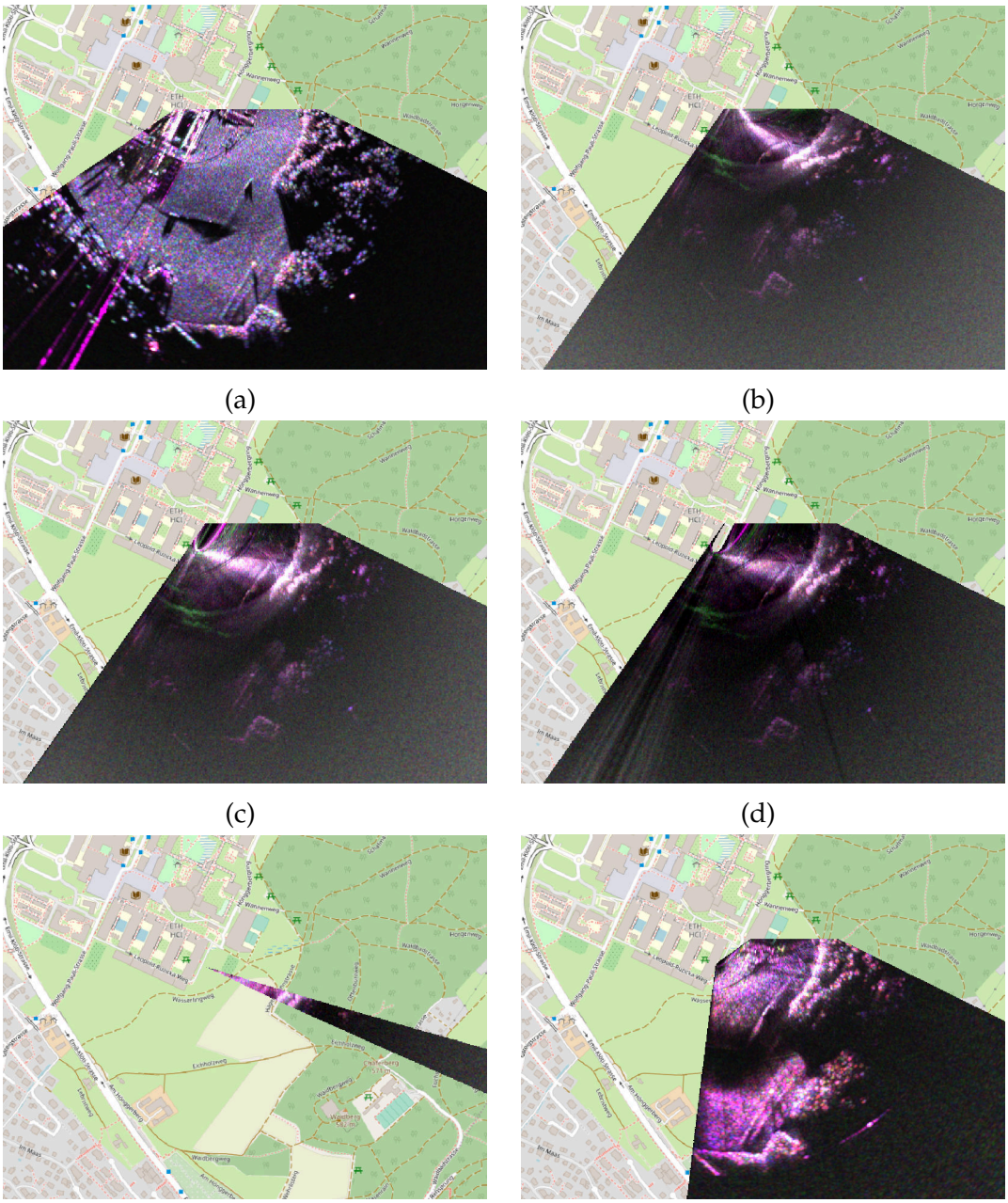

(a) (b) (c) (d) (e) (f)

FIGURE 2.16: Visualization of key processing steps in the bistatic processing pipeline. Data acquired on the ETH Hönggerberg campus. Polarimetric data is presented in the Pauli color basis (R: HH-VV, G: HV, B: HH+VV). Map data © openstreetmap.org contributors. (a) Monostatic image. The primary device was placed on top of a building and thus had very good line of sight over the observed area. (b) Bistatic image acquired by the secondary device and "naively" processed using the monostatic pipeline. Note the much lower coverage, incorrect placement and orientation of the treeline, as well as intensity gradients in both range and azimuth. (c) Range correction per eq. (2.30). Data are now correctly located, however, the intensity values are still too high in the vicinity of the receiver. (d) Intensity correction per eq. (2.31). Intensity gradient in range is now corrected, however, the azimuth gradient caused by the horn antenna pattern is still well visible. (e) Cropping of off-center data values. Only values that lie up to $\pm 4°$ from central azimuth direction are kept (up to $\pm 6°$, corresponding to $-3\,\mathrm{dB}$ beamwidth, is possible). Multiple acquisitions are necessary to cover a wider area. Polarimetric calibration is now applied. (f) Mosaicking of multiple bistatic acquisitions with varying horn receiver orientations in order to achieve larger coverage. Only areas with direct line of sight to both primary and secondary devices are imaged. This mosaicking method causes radial "stripes" emanating from the position of the secondary receiver to appear in the image, which is an artifact caused by the modulation of intensity by the receiver antenna pattern. This only affects radiometric information—relative intensities and phases between individual polarimetric channels are preserved.

of a typical acquisition ($10 - 60\,\mathrm{s}$), the start time offset Δt can reach a value of several tens of nanoseconds. The observed drift of the reference peak's range coordinate over the slow time also confirms that uncorrected accumulation of Δt would cause incorrect range determination for the reference signal, as well as the observed scene.

The corrected deramped signal $s_{\text{d-corr}}(t)$ can be expressed through equations (2.5a), (2.17a), and (2.19a) as:

$$s_{\text{d-corr}}(t) = s_{\text{d}}(t) s_{\text{d-ref}}(t)^* e^{j2\pi \frac{b\gamma}{c} t} \tag{2.51a}$$

$$= s_{\text{sr}}(t)^* s_{\text{st}}(t) s_{\text{sr-ref}}(t) s_{\text{st}}(t)^* e^{j2\pi \frac{b\gamma}{c} t} \tag{2.51b}$$

$$= s_{\text{sr}}(t)^* s_{\text{sr-ref}}(t) e^{j2\pi \frac{b\gamma}{c} t}. \tag{2.51c}$$

Notably, eq. (2.51c) shows that $s_{\text{d-corr}}(t)$ does not directly depend on the particular form of $s_{\text{sr-ref}}(t)$, and thus, the method could be used to correct chirps that have a form different from the specific one described by eq. (2.4). However, knowledge of the properties of $s_{\text{sr-ref}}(t)$ (especially its frequency spectrum) is still important—especially in the KAPRI configuration—since the bistatic reference signal $s_{\text{d-ref}}(t)$ is not captured in its own dedicated channel, but is instead superimposed on $s_{\text{d}}(t)$. Its recovery is then performed by windowing in the range-compressed domain as shown in eq. (2.20), which requires the frequency spectrum of $s_{\text{d-ref}}(t)$ to be disjoint from the spectrum of $s_{\text{d}}(t)$. The reference signal $s_{\text{d-ref}}$ is transmitted one way along the bistatic baseline, as opposed to the two-way path of the scene signal s_{d}. This means that the intensity of $s_{\text{d-ref}}$ is inversely proportional to the square of the length scale of the scene, as opposed to the inverse third power dependence of intensity of s_{d} (assuming scattering from a surface of distributed targets). Furthermore, in a typical acquisition geometry, the scene antenna beams are pointed away from the radar devices themselves (i.e., the radars do not point the antennas at each other) and thus signal from areas where $p \approx b$ is suppressed, which results in a negligible clutter contribution in the range cell of the reference signal. These two effects result in very good reference signal recovery from the superimposed signal. This is shown in Fig. 2.12 where the reference signal can be seen as a very clear modulation of the deramped signal in channel RX2, resulting in a sharp peak in the range-compressed signal at perceived range coordinate $\sim 100\,\mathrm{m}$ (i.e., half of the physical bistatic baseline).

Just like in monostatic configuration, phase retrieval accuracy is influenced by the scene SNR, which is reduced in the bistatic case due to the use of lower gain antennas, with an expected phase noise standard deviation increase by a factor of 4. Table 2.3 shows the

polarization purity and standard deviation of the co-polar phase difference of two corner reflectors CR1 and CR2. The lower values of polarization purity and higher phase noise of CR2 for the primary device suggest that there was a higher presence of clutter at CR2's position. For the secondary device, the effect of clutter is exacerbated by the lower gain (and higher beamwidth) of the receiver antennas and results in a $\sim 4\times$ increase of the phase standard deviation, in agreement with eq. (2.28). The equal values of phase noise for CR1 can be interpreted in a way that there was a very low amount of background clutter present in the scene near CR1, and thus, the SNR for both primary and secondary devices was sufficiently high so that the majority of the observed variation of phase is not caused by signal noise, but by other effects such as atmospheric variations, antenna vibrations, and other temporal phenomena that equally affect both the primary and secondary datasets.

2.4.3 *Polarimetric Calibration*

Table 2.3 shows that overall polarization purity of ~ 30 dB for the bistatic secondary receiver is lower than the ~ 40 dB value for the primary device [40]. This is caused by the use of horn antennas for the secondary receiver since these antennas have a smaller form factor and only a single mounting point, which makes them more sensitive to small mounting orientation variations. The bistatic configuration nevertheless still shows very good polarization isolation and is suitable for application of the polarimetric calibration method [38].

Table 2.4 compares the monostatic calibration method (CR), which uses corner reflectors and applies the reciprocity principle, to the novel calibration method by an active calibrator (VSPARC). Both methods provide comparable estimates of the calibration parameters f, g, ϕ_r, ϕ_t. Amplitude imbalance values close to 1 indicate that there is only a small variation in the real gain of the devices' antennas between individual channels. Coefficients reported in [40, Table V] across multiple corner reflectors exhibit similar variation as the results in Table 2.4, and within Table 2.4 for both the primary and the secondary device, the VSPARC results are well aligned with the CR1 and CR2 results. It is not expected that the values of parameters f and $\phi_r + \phi_t$ given in [40] and the primary device parameters of Table 2.4 should be numerically equal since the coefficients reported in [40] are residuals computed on already calibrated data. Furthermore, any component changes to the device configuration such as the addition of the directional coupler also affect the parameter values.

Since both the primary and the secondary device use the same pair of transmitting antennas, the estimate of phase offset at transmission ϕ_t should have equal value for both devices, which is confirmed in the data with all estimates close to the value of $-90°$. The

phase offset at reception ϕ_r is unrelated between the primary and the secondary device; however, for both devices, there is a good match between the estimate of the new and the old method. The data indicate that the accuracy of 20° can be achieved for the phase calibration in regular operation using the active calibration device.

The CR method [40] derives the phase offsets ϕ_r, ϕ_t from eqs. (2.38b) and (2.38d), where their sum and their difference are estimated from the phases of particular elements of corresponding covariance matrices. However, in case either the sum or the difference of the two parameters exceeds the phase-wrapping threshold of $\pm 180°$, one of the covariance matrix elements on the right-hand side of eqs. (2.38b) and (2.38d) will be phase-wrapped, and as a result, the estimates of parameters ϕ_r and ϕ_t will be shifted by 180°. Table 2.5 showcases this situation, where the VSPARC observations suggest that the difference $\phi_t - \phi_r$ is phase-wrapped and CR1 and CR2 observations are phase-shifted from the VSPARC observations by 180° (within the margin of error). While it is trivial to recover the true coefficients from the CR1 and CR2 estimates, the CR method provides no way to detect the situation when the phase-wrapping criterion is triggered and the 180° correction is necessary. The VSPARC method provides direct access to ϕ_r, ϕ_t from eqs. (2.41c) and (2.41d) respectively and thus is not affected by this phase-wrapping phenomenon.

Theoretically it would also be possible to derive the phase offsets ϕ_r, ϕ_t from measurements of the VSPARC device in the three configurations described by eqs. (2.39a), (2.39b) and (2.39c), thus eliminating the need for measurement in the XX configuration described by eq. (2.39e). However, the XX configuration has the benefit that both offsets are calculated from a single acquisition in one configuration. This eliminates any errors caused by atmospheric phase screen variations, temporal drift, or any mechanical phase offsets that would be introduced while adjusting the calibration device's configuration—these mechanical offsets can be observed as small deviations of the signal phase from the constant fit line in Fig. 2.15 and are an expression of the $e^{j\phi_{\text{abs}}(\varphi_\text{T},\varphi_\text{R})}$ term of eq. (2.35). Conversely, for the estimation of amplitude imbalances f and g, employment of only the XX configuration would be very sensitive to small deviations of the antenna rotation angles $\varphi_\text{T}, \varphi_\text{R}$ from the optimal 45° value, since (as eq. (2.35) predicts), at this value, even a small deviation causes a considerable change in signal amplitude (as can be seen in Fig. 2.15, where the intensity curves have the steepest slope at angle $\varphi_R = 45°$). By deriving the amplitude imbalance estimates f, g from measurements where the antenna rotation angles have value 0° or 90° (i.e., the stationary points of the intensity curves), this sensitivity to small variations of angles $\varphi_\text{T}, \varphi_\text{R}$ is mitigated.

As opposed to the CR method's employment of a passive corner reflector, the VSPARC method necessitates active operation of the device during calibration. The active calibrator design, however, enables polarimetric calibration in configurations with nonzero bistatic angle, which is necessary for bistatic KAPRI operation.

2.4.4 *Applications*

Full-polarimetric-interferometric capabilities of bistatic KAPRI, combined with its flexibility in temporal sampling rates and coverage periods, open up possibilities for investigations in several areas:

2.4.4.1 *Three-Dimensional Displacement Monitoring*

Bistatic interferometric capabilities of KAPRI allow reconstruction of 3-D displacement vector fields [3, 61], with high temporal sampling frequency for monitoring of phenomena that occur both on timescales faster than the ones that can be monitored using satellite-based SAR and longer timescales than those that can be reasonably monitored using airborne instruments. The reduced SNR and wider antenna pattern of the secondary device will result in a reduction of precision by an estimated factor of 4; however, given the excellent resolution and sensitivity of the monostatic GPRI and Ku-band wavelength, the bistatic add-on can still provide submillimeter sensitivity (0.25-mm path length measurement standard deviation at 10° phase noise standard deviation [48]), as well as providing opportunities for enhancement of atmospheric phase screen compensation models that affect terrestrial radar observations [47].

2.4.4.2 *Top-Layer Vegetation Monitoring*

Past research has demonstrated sensitivity of Ku-band radar to biophysical properties of top-layer vegetation [62]. Investigation of bistatic polarimetric radar signatures of vegetated land over the growth cycle is a possible pathway toward improvement of methods of surface and biophysical parameter retrieval [7–9, 63].

2.4.4.3 *Snow and Ice*

Certain scattering phenomena occurring in snow and ice layers are only detectable in the bistatic regime, such as the coherent backscatter opposition effect [64, 65]. As a portable

real-aperture fully polarimetric bistatic system, KAPRI is a suitable tool for investigation of this and similar phenomena.

2.5 CONCLUSION

In this article, we presented the calibration and the long-baseline bistatic acquisition configuration of KAPRI. By transmitting a synchronization signal directly between the two devices, we are able to compensate for oscillator drift effects without compromising the phase retrieval accuracy of the secondary device, due to the high SNR of the bistatic reference signal. The phase retrieval accuracy of the secondary receiver is then mainly affected by reduced SNR due to lower gain of the receiver antennas, which results in a $4\times$ increase in standard deviation of phase noise.

For polarimetric calibration, we developed a simple active transponder design VSPARC, which allows calibration of all polarimetric channels based on five measurements of its scattering matrix in specified configurations. This design is well-suited for field operations and can be used for bistatic as well as monostatic calibration, in which case the returned coefficients match the coefficients retrieved from the previously used monostatic method within 20° and 5% for phase and amplitude imbalances, respectively. We suggest that the VSPARC device and the associated calibration method can also be applied to calibrate other bistatic radar systems with good polarization isolation.

A fully calibrated KAPRI system can be used to investigate the suitability of bistatic Ku-band radar for probing of a variety of natural phenomena, such as 3-D land movements, vegetation growth, and structural changes in snow and ice.

REFERENCES

1. Lee, J.-S. & Pottier, E. *Polarimetric radar imaging: from basics to applications* (CRC press, 2009).
2. Everaere, E. *Polarimetry in bistatic configuration for ultra high frequency radar measurements on forest environment* PhD thesis (Ecole Polytechnique, 2015).
3. Moreira, A., Krieger, G., Hajnsek, I., Papathanassiou, K., Younis, M., Lopez-Dekker, P., Huber, S., Villano, M., Pardini, M., Eineder, M., De Zan, F. & Parizzi, A. Tandem-L: A Highly Innovative Bistatic SAR Mission for Global Observation of Dynamic

Processes on the Earth's Surface. *IEEE Geoscience and Remote Sensing Magazine* **3**, 8. doi:10.1109/MGRS.2015.2437353 (2015).

4. Pieraccini, M. & Miccinesi, L. *Bistatic GBSAR for detecting target elevation* in *2017 IEEE International Conference on Microwaves, Antennas, Communications and Electronic Systems (COMCAS)* (2017), 1. doi:10.1109/COMCAS.2017.8244728.

5. Dubois-Fernandez, P., Cantalloube, H., Vaizan, B., Krieger, G., Horn, R., Wendler, M. & Giroux, V. ONERA-DLR bistatic SAR campaign: Planning, data acquisition, and first analysis of bistatic scattering behavior of natural and urban targets. *Radar, Sonar and Navigation, IEE Proceedings* - **153**, 214. doi:10.1049/ip-rsn:20045117 (2006).

6. Al-Ashwal, W., Balleri, A., Griffiths, H., Miceli, W., Woodbridge, K., Harmanny, R., Ritchie, M., Stove, A., Watts, S., Baker, C., Inggs, M., Sandenbergh, J., Tough, R. & Ward, K. *Measurements of bistatic radar sea clutter* in *2011 IEEE RadarCon (RADAR)* (IEEE, 2011), 217. doi:10.1109/RADAR.2011.5960531.

7. Villard, L., Hajnsek, I., Borderies, P. & Papathanassiou, K. Pol-InSAR Simulations in Forest Bistatic Scattering. *7th European Conference on Synthetic Aperture Radar*, 3 (2008).

8. Khadhra, K. B., Boerner, T., Hounam, D. & Chandra, M. Surface Parameter Estimation Using Bistatic Polarimetric X-Band Measurements. *Progress In Electromagnetics Research B* **39**, 197. doi:10.2528/PIERB12020112 (2012).

9. Erten, E., Lopez-Sanchez, J. M., Yuzugullu, O. & Hajnsek, I. Retrieval of agricultural crop height from space: A comparison of SAR techniques. *Remote Sensing of Environment* **187**, 130. doi:10.1016/j.rse.2016.10.007 (2016).

10. Skolnik, M. I. An analysis of bistatic radar. *IRE Transactions on Aerospace and Navigational Electronics*, 19. doi:10.1109/TANE3.1961.4201772 (1961).

11. Griffiths, H. D. *From a Different Perspective : Principles, Practice and Potential of Bistatic Radar* in *2003 Proceedings of the International Conference on Radar (IEEE Cat. No. 03EX695)* (2003), 1. doi:10.1109/RADAR.2003.1278701.

12. Gierull, C. H. *Bistatic Synthetic Aperture Radar, TIF-Report (Phase I)* tech. rep. (Defence Research and Development Canada, Ottawa, Ontario, Canada, 2004).

13. Moccia, A., Salzillo, G., D'Errico, M., Rufino, G., Alberti, G., Salzillo, G. & Alberti, G. Performance of Spaceborne Bistatic Synthetic Aperture Radar. *IEEE Transactions on Aerospace and Electronic Systems* **41**, 1383. doi:10.1109/TAES.2005.1561891 (2005).

14. Moccia, A., Rufino, G., D'Errico, M., Alberti, G. & Salzillo, G. *BISSAT: A bistatic SAR for earth observation* in *International Geoscience and Remote Sensing Symposium (IGARSS)* **5** (IEEE, 2002), 2628. doi:10.1109/igarss.2002.1026723.

15. Massonnet, D. The interferometric cartwheel: A constellation of passive satellites to produce radar images to be coherently combined. *International Journal of Remote Sensing* **22**, 2413. doi:10.1080/01431160118952 (2001).

16. Zebker, H. A., Farr, T. G., Salazar, R. P. & Dixon, T. H. Mapping the World's Topography Using Radar Interferometry: The TOPSAT Mission. *Proceedings of the IEEE* **82**, 1774. doi:10.1109/5.338070 (1994).

17. Gebert, N., Carnicero Dominguez, B., Davidson, M. W. J., Diaz Martin, M. & Silvestrin, P. *SAOCOM-CS - A passive companion to SAOCOM for single-pass L-band SAR interferometry* in *EUSAR 2014; 10th European Conference on Synthetic Aperture Radar* (2014), 1.

18. Lopez-Dekker, P., Rott, H., Prats-Iraola, P., Chapron, B., Scipal, K. & Witte, E. D. *Harmony: an Earth Explorer 10 Mission Candidate to Observe Land, Ice, and Ocean Surface Dynamics* in *IGARSS 2019 - 2019 IEEE International Geoscience and Remote Sensing Symposium* (IEEE, 2019), 8381. doi:10.1109/IGARSS.2019.8897983.

19. Davidson, M., Chini, M., Dierking, W., Djavidnia, S., Haarpaintner, J., Hajduch, G., Laurin, G. V., Lavalle, M., López-Martinez, C., Nagler, T., Pierdicca, N. & Su, B. Copernicus L-band SAR Mission Requirements Document. *European Space Agency, ESA-EOPSM-CLIS-MRD-3371* (2019).

20. Farr, T. G., Rosen, P. A., Caro, E., Crippen, R., Duren, R., Hensley, S., Kobrick, M., Paller, M., Rodriguez, E., Roth, L., Seal, D., Shaffer, S., Shimada, J., Umland, J., Werner, M., Oskin, M., Burbank, D. & Alsdorf, D. The Shuttle Radar Topography Mission. *Reviews of Geophysics* **45**, RG2004. doi:10.1029/2005RG000183 (2007).

21. Krieger, G., Moreira, A., Fiedler, H., Hajnsek, I., Werner, M., Younis, M. & Zink, M. TanDEM-X: A satellite formation for high-resolution SAR interferometry. *IEEE Transactions on Geoscience and Remote Sensing* **45**, 3317. doi:10.1109/TGRS.2007.900693 (2007).

22. Meta, A., Trampuz, C., Coccia, A., Ortolani, M. & Turtolo, R. *First results of the BelSAR L band airborne bistatic fully polarimetric Synthetic aperture radar campaign* in *2017 IEEE International Geoscience and Remote Sensing Symposium (IGARSS)* (2017), 1040. doi:10.1109/IGARSS.2017.8127133.

23. De MacEdo, K. A., Placidi, S. & Meta, A. Bistatic and Monostatic InSAR Results with the MetaSensing Airborne SAR System. *2019 6th Asia-Pacific Conference on Synthetic Aperture Radar, APSAR 2019*. doi:10.1109/APSAR46974.2019.9048392 (2019).

24. Rodriguez-Cassola, M., Baumgartner, S., Krieger, G. & Moreira, A. Bistatic TerraSAR-X/F-SAR Spaceborne & Airborne SAR Experiment: Description, Data Processing, and Results. *IEEE Transactions on Geoscience and Remote Sensing* **48**, 781. doi:10.1109/TGRS.2009.2029984 (2010).

25. Walterscheid, I., Espeter, T., Brenner, A. R., Klare, J., Ender, J. H. G., Nies, H., Wang, R. & Loffeld, O. Bistatic SAR experiments with PAMIR and TerraSAR-X-setup, processing, and image results. *IEEE Transactions on Geoscience and Remote Sensing* **48**, 3268. doi:10.1109/TGRS.2010.2043952 (2010).

26. Lukin, K. A., Mogyla, A. A., Palamarchuk, V. P., Vyplavin, P. L., Zemlyaniy, O. V., Shiyan, Y. A. & Zaets, M. Ka-band bistatic ground-based noise waveform SAR for short-range applications. *IET Radar, Sonar & Navigation* **2**, 233. doi:10.1049/iet-rsn:20080017 (2008).

27. Pieraccini, M. & Miccinesi, L. *Bistatic ArcSAR* in *2018 2nd URSI Atlantic Radio Science Meeting (AT-RASC)* (2018), 1. doi:10.23919/URSI-AT-RASC.2018.8471632.

28. Wang, S., Feng, W., Kikuta, K., Chernyak, G. & Sato, M. *Ground-Based Bistatic Polarimetric Interferometric Synthetic Aperture Radar System* in *IGARSS 2019 - 2019 IEEE International Geoscience and Remote Sensing Symposium* (IEEE, 2019), 8558. doi:10.1109/IGARSS.2019.8900455.

29. Anghel, A., Cacoveanu, R., Moldovan, A. S., Rommen, B. & Datcu, M. COBIS: Opportunistic C-Band Bistatic SAR Differential Interferometry. *IEEE Journal of Selected Topics in Applied Earth Observations and Remote Sensing* **12**, 3980. doi:10.1109/JSTARS.2019.2939194 (2019).

30. Maslikowski, L., Samczynski, P., Baczyk, M., Krysik, P. & Kulpa, K. Passive bistatic SAR imaging - Challenges and limitations. *IEEE Aerospace and Electronic Systems Magazine* **29**, 23. doi:10.1109/MAES.2014.130141 (2014).

31. Reuter, S., Behner, F., Nies, H., Loffeld, O., Matthes, D. & Schiller, J. Development and experiments of a passive SAR receiver system in a bistatic spaceborne/stationary configuration. *International Geoscience and Remote Sensing Symposium (IGARSS)*, 118. doi:10.1109/IGARSS.2010.5653797 (2010).

32. Sanz-Marcos, J., Lopez-Dekker, P., Mallorqui, J. J., Aguasca, A. & Prats, P. SABRINA: A SAR bistatic receiver for interferometric applications. *IEEE Geoscience and Remote Sensing Letters* **4**, 307. doi:10.1109/LGRS.2007.894144 (2007).

33. López-Dekker, P., Mallorquí, J. J., Serra-Morales, P. & Sanz-Marcos, J. Phase synchronization and doppler centroid estimation in fixed receiver bistatic SAR systems. *IEEE Transactions on Geoscience and Remote Sensing* **46**, 3459. doi:10.1109/TGRS.2008.923322 (2008).

34. Duque, S., Lopéz-Dekker, P. & Mallorqui, J. J. Single-pass bistatic sar interferometry using fixed-receiver configurations: Theory and experimental validation. *IEEE Transactions on Geoscience and Remote Sensing* **48**, 2740. doi:10.1109/TGRS.2010.2041063 (2010).

35. Willis, N. J. *Bistatic Radar* (eds Willis & Griffiths) doi:10.1049/SBRA003E (Institution of Engineering and Technology, 2005).

36. Cherniakov, M. *Bistatic Radar* (ed Cherniakov, M.) 1. doi:10.1002/9780470985755 (John Wiley & Sons, Ltd, Chichester, UK, 2008).

37. Sarabandi, K. & Ulaby, F. T. A convenient technique for polarimetric calibration of single-antenna radar systems. *IEEE Transactions on Geoscience and Remote Sensing* **28**, 1022. doi:10.1109/36.62627 (1990).

38. Sarabandi, K., Ulaby, F. T. & Tassoudji, M. A. Calibration of Polarimetric Radar Systems With Good Polarization Isolation. *IEEE Transactions on Geoscience and Remote Sensing* **28**, 70. doi:10.1109/36.45747 (1990).

39. Fujita, M., Masuda, T., Fujino, Y. & Satake, M. Polarimetric calibration of the SIR-C C-band channel using active radar calibrators and polarization selective dihedrals. *IEEE transactions on geoscience and remote sensing* **36**, 1872. doi:10.1109/36.729358 (1998).

40. Baffelli, S., Frey, O., Werner, C. & Hajnsek, I. Polarimetric Calibration of the Ku-Band Advanced Polarimetric Radar Interferometer. *IEEE Transactions on Geoscience and Remote Sensing* **56**, 2295. doi:10.1109/TGRS.2017.2778049 (4 2018).

41. Beaudoin, C., Horgan, T., Demartinis, G., Coulombe, M. J., Gatesman, A. J. & Nixon, W. E. Fully polarimetric bistatic radar calibration with modified dihedral objects. *IEEE Transactions on Antennas and Propagation* **66**, 937. doi:10.1109/TAP.2017.2783191 (2017).

42. Kahny, D., Schmitt, K. & Wiesbeck, W. Calibration of bistatic polarimetric radar systems. *IEEE transactions on geoscience and remote sensing* **30**, 847. doi:10.1109/36.175318 (1992).

43. Monzon, C. A cross-polarized bistatic calibration device for RCS measurements. *IEEE Transactions on Antennas and Propagation* **51**, 833. doi:10.1109/TAP.2003.811071 (2003).

44. Brunfeldt, D. R. & Ulaby, F. T. Active reflector for radar calibration. *IEEE Transactions on Geoscience and Remote Sensing*, 165. doi:10.1109/TGRS.1984.350610 (1984).

45. Pienaar, M., Odendaal, J. W., Joubert, J., Cilliers, J. E. & Smit, J. C. Active calibration target for bistatic radar cross-section measurements. *Radio Science* **51**, 515. doi:10.1002/2015RS005931 (2016).

46. Baffelli, S., Frey, O. & Hajnsek, I. Polarimetric Analysis of Natural Terrain Observed With a Ku -Band Terrestrial Radar. *IEEE Journal of Selected Topics in Applied Earth Observations and Remote Sensing* **12**, 5268. doi:10.1109/JSTARS.2019.2953206 (2019).

47. Baffelli, S., Frey, O. & Hajnsek, I. Geostatistical Analysis and Mitigation of the Atmospheric Phase Screens in Ku-Band Terrestrial Radar Interferometric Observations of an Alpine Glacier. *IEEE Transactions on Geoscience and Remote Sensing* **58**, 7533. doi:10.1109/TGRS.2020.2976656 (2020).

48. Werner, C., Wiesmann, A., Strozzi, T., Kos, A., Caduff, R. & Wegmiüler, U. *The GPRI multi-mode differential interferometric radar for ground-based observations* in *EUSAR 2012; 9th European Conference on Synthetic Aperture Radar* (2012), 304.

49. Strozzi, T., Werner, C., Wiesmann, A. & Wegmuller, U. Topography mapping with a portable real-aperture radar interferometer. *IEEE Geoscience and Remote Sensing Letters* **9**, 277. doi:10.1109/LGRS.2011.2166751 (2011).

50. Caduff, R., Kos, A., Schlunegger, F., McArdell, B. W. & Wiesmann, A. Terrestrial radar interferometric measurement of hillslope deformation and atmospheric disturbances in the Illgraben debris-flow catchment, Switzerland. *IEEE Geoscience and Remote Sensing Letters* **11**, 434. doi:10.1109/LGRS.2013.2264564 (2014).

51. Wiesmann, A., Caduff, R. & Mätzler, C. Terrestrial radar observations of dynamic changes in alpine snow. *IEEE Journal of Selected Topics in Applied Earth Observations and Remote Sensing* **8**, 3665. doi:10.1109/JSTARS.2015.2400972 (2015).

52. Rodriguez-Cassola, M., Prats, P., Schulze, D., Tous-Ramon, N., Steinbrecher, U., Marotti, L., Nannini, M., Younis, M., López-Dekker, P., Zink, M., Reigber, A., Krieger, G. & Moreira, A. First bistatic spaceborne SAR experiments with TanDEM-X. *IEEE Geoscience and Remote Sensing Letters* **9**, 33. doi:10.1109/LGRS.2011.2158984 (2012).

53. Stove, A. G. *Linear FMCW radar techniques* in *IEE Proceedings F (Radar and Signal Processing)* **139** (1992), 343. doi:10.1049/ip-f-2.1992.0048.

54. Rodriguez, E. & Martin, J. M. Theory and design of interferometric synthetic aperture radars. *IEE Proceedings, Part F: Radar and Signal Processing* **139**, 147. doi:10.1049/ip-f-2.1992.0018 (1992).

55. Just, D. & Bamler, R. Phase statistics of interferograms with applications to synthetic aperture radar. *Applied Optics* **33**, 4361. doi:10.1364/AO.33.004361 (1994).

56. Kay, S. M. *Fundamentals of statistical signal processing: Estimation theory* (Prentice Hall PTR, 1993).

57. NAWCWD Avionics Department. Electronic Warfare and Radar Systems Engineering Handbook. *Published in association with MTTS & IEEE*, 455 (1997).

58. Budge, M. C. & German, S. R. *Basic radar analysis* (Artech house, 2015).

59. Weiner, M. M. & Kaplan, P. D. *Bistatic surface clutter resolution area at small grazing angles* tech. rep. (MITRE CORP BEDFORD MA, 1982).

60. Bradley, C. J., Collins, P. J., Fortuny-Guasch, J., Hastriter, M. L., Nesti, G., Terzuoli, A. J. & Wilson, K. S. An investigation of bistatic calibration techniques. *IEEE Transactions on Geoscience and Remote Sensing* **43**, 2185. doi:10.1109/TGRS.2005.855130 (2005).

61. Krieger, G., Hajnsek, I., Papathanassiou, K. P., Younis, M. & Moreira, A. Interferometric Synthetic Aperture Radar (SAR) Missions Employing Formation Flying. *Proceedings of the IEEE* **98**, 816. doi:10.1109/JPROC.2009.2038948 (2010).

62. Inoue, Y., Kurosu, T., Maeno, H., Uratsuka, S., Kozu, T., Dabrowska-Zielinska, K. & Qi, J. Season-long daily measurements of multifrequency (Ka, Ku, X, C, and L) and full-polarization backscatter signatures over paddy rice field and their relationship with biological variables. *Remote Sensing of Environment* **81**, 194. doi:10.1016/S0034-4257(01)00343-1 (2002).

63. Erten, E., Rossi, C. & Yüzügüllü, O. Polarization impact in TanDEM-X data over vertical-oriented vegetation: The paddy-rice case study. *IEEE Geoscience and Remote Sensing Letters* **12**, 1501. doi:10.1109/LGRS.2015.2410339 (2015).

64. Akkermans, E., Wolf, P. E. & Maynard, R. Coherent backscattering of light by disordered media: Analysis of the peak line shape. *Physical review letters* **56**, 1471. doi:10.1103/PhysRevLett.56.1471 (1986).

65. Tan, S., Chang, W., Tsang, L., Lemmetyinen, J. & Proksch, M. Modeling Both Active and Passive Microwave Remote Sensing of Snow Using Dense Media Radiative Transfer (DMRT) Theory with Multiple Scattering and Backscattering Enhancement. *IEEE Journal of Selected Topics in Applied Earth Observations and Remote Sensing* **8**, 4418. doi:10.1109/JSTARS.2015.2469290 (2015).

3

POLARIMETRIC ANALYSIS OF MULTI-SEASONAL MONOSTATIC AND BISTATIC RADAR OBSERVATIONS OF A GLACIER ACCUMULATION ZONE AT KU-BAND

Marcel Stefko[1], Philipp Bernhard[1], Othmar Frey[1,2], and Irena Hajnsek[1,3]

[1] Chair of Earth Observation and Remote Sensing, ETH Zurich, Switzerland

[2] GAMMA Remote Sensing AG, Switzerland

[3] Microwaves and Radar Institute, German Aerospace Center DLR, Germany

Article submitted for publication in

IEEE Journal of Selected Topics in Applied Earth Observations and Remote Sensing

Key findings/developments:

- The decorrelation time of snow cover on top of the Jungfraufirn area at Ku-band was characterized.
- The inter-seasonal and intra-day behaviour of monostatic and bistatic polarimetric parameters of the snow cover (entropy, mean alpha angle, polarization phase differences) were characterized.
- Non-reciprocal scattering was confirmed to occur in the bistatic regime through measurement of the cross-polarized phase difference.

The author's contributions:

- coordinated the campaigns at High Altitude Research Station Jungfraujoch,
- operated the radar systems during acquisitions,
- processed and analyzed the acquired radar data,
- wrote the manuscript.

The co-authors' contributions:

- Philipp Bernhard contributed to campaign preparation, participated in data collection campaigns, collected the in-situ data, and provided feedback on the manuscript.
- Othmar Frey contributed to campaign preparation, data evaluation, and provided feedback on the manuscript.
- Irena Hajnsek contributed to study design, campaign preparation, data evaluation, and provided feedback on the manuscript.

This chapter is a pre-print of the above-listed manuscript, differing from the submitted version only in terms of layout, formatting, and citation style.

Terrestrial radar is a flexible tool well-suited for exploration of natural environments. Terrestrial acquisitions can be particularly useful for investigation of radar scattering behaviour of natural media on short time scales, at less commonly used frequency bands, or when less commonly used techniques (such as bistatic radar) are applied. The outcomes of such explorations can drive the design of Earth Observation missions applied on larger scales, such as airborne or spaceborne missions, as well as provide insights for modeling research.

We present ground-based Ku-band radar observations of the snow cover on top of the Great Aletsch Glacier carried out over two observation periods, in August 2021 and in March 2022. The observations – carried out with the combined mono/bistatic version of KAPRI, a full-polarimetric radar system – revealed substantial differences between the scattering behaviour of the snow cover between the two seasons. We first present the experimental setup of the two devices, including a digital-elevation-model-assisted range correction algorithm capable of range correction of fan-beam real-aperture radar data in an arbitrary bistatic acquisition geometry. Afterwards we analyze the spatial and temporal behaviour of polarimetric and interferometric parameters including temporal decorrelation, the scattering entropy, the mean polarimetric alpha angle, and the co- and cross-polarized phase differences.

The results indicate that snow cover decorrelates at Ku-band on the timescales of $4 - 12$ *hours in winter and summer, which has implications for repeat-pass methods with long temporal baselines. The analysis of the co-polarized phase difference in winter indicates that the parameter is prone to phase wrapping, which may complicate inversion procedures aiming to extract snow parameters from CPD observations at Ku-band. In summer, its value exhibits smooth spatial trend and a strong sensitivity to changes in incidence angle and liquid water content. The bistatic cross-polarized phase difference also acquires a non-zero value, indicating the presence of non-reciprocal scattering, which has implications for possible calibration procedures of bistatic systems. These results also aim to serve as a reference for snow scattering behaviour at Ku-band, which can aid planning of future data acquisition campaigns and satellite missions.*

3.1 INTRODUCTION

3.1.1 *Snow and ice investigations at Ku-band*

The Ku-band frequency range of the electromagnetic spectrum (between 12 GHz and 18 GHz) is attractive for radar investigations of snow and ice [1–4]. This is due to the relatively short but non-zero penetration depth into dry snow, which allows a large fraction of the incident radio waves to interact with the snow volume, thus providing opportunities for probing of the physical properties of the snow layer, especially when the layer thickness is insufficient for use of lower frequency bands such as the X-band [5, 6]. The snow parameters of interest include, among others, the snow water equivalent (SWE) [2, 7, 8], grain size and autocorrelation length [9, 10], snow anisotropy [11, 12], or firn depth [13]. Several spaceborne synthetic aperture radar (SAR) missions using Ku-band for snow and ice research were

proposed in the past decade (CoReH2O [14], SCLP [15, Part II]) and also are under current investigation (TSMM [16]).

3.1.2 *Bistatic radar investigations of snow*

Bistatic radar (i.e., a radar measurement configuration where the transmitter (Tx) and the receiver (Rx) are spatially separated) is a technology which can potentially provide a complementary method of access to snow parameters to the widely used methods based on monostatic radar data (where the spatial separation of the transmitter and the receiver is negligible). It provides an opportunity to expand the observation parameter space, through variation of the bistatic angle β, which is defined as the spatial angle between the transmitter and the receiver from the point of view of the scatterer. Observations under varying values of β provide access, e.g., to a larger number of polarimetric parameters [17, 18]. This bistatic parameter space remains relatively unexplored, mainly due to bistatic radar's higher operational complexity as opposed to monostatic radar. The only bistatic spaceborne mission currently operating is TanDEM-X [19], whose bistatic capabilities were used to characterize snow both through investigations of the bistatic signal phase [20, 21], as well as bistatic intensity variations [22]. However, the nominal operational mode of TanDEM-X involves the use of very small bistatic angles (less than 1°). There are currently no bistatic spaceborne missions with larger bistatic angles. Ongoing interest in further development of bistatic radar missions is reflected in current proposals of spaceborne radar missions such as Harmony [23],as well as past proposals [24–27].

Modeling research of snow and ice has so far focused primarily on integrating passive and monostatic active radar observations [9–13, 28–31]. However, it should be noted that many radar devices (even those conventionally considered monostatic, such as SnowScat [32]) have a non-zero spatial separation between the transmitting and receiving antenna. In certain cases (especially at short ranges), this separation can result in a bistatic angle value which can non-negligibly affect the observed backscatter, especially in volumetric scattering media such as snow [22, Section 4.3].

3.1.3 *Scattering characteristics of snow*

Scattering characteristics of snow are strongly dependent on the properties of the incident radiation (frequency, polarization), physical parameters of the snow medium (grain size, water content, layer parameters), as well as observation geometry (incidence, scattering

angle). Extensive review literature is available on the topic, e.g., [4, 33–36]. In the following paragraphs we shortly summarize the most relevant properties of snow with regard to our radar measurements.

Liquid water content has a strong effect on dielectric properties of snow, and thus strongly affects backscatter intensity, which becomes much weaker as water content increases. Furthermore, the penetration depth becomes much shorter with increasing water content due to absorption. This causes the majority of backscatter from wet snow to come from the uppermost layer of the medium with penetration depth on the order of only a few centimeters [37, Section 4.6],[38], and thus limits the possibilities of probing the deeper layers. Conversely, dry snow allows strong penetration of several meters [37, Figure 4.15], and is a strongly scattering and weakly absorbing medium.

Seasonal snow often exhibits an anisotropic orientation of ice crystals and anisotropy of the large-scale structure, which can impose a polarization-dependent phase delay on the scattering waves. The co-polar phase difference (CPD) defined as

$$\phi_{\mathrm{HH-VV}} = \phi_{\mathrm{HH}} - \phi_{\mathrm{VV}} = \arg(S_{\mathrm{HH}} S_{\mathrm{VV}}^{*}) \tag{3.1}$$

quantifies the difference between the phase of the horizontally-polarized transmitted and received waves ϕ_{HH} and the vertically-polarized equivalents ϕ_{VV}. The CPD is often used to characterize this polarization-dependent delay, and is strongly affected by changes in snow metamorphism and depth [11, 13]. Observations at L- to Ku-band have been used to infer structural properties of the snow cover from CPD measurements [11, 13]. The short wavelength of the Ku-band makes the CPD very sensitive to small variations of these properties, however it also makes it potentially prone to phase-wrapping already at layer depths of several tens of centimeters, especially at high incidence angles.

The cross-polarized phase difference (XPD)

$$\phi_{\mathrm{HV-VH}} = \phi_{\mathrm{HV}} - \phi_{\mathrm{VH}} = \arg(S_{\mathrm{HV}} S_{\mathrm{VH}}^{*}), \tag{3.2}$$

quantifies the phase difference between the two cross-polarized channels, HV and VH. In literature it is sometimes also labeled as cross-cross polarized phase difference. In the monostatic case, the reciprocity principle dictates that $S_{\mathrm{HV}} = S_{\mathrm{VH}}$, and thus the XPD is zero by definition. This fact is often used for calibration of cross-polarized channels. However in the bistatic case, the XPD does not necessarily need to be zero. Due to a low availability of bistatic full-polarimetric systems and datasets, the XPD has not been as thoroughly explored and modeled as it's co-polarized counterpart. *Note:* Some publications may use the name

"cross-polarized phase difference" for a different parameter, such as $\phi_{\mathrm{HV}} - \phi_{\mathrm{HH}}$ or similar. In this publication we use exclusively the definition in eq. (3.2).

The two main scattering processes occurring in snow are surface scattering (from the air-snow boundary, snow-ground boundary, or internal layers such as melt-freeze crusts), and volume scattering occurring throughout the snow volume [35]. Dihedral scattering can also occur from one or several of these boundaries. These processes have different polarimetric signatures – the 4-dimensional Pauli scattering vector [17, Sections 3.2, 6.5]

$$\mathbf{k}_{\mathrm{P}} = \frac{1}{\sqrt{2}} \begin{bmatrix} S_{\mathrm{HH}} + S_{\mathrm{VV}} \\ S_{\mathrm{HH}} - S_{\mathrm{VV}} \\ S_{\mathrm{HV}} + S_{\mathrm{VH}} \\ j(S_{\mathrm{HV}} - S_{\mathrm{VH}}) \end{bmatrix}, \tag{3.3}$$

where S is the Sinclair scattering matrix and j is the imaginary unit, is often used to distinguish between these processes. Surface scattering exhibits a large magnitude of the first component $S_{\mathrm{HH}} + S_{\mathrm{VV}}$, while volume scattering exhibits a comparatively strong third component $S_{\mathrm{HV}} + S_{\mathrm{VH}}$. Dihedral scattering can manifest itself in the second ($S_{\mathrm{HH}} - S_{\mathrm{VV}}$) or third component, depending on the orientation of the scattering surfaces. The fourth component $j(S_{\mathrm{HV}} - S_{\mathrm{VH}})$ is always equal to zero in the monostatic case, however in a bistatic measurement configuration it can have a non-zero value. A graphical visualization of the Pauli scattering vector component magnitudes is often used for a qualitative analysis of scattering processes occurring within the snow medium. A quantitative analysis is often performed through second-order polarimetric parameters, such as the scattering entropy H and polarimetric alpha angle α [17, Chapter 7], [39, Section 2.3], [40, Chapter 4].

Snow is a medium that undergoes significant micro-structural changes over time, with varying rates of change depending on snow type, snow cover age, and ambient conditions. These changes significantly affect the scattering behaviour, and can have a strong effect especially on the interferometric coherence γ and its temporal behaviour, which are important for all radar interferometry-based observation methods. The complex interferometric coherence $\tilde{\gamma}$ is computed from two single-look complex (SLC) radar images s_1, s_2 as follows:

$$\tilde{\gamma} = \frac{\sum_{\mathrm{W}} s_1 s_2^*}{\sqrt{\sum_{\mathrm{W}} s_1^2} \sqrt{\sum_{\mathrm{W}} s_2^2}}, \tag{3.4}$$

where W is a boxcar moving window. Its final absolute value γ is constrained between 0 (no coherence) and 1 (full coherence). It is affected by several contributing factors, and can be expressed as [19]

$$\gamma = \gamma_{\text{SNR}}\gamma_{\text{Quant}}\gamma_{\text{Amb}}\gamma_{\text{Rg}}\gamma_{\text{Az}}\gamma_{\text{Vol}}\gamma_{\text{Temp}}. \tag{3.5}$$

These terms respectively describe the reductions in coherence due to SNR, quantization, ambiguities, baseline decorrelation, relative shift of the Doppler spectra, volume decorrelation, and temporal decorrelation. The relevance of each individual term varies based on sensor type, observation geometry, and the observed medium. The final term, γ_{Temp} is the temporal decorrelation between the two acquisitions, which in snow can occur due to, e.g., change of liquid water content (i.e., snowmelt or refreezing), or redistribution of the snow particles due to wind or displacement [41]. At Ku-band, scatterer displacement on the scale of 2-3 mm can already cause significant decorrelation [42, eq. (23)]. Furthermore, temporal decorrelation can also be caused by glacier motion – even if the snow cover on top of the glacier remains stable, the motion of the glacier will over time cause the scatterers to move out of their original range cell, which will also cause the scene to decorrelate. This effect is strongly dependent on the observation parameters, namely the range and azimuth sampling resolutions, and the orientation and rate of glacier flow with respect to the sensor. In general, the value of γ_{Temp} non-linearly reduces with increasing time between acquisitions. Its temporal behaviour can provide an upper bound on the realistic length of acquisition windows for repeat-pass methods such as differential interferometry or SAR tomography, since after a certain time period, the two acquisitions will no longer be sufficiently coherent. Knowledge of the decorrelation time is thus vital, amongst other use cases, for planning and evaluation of viability of airborne and spaceborne data acquisition campaigns. This is especially true at Ku-band, since temporal decorrelation is generally faster at shorter wavelengths [41].

3.1.4 *Terrestrial radar instruments for snow investigations*

While this section focuses on ground-based instruments, airborne radar sensors (e.g., [31, 43–48]) are a powerful tool for snow monitoring. As opposed to terrestrial sensors, they usually provide superior spatial coverage, and can be easier to deploy in hard-to-access environments. However, they are usually more costly to operate, and offer only limited capabilities for long-term measurements with fine temporal resolution (i.e., maintaining regular sampling intervals over observation windows on the scales of days to months is difficult).

Comprehensive datasets using different radar imaging modalities in the cryospheric environment with very quick revisit times and virtually unlimited time-series durations

can be acquired with terrestrial radar sensors. The following is a (non-exhaustive) list of terrestrial radar sensors employed for cryospheric investigations in the past decade:

- The dual-frequency X-/Ku-band UW-Scat instrument analyzed seasonal backscatter trends of snow cover in relation to snow properties [5, 49].
- As part of Phase A studies for the CoReH2O candidate mission, the NoSREx field experiment [3] carried out active and passive microwave measurements of snow. The active measurements spanning from 9.15 GHz to 17.9 GHz were performed with the SnowScat instrument [32].
- As part of the NASA SnowEx project, the SRT3 full-polarimetric radar performed X- and Ku-band observations of snow cover [50] and the observations were used for parameter retrieval [51, 52].
- The SnowScat [38, 53, 54] and WBSCAT [55] scatterometers are used for measuring microwave signatures of snow in support of the ESA SnowLab project [56]. SnowScat covers the frequency range from 9.2 GHz to 17.8 GHz, WBSCAT from 1 GHz to 40 GHz. Both are used, among other purposes, to investigate the relationship between snow parameters and the corresponding detected radar characteristics, and for tomographic profiling.
- The terrestrial Ku-band radar system KAPRI is capable of bistatic full-polarimetric interferometric imaging of areas kilometers in size [57]. It is based on the terrestrial interferometer Gamma GPRI [58–61]. Its bistatic capabilities were previously applied to investigate the occurrence of the coherent backscatter opposition effect in seasonal snow [22]. It was also previously used (in the monostatic configuration) to monitor the Alpine glacier Bisgletscher in the context of a geostatistical analysis of the spatial and temporal behaviors of the atmospheric phase screen (APS) in Ku-band [62, 63], as well as polarimetric analysis of natural terrain [64].

3.1.5 *Contributions of this Article*

In August 2021 and March 2022, we carried out time series observations of the Jungfraufirn area of the Great Aletsch Glacier in Switzerland with KAPRI, acquiring a fully-polarimetric interferometric time series of both monostatic and simultaneous bistatic observations of the glacier's accumulation zone. In this article, we

1. describe the acquisition setup and the acquired data;

2. describe the data processing pipeline, including an updated range correction method to correctly geocode data in the complicated bistatic radar geometry, and to compensate for the topographic phase;

3. analyze the temporal decorrelation behaviour of snow cover at Ku-band, including development of a simple model to estimate the effect of glacier drift;

4. analyze the observed polarimetric characteristics of the snow cover (both monostatic and bistatic), and their spatial and temporal variation;

5. discuss the observed Ku-band scattering behaviour and its implications for multistatic monitoring and modeling of snow and ice at Ku-band.

The paper is organized as follows: Section 3.2 describes the observation site and ambient conditions during the measurements, the methodology of the multistatic radar acquisition setup, processing and calibration, in-situ data collection, and data analysis. Section 3.3 analyzes the resulting data, namely the spatial and temporal behaviour of coherence (including an assessment of influence of glacier drift), scattering entropy, mean alpha angle, and co- and cross-polar phase differences, both in monostatic and bistatic geometries. A discussion of the behaviour of these parameters and the possible underlying causes is given in Section 3.4. A conclusion is given in Section 3.5.

3.2 METHODS

3.2.1 *Radar observations*

An in-depth description of the bistatic KAPRI system used for the observations can be found in [57]. The two devices were deployed on two terraces of the High Altitude Research Station Jungfraujoch, both with direct line-of-sight to the ROIs in the Jungfraufirn area of the Great Aletsch Glacier, and with direct line of sight between each other for synchronization purposes. Photographs of the two devices are shown in Figure 3.1. A map of the observed area with marked positions of devices and observed scene is shown in Figure 3.2.

The radars performed repeated acquisitions over the acquired area, with repetition times on the order of $2-4$ minutes. The winter acquisition spanned ~ 30 hours, while the summer acquisition spanned ~ 25 hours. In summer, for logistical reasons there is a ~ 9.5-hour interval during the day in which no acquisitions were made. The key parameters of the radar observation periods are summarized in Table 3.1.

FIGURE 3.1: Photos of both devices deployed at the High Altitude Research Station Jungfraujoch complex. The primary device (top) was deployed on top of the Research Station terrace, the secondary device (bottom) was deployed on the terrace of the East Ridge (*Ostgrat*) building. Both devices observe the Jungfraufirn area, visible in the background of both images. The synchronization antennas pointed along the bistatic baseline are visible in bottom right and top left parts of the two images respectively.

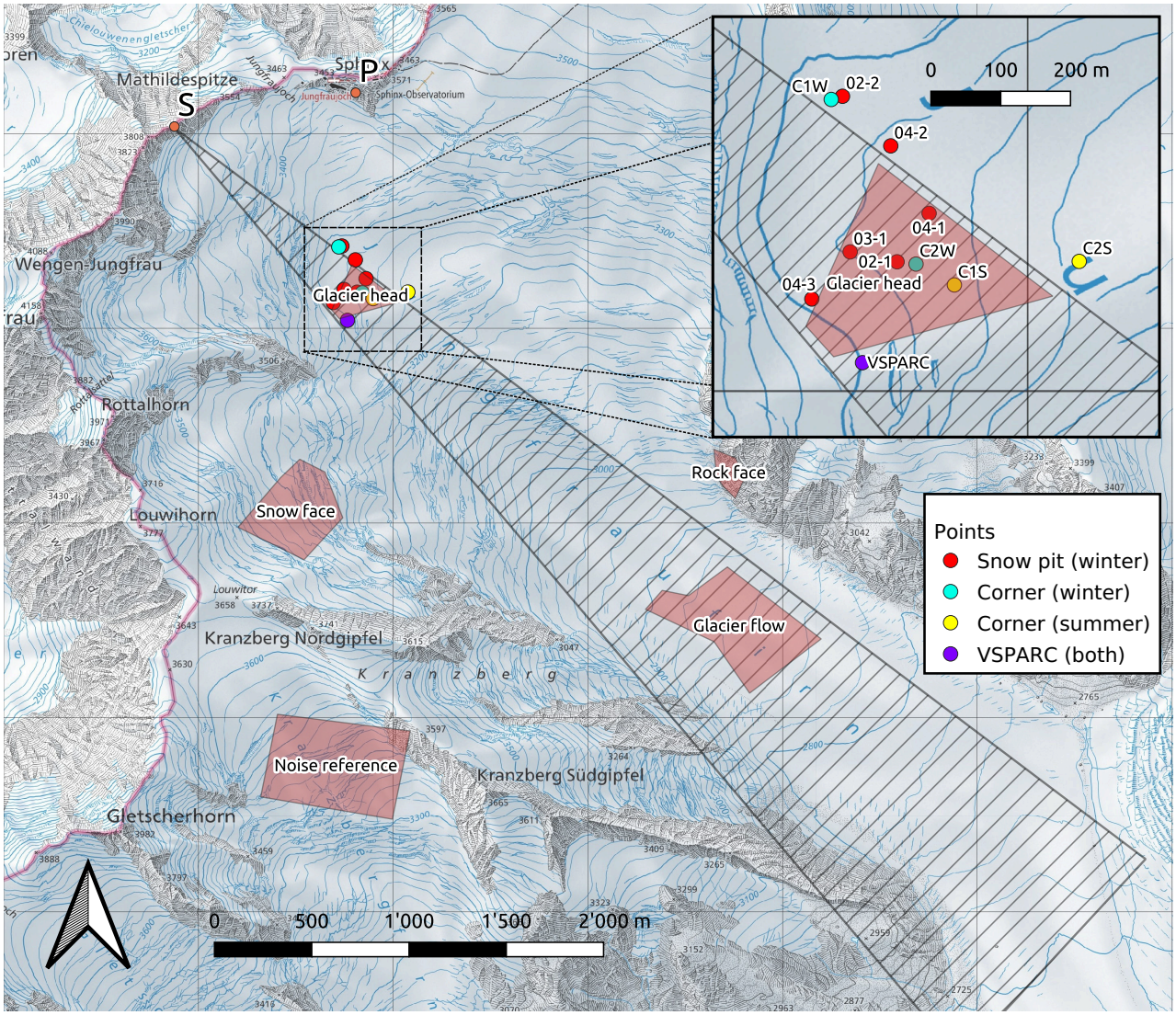

FIGURE 3.2: Map of the observed area of the Jungfraufirn region of the Great Aletsch Glacier. The positions of the primary and secondary radar are marked as P and S respectively. The regions of interest (ROIs) are marked as red polygons. The locations of the six snow pits are marked as red points. C1S, C2S and C1W, C2W mark the positions of the two reference corner reflectors in summer and winter respectively. VSPARC denotes the position of the active radar calibrator. The patterned triangle denotes the coverage of the secondary receiver's antennas (i.e., bistatic coverage).

TABLE 3.1: Radar acquisition parameters and temperature conditions during acquisition campaigns. The (D+1) mark indicates that the time stamp corresponds to the day following the start date of the acquisition period.

Period	summer	winter
Date (D+0)	2021-08-19	2022-03-02
Time span (UTC)	04:15 – 08:15 17:50 – 05:15 (D+1)	09:00 – 15:40 (D+1)
Angular sweep	1 deg/s	2 deg/s
Repetition time	∼3 min	∼2 min
Polarization	Full-pol (HH, HV, VH, VV)	
Modality	Monostatic + bistatic	
Temperature (max)	4 °C	−10 °C
Temperature (min)	−2 °C	−15 °C

3.2.2 *In-situ data*

Several snow pits were dug over the course of the winter campaign, and vertical profiles of snow density, temperature, and grain size were acquired. The location of snow pits is shown in Fig. 3.2. In summer no snow pits were dug due to logistical reasons. In summer the snow cover showed to be hard, recrystallized and firn-like, caused by repeated melt-freeze events over the course of the preceding season. In winter, snow pits revealed a fresh seasonal snow layer of more than 2 meter depth at each site. No fresh snowfall events occurred during the summer nor the winter season. As shown in Table 3.1, snow melt was occurring during summer due to above-zero temperatures. In winter, temperatures remained well below zero and no snow melt was observed. Weather station data from a nearby automated meteostation during the observation periods can be found in supplementary Fig. S3.1. Snow pit data showing the vertical profiles of snow grain size, density and temperature acquired over the course of the winter campaign can be found in supplementary Fig. S3.2.

3.2.3 *DEM-assisted range and topographic phase correction*

In the processing pipeline of the data acquired by the secondary radar, a range correction step is necessary to relate the observed signal travel path length p to slant-range distance

from the primary radar r_P. This is done by establishing a bistatic-north coordinate system (shown in [57, Figs. 1, 5]) and a geometrical transform [57, Section II-F], [65, Chapter 3]

$$r_P = \frac{p^2 - b^2}{2(p - b\sin\theta_P)} \tag{3.6}$$

where b is the length of the bistatic baseline, and θ_P is the azimuth coordinate of the target point within the bistatic-north coordinate system. In case of a horizontal bistatic baseline, θ_P is equal to the azimuthal rotation angle of the primary device's antennas θ'_P, i.e., $\theta_P = \theta'_P$. However, if the P and S devices are placed at different altitudes, then in general $\theta_P \neq \theta'_P$, i.e. the internal azimuthal coordinate of the primary device's positioner is not equal to the azimuth coordinate of the target within the bistatic-north coordinate system, but a coordinate transform is required. This is the case of our experiment, since the primary and secondary device were positioned at altitudes of ∼3500 m and ∼3800 m respectively, with the bistatic baseline $b \approx 960$ m. This altitude difference results in a non-negligible angle of the bistatic baseline with respect to the horizontal plane $\alpha \approx 13°$. A coordinate transformation (specifically a rotation) is thus used to transform the data from the internal polar coordinate system of the primary device (θ'_P, r'_P) into the bistatic-north coordinate system (θ_P, r_P) which has its "east" axis aligned with the bistatic baseline (shown in [57, Fig. 1]). The relation between the two coordinate systems is shown in Figure 3.3. The bistatic coordinates (θ_P, r_P) can be computed by considering the 3-dimensional polar coordinate system centered on the primary device $(r'_P, \theta'_P, \varepsilon')$ and transforming it into Cartesian coordinates [66]:

$$x' = r'_P \sin\theta'_P \cos\varepsilon' \tag{3.7}$$

$$y' = r'_P \cos\theta'_P \cos\varepsilon' \tag{3.8}$$

$$z' = r'_P \sin\varepsilon' \tag{3.9}$$

In these equations ε' is the elevation angle of the target with respect to the horizontal plane, and θ'_P is the azimuth angle. Now we rotate this coordinate system by angle $-\alpha$ around the $\mathbf{y}' = \mathbf{y}$ axis:

$$x = x'\cos\alpha + z'\sin\alpha \tag{3.10}$$

$$y = y' \tag{3.11}$$

$$z = z'\cos\alpha - x'\sin\alpha \tag{3.12}$$

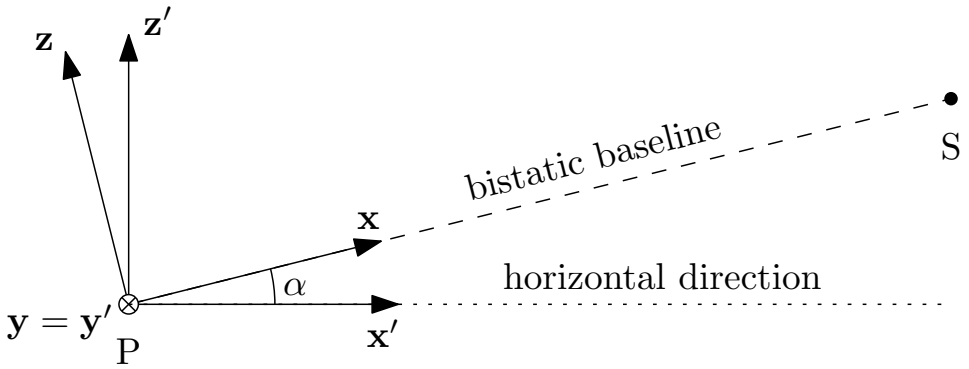

FIGURE 3.3: Diagram of the two coordinate systems used for bistatic range correction. Both coordinate systems originate at the primary device's location P. The bistatic-north Cartesian coordinate system **xyz** has its **x** axis aligned with the bistatic baseline, and the **y** axis aligned with the horizontal plane, pointing towards the observed scene ("into" the paper in the figure). α is the elevation angle of the bistatic baseline with respect to the horizontal plane. The target's azimuthal angle θ_P is computed as the angle between the target vector, and the **yz** plane. The target's elevation angle ε is computed as the angle between the target vector and the **xy** plane. The internal Cartesian coordinate system $\mathbf{x}'\mathbf{y}'\mathbf{z}'$ has its $\mathbf{z}'$ axis oriented vertically, and its $\mathbf{y}'$ axis aligned with the **y** axis. The target's azimuthal and elevation angles θ'_P, ε' are then computed correspondingly with respect to planes $\mathbf{y}'\mathbf{z}'$ and $\mathbf{x}'\mathbf{y}'$.

and transform back into polar coordinates:

$$r_P = \sqrt{x^2 + y^2 + z^2} = \ldots = r'_P \tag{3.13}$$

$$\theta_P = \arctan \frac{x}{y} = \arctan \frac{x' \cos\alpha + z' \sin\alpha}{y'} \tag{3.14}$$

$$= \arctan \frac{\sin\theta'_P \cos\varepsilon' \cos\alpha + \sin\varepsilon' \sin\alpha}{\cos\theta'_P \cos\varepsilon'} \tag{3.15}$$

$$= \arctan \left(\tan\theta'_P \cos\alpha + \tan\varepsilon' \sec\theta'_P \sin\alpha\right) \tag{3.16}$$

The bistatic-north azimuthal angle θ_P can thus be computed from the internal azimuthal angle θ'_P, the elevation angle of the target ε', and the elevation angle of the bistatic baseline α using eq. (3.16). For any scatterer, the parameters α and θ'_P can be retrieved from the acquisition geometry and scan parameters. However, since KAPRI's beam has considerable width in elevation, it is not possible to determine the scatterer's elevation angle ε' purely from the radar signal. Assuming that the scatterer is placed at ground level, its ε can be determined with aid of an external digital elevation model (DEM):

$$\varepsilon'(\theta'_P, r'_P) = \arcsin \frac{h_{DEM}(\theta'_P, r'_P) - h_P}{r'_P} \tag{3.17}$$

In this equation $h_{\mathrm{DEM}}(\theta'_{\mathrm{P}}, r'_{\mathrm{P}})$ is the altitude of the DEM at coordinates $(\theta'_{\mathrm{P}}, r'_{\mathrm{P}})$ with respect to the primary device's internal polar coordinate system, and h_{P} is the altitude of the primary radar device. Eq. (3.17) might have no solutions for low values of slant range r_{P} in case the primary device is positioned high above the observed terrain, e.g. on a tower. Furthermore, in areas where layover occurs, $h_{\mathrm{DEM}}(\theta'_{\mathrm{P}}, r'_{\mathrm{P}})$ is ill-defined. These areas need to be masked out from the final range-corrected dataset.

Finally, for each point of the final monostatic-like SLC sampling grid $\mathrm{SLC}_{\mathrm{mono}}(\theta'_{\mathrm{P}}, r'_{\mathrm{P}})$, the corresponding point in the acquired bistatic dataset $\mathrm{SLC}_{\mathrm{bist}}(\theta'_{\mathrm{P}}, p)$ can be found by inverting eq. (3.6):

$$p(r_{\mathrm{P}}, \theta'_{\mathrm{P}}) = \sqrt{b^2 + 2br_{\mathrm{P}} \sin(\theta_{\mathrm{P}}) + r_{\mathrm{P}}^2} + r_{\mathrm{P}}, \tag{3.18}$$

and computing θ_{P} from eqs. (3.16) and (3.17) using parameters of the bistatic geometry $b, h_{\mathrm{P}}, \alpha$, and external DEM data h_{DEM}.

The topographic phase has to receive a similar treatment. The one-way phase delay between two antennas placed vertically above one another with vertical baseline B can be expressed as:

$$\Delta\phi = \frac{2\pi}{\lambda} B \cos\theta \tag{3.19}$$

where θ is the incidence angle. Since the two devices are placed at different altitudes and ground range distances, the incidence angle for a chosen scene point will in general be different for the primary and for the secondary device. This means that for the bistatic dataset, the topographic phase compensation described in [67, Section II-E] has to be applied separately for the transmission and reception leg of the signal's path.

3.2.4 *Polarimetric calibration*

Polarimetric calibration was performed using corner reflectors and an active calibration device VSPARC. The primary device was calibrated using the corner-reflector based method described in [67], which determined the four real-valued calibration parameters $f, g, \phi_{\mathrm{t}}, \phi_{\mathrm{r}}$. VSPARC was used for the primary dataset to verify proper calibration of cross-polar phases (see [57, Section IV-C]). The primary dataset's phase offset at transmission ϕ_{t} and the amplitude offset between transmitting antennas $t = fg$ were also applied to the secondary dataset, since the transmitting antennas are shared between the primary and secondary device. For the secondary device's receivers, the VSPARC method described in [57, Section II-I] was used to determine the amplitude imbalance at reception $r = f/g$ and phase offset

at reception ϕ_r. Table 3.2 shows the residuals of polarimetric calibration parameters of the primary device several hours after calibration was performed.

TABLE 3.2: Residuals of polarimetric calibration of the primary device. The residuals are computed on data acquired several hours after the data from which the calibration parameters were determined. The primary device was dis- and re-assembled in-between. The results show the mean value and the interval in which all observed values are contained. 15 consecutive acquisitions were analyzed for each season.

Season	f	g	$\phi_t + \phi_r$	$\phi_t - \phi_r$
Summer	1.02 ± 0.01	1.01 ± 0.01	$12° \pm 3°$	$-3° \pm 2°$
Winter	1.03 ± 0.02	1.02 ± 0.01	$11° \pm 3°$	$-4° \pm 1°$

Due to unstable temperature of the radar instruments' electronics, their sensitivity/gain exhibits a thermal-drift-caused instability. This precludes a detailed analysis of absolute backscatter intensity values without an external correction. However, an analysis of polarimetric intensity ratios, e.g. the co-polar backscatter intensity ratio I_{HH}/I_{VV}, is possible without further correction, as the drift affects all polarimetric channels equally.

3.2.5 *Regions of interest*

For a time series analysis, several regions of interest (ROIs) were defined, encompassing different parts of the observed scene. The ROIs are shown in Figure 3.2 and described in Table 3.3.

TABLE 3.3: Description of ROIs.

ROI label	Surface type	Approx. range	Bist. coverage	β
Glacier head	Snow	800 m	yes	$\sim 40°$
Glacier flow	Snow	3000 m	yes	$\sim 10°$
Rock face	Rock	2500 m	no	N/A
Snow face	Snow	2000 m	no	N/A

3.2.6 *Temporal coherence analysis*

In order to explore the behaviour of temporal decorrelation γ_{Temp}, the contribution of all other effects in Eq. 3.5 needs to be quantified. Several of these terms can be neglected due to

the setup of the measurement – zero volume decorrelation can be assumed since there is zero spatial baseline between the individual repeat-pass measurements ($\gamma_{\text{Vol}} \approx 1$). Due to the high bit depth of the receiver's ADC (14 bits/sample), quantization error can also be neglected ($\gamma_{\text{Quant}} \approx 1$).

The azimuth ambiguities can have a contribution towards reduction of coherence through the term γ_{Amb}. The corresponding coherence loss can be approximated by [19, Eq. 26]

$$\gamma_{\text{Amb}} = \frac{1}{(1 + \text{RASR})(1 + \text{AASR})} \tag{3.20}$$

where RASR and AASR are the range and azimuth ambiguity-to-signal ratios, respectively.

The FMCW chirp length $\tau = 4\,\text{ms}$ was set sufficiently long so that no areas within direct line of sight to the radar system can cause range ambiguities (RASR ≈ 0). The primary device's antennas have a one-way peak sidelobe ratio (PSLR) of $-15\,\text{dB}$. For the primary device, this ratio is applied both ways, resulting in negligible coherence loss:

$$\text{AASR}_{\text{mono}} = -30\,\text{dB} \implies \gamma_{\text{Amb,mono}} = \frac{1}{1 + 10^{-3}} > 0.99 \tag{3.21}$$

In the bistatic case, the return path provides no sidelobe attenuation, thus the estimated decorrelation is

$$\text{AASR}_{\text{bist}} = -15\,\text{dB} \implies \gamma_{\text{Amb,bist}} = \frac{1}{1 + 10^{-1.5}} \approx 0.97 \tag{3.22}$$

this value is also negligible compared to the remaining terms and can thus be neglected ($\gamma_{\text{Amb}} \approx 1$).

3.2.6.1 *Glacier drift*

Due to the real-aperture nature of the measurement there is zero shift of the Doppler spectra, and due to zero spatial baseline the incidence angle on flat surfaces remains constant. The only factor affecting terms γ_{Rg} and γ_{Az} is thus possible mis-coregistration of datasets. This misregistration can be caused by glacier drift over time, since it can cause scatterers to move out of their original range cell. We can introduce a term

$$\gamma_{\text{Drift}} = \gamma_{\text{Rg}} \gamma_{\text{Az}} \tag{3.23}$$

which represents the drop of temporal coherence between times T_0 and T which occurs when glacier displacement along range and azimuth $d_{\text{rng}}, d_{\text{azm}}$ accumulates a non-negligible

value compared to the resolution cell dimensions $\delta_{\text{rng}}, \delta_{\text{azm}}$. The value of γ_{Drift} starts at 1 when $T = T_0$, and reduces to 0 once drift causes all the original scatterers to leave the range cell. Figure 3.4 visualizes this phenomenon. The values of γ_{Rg} and γ_{Az} can be approximated as [19]

$$\gamma_{\text{Rg}} \approx \text{sinc}(\pi \frac{d_{\text{rng}}}{\delta_{\text{rng}}}), \tag{3.24}$$

and equivalently for the azimuth shift

$$\gamma_{\text{Az}} \approx \text{sinc}(\pi \frac{d_{\text{azm}}}{\delta_{\text{azm}}}). \tag{3.25}$$

Thus, if it is not possible to correct the drift effect by precise coregistration, its influence can be arbitrarily mitigated by decimation of the SLC, which increases δ_{rng} and/or δ_{azm}.

Glacier drift rate can be estimated from KAPRI data using repeat-pass differential interferometry, provided that the temporal sampling rate is dense enough to avoid phase unwrapping errors caused by rapid drift of atmospheric phase screen variations. The drift along the slant-range direction $d_{\text{slant-range}}$ is related to total horizontal drift d_{horiz}:

$$d_{\text{horiz}} = \frac{d_{\text{slant-range}}}{\cos \phi_{\text{drift}} \sin \theta_{\text{inc}}}. \tag{3.26}$$

In this equation ϕ_{drift} is the angle between the slant-range look vector and the glacier drift vector, and θ_{inc} is the incidence angle.

KAPRI's non-decimated range sampling resolution is 0.75 m. Using a range decimation factor of 6, the effective range cell size is increased to $\delta_{\text{rng}} = 4.5\,\text{m}$. The azimuthal width of the range cell is range-dependent (due to the real aperture). Using a beamwidth of 0.35° the width within the ROIs (which are placed at ranges above 800 m) is 5 m or more. An azimuthal decimation factor of 2 will thus result in the range cell width $\delta_{\text{azm}} \geq 10\,\text{m}$.

In this publication, we are investigating temporal coherence decays on scales of less than 24 hours. Based on our own data (see Section 3.3.1) as well as satellite measurements [21], we estimate the worst-case drift values for both range and azimuth as $D_{\text{max}} \approx 0.25\,\text{m}$. We can thus consider the glacier drift effect non-negligible over temporal baselines longer than several hours, if non-decimated data is used ($\delta_{\text{rng}} = 0.75\,\text{m}, \delta_{\text{azm}} \geq 5\,\text{m}$). Using a 6× range decimation factor and a 2× azimuth decimation factor, the upper ceiling of the effect of glacier drift on temporal coherence after 24 hours can be estimated as a negligible value of

$$\gamma_{\text{Drift,24-hr}} = \text{sinc}\left(\pi \frac{0.25\,\text{m}}{4.5\,\text{m}}\right) \text{sinc}\left(\pi \frac{0.25\,\text{m}}{10\,\text{m}}\right) > 0.99. \tag{3.27}$$

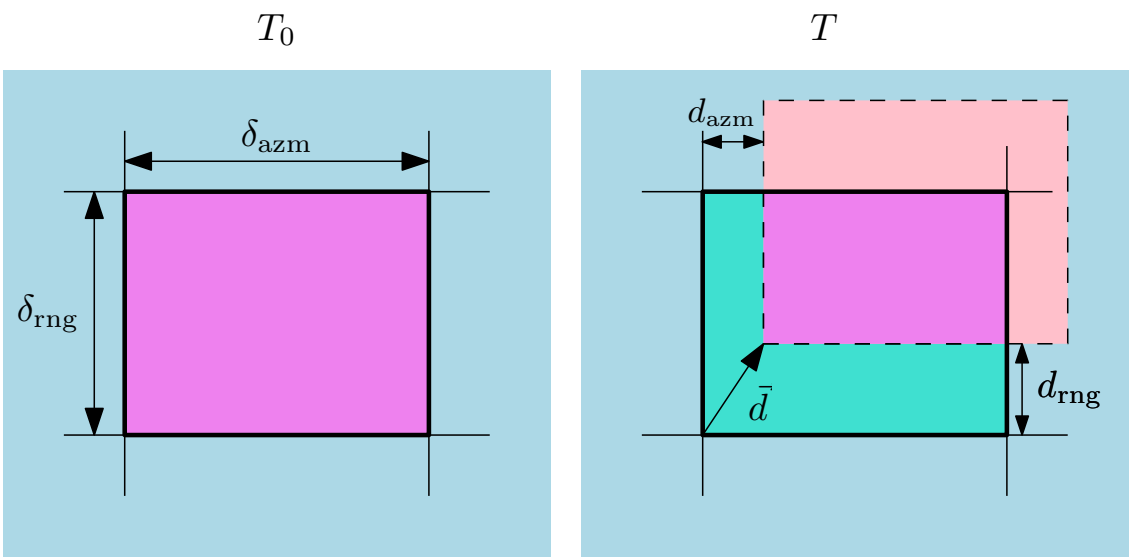

FIGURE 3.4: Linear model visualizing the relationship between glacier drift $\vec{d} = (d_{\text{rng}}, d_{\text{azm}})$ and the coherence loss γ_{Drift}. At time T_0, all original scatterers (violet) are present in the range cell, thus $\gamma_{\text{Drift}} = 1$. As the glacier drifts, part of the original scatterers depart the range cell (light pink), while new scatterers enter the range cell (cyan). The drift coherence factor γ_{Drift} thus reduces according to eqs. (3.23), (3.24), and (3.25).

For comparison, using non-decimated data would result in a 24-hour drift coherence loss of $\gamma_{\text{Drift,24-hr}} = 0.82$.

3.2.6.2 *Temporal decorrelation*

The two remaining terms have the biggest impact on the coherence of the measurement:

$$\gamma \approx \gamma_{\text{SNR}} \gamma_{\text{Temp}}. \tag{3.28}$$

The SNR term varies greatly depending on range distance, local incidence angle, and scattering properties. Its value can be estimated from the data by dividing the multi-looked intensity (MLI) by the noise floor. Then the decorrelation due to noise can be estimated as [68]

$$\gamma_{\text{SNR}}[T_1, T_2] = \frac{1}{\sqrt{(1 + \text{SNR}_{T_1}^{-1})(1 + \text{SNR}_{T_2}^{-1})}}, \tag{3.29}$$

where SNR_T denotes the signal-to-noise ratio of the acquisition taken at time T. This ratio can change over time in case of changes in the observed scene (such as snowmelt/refreezing), or changes in the received (e.g. thermal drift). The temporal evolution of the temporal

decorrelation starting at time T_0 can thus be estimated from the observed coherence $\gamma[T_0, T]$ as

$$\gamma_{\text{Temp}}[T_0, T] \approx \frac{\gamma[T_0, T]}{\gamma_{\text{SNR}}[T_0, T]}. \tag{3.30}$$

Assuming that γ_{SNR} and γ_{Temp} are uncorrelated, one can apply the variance formula for error propagation [69] to eq. (3.28) and derive

$$\Delta\gamma_{\text{Temp}} \approx \frac{\sqrt{\Delta\gamma^2 - \gamma_{\text{Temp}}^2 \Delta\gamma_{\text{SNR}}^2}}{\gamma_{\text{SNR}}}, \tag{3.31}$$

where $\Delta\gamma_{...}$ signifies the error estimate of $\gamma_{...}$. This indicates that when SNR is low (and thus γ_{SNR} is low, such as at high ranges or in the bistatic regime), the uncertainty of the γ_{Temp} estimate diverges.

3.2.7 *Reciprocity principle considerations*

Due to the reciprocity principle, in the monostatic case the cross-polarized channels HV and VH should be equal, i.e. $S_{\text{HV}} = S_{\text{VH}}$. This fact has been long-used to simplify polarimetric relations by reducing the dimensionality of the data [17, 39, 40], and can also be used for, e.g., calibration [67] or noise filtering [70]. However in the bistatic case the principle no longer generally applies, and in general S_{HV} and S_{VH} do not need to be equal. It is therefore of interest to investigate the (possibly non-zero) additional polarimetric parameters. These parameters include the cross-polar phase difference $\phi_{\text{HV}-\text{VH}}$, the cross-polar intensity ratio $I_{\text{HV}}/I_{\text{VH}}$, or the fourth (i.e. smallest) eigenvalue λ_4 of the coherency matrix T [17, 70]:

$$T = \left\langle \mathbf{k}_{\text{P}} \cdot \mathbf{k}_{\text{P}}^{\dagger} \right\rangle. \tag{3.32}$$

3.2.8 *Sign of the phase differences*

The sign convention of the polarimetric phase differences is important to define for their proper interpretation and comparison with other literature. In a typical radar processing workflow there are several possible ways the sign of the phase can be flipped (and thus differ between publications), from the choice of coordinate systems (FSA vs. BSA) [17, 40], definition of the phasor rotation direction with increasing range, or ordering of the terms in definitions of phase differences (cf. e.g. [13, 31, 71] which use the HH-VV ordering, and [11, 72–74] where VV-HH ordering is used).

In this publication, the phase ϕ is defined to decrease with increasing range of the scattering target, i.e. when a target increases its distance from the sensor, the phase of its scattering response decreases:

$$\phi(r) = -\frac{4\pi}{\lambda} r. \tag{3.33}$$

The implication for polarization phase differences is that if the HH phase center is further away from the radar sensor along range direction as opposed to the VV phase center, and phase wrapping does not occur, the CPD will be negative. For example, if the HH phase center is further away by range distance $\lambda/8$, the resulting CPD according to eq. (3.1) will be $\phi_{\mathrm{HH-VV}} = \phi_{\mathrm{HH}} - \phi_{\mathrm{VV}} = -\pi/2$. The same applies for XPD for HV and VH phase centers respectively.

3.3 DATA AND RESULTS

To provide a reference frame for interpretation of polarimetric data, in Figure 3.5 we show the Pauli RGB representation of backscatter images for the morning of both seasons, for both monostatic and bistatic data. Figure 3.6 shows the time series of estimated SNR (i.e. radar brightness β_0 divided by the noise floor) for each ROI defined in Table 3.3. The data shows that the bistatic dataset, especially the "Glacier flow" ROI, exhibits very low SNR once snowmelt sets in in summer. The bistatic SNR in the winter season in this ROI is also low. Care thus has to be taken when interpreting bistatic observations in this region, since noise will have considerable influence.

3.3.1 *Glacier drift and temporal coherence*

In order to validate the drift estimates described in Section 3.2.6.1, we estimated the glacier drift in the ROIs from monostatic KAPRI observations using differential interferometry. Figure 3.7 shows the slant-range drift rate for both season estimated by unwrapping the differential interferometric phase. The slant range drift rate in the glacier ROIs is estimated at approx. 25cm/day. For the Glacier body ROI, this estimate is close to the total drift value, since incidence angle is very shallow and the glacier flow is oriented along range. For the Glacier top ROI, we can assume that the drift vector has an approximately 45 degree angle ϕ_{drift} with the range direction. We can thus compute the total drift and the drift components along azimuth and range using eq. (3.26). Table 3.4 shows the calculated displacement values along range and azimuth for the two glacier ROIs.

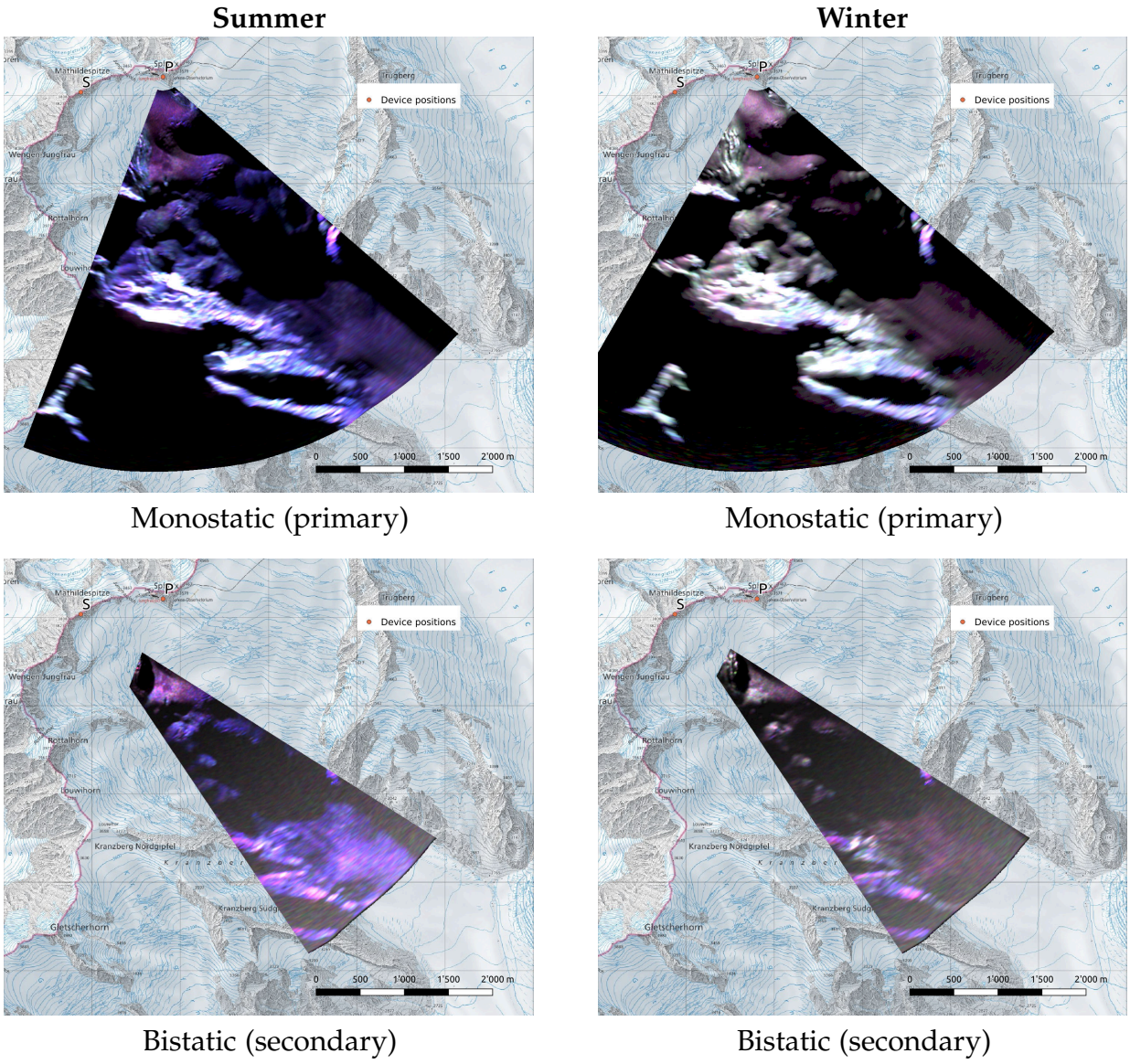

FIGURE 3.5: Comparison of the Pauli representation (B:HH+VV, R:HH-VV, G:HV+VH) of polarimetric data for the summer (left) and winter (right) seasons, showing both monostatic (top) and bistatic (bottom) data. The gamma-scaling of each image was individually adjusted for better contrast and feature visibility. Bistatic images were cropped to show only the area covered by the main lobe of the secondary receiver antennas. The images show that backscatter behavior is dramatically different between the two seasons. The predominantly blue color of summer acquisitions indicates dominance of surface-type scattering, while the mixed color of winter acquisitions indicates a higher diversity of scattering processes. The reduced signal-to-noise ratio of bistatic images due to use of lower-gain antennas is visible as noise in the far-range regions of the images.

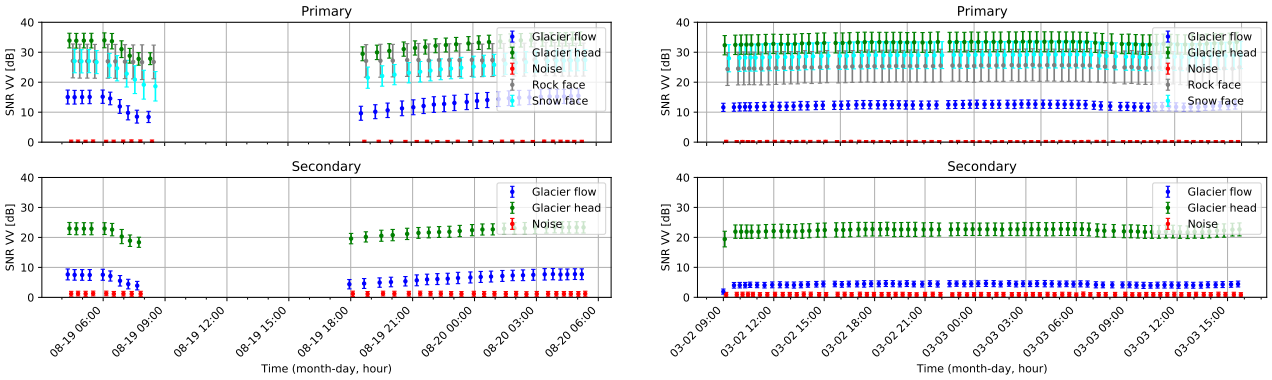

FIGURE 3.6: Time series of signal-to-noise ratio (SNR) in the VV polarization for summer (left) and winter (right) seasons, for both monostatic (top) and bistatic (bottom) data, per ROI. The noise reference level was derived as the mean intensity of all areas with single-pass interferometric coherence $\gamma < 0.1$. The bistatic SNR is in general lower than monostatic SNR due to use of lower-gain antennas. In summer, snowmelt during the day causes additional reduction of SNR, leading to critically-low SNR values in the "Glacier flow" ROI of < 5 dB.

TABLE 3.4: Drift values over a 24-hour period estimated from KAPRI differential interferometric measurements (Figure 3.7). The difference between summer and winter values is negligible for purposes of estimation of drift effects on coherence.

ROI label	ϕ_{drift}	$d_{\text{slant range}}$	d_{horiz}	d_{rng}	d_{azm}
Glacier top	45°	23 cm	33 cm	23 cm	23 cm
Glacier body	0°	21 cm	22 cm	22 cm	0 cm

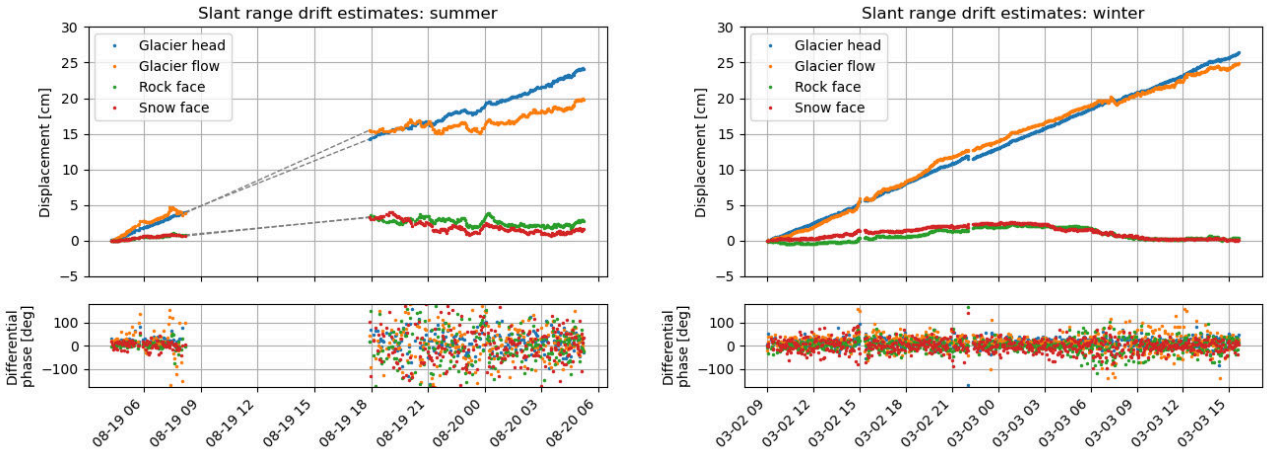

FIGURE 3.7: Slant-range glacier drift of the glacier within individual ROIs estimated from the monostatic radar data by differential interferometry. The drift during the sampling gap in the summer dataset is linearly extrapolated (dashed lines) from the preceding observations. The winter dataset (sampled at 2 mins) shows stable drift of approx. 21cm/day. In the summer dataset, stronger phase variance is observed. This can be explained by more turbulent atmospheric conditions, lower SNR (see Fig. 3.6), and a longer sampling rate of approx. 3-4 minutes. This can cause possible phase wrapping, which likely leads to underestimation of the final drift estimate value, especially for the further-placed Glacier body ROI. However, extrapolation of the initial, stable part of the drift curve results in a summer drift estimate of approx. 23cm/day.

The drift estimates were then used to assess the influence of range cell drift on temporal coherence estimates and apply decimation in order to mitigate this effect (Section 3.2.6.1). Figure 3.8 shows the resulting time series of estimation of temporal coherence $\gamma[T_0, T]$ for the two seasons, with the reference time of day T_0 chosen in the evening of each observation period, in order to avoid further snow melt and maximize time series span. Supplementary Figure S3.3 shows the maps of this observed coherence $\gamma[T_0, T]$ over spans of approximately 2, 4, and 8 hours, for the summer and winter seasons respectively.

3.3.2 *Second-order polarimetric parameters*

For a high-level characterization of scattering processes occurring within the observed areas at Ku-band, and their temporal evolution, we investigate closer the second-order polarimetric parameters, specifically the scattering entropy H and the mean alpha angle $\bar{\alpha}$.

The scattering entropy H can serve as a measure of the diversity of scattering processes. Figure 3.9 shows the value of entropy in the monostatic dataset for morning and evening of each season. For brevity, maps of these parameters for the bistatic dataset are not shown, however the bistatic behaviour can be assessed through investigation of the time series – this is shown in Fig. 3.10 and shows monostatic and bistatic values of these parameters for

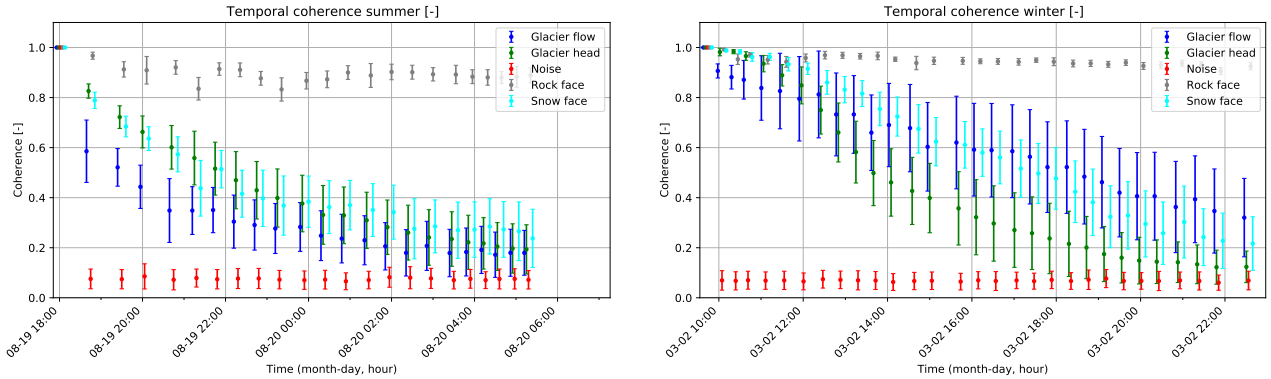

FIGURE 3.8: Time series of coherence $\gamma[T_0, T]$ for the summer (left) and winter (right) seasons. Time T_0 in summer was chosen in the evening to avoid the increase of liquid water content during the day, and to maximize the uninterrupted time series length. Due to stability of the scene in winter, the choice of T_0 has negligible impact on data in winter. For both seasons, the time axis spans 13 hours. The points and error bars represent the mean and the standard deviation of the coherence within each ROI.

each ROI as specified in Figure 3.2. This data shows a large difference between the entropy behaviour in summer and in winter. Furthermore, entropy exhibits intra-day variation in summer, while in winter it remains stable throughout the whole observation period, for both monostatic and bistatic datasets.

For an assessment of the type of dominant scattering processes, Figures 3.11 and 3.12 correspondingly show the maps and time series for the mean alpha angle $\bar{\alpha}$. Behaviour similar to scattering entropy H is observed, where $\bar{\alpha}$ has an overall lower value in summer as opposed to winter, and exhibits intra-day variation in summer, while remaining stable in winter.

In order to investigate possible occurrence of non-reciprocal scattering processes (i.e. processes where $S_{\mathrm{HV}} \neq S_{\mathrm{VH}}$, Figure 3.13 shows the time series of the relative values of the fourth eigenvalue of the coherency matrix λ_4 compared to the sum of all four eigenvalues, i.e. the plotted value is:

$$\hat{\lambda}_4 = \frac{\lambda_4}{\sum_{n=1}^{4} \lambda_n}. \tag{3.34}$$

The data shows a low value of the $\hat{\lambda}_4$ in the monostatic datasets irrespective of the season. Bistatic datasets however show a higher value, thus indicating possible presence of non-reciprocal scattering.

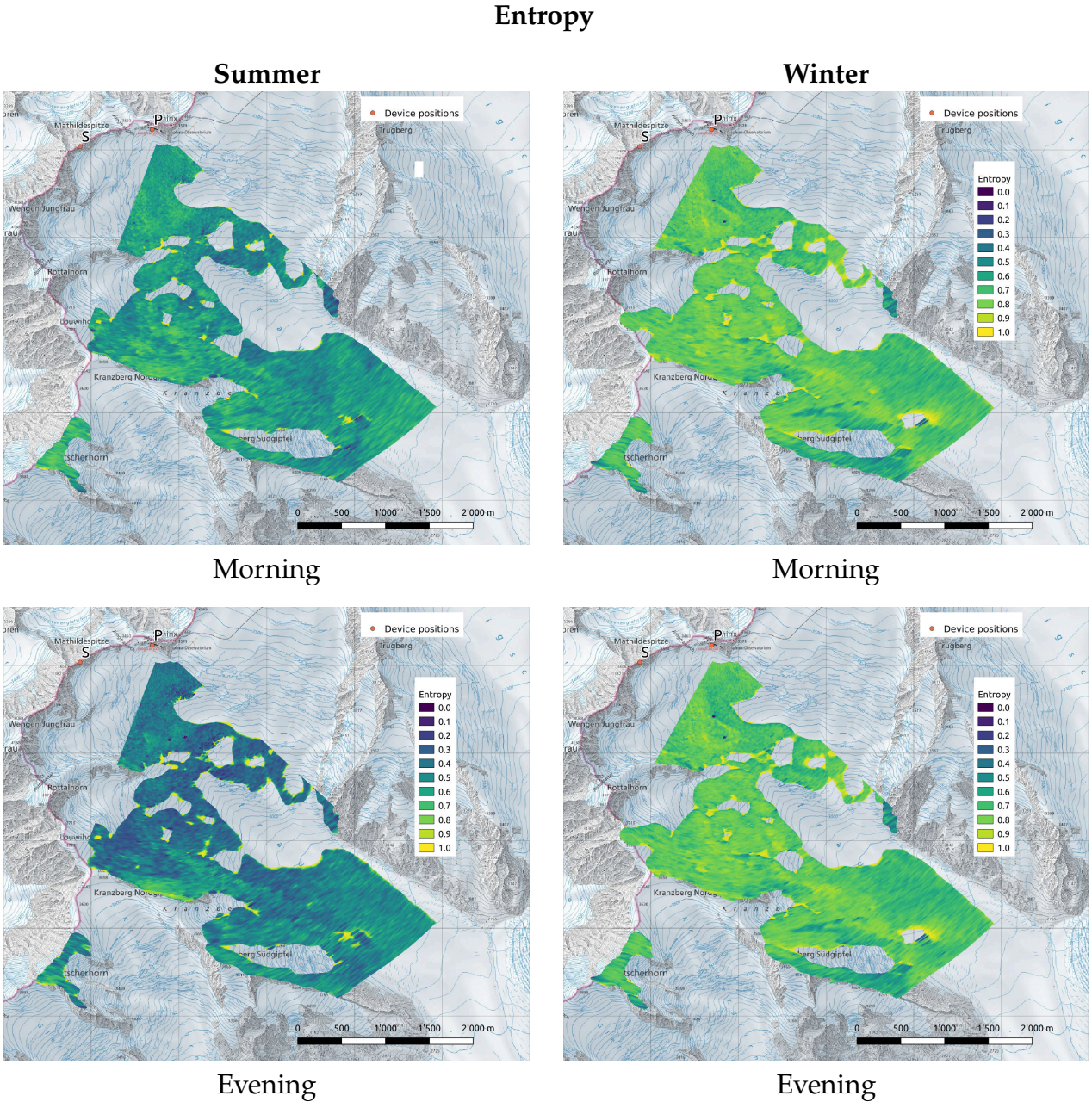

FIGURE 3.9: Comparison of the observed monostatic entropy H for the summer (left) and winter (right) seasons, for morning (top) and evening (bottom) times of day. In winter, the entropy retains a high value throughout the day. In summer, entropy is comparably lower. It also further reduces during the day and reaches its minimal value after sunset. The exception are exposed rock areas which retain a low entropy value throughout.

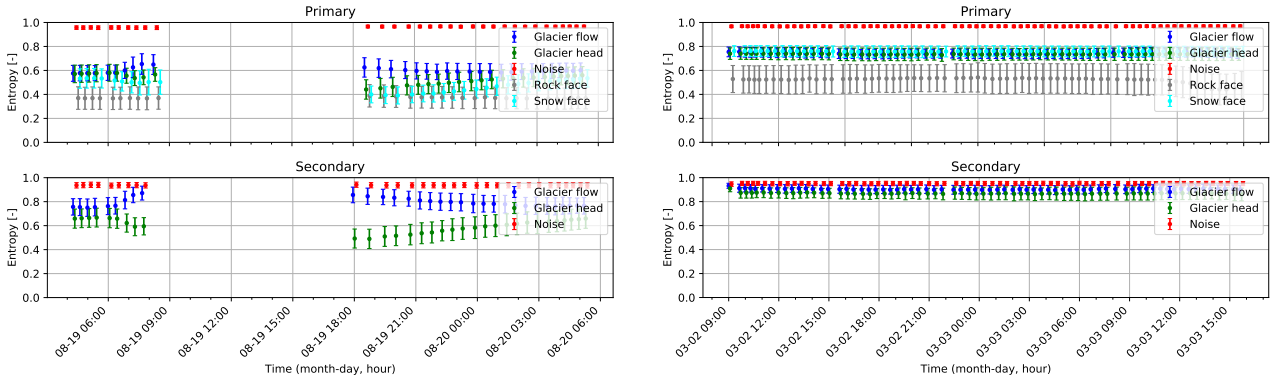

FIGURE 3.10: Time series of entropy H for summer (left) and winter (right) seasons, for both monostatic (top) and bistatic (bottom) data, per ROI.

3.3.3 *Polarimetric phase differences*

Polarimetric phase differences $\phi_{\mathrm{HH-VV}}$ and $\phi_{\mathrm{HV-VH}}$ can be used for investigation of anisotropy of the snow pack, as well as investigation of possible non-reciprocal scattering in the bistatic regime. All phase differences shown in this section follow the sign convention described in Section 3.2.8.

In order to assess the spatial and temporal behaviour of the co-polar phase difference $\phi_{\mathrm{HH-VV}}$, Figures 3.14 and 3.15 show the maps of $\phi_{\mathrm{HH-VV}}$ for both devices and seasons, for the morning and evening time respectively. The time series of $\phi_{\mathrm{HH-VV}}$ can be found in supplementary Fig. S3.7. Similarly to entropy and mean alpha angle, a large difference in behaviour between seasons, and intra-day variation in summer is observed.

The cross-polarized phase difference $\phi_{\mathrm{HV-VH}}$ should have a zero value in the monostatic observations due to the reciprocity principle (this is confirmed in supplementary Fig. S3.9), and thus the bistatic behaviour is of larger interest, as its non-zero value is an indicator of non-reciprocal scattering. Figure 3.16 shows the maps of $\phi_{\mathrm{HV-VH}}$ for the secondary device in both seasons, for both the morning and evening time. The time series is shown in supplementary Fig. S3.8. The data confirms that $\phi_{\mathrm{HV-VH}}$ acquires a non-zero value in the bistatic regime, and the spatial and temporal behaviour varies dramatically between the summer and the winter season.

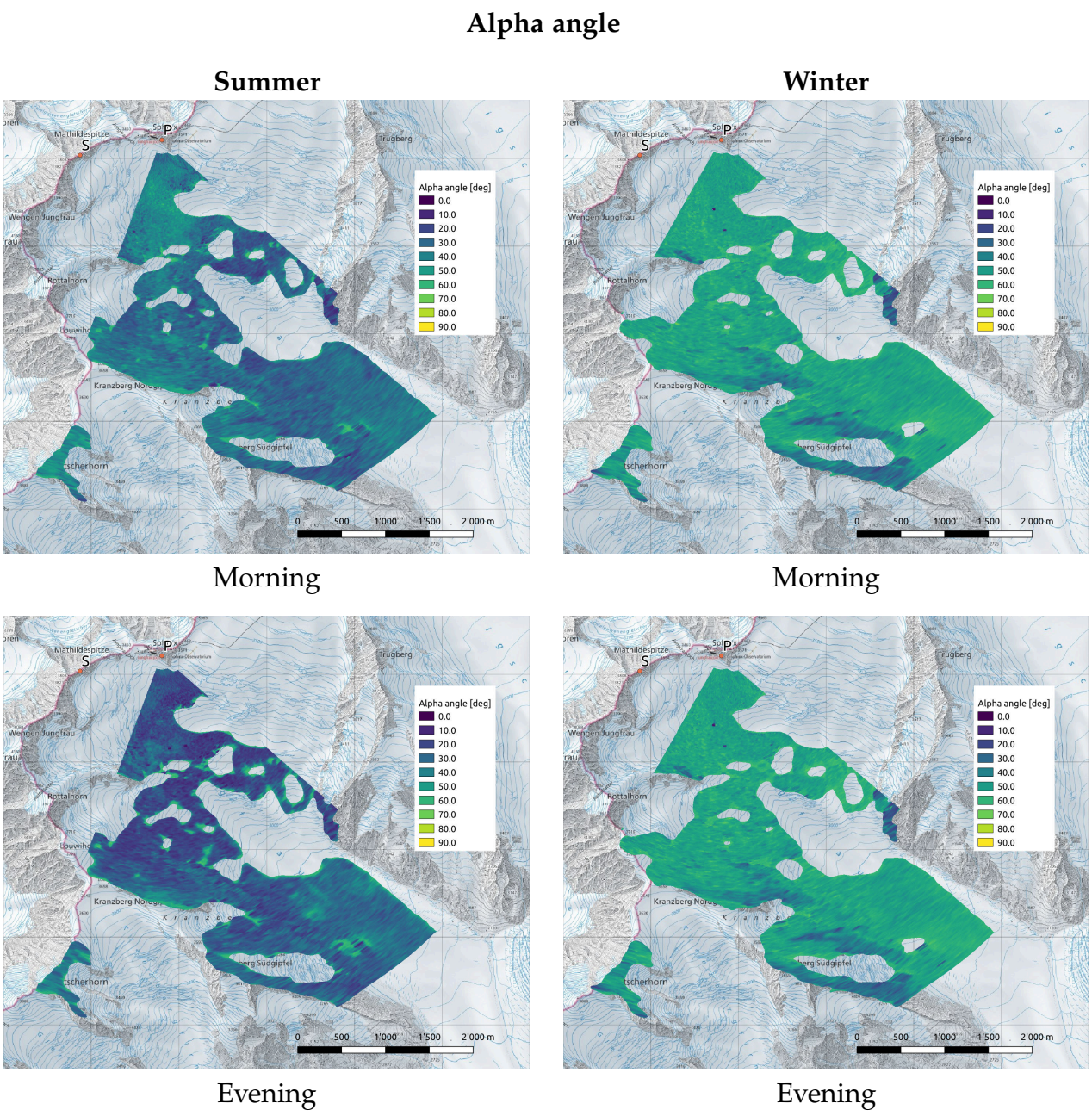

FIGURE 3.11: Comparison of the observed monostatic mean alpha angle $\bar{\alpha}$ for the summer (left) and winter (right) seasons, for morning (top) and evening (bottom) times of day. In winter, $\bar{\alpha}$ retains a medium value throughout the day. In summer, $\bar{\alpha}$ is comparably lower. It also further reduces during the day and reaches its minimal value after sunset, in a manner similar to entropy in Fig. 3.9. The exception are exposed rock areas which retain a low entropy value throughout.

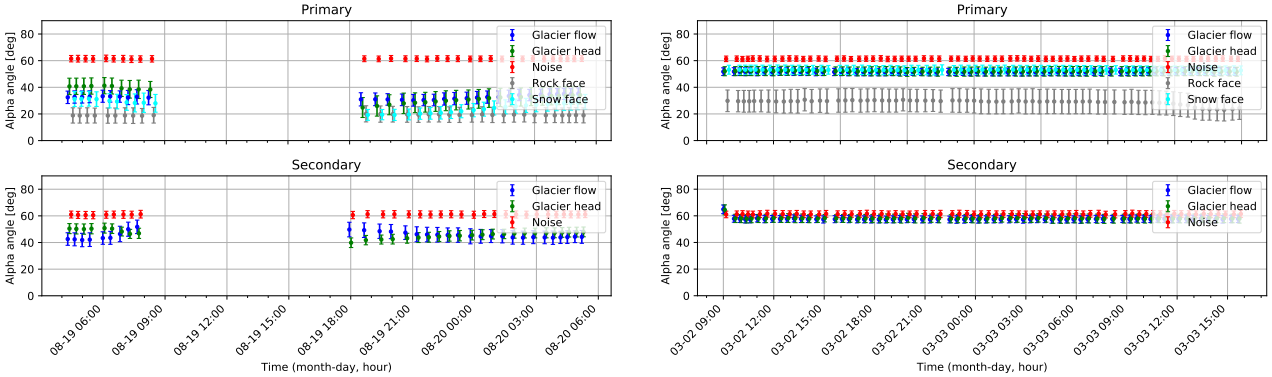

FIGURE 3.12: Time series of mean alpha angle $\bar{\alpha}$ for summer (left) and winter (right) seasons, for both monostatic (top) and bistatic (bottom) data, per ROI.

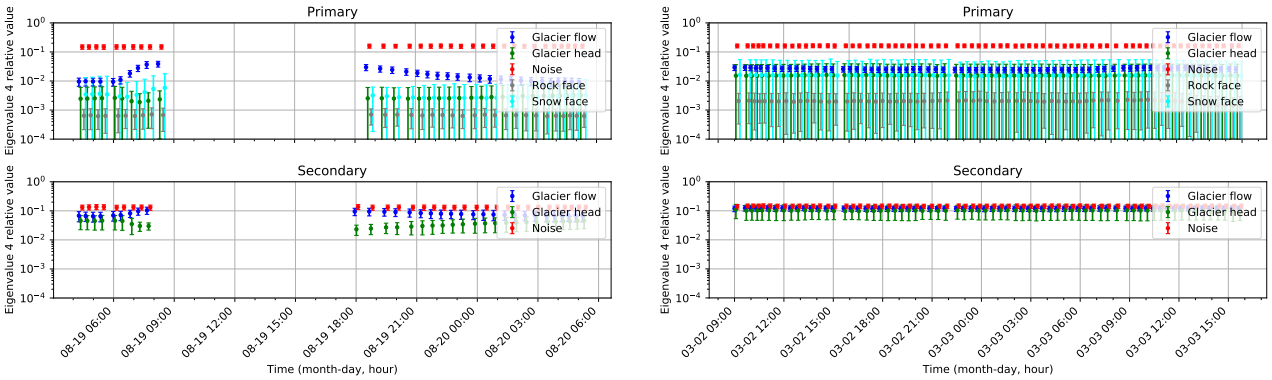

FIGURE 3.13: Time series of the fourth eigenvalue $\hat{\lambda}_4$ as defined in eq. (3.34) for summer (left) and winter (right) seasons, for both monostatic (top) and bistatic (bottom) data, per ROI. The y-axis is logarithmic. The primary (monostatic) datasets exhibit an overall low value irrespective of season or time of day. The temporal rise of $\hat{\lambda}_4$ value in the Glacier flow ROI in summer is correlated with the SNR reduction (see Fig. 3.6). The bistatic datasets (secondary) show a higher value of $\hat{\lambda}_4$, indicating presence of non-reciprocal scattering.

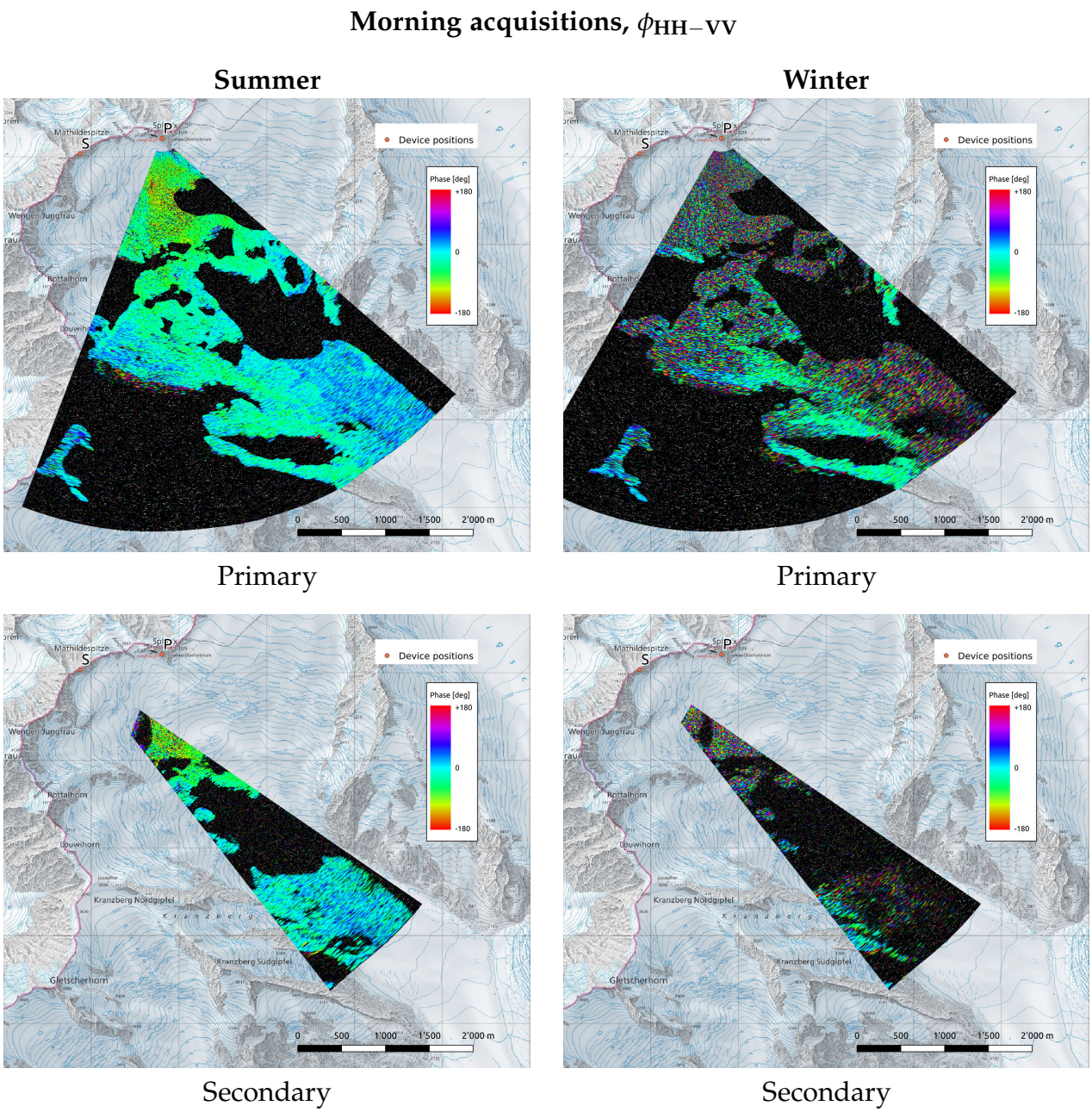

FIGURE 3.14: Comparison of the observed CPD for the summer (left) and winter (right) seasons, for the primary (top, monostatic) and the secondary (bottom, bistatic) dataset. The data was acquired in the morning. In order to enhance the signal, 10 consecutive interferograms were coherently averaged. In summer, the CPD has a "well-behaved" value, and does not appear to exhibit phase wrapping, neither in the monostatic nor the bistatic dataset. It exhibits an incidence angle dependent behaviour, where its value increases with increasing incidence angle. In winter, the CPD varies rapidly over very short spatial scales, and appears to exhibit rapid phase wrapping. The exception are exposed rock areas which retain a CPD value of close to 0.

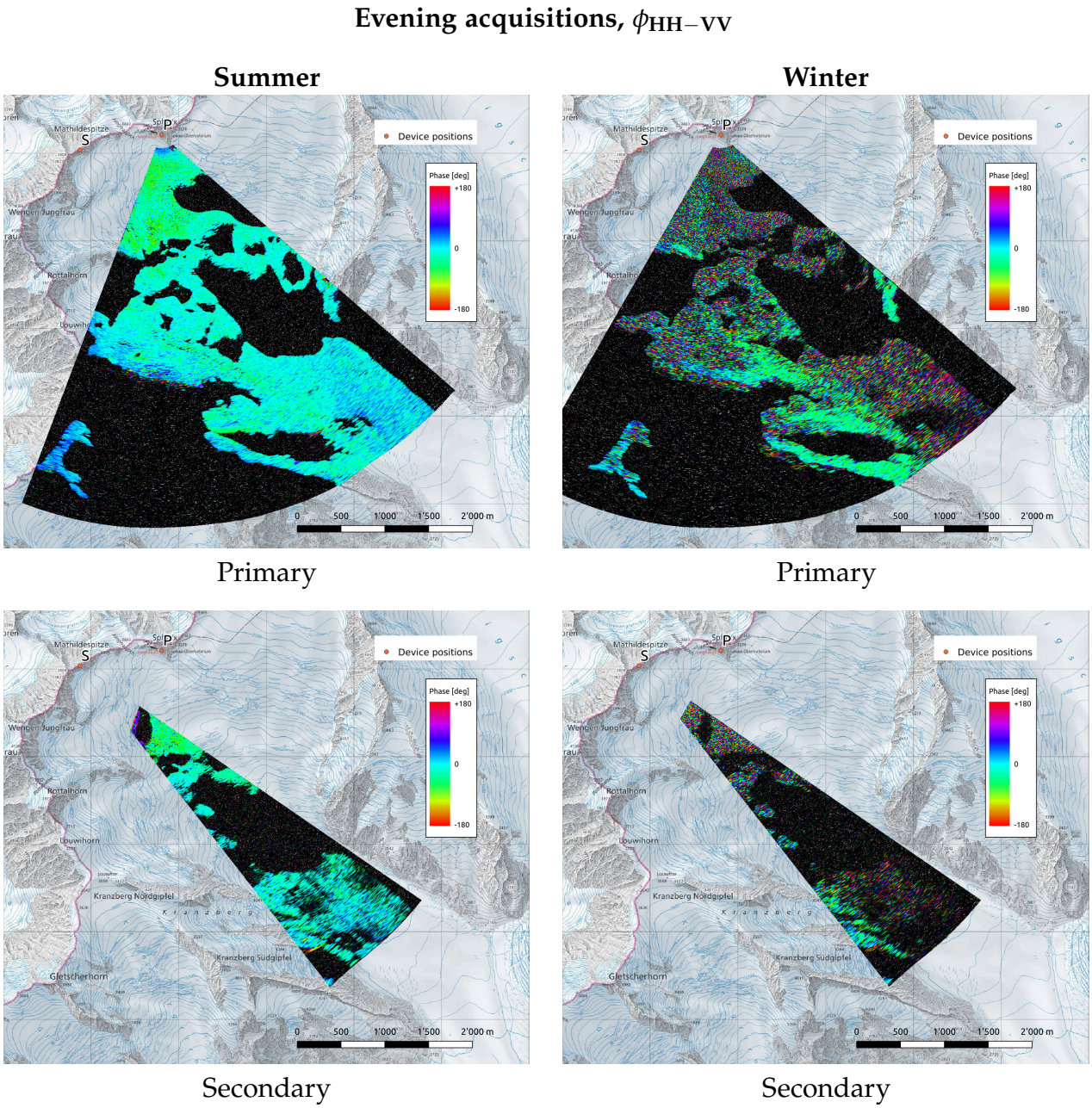

FIGURE 3.15: Comparison of the observed CPD for the summer (left) and winter (right) seasons, for the primary (top, monostatic) and the secondary (bottom, bistatic) dataset. The acquisitions were taken in the evening. In order to enhance the signal, 10 consecutive interferograms were coherently averaged. Compared to the morning acquisitions (Fig. 3.14), the phase gradient in summer has flattened and the values are closer to zero throughout the scene. In winter, the rapid spatial variation of CPD remains throughout the day.

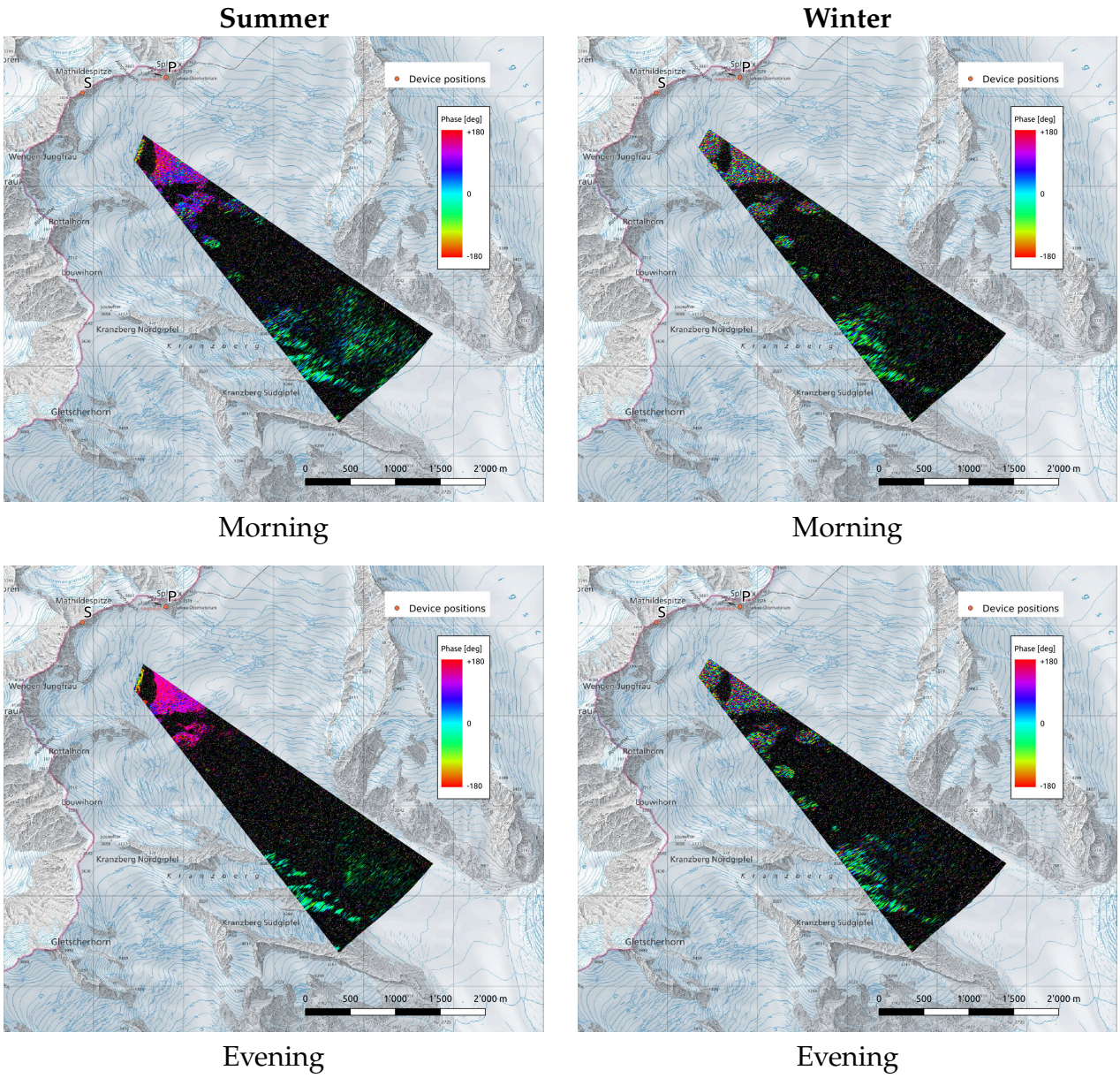

FIGURE 3.16: Comparison of the cross-polar phase difference (XPD) observed by the secondary (bistatic) device, for the summer (left) and winter (right) seasons, for morning (top and evening (bottom) acquisition time respectively. In order to enhance the signal, 10 consecutive interferograms were coherently averaged. For both seasons, the bistatic acquisitions show significant deviations from this zero value throughout the scene. In summer, in the near range at steeper incidence angles and large bistatic angle the XPD has a large value near 180°. With increasing range and incidence angle (and decreasing bistatic angle), this value appears to reduce towards zero, however precise interpretation is difficult due to low coverage of medium bistatic angles. In the evening, the bistatic XPD in summer has a smoother behaviour, however the strong deviation from the zero value remains. In winter, the XPD exhibits similar behaviour to CPD, varying rapidly on short spatial scales. Even with 10× coherent averaging, the bistatic dataset exhibits very low SNR in the far range.

3.4 DISCUSSION

3.4.1 *Polarimetric calibration and limitations of the dataset*

Polarimetric calibration in the large-angle bistatic regime, where neither the reciprocity principle nor corner reflectors can be used, is usually more challenging than monostatic calibration. The bistatic calibration in this experiment was performed with the VSPARC active calibrator, while the monostatic calibration was carried out using a combination of corner reflectors and the application of the reciprocity principle. Table 3.2 shows the residuals of the polarimetric calibration of the primary device, however these residuals are not available for the secondary device, since a second, independent validation target was not available. The observed data (e.g. bistatic alpha angle $\bar{\alpha}$) and a visual assessment of the Pauli basis scattering in Fig. 3.5 do suggest correctness of calibration, however this limited validation has to be kept in mind when interpreting bistatic data.

Due to the processing complexity of polarimetric KAPRI data and topographic phase correction, care has to be taken that the shown polarimetric phase difference values in Figs. 3.14 through 3.16 are not just an artifact of inaccurate phase compensation. There are several indications that the observed phase differences are real. Firstly, the shown XPD/CPD is relatively constant and no fringes – which are typically present when the topographic phase is incorrectly compensated – are observed. Secondly, the CPD observed in summer behaves similarly between the monostatic and bistatic dataset, starting with a strong offset in the morning and flattening in the evening. Finally, for the XPD, the VSPARC calibrator was placed near the Glacier head ROI in the summer acquisitions. It was set to the constant phase response configuration (described by [57, eq. (39e)]), and thus there was zero phase delay between VSPARC's signal in all polarimetric channels. Accordingly, in the bottom left map in Fig. 3.16 VSPARC can be seen as a point target exhibiting a zero XPD. There is thus a high degree of confidence that the XPD data in VSPARC's vicinity is correctly unwrapped and compensated. However, independent validation (preferably with a second cross-polarizing bistatic target placed in a second location) is desirable for future acquisitions to achieve certainty about the observed phase differences.

The combined monostatic/bistatic setup allows us to investigate the behaviour of observed polarimetric parameters as the bistatic angle changes from zero to a relatively high value of 50°. However, the geometry limitations do not allow sampling of a continuous β spectrum up to this maximal value. The sampling is instead limited only to the two ROIs within the bistatic beam (Glacier head and Glacier flow), with bistatic angle values of 40° and

10° respectively. Bistatic angles other than these values remain unavailable, and thus the behaviour cannot be easily generalized. Furthermore, the ground-based acquisition geometry also results in relatively shallow incidence angles of 75° and 80° in the two ROIs. The snow and rock face ROIs provide a relatively steep local incidence angle due to the mountainous geometry, however are for the same reason more susceptible to foreshortening effects.

3.4.2 *Temporal coherence*

The estimated glacier drift shown in Fig. 3.7 and Table 3.4 matches very well the results from previous investigations using TanDEM-X and in-situ GNSS data [21], which determined the median horizontal glacier velocity of $\sim 0.3\,\mathrm{m/day}$ in the Glacier top ROI, and $\sim 0.2\,\mathrm{m/day}$ in the Glacier body ROI. The same data also suggests that the drift rate is close to its yearly median value during both acquisition periods (early March, late August). This value justifies the decimation approach chosen in 3.2.6.1 which mitigates the influence of drift on the observed coherence.

The temporal decay of coherence shown in Fig. 3.8 indicates that coherence exhibits an exponential-like decay on the scale of hours during both seasons. In winter the major contributing factor is likely small microstructural variations which, even when small, have a considerable effect at short wavelengths. In summer, the "aged" snowpack can be possibly considered more stable in terms of microstructure, however the considerable and periodic changes in liquid water content contribute to rapid changes in scattering characteristics and thus cause decorrelation. Since the start time T_0 was chosen in the evening, the snowpack was refreezing during the coherence monitoring window, and thus there was no further loss of coherence due to reduction of SNR. However, the relatively low value of SNR can be a partial contributor to the low coherence estimate, especially in summer in the Glacier flow ROI, for which eq. 3.29 and SNR values from Fig. 3.6 predict an SNR coherence loss factor $\gamma_{\mathrm{SNR}} \approx 0.9$.

The characteristic decorrelation timescale (i.e. the timescale on which coherence reduces to $1/e \approx 0.36$) can be estimated as $4 - 8$ hours in summer, and $6 - 12$ hours in winter. This has strong implications for repeat-pass interferometric methods – applying repeat-pass interferometric methods with temporal baselines longer than a few hours may not be feasible due to almost complete decorrelation of the snowpack. Spaceborne SAR missions are particularly affected, since their revisit times usually have a value on scale of several days. Spaceborne Ku-band SAR missions might thus not be able to apply repeat-pass interferometric methods over snow-covered areas, unless steps are taken to reduce this

temporal baseline, through use of e.g. constellations. It is however possible that the expected decorrelation time temporarily increases during some times of the year, for example in spring once snow cover has settled but snow melt has not yet set in, or in autumn once the partially melted snow cover has completely refrozen but no fresh snow is yet present – further measurements are needed to confirm year-round validity of the observed decorrelation timescales.

It should be noted that in some experiments under different conditions and in different observation areas, the decorrelation time of snow cover at Ku-band was observed to be longer – for example, data in [53] shows sustained coherence between Ku-band tomograms of snow cover over baselines up to 14 hours.

3.4.3 *Second-order polarimetric parameters*

3.4.3.1 *Entropy*

The time series of entropy (Fig. 3.10) follows an expected trend in all datasets – the polarimetric entropy is high in winter and constant over time, which suggests a large diversity of scattering processes. In summer, the entropy is lower overall, and also exhibits a variation over the course of the day. This suggest that deterministic scattering processes, such as surface scattering, have a higher proportion, which is in agreement with the interpretation that melt-freeze crusts are present close to the surface in summer and cause a contribution of low-entropy surface scattering. Furthermore, the temporal variation indicates that entropy reduces further as snow melt sets in during daytime, which increases liquid water content and reduces penetration depth, resulting in even larger contribution of surface scattering to total observed backscatter. The only exception is the behaviour of "Glacier body" ROI in the bistatic dataset in summer, where the rise in entropy with increasing snow melt can be explained as loss of signal, i.e. the entropy is calculated mostly on noise, which has very high intrinsic entropy.

3.4.3.2 *Mean alpha angle*

The mean alpha angle $\bar{\alpha}$ (Fig. 3.12 exhibits behaviour very similar to entropy, and can be explained with the same interpretation. The value of $\bar{\alpha}$ between 40° and 60° is in agreement with dominance of volume scattering in winter. Lower values in summer suggest a larger contribution of surface scattering, and the temporal behaviour is in agreement with increasing contribution of surface scattering due to increased liquid water content, with the

"Glacier body" ROI in the secondary dataset once again exhibiting an exceptional increase due to loss of SNR.

3.4.3.3 *Fourth eigenvalue λ_4*

The fourth eigenvalue λ_4 of the coherency matrix T should have a zero value in the monostatic case due to the reciprocity principle. This is confirmed in Fig. 3.13 which shows that the estimate of the value of $\hat{\lambda}_4$ does not exceed 0.03, with the exception of the evening of the summer period, where noise becomes a considerable factor. The slightly higher estimates in winter can be caused by a higher diversity of cross-polarizing scattering processes which could "leak" into the fourth Pauli component and thus into the fourth eigenvalue. The effect in the monostatic dataset is however very limited and the absolute value remains low.

In the bistatic case, $\hat{\lambda}_4$ is higher overall – this can be due to several contributing factors. Firstly, the SNR is overall lower in the bistatic case, which could cause an increase in the estimate of $\hat{\lambda}_4$. However, the comparison of monostatic summer SNR in Glacier flow ROI with the bistatic SNR in Glacier head ROI indicates that the bistatic data should have sufficient SNR. The second contributing factor could be a higher diversity of cross-polarizing scattering processes, just like in the monostatic winter data. This however does not completely explain why the value is also high in summer, where cross-polarizing contributions are quite low. The third possible factor is miscalibration, which could cause a contribution in case the amplitudes or phases of cross-polarized channels are not precisely calibrated. This effect certainly can not be excluded, due to factors mentioned in Section 3.4.1. However, miscalibration likely is not the only factor, since the higher values of $\hat{\lambda}_4$ are detected in both seasons which were calibrated separately, and $\hat{\lambda}_4$ also exhibits a slight temporal trend in the Glacier head ROI, which indicates that it is caused by a true scattering signal. Furthermore, the XPD maps shown in Fig. 3.16 (and timeseries in supplementary Fig. S3.8) indicate that there are non-reciprocal scattering processes occurring in the scene, which will then result in non-zero value of the fourth Pauli component $k_{P_4} = \frac{j}{\sqrt{2}}(S_{HV} - S_{VH})$, and non-zero fourth eigenvalue of the T matrix. The non-zero value of $\hat{\lambda}_4$ is thus most likely caused by the same non-reciprocal processes that cause the non-zero cross-polarized phase difference, and the quantification of $\hat{\lambda}_4$ in Fig. 3.13 can be used as an estimate of the contribution of these processes to total backscatter.

3.4.4 *Polarimetric phase differences*

3.4.4.1 *Co-polar phase difference*

The co-polar phase difference $\phi_{\mathrm{HH-VV}}$ exhibits a similar behavior between monostatic and bistatic datasets. In summer, it exhibits an incidence angle dependence which varies with time of day. When the snow cover is frozen (i.e. in the morning), $\phi_{\mathrm{HH-VV}}$ has a strong negative value at low incidence angles (near-range), and trends towards a slight positive value at high incidence angles (far-range), for both the monostatic and the bistatic dataset. It is difficult to interpret the change of the sign of CPD between these two areas as an effect caused purely by birefringence, since it would require a large change in the snow cover's structure and anisotropy between the two observed regions. An alternative interpretation of the change of the sign of CPD could be a change in the relative contribution of dihedral (double-bounce) scattering between the two geometries, where the contribution is larger at lower local incidence angles (i.e. near range). Fig. 3.5, acquired in the morning, shows a more dominant red color in the near-range region in summer, indicating a higher contribution of dihedral scattering. Dihedral scattering contribution has opposing effects on phases of the HH and VV channels (increasing the phase of one and decreasing the phase of the other, all else being equal), and thus could cause a sign flip of $\phi_{\mathrm{HH-VV}}$ if the relative contribution of double-bounce scattering to total backscatter changes.

This observed spatial trend of $\phi_{\mathrm{HH-VV}}$ in summer can be compared with literature. The incidence angle dependence has the opposite trend to values observed at X-band in Greenland [31, Figures 3-5] and L-band in Svalbard [75, Figures 8-9], where the $\phi_{\mathrm{HH-VV}}$ phase difference showed divergence from the zero value with increasing range. In SnowScat observations of fresh snow at Ku-band [11, Figure 6] (note that the values in the referenced figure show $\phi_{\mathrm{VV-HH}}$), the $\phi_{\mathrm{HH-VV}}$ value was observed to be increasingly negative with increasing incidence angle, also a trend opposite to our observations. It should be noted however that the snow and observation conditions in these mentioned publications greatly differed from the setup and conditions of our observations, since our observations in summer were observing aged seasonal snow cover which has repeatedly melted and refrozen over the course of the preceding season. Determination of the precise cause of the observed CPD behaviour remains an open question which certainly warrants further quantitative analysis.

Temporally, the summer CPD observations show that as liquid water content increases throughout the day, for all ROIs the phase difference tends towards zero. This is in agreement with the interpretation that liquid water reduces penetration and thus the scattering behavior becomes more surface-like. Afterwards, over night when the snow cover refreezes, the CPD

recovers towards its original value. A similar trend was observed in melting and refreezing snow at 95 GHz in [72, Figure 7], where the accumulation of fresh snow cover observed under a 60° incidence angle caused a strong negative value of $\phi_{\mathrm{HH-VV}}$ which quickly reverted towards zero once the snow cover started melting.

In winter, a rapid variation of the CPD is observed, which can be attributed to a high contribution of volume scattering, together with a range cell size orders of magnitude larger than the wavelength, causing the positions of the HH and VV phase centers to vary on scales longer than the wavelength. Only the exposed rock face maintains the zero value of CPD, as expected for surface-type scattering. This has implications for scattering models which might aim to invert the CPD for estimates of structural anisotropy or depth – this approach is often applied at longer wavelengths. However, due to the short Ku-band wavelength, even small values and variations of anisotropy or relatively short depths can cause sufficient phase delay between the two polarizations so as to cause phase-wrapping. We confirmed this by an exploratory analysis of the model presented in [13] which relates the CPD to snow grain shape anisotropy – it has shown that at the Ku-band, with a density fraction value of 0.3 and snow depth of 3 m even small variation of any input model parameter causes rapid CPD change and phase wrapping. This is corroborated by the observed winter data which shows rapid variation of CPD even in areas which otherwise appear uniform both visually and in terms of observed backscatter intensity. This variation and phase wrapping makes simple parameter inversion challenging since there is no bijective function between CPD and model parameter values.

However, while the CPD in winter might appear to behave like noise spatially, it remains temporally stable for any particular point on scales of minutes to hours. Thus, by monitoring the CPD with a sufficient temporal resolution, one can monitor this CPD evolution and possibly derive information about the temporal influence of parameters that affect the CPD, such as redistribution and settling of snowpack. This temporal evolution could be particularly interesting to observe just after fresh snowfall – this did unfortunately not occur during our observation windows, but is an observation scenario of interest for future investigations.

3.4.4.2 *Cross-polar phase difference*

The cross-polar phase difference $\phi_{\mathrm{HV-VH}}$ confirms the validity of the reciprocity principle ($S_{\mathrm{HV}} = S_{\mathrm{VH}}$), as all monostatic datasets (supplementary Fig. S3.9) exhibit a zero value of $\phi_{\mathrm{HV-VH}}$, regardless of the scattering medium. However it exhibits a very interesting behaviour in the bistatic datasets (Fig. 3.16). In winter, it varies rapidly on short spatial

scales, similarly to the cross-polar phase difference. This can also be interpreted as a large contribution of volume scattering which causes a large variation of the HV and VH phase center positions.

In summer, a large positive value of $\phi_{\mathrm{HV-VH}}$ (approx. $+150°$) is observed in the Glacier head ROI. This value appears to further increase with increase of liquid water content due to snowmelt. In the far range (and low bistatic angles), the XPD appears to trend toward the zero value, however the SNR is relatively weak due to the long range, use of low gain antennas, and absorption by liquid water.

One interpretation of the non-zero XPD value can be proposed as a combination of snow birefringence (which also causes the CPD) and a geometric effect caused by the difference between local incidence angles of the transmission and reception legs of the scattered signal (i.e., a different local incidence angle from the point of view of the primary and of the secondary device). This can cause a different phase delay contribution of the two journey segments (the primary-to-scatterer segment and the scatterer-to-secondary segment), which thus do not cancel each other out between the HV and VH channels as they would when monostatic observations are made – Fig. 3.17 visualizes this interpretation. To the best of our knowledge, there are no similar observations of snow cover at large bistatic angles at radio frequencies available in literature to date, and thus no comparisons with results from other observations can be made. The definitive identification of the mechanism causing the non-zero XPD value remains an open question which certainly invites further investigation.

Regardless of the cause, both the summer and the winter observations show that non-reciprocal backscatter does occur in snow cover at non-zero bistatic angles, and thus care has to be taken not to automatically assume reciprocity during calibration/analysis of bistatic radar backscatter over snow-covered regions.

3.5 CONCLUSION

In this publication we presented the first application of a long-baseline bistatic KAPRI radar setup to monitoring of natural environments. To the best of our knowledge, this dataset, acquired on top of the Jungfraufirn region of the Great Aletsch Glacier, provides the first polarimetric characterization of Ku-band backscatter from snow-covered areas at non-negligible bistatic angles on range scales of kilometers. The observations revealed high variability of polarimetric properties of backscatter from the observed snow cover between the late summer and late winter seasons, and in some cases also variability between the monostatic and bistatic backscatter, as well as temporal variability in summer.

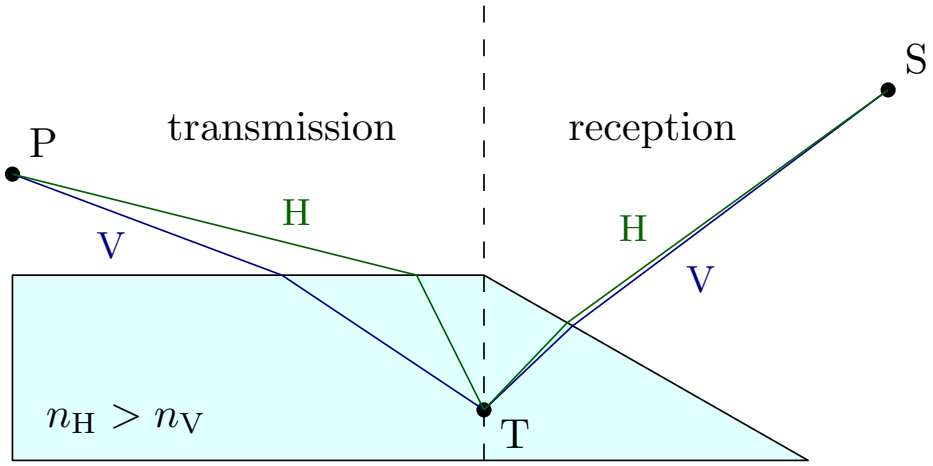

FIGURE 3.17: Possible interpretation of non-zero ϕ_{HV-VH} value caused by combination of birefringence of the snow pack (i.e. difference in refractive indices n_H and n_V) and difference in incidence angles of the transmission and reception legs of the signal's path. The transmission leg causes a significant difference between the phase delays of the H- and V- polarized waves. The reception leg then causes a much smaller difference in the opposite direction, thus the combined VH pathway accumulates a longer phase delay than the HV pathway, resulting in positive value of ϕ_{HV-VH}. In the monostatic case (where both transmission and reception paths occur on the left side of this diagram), the phase differential accumulated during the transmission leg is cancelled out by the reversed differential during the reception leg.

We observed that temporal decorrelation of snow cover in the observed area at Ku-band occurs on timescales of hours, with coherence reducing to $1/e$ within time ranging between 4 and 12 hours. While this value might be different in other times of year and areas, the timescale of hours provides an order-of-magnitude estimate of the upper limit on the revisit time of repeat-pass methods such as differential interferometry or SAR tomography. The limit on the scale of hours (or lower tens of hours) will make using these methods with spaceborne Ku-band systems extremely challenging, since spaceborne systems usually have revisit times on the order of days.

The second-order polarimetric parameters, the entropy H and mean alpha angle $\bar{\alpha}$ exhibit an expected trend of a lower value in summer when the snow cover has aged and liquid water content causes dominance of surface scattering, and a higher value in winter when fresh snow allows deep penetration and occurrence of a higher diversity of scattering processes.

The polarization phase differences ϕ_{HH-VV} and ϕ_{HV-VH} show a very interesting behavior, both between the two seasons, and between monostatic and bistatic acquisitions. The CPD in winter varies rapidly on short spatial scales, which confirms that CPD-based inversion methods are challenging to apply at Ku-band due to the phase-wrapping tendency when observing snow layers thicker than several tens of centimeters. In summer, it exhibits a smooth incidence-angle-dependent trend, and its value also exhibits an intra-day cycle,

which can likely be attributed to changes in liquid water content of the snow cover. The cross-polar phase difference exhibits an expected zero value in all monostatic datasets, however in the bistatic datasets there is a substantial deviation from this zero value. This indicates the presence of non-reciprocal scattering behaviours at non-zero bistatic angles in snow, which has implications both for snow modeling using bistatic data, as well as polarimetric calibration procedures which can no longer rely on the reciprocity principle.

Besides the above-mentioned information about behaviour of polarimetric parameters at Ku-band, lessons learned from the two observation campaigns also suggest attractive future observation targets, such as the observation of the minute-scale temporal behaviour of polarization phase differences during and immediately after fresh snowfall, as well as long-term monitoring of the transition from fresh winter snow to refrozen summer snow. The presented data can also already serve as a reference overview for polarimetric Ku-band scattering behaviour of snow under a variety of conditions, which can aid planning and development of airborne and spaceborne missions operating at similar wavelengths.

ACKNOWLEDGMENTS

We acknowledge that the International Foundation High Altitude Research Stations Jungfraujoch and Gornergrat (HFSJG), 3012 Bern, Switzerland, made it possible for us to carry out our experiments at the High Altitude Research Station at Jungfraujoch. We thank the custodians Daniela Bissig, Erich Furrer, and Christine and Ruedi Käser for the support of our activities.

We would also like to thank Michael Arnold, Jorit Schmelzle, and Pol Villalvilla for their invaluable support during campaigns, and Silvan Leinss and Charles Werner for their technical support regarding radar operation.

Map underlay: Landeskarte 1:25000, © Federal Office of Topography swisstopo.

REFERENCES

1. Nolin, A. W. Recent advances in remote sensing of seasonal snow. *Journal of Glaciology* **56**, 1141. doi:10.3189/002214311796406077 (2010).
2. King, J., Kelly, R., Kasurak, A., Duguay, C., Gunn, G., Rutter, N., Watts, T. & Derksen, C. Spatio-temporal influence of tundra snow properties on Ku-band (17.2 GHz) backscatter. *Journal of Glaciology* **61**, 267. doi:10.3189/2015JoG14J020 (2015).

3. Lemmetyinen, J., Kontu, A., Pulliainen, J., Vehviläinen, J., Rautiainen, K., Wiesmann, A., Mätzler, C., Werner, C., Rott, H., Nagler, T., Schneebeli, M., Proksch, M., Schüttemeyer, D., Kern, M. & Davidson, M. W. J. Nordic Snow Radar Experiment. *Geoscientific Instrumentation, Methods and Data Systems* **5**, 403. doi:10.5194/gi-5-403-2016 (2016).

4. Tsang, L., Durand, M., Derksen, C., Barros, A. P., Kang, D.-H., Lievens, H., Marshall, H.-P., Zhu, J., Johnson, J., King, J., Lemmetyinen, J., Sandells, M., Rutter, N., Siqueira, P., Nolin, A., Osmanoglu, B., Vuyovich, C., Kim, E. J., Taylor, D., Merkouriadi, I., Brucker, L., Navari, M., Dumont, M., Kelly, R., Kim, R. S., Liao, T.-H. & Xu, X. Review Article: Global Monitoring of Snow Water Equivalent using High Frequency Radar Remote Sensing. *The Cryosphere Discussions* **2021**, 1. doi:10.5194/tc-2021-295 (2021).

5. Thompson, A., Kelly, R. & King, J. Sensitivity of Ku- and X-Band Radar Observations to Seasonal Snow in Ontario, Canada. *Canadian Journal of Remote Sensing* **45**, 829. doi:10.1080/07038992.2019.1704621 (2019).

6. Shi, J. & Dozier, J. Mapping seasonal snow with SIR-C/X-SAR in mountainous areas. *Remote Sensing of Environment* **59**, 294. doi:https://doi.org/10.1016/S0034-4257(96)00146-0 (1997).

7. Rutter, N., Sandells, M. J., Derksen, C., King, J., Toose, P., Wake, L., Watts, T., Essery, R., Roy, A., Royer, A., Marsh, P., Larsen, C. & Sturm, M. Effect of snow microstructure variability on Ku-band radar snow water equivalent retrievals. *The Cryosphere* **13**, 3045. doi:10.5194/tc-13-3045-2019 (2019).

8. Derksen, C., Lemmetyinen, J., King, J., Belair, S., Garnaud, C., Lapointe, M., Crevier, Y., Burbidge, G. & Siqueira, P. *A Dual-Frequency Ku-Band Radar Mission Concept for Seasonal Snow* in *IGARSS 2019 - 2019 IEEE International Geoscience and Remote Sensing Symposium* (2019), 5742. doi:10.1109/IGARSS.2019.8898030.

9. Wiesmann, A., Mätzler, C. & Weise, T. Radiometric and structural measurements of snow samples. *Radio Science* **33**, 273. doi:10.1029/97RS02746 (1998).

10. Lemmetyinen, J., Derksen, C., Toose, P., Proksch, M., Pulliainen, J., Kontu, A., Rautiainen, K., Seppänen, J. & Hallikainen, M. Simulating seasonally and spatially varying snow cover brightness temperature using HUT snow emission model and retrieval of a microwave effective grain size. *Remote Sensing of Environment* **156**, 71. doi:https://doi.org/10.1016/j.rse.2014.09.016 (2015).

11. Leinss, S., Löwe, H., Proksch, M., Lemmetyinen, J., Wiesmann, A. & Hajnsek, I. Anisotropy of seasonal snow measured by polarimetric phase differences in radar time series. *Cryosphere* **10**, 1771. doi:10.5194/tc-10-1771-2016 (2016).

12. Rathmann, N. M., Lilien, D. A., Grinsted, A., Gerber, T. A., Young, T. J. & Dahl-Jensen, D. On the limitations of using polarimetric radar sounding to infer the crystal orientation fabric of ice masses. *Geophysical Research Letters*. doi:10.1029/2021gl096244 (2021).

13. Parrella, G., Hajnsek, I. & Papathanassiou, K. P. Retrieval of Firn Thickness by Means of Polarisation Phase Differences in L-Band SAR Data. *Remote Sensing* **13**. doi:10.3390/rs13214448 (2021).

14. Rott, H., Cline, D. W., Duguay, C., Essery, R., Etchevers, P., Hajnsek, I., Kern, M., Macelloni, G., Malnes, E., Pulliainen, J., *et al. CoReH2O, a dual frequency radar mission for snow and ice observations* in *2012 IEEE International Geoscience and Remote Sensing Symposium* (2012), 5550. doi:10.1109/IGARSS.2012.6352348.

15. National Research Council. *Earth Science and Applications from Space: National Imperatives for the Next Decade and Beyond* doi:10.17226/11820 (The National Academies Press, Washington, DC, 2007).

16. Derksen, C., King, J., Belair, S., Garnaud, C., Vionnet, V., Fortin, V., Lemmetyinen, J., Crevier, Y., Plourde, P., Lawrence, B., van Mierlo, H., Burbidge, G. & Siqueira, P. *Development of the Terrestrial Snow Mass Mission* in *2021 IEEE International Geoscience and Remote Sensing Symposium IGARSS* (2021), 614. doi:10.1109/IGARSS47720.2021.9553496.

17. Lee, J.-S. & Pottier, E. *Polarimetric radar imaging: from basics to applications* (CRC press, 2009).

18. Germond, A.-L., Pottier, E. & Saillard, J. *Foundations of bistatic radar polarimetry theory* in *Radar 97 (Conf. Publ. No. 449)* (1997), 833.

19. Krieger, G., Moreira, A., Fiedler, H., Hajnsek, I., Werner, M., Younis, M. & Zink, M. TanDEM-X: A satellite formation for high-resolution SAR interferometry. *IEEE Transactions on Geoscience and Remote Sensing* **45**, 3317. doi:10.1109/TGRS.2007.900693 (2007).

20. Rizzoli, P., Martone, M., Rott, H. & Moreira, A. Characterization of Snow Facies on the Greenland Ice Sheet Observed by TanDEM-X Interferometric SAR Data. *Remote Sensing* **9**. doi:10.3390/rs9040315 (2017).

21. Leinss, S. & Bernhard, P. TanDEM-X:Deriving InSAR Height Changes and Velocity Dynamics of Great Aletsch Glacier. *IEEE Journal of Selected Topics in Applied Earth Observations and Remote Sensing* **14**, 4798. doi:10.1109/JSTARS.2021.3078084 (2021).

22. Stefko, M., Leinss, S., Frey, O. & Hajnsek, I. Coherent backscatter enhancement in bistatic Ku- and X-band radar observations of dry snow. *Cryosphere* **16**, 2859. doi:10.5194/tc-16-2859-2022 (2022).

23. Lopez-Dekker, P., Rott, H., Prats-Iraola, P., Chapron, B., Scipal, K. & Witte, E. D. *Harmony: an Earth Explorer 10 Mission Candidate to Observe Land, Ice, and Ocean Surface Dynamics* in *IGARSS 2019 - 2019 IEEE International Geoscience and Remote Sensing Symposium* (IEEE, 2019), 8381. doi:10.1109/IGARSS.2019.8897983.

24. Moccia, A., Rufino, G., D'Errico, M., Alberti, G. & Salzillo, G. *BISSAT: A bistatic SAR for earth observation* in *International Geoscience and Remote Sensing Symposium (IGARSS)* **5** (IEEE, 2002), 2628. doi:10.1109/igarss.2002.1026723.

25. Massonnet, D. The interferometric cartwheel: A constellation of passive satellites to produce radar images to be coherently combined. *International Journal of Remote Sensing* **22**, 2413. doi:10.1080/01431160118952 (2001).

26. Zebker, H. A., Farr, T. G., Salazar, R. P. & Dixon, T. H. Mapping the World's Topography Using Radar Interferometry: The TOPSAT Mission. *Proceedings of the IEEE* **82**, 1774. doi:10.1109/5.338070 (1994).

27. Gebert, N., Carnicero Dominguez, B., Davidson, M. W. J., Diaz Martin, M. & Silvestrin, P. *SAOCOM-CS - A passive companion to SAOCOM for single-pass L-band SAR interferometry* in *EUSAR 2014; 10th European Conference on Synthetic Aperture Radar* (2014), 1.

28. Tan, S., Chang, W., Tsang, L., Lemmetyinen, J. & Proksch, M. Modeling Both Active and Passive Microwave Remote Sensing of Snow Using Dense Media Radiative Transfer (DMRT) Theory with Multiple Scattering and Backscattering Enhancement. *IEEE Journal of Selected Topics in Applied Earth Observations and Remote Sensing* **8**, 4418. doi:10.1109/JSTARS.2015.2469290 (2015).

29. Wiesmann, A. & Mätzler, C. Microwave emission model of layered snowpacks. *Remote sensing of environment* **70**, 307. doi:10.1016/S0034-4257(99)00046-2 (1999).

30. Rees, A., Lemmetyinen, J., Derksen, C., Pulliainen, J. & English, M. Observed and modelled effects of ice lens formation on passive microwave brightness temperatures over snow covered tundra. *Remote Sensing of Environment* **114**, 116. doi:10.1016/j.rse.2009.08.013 (2010).

31. Parrella, G., Hajnsek, I. & Papathanassiou, K. P. Model-Based Interpretation of PolSAR Data for the Characterization of Glacier Zones in Greenland. *IEEE Journal of Selected Topics in Applied Earth Observations and Remote Sensing* **14**, 11593. doi:10.1109/JSTARS.2021.3126069 (2021).

32. Wiesmann, A., Werner, C., Strozzi, T., Mätzler, C., Nagler, T., Rott, H., Schneebeli, M. & Wegmuller, U. *SnowScat, X-to Ku-band scatterometer development* in *ESA Living Planet Symposium* **686** (2010), 160.

33. Tsai, Y. L. S., Dietz, A., Oppelt, N. & Kuenzer, C. Remote sensing of snow cover using spaceborne SAR: A review. *Remote Sensing* **11**. doi:10.3390/rs11121456 (2019).

34. Snehmani, Singh, M. K., Gupta, R. D., Bhardwaj, A. & Joshi, P. K. Remote sensing of mountain snow using active microwave sensors: a review. *Geocarto International* **30**, 1. doi:10.1080/10106049.2014.883434 (2015).

35. Awasthi, S. & Varade, D. Recent advances in the remote sensing of alpine snow: a review. *GIScience & Remote Sensing* **58**, 852. doi:10.1080/15481603.2021.1946938 (2021).

36. Dietz, A. J., Kuenzer, C., Gessner, U. & Dech, S. Remote sensing of snow – a review of available methods. *International Journal of Remote Sensing* **33**, 4094. doi:10.1080/01431161.2011.640964 (2012).

37. Mätzler, C. Applications of the interaction of microwaves with the natural snow cover. *Remote Sensing Reviews* **2**, 259. doi:10.1080/02757258709532086 (1987).

38. Frey, O., Werner, C. L., Caduff, R. & Wiesmann, A. *Tomographic Profiling with Snowscat Within the ESA Snowlab Campaign: Time Series of Snow Profiles Over three Snow Seasons* in *IGARSS 2018 - 2018 IEEE International Geoscience and Remote Sensing Symposium* (IEEE, 2018), 6512. doi:10.1109/IGARSS.2018.8517692.

39. Everaere, E. *Polarimetry in bistatic configuration for ultra high frequency radar measurements on forest environment* PhD thesis (Ecole Polytechnique, 2015).

40. Cloude, S. *Polarisation: Applications in Remote Sensing* doi:10.1093/acprof:oso/9780199569731.001.0001 (Oxford University Press, 2009).

41. Leinss, S., Wiesmann, A., Lemmetyinen, J. & Hajnsek, I. Snow Water Equivalent of Dry Snow Measured by Differential Interferometry. *IEEE Journal of Selected Topics in Applied Earth Observations and Remote Sensing* **8**, 3773. doi:10.1109/JSTARS.2015.2432031 (2015).

42. Zebker, H. A., Villasenor, J., *et al.* Decorrelation in interferometric radar echoes. *IEEE Transactions on geoscience and remote sensing* **30**, 950. doi:10.1109/36.175330 (1992).

43. Hawley, R. L., Morris, E. M., Cullen, R., Nixdorf, U., Shepherd, A. P. & Wingham, D. J. ASIRAS airborne radar resolves internal annual layers in the dry-snow zone of Greenland. *Geophysical Research Letters* **33**. doi:https://doi.org/10.1029/2005GL025147 (2006).

44. Yueh, S., Cline, D. & Elder, K. Airborne Ku-band radar remote sensing of terrestrial snow cover. *International Geoscience and Remote Sensing Symposium (IGARSS)* **47**, 1211. doi:10.1109/IGARSS.2007.4423023 (2007).

45. Coccia, A., Trampuz, C., Ortolani, M., Turtolo, R., Wieffering, T. & Meta, A. *Deployment of the SnowSAR sensor in the SnowEx campaign by NASA and preliminary results* in *2017 IEEE International Geoscience and Remote Sensing Symposium (IGARSS)* (2017), 1403. doi:10.1109/IGARSS.2017.8127227.

46. Cantalloube, H. M.-J. *Imaging of Snow/Ice Subsurface Features from Airborne Sar At UHF, L And X Band. The Onera Sar Campaign in South Greenland* in *IGARSS 2019 - 2019 IEEE International Geoscience and Remote Sensing Symposium* (2019), 4157. doi:10.1109/IGARSS.2019.8898600.

47. Osmanoglu, B., Rincon, R., Bonds, Q., Racette, P., Brucker, L. & Perrine, M. *SWESARR: Snow Water Equivalent Radar and Radiometer* in *AGU Fall Meeting Abstracts* **2018** (2018), C13D.

48. Lemmetyinen, J., Cohen, J., Kontu, A., Vehviläinen, J., Hannula, H.-R., Merkouriadi, I., Scheiblauer, S., Rott, H., Nagler, T., Ripper, E., Elder, K., Marshall, H.-P., Fromm, R., Adams, M., Derksen, C., King, J., Meta, A., Coccia, A., Rutter, N., Sandells, M., Macelloni, G., Santi, E., Leduc-Leballeur, M., Essery, R., Menard, C. & Kern, M. Airborne SnowSAR data at X- and Ku- bands over boreal forest, alpine and tundra snow cover. *Earth System Science Data Discussions* **2021**, 1. doi:10.5194/essd-2021-239 (2021).

49. King, J. M. L., Kelly, R., Kasurak, A., Duguay, C., Gunn, G. & Mead, J. B. UW-Scat: A Ground-Based Dual-Frequency Scatterometer for Observation of Snow Properties. *IEEE Geoscience and Remote Sensing Letters* **10**, 528. doi:10.1109/LGRS.2012.2212177 (2013).

50. Xu, X., Baldi, C. A., De Bleser, J.-W., Lei, Y., Yueh, S. & Esteban-Fernandez, D. *Multi-Frequency Tomography Radar Observations of Snow Stratigraphy at Fraser During SnowEx* in *IGARSS 2018 - 2018 IEEE International Geoscience and Remote Sensing Symposium* (2018), 6269. doi:10.1109/IGARSS.2018.8519538.

51. Xu, X., Shen, H., Xu, H. & Tsang, L. *Modeling Multi-Frequency Tomograms for Snow Stratigraphy* in *IGARSS 2020 - 2020 IEEE International Geoscience and Remote Sensing Symposium* (2020), 3436. doi:10.1109/IGARSS39084.2020.9324184.

52. Lei, Y., Xu, X., Baldi, C. A., De Bleser, J.-W., Yueh, S. H., Esteban-Fernandez, D., Elder, K., Starr, B. & Siqueira, P. Dry Snow Parameter Retrieval With Ground-Based Single-Pass Synthetic Aperture Radar Interferometry. *IEEE Transactions on Geoscience and Remote Sensing* **60**, 1. doi:10.1109/TGRS.2022.3171269 (2022).

53. Frey, O., Werner, C. L., Caduff, R. & Wiesmann, A. *A time series of tomographic profiles of a snow pack measured with SnowScat at X-/Ku-band* in *2016 IEEE International Geoscience and Remote Sensing Symposium (IGARSS)* (IEEE, 2016), 17. doi:10.1109/IGARSS.2016.7728995.

54. Frey, O., Werner, C. L., Caduff, R. & Wiesmann, A. *Inversion of SNOW structure parameters from time series of tomographic measurements with SnowScat* in *2017 IEEE International Geoscience and Remote Sensing Symposium (IGARSS)* (IEEE, 2017), 2472. doi:10.1109/IGARSS.2017.8127494.

55. Werner, C., Frey, O., Naderpour, R., Wiesmann, A., Suess, M. & Wegmüller, U. *Aperture Synthesis and Calibration of the WBSCAT Ground-Based Scatterometer* in *2021 IEEE International Geoscience and Remote Sensing Symposium IGARSS* (2021), 1947. doi:10.1109/IGARSS47720.2021.9554592.

56. Wiesmann, A., Caduff, R., Werner, C., Frey, O., Schneebeli, M., Löwe, H., Jaggi, M., Schwank, M., Naderpour, R. & Fehr, T. *ESA SnowLab Project: 4 Years Of Wide Band Scatterometer Measurements Of Seasonal Snow* in *IGARSS 2019 - 2019 IEEE International Geoscience and Remote Sensing Symposium* (2019), 5745. doi:10.1109/IGARSS.2019.8898961.

57. Stefko, M., Frey, O., Werner, C. & Hajnsek, I. Calibration and Operation of a Bistatic Real-Aperture Polarimetric-Interferometric Ku-Band Radar. *IEEE Transactions on Geoscience and Remote Sensing* **60**, 1. doi:10.1109/TGRS.2021.3121466 (2022).

58. Werner, C., Wiesmann, A., Strozzi, T., Kos, A., Caduff, R. & Wegmiüler, U. *The GPRI multi-mode differential interferometric radar for ground-based observations* in *EUSAR 2012; 9th European Conference on Synthetic Aperture Radar* (2012), 304.

59. Caduff, R., Kos, A., Schlunegger, F., McArdell, B. W. & Wiesmann, A. Terrestrial radar interferometric measurement of hillslope deformation and atmospheric disturbances in the Illgraben debris-flow catchment, Switzerland. *IEEE Geoscience and Remote Sensing Letters* **11**, 434. doi:10.1109/LGRS.2013.2264564 (2014).

60. Strozzi, T., Werner, C., Wiesmann, A. & Wegmuller, U. Topography mapping with a portable real-aperture radar interferometer. *IEEE Geoscience and Remote Sensing Letters* **9**, 277. doi:10.1109/LGRS.2011.2166751 (2011).

61. Wiesmann, A., Caduff, R. & Mätzler, C. Terrestrial radar observations of dynamic changes in alpine snow. *IEEE Journal of Selected Topics in Applied Earth Observations and Remote Sensing* **8**, 3665. doi:10.1109/JSTARS.2015.2400972 (2015).

62. Baffelli, S., Frey, O. & Hajnsek, I. Geostatistical Analysis and Mitigation of the Atmospheric Phase Screens in Ku-Band Terrestrial Radar Interferometric Observations of an Alpine Glacier. *IEEE Transactions on Geoscience and Remote Sensing* **58**, 7533. doi:10.1109/TGRS.2020.2976656 (2020).

63. Izumi, Y., Frey, O., Baffelli, S., Hajnsek, I. & Sato, M. Efficient Approach for Atmospheric Phase Screen Mitigation in Time Series of Terrestrial Radar Interferometry Data Applied to Measure Glacier Velocity. *IEEE Journal of Selected Topics in Applied Earth Observations and Remote Sensing* **14**, 7734. doi:10.1109/JSTARS.2021.3099873 (2021).

64. Baffelli, S., Frey, O. & Hajnsek, I. Polarimetric Analysis of Natural Terrain Observed With a Ku -Band Terrestrial Radar. *IEEE Journal of Selected Topics in Applied Earth Observations and Remote Sensing* **12**, 5268. doi:10.1109/JSTARS.2019.2953206 (2019).

65. Willis, N. J. *Bistatic Radar* (eds Willis & Griffiths) doi:10.1049/SBRA003E (Institution of Engineering and Technology, 2005).

66. Pflughoeft, D. *Rotating body from spherical coordinates* https://stackoverflow.com/a/5279478.

67. Baffelli, S., Frey, O., Werner, C. & Hajnsek, I. Polarimetric Calibration of the Ku-Band Advanced Polarimetric Radar Interferometer. *IEEE Transactions on Geoscience and Remote Sensing* **56**, 2295. doi:10.1109/TGRS.2017.2778049 (4 2018).

68. Just, D. & Bamler, R. Phase statistics of interferograms with applications to synthetic aperture radar. *Applied Optics* **33**, 4361. doi:10.1364/AO.33.004361 (1994).

69. Ku, H. H. *et al.* Notes on the use of propagation of error formulas. *Journal of Research of the National Bureau of Standards* **70**, 263 (1966).

70. Hajnsek, I., Papathanassiou, K. P. & Cloude, S. R. *Removal of additive noise in polarimetric eigenvalue processing* in *IGARSS 2001. Scanning the Present and Resolving the Future. Proceedings. IEEE 2001 International Geoscience and Remote Sensing Symposium (Cat. No.01CH37217)* **6** (2001), 2778. doi:10.1109/IGARSS.2001.978160.

71. Rignot, E. J. Backscatter model for the unusual radar properties of the Greenland ice sheet. *Journal of Geophysical Research* **100**, 9389. doi:10.1029/95JE00485 (1995).

72. Chang, P., Mead, J., Knapp, E., Sadowy, G., Davis, R. & McIntosh, R. Polarimetric backscatter from fresh and metamorphic snowcover at millimeter wavelengths. *IEEE Transactions on Antennas and Propagation* **44**, 58. doi:10.1109/8.477529 (1996).

73. Leinss, S., Parrella, G. & Hajnsek, I. Snow height determination by polarimetric phase differences in X-Band SAR Data. *IEEE Journal of Selected Topics in Applied Earth Observations and Remote Sensing* **7**, 3794. doi:10.1109/JSTARS.2014.2323199 (2014).

74. Belinska, K., Fischer, G., Nagler, T. & Hajnsek, I. Snow Water Equivalent Estimation Using Differential SAR Interferometry and Co-Polar Phase Differences from Airborne SAR Data. *International Geoscience and Remote Sensing Symposium (IGARSS)* **2022-July**, 4545. doi:10.1109/IGARSS46834.2022.9883110 (2022).

75. Parrella, G., Hajnsek, I. & Papathanassiou, K. P. Polarimetric decomposition of L-Band PolSAR backscattering over the austfonna ice cap. *IEEE Transactions on Geoscience and Remote Sensing* **54**, 1267. doi:10.1109/TGRS.2015.2477168 (2016).

SUPPLEMENT

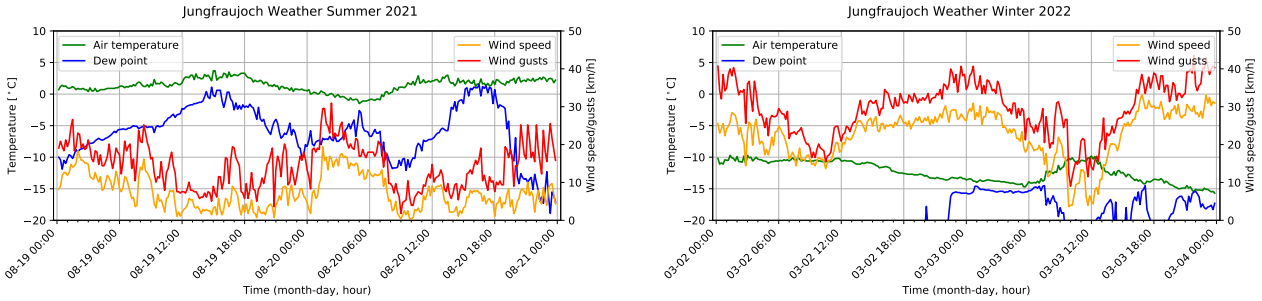

FIGURE S3.1: Weather station data from the Jungfraujoch automated weather station for the periods covered by radar observations. In summer (left) the temperature was close to zero degrees Celsius. This caused snowmelt to occur during daily sunshine periods, with refreezing at night. In winter (right), the temperature was well below zero degrees, preventing any snow melt. No precipitation occurred during the observation periods. Data source: MeteoSwiss, station JUN, WIGOS Identifier 0-20000-0-06730.

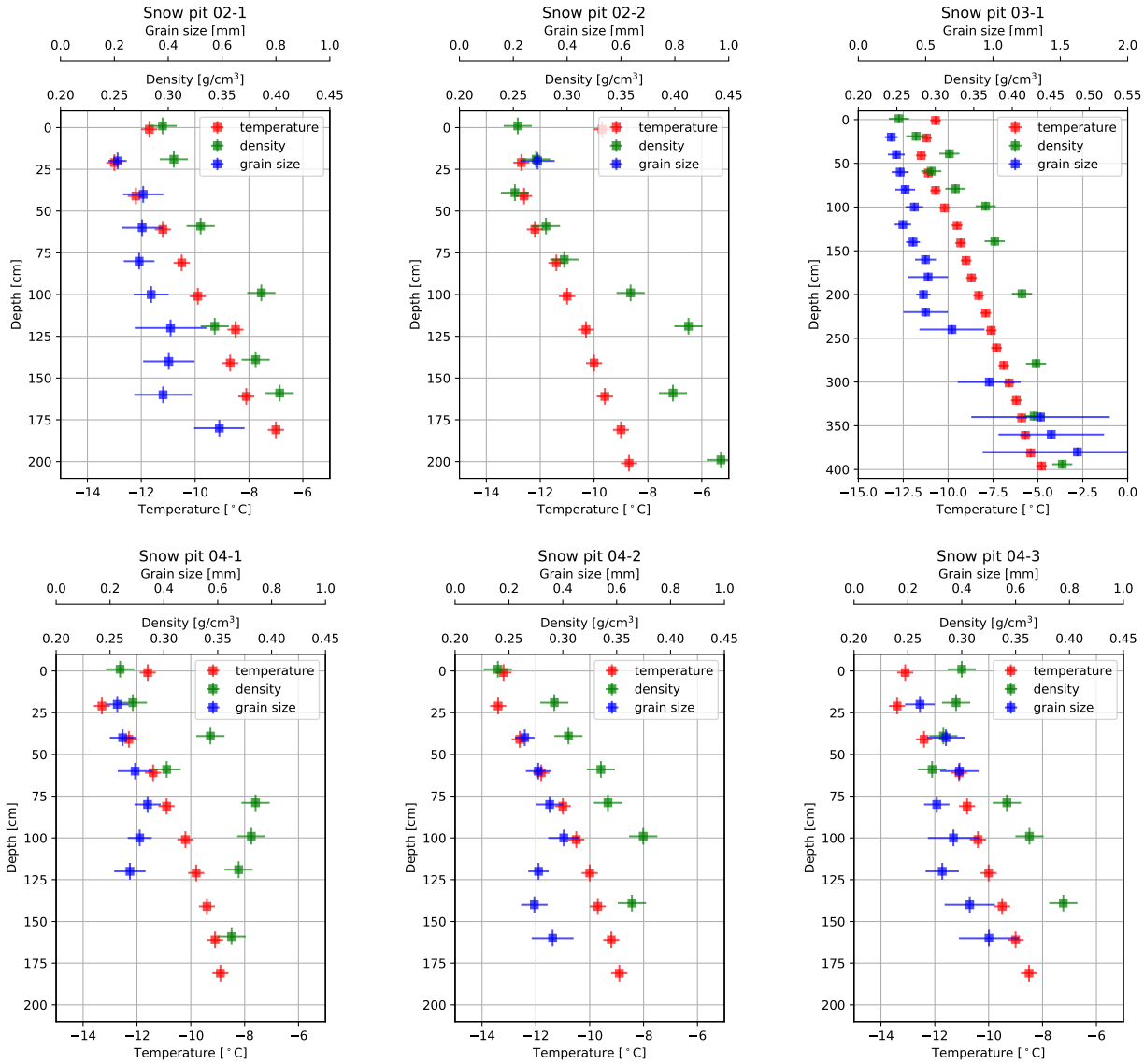

FIGURE S3.2: Snow pit measurements of vertical profiles of snow temperature, snow density, and snow grain size during the winter acquisition season. Horizontal errorbars represent the standard deviation for grain size, and estimated instrument/measurement imprecision for density and temperature. Vertical errorbars represent a depth uncertainty estimate of ±5 cm. Axis limits for snow pit 03-1 differ from the remaining five.

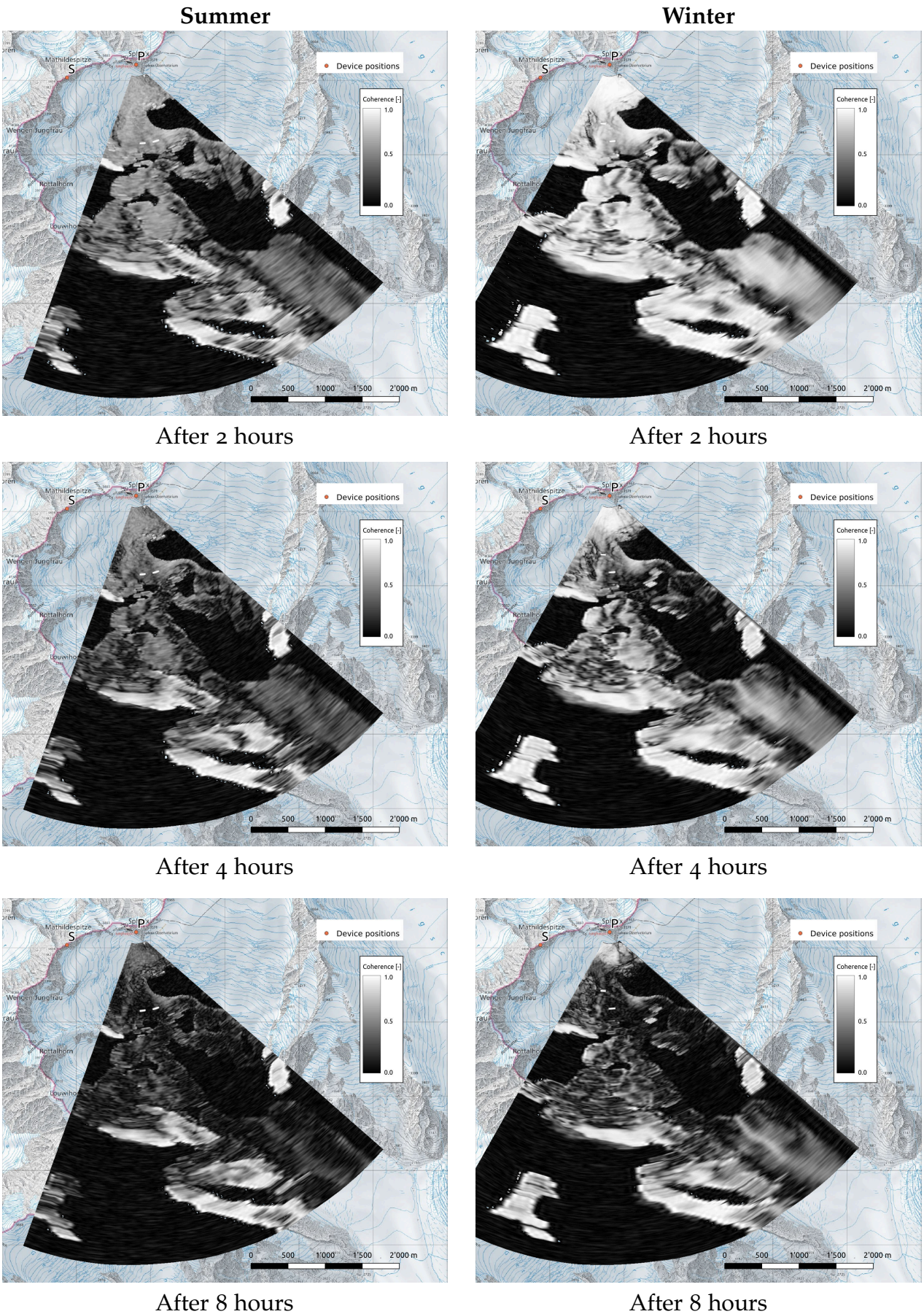

FIGURE S3.3: Maps of coherence $\gamma[T_0, T]$ for the summer (left) and winter (right) seasons. Time T_0 in summer was chosen in the evening to avoid the increase of liquid water content during the day, and to maximize the uninterrupted time series length. Due to stability of the scene in winter, the choice of T_0 has negligible impact on data in winter.

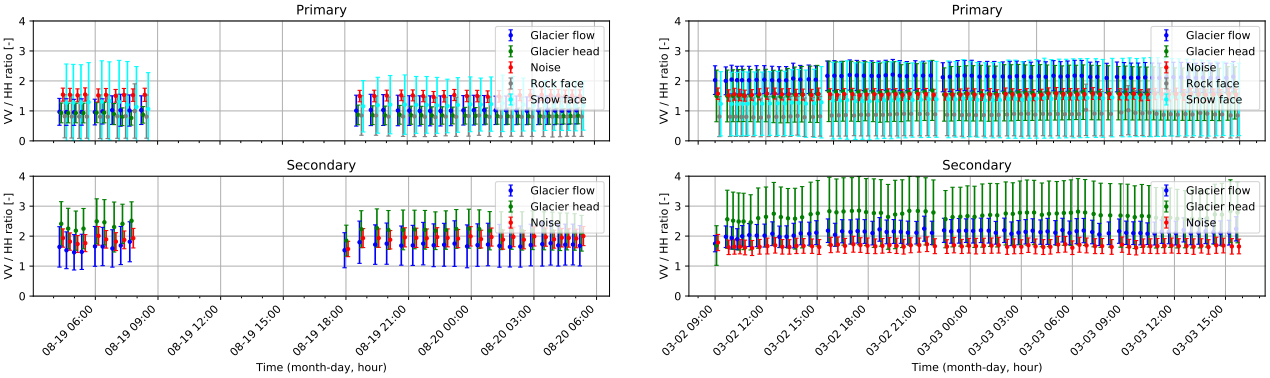

FIGURE S3.4: Time series of polarimetric ratio I_{VV}/I_{HH} for summer (left) and winter (right) seasons, for both monostatic (top) and bistatic (bottom) data, per ROI.

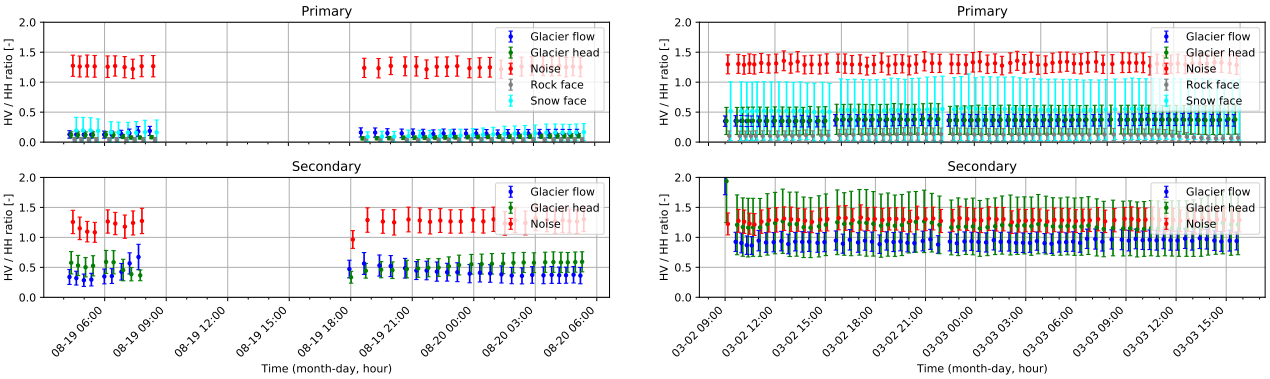

FIGURE S3.5: Time series of polarimetric ratio I_{HV}/I_{HH} for summer (left) and winter (right) seasons, for both monostatic (top) and bistatic (bottom) data, per ROI.

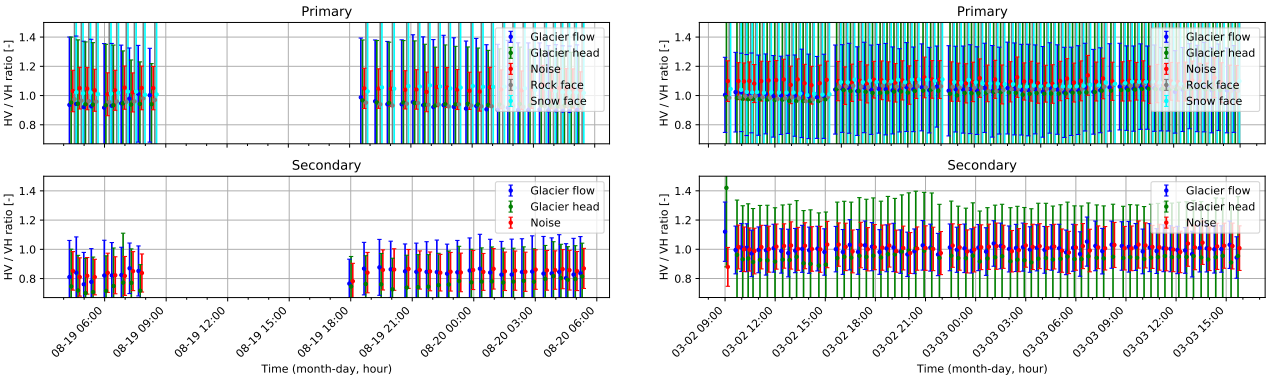

FIGURE S3.6: Time series of polarimetric ratio I_{HV}/I_{VH} for summer (left) and winter (right) seasons, for both monostatic (top) and bistatic (bottom) data, per ROI.

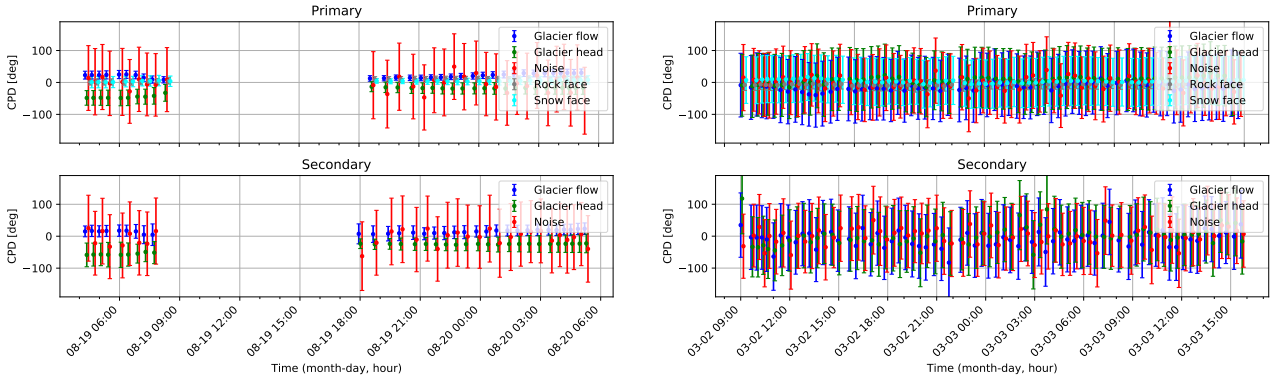

FIGURE S3.7: Time series of CPD for summer (left) and winter (right) seasons, for both monostatic (top) and bistatic (bottom) data, per ROI.

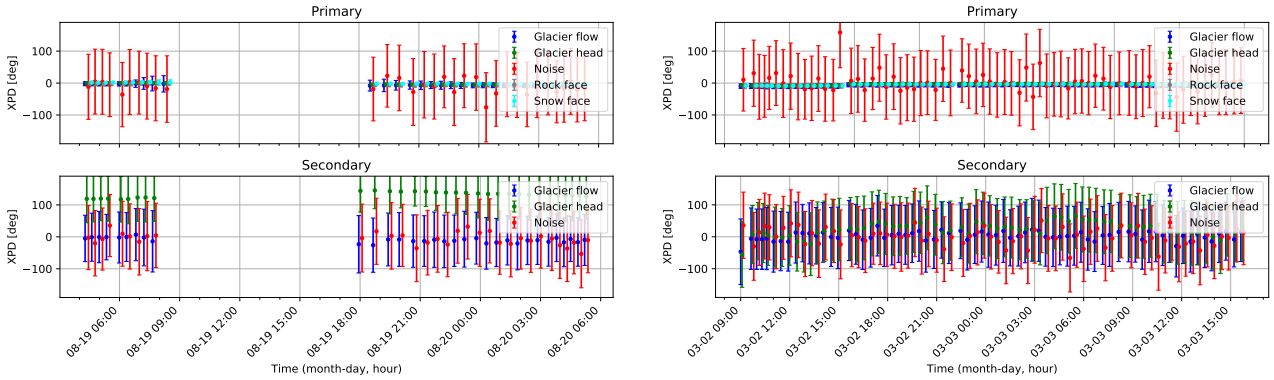

FIGURE S3.8: Time series of XPD for summer (left) and winter (right) seasons, for both monostatic (top) and bistatic (bottom) data, per ROI. Monostatic data shows almost perfect stability of the XPD around the value of zero. For bistatic data, only the Glacier head ROI can be meaningfully interpreted due to poor SNR. A large positive value of the XPD is detected in summer. The data also indicates that increasing liquid water content further slightly increases the XPD. In winter, the XPD in the bistatic Glacier head ROI spatially varies, and the mean value shows a slight bias towards positive values.

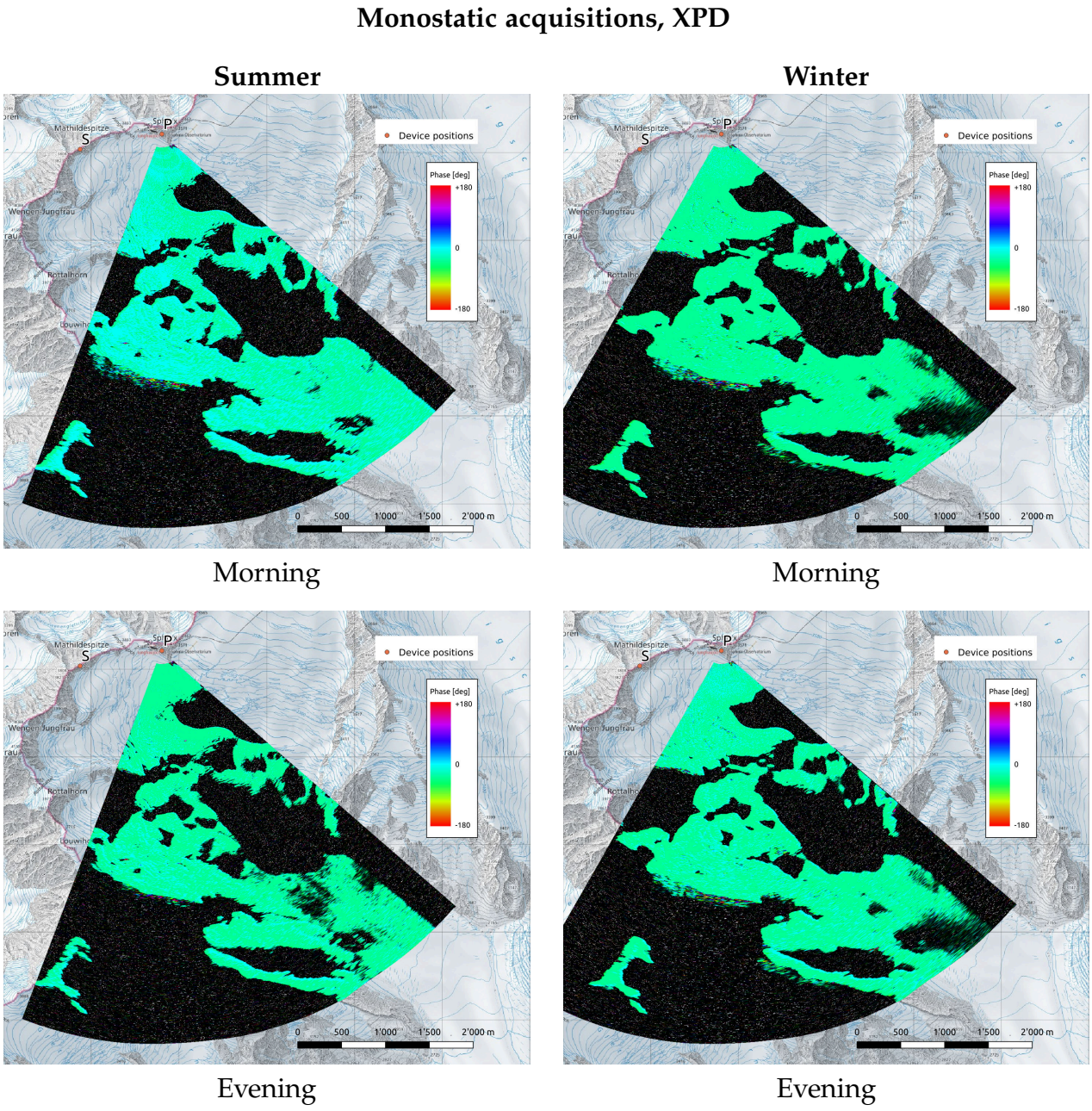

FIGURE S3.9: Comparison of the cross-polar phase difference (XPD) observed by the primary (monostatic) device, for the summer (left) and winter (right) seasons, for morning (top) and evening (bottom) acquisition time respectively. In order to enhance the signal, 10 consecutive interferograms were coherently averaged. For both seasons, the monostatic acquisitions show an expected constant near-zero value of XPD due to the reciprocity principle. Slight offset from this zero value is caused by imperfections in polarimetric calibration.

NOTES

Impact of ambiguities on coherence in Section 3.2.6 might be stronger than the shown estimates in case of presence of multipath effects (range) or when imaging dark regions located next to bright scatterers (azimuth). Furthermore, such ambiguities would not behave like noise, but instead would appear coherently in all interferograms, and could thus bias the coherence estimates. Care thus needs to be taken when interpreting coherence estimates close to areas with bright scatterers (i.e. within a few degrees in azimuth and at same range), or in areas where multipath phenomena can occur.

The regions of interest (ROIs) where coherence was estimated are not expected to be affected by bright azimuth ambiguities, as there are no comparatively brighter scatterers within their vicinity. Similarly, due to the topography of the experiment, no multipath effects are expected to be present in the ROIs. One exception could be the "Snow face" ROI, due to the flat plateau present between the primary device and the ROI which could cause multipath effects along range. While the ROI has a stronger radar brightness as opposed to the plateau due to a steeper local incidence angle, which should mitigate the effect, a certain degree of influence of multipath scattering from the area of the "Glacier head" ROI on coherence estimates of the "Snow face" ROI can not be definitively excluded. The coherence estimates in other ROIs, and the rest of the publication, should not be affected by these additional considerations.

4

COHERENT BACKSCATTER ENHANCEMENT IN BISTATIC KU- AND X-BAND RADAR OBSERVATIONS OF DRY SNOW

Marcel Stefko[1,†], Silvan Leinss[1,2,3,†], Othmar Frey[1,3], and Irena Hajnsek[1,4]

[1] Chair of Earth Observation and Remote Sensing, ETH Zurich, Switzerland

[2] LISTIC, Université Savoie Mont Blanc, France

[3] GAMMA Remote Sensing AG, Switzerland

[4] Microwaves and Radar Institute, German Aerospace Center DLR, Germany

[†] These authors contributed equally to this work

Article published in

The Cryosphere

Citation: Stefko, M., Leinss, S., Frey, O., and Hajnsek, I.: Coherent backscatter enhancement in bistatic Ku- and X-band radar observations of dry snow, The Cryosphere, 16, 2859–2879, https://doi.org/10.5194/tc-16-2859-2022, 2022.

Key findings/developments:

- The coherent backscatter opposition effect (CBOE) was confirmed to occur in dry seasonal snow at Ku-band and deep firn at X-band.
- The properties (angular shape, width, height) of the CBOE angular peak were characterized.
- A CBOE scattering model was applied in order to to estimate the properties of snow medium from the CBOE observations, specifically estimation of the scattering and absorption mean free paths.

The author's contributions:

- planned and participated in the ground-based measurements,
- processed and evaluated the ground-based measurement data,
- co-developed the model interpretation of the measurements,
- co-wrote the manuscript.

The co-authors' contributions:

- Silvan Leinss conceived the study, participated in the ground-based measurements, processed and evaluated the satellite data, co-developed the model and co-wrote the manuscript.
- Othmar Frey contributed to data and model evaluation, and writing of the manuscript.
- Irena Hajnsek contributed to data and model evaluation, and writing of the manuscript.

The coherent backscatter opposition effect (CBOE) enhances the backscatter intensity of electromagnetic waves by up to a factor of 2 in a very narrow cone around the direct return direction when multiple scattering occurs in a weakly absorbing, disordered medium. So far, this effect has not been investigated in terrestrial snow in the microwave spectrum. It has also received little attention in scattering models. We present the first characterization of the CBOE in dry snow using ground-based and spaceborne bistatic radar systems. For a seasonal snowpack in the Ku-band (17.2 GHz), we found backscatter enhancement of 50 %–60 % (+1.8–2.0 dB) at a zero bistatic angle and a peak half-width at half-maximum (HWHM) of 0.25°. In the X-band (9.65 GHz), we found backscatter enhancement of at least 35 % (+1.3 dB) and an estimated HWHM of 0.12° in the accumulation areas of glaciers in the Jungfrau–Aletsch region, Switzerland. Sampling of the peak shape at different bistatic angles allows estimating the scattering and absorption mean free paths, Λ_T and Λ_A. In the VV polarization, we obtained $\Lambda_T = 0.4 \pm 0.1\,m$ and $\Lambda_A = 19 \pm 12\,m$ at the Ku-band and $\Lambda_T = 2.1 \pm 0.4\,m$ and $\Lambda_A = 21.8 \pm 2.7\,m$ at the X-band, assuming an optically thick medium. The HH polarization yielded similar results. The observed backscatter enhancement is thus significant enough to require consideration in backscatter models describing monostatic and bistatic radar experiments. Enhanced backscattering beyond the Earth, on the surface of solar system bodies, has been interpreted as being caused by the presence of water ice. In agreement with this interpretation, our results confirm the presence of the CBOE at X- and Ku-band frequencies in terrestrial snow.

4.1 INTRODUCTION

The scattering of electromagnetic waves in any type of medium can be used to characterize some of its structural properties. In radar remote sensing, the scattering characteristics of snow have been intensely studied to derive properties of the snowpack. However, an important effect, the coherent backscatter opposition effect (CBOE), can enhance the radar backscatter return by up to a factor of 2. This effect has rarely been considered in descriptions of the backscatter return from snow in monostatic radar experiments (where the transmitter and the receiver are co-located) because even though the CBOE is present, its magnitude cannot be quantified without a bistatic reference measurement (where the transmitter and the receiver are at separate locations). To fully characterize the CBOE, bistatic radar experiments need to be performed.

4.1.1 *Opposition effects in random media*

An opposition effect (also referred to as "opposition peak", "opposition surge", "enhanced backscattering", "hot spot", and similar) is any phenomenon in which electromagnetic (EM) radiation scattered from a particular medium exhibits an increase in intensity in the direct

return direction and its vicinity. Opposition effects occur at a variety of wavelengths and scattering media and are caused by a variety of underlying physical phenomena [1].

The *coherent* backscatter opposition effect (CBOE), also referred to as coherent backscatter enhancement or weak localization of electromagnetic radiation, occurs when coherent EM radiation is scattered two or more times within a weakly absorbing, disordered medium. In the direct return direction, where wave vectors of the incident and scattered wave are parallel, the EM waves, traveling through the medium along each possible scattering path, interfere constructively with their time-reversed counterparts [1–5]. This constructive interference enhances the backscatter intensity within a very narrow cone of about 0.01–1° width by up to a factor of 2, whereas transmission is reduced. In all other directions, scattered waves sum incoherently and form the incoherent background scatter signal. The angular half-width at half-maximum (HWHM) of the CBOE peak is proportional to the ratio of the free-space wavelength λ and the scattering mean free path Λ_T ([1], Eq. 9.42). The peak tip can be very sharp when high orders of scattering contribute. The peak becomes rounder, wider, and less intense when absorption and finite sample thickness limit the contribution of multiple scattering ([4], Fig. 7; [6], Fig. 20).

The CBOE can occur together with the shadow-hiding opposition effect (SHOE). However, the SHOE requires particles to be large enough to cast sharp shadows within a porous medium (fine dust, vegetation canopy). Particles can then hide their own shadow in the direct return direction [7, 8]. In contrast to the CBOE, the SHOE is caused by single scattering, while multiple scattering weakens the SHOE; absorption is not critical. The HWHM of the SHOE peak is given by the ratio of the particle radius to the particle-to-shadow distance or extinction length in the medium ([1], Eq. 9.24). For the surface of the Moon, acting as a prototype for virtually all solar system objects with exposed surfaces, both the CBOE and the SHOE contribute with similar parts to the scattered light in the visible spectrum in the direct return direction [9].

4.1.2 *Observations of the CBOE*

Most quantitative measurements of the CBOE that characterize the whole angular width of the peak have been carried out at visible-light wavelengths through laboratory experiments which are easier to realize than radio-frequency field and planetary experiments [2, 7, 8, 10–17]. In the context of the Earth's cryosphere, [18] investigated and confirmed the presence of 10 %–60 % backscatter enhancement in snow at optical wavelengths (632.8 nm)

and interpreted the observed narrow angular peak width of 0.1–1° at HWHM as dominated by the CBOE.

In the radio-frequency spectrum, the CBOE is mostly discussed in connection with snow and ice deposits where microwave absorption is weak [19–21]. In planetary science, the CBOE was proposed as an explanation for the unusually high radar cross-sections of surfaces of various solar system bodies [22–24]. The CBOE was also discussed as a potential cause of the unusual radar echoes from the Greenland ice sheet [25], although internal reflections were proposed as an alternative explanation [26]. In both of these contexts, additional measurements at small but non-zero bistatic angles were desired (but not feasible), as they would have provided a way to more easily and robustly characterize the effect [26, 27]. Bistatic radar measurements of surfaces of solar system bodies are possible by using an orbiting spacecraft in combination with the deep space network receivers on the Earth [28, 29]. However, such experiments require a very specific geometric alignment of the spacecraft's orbit with respect to the Earth and are thus not common. Nevertheless, several experiments have been carried out with the Moon as the target [30]: the Clementine bistatic radar experiment observed an opposition peak in certain areas of the lunar surface. This peak was suggested to be attributable to the CBOE, implying the existence of ice deposits on the surface [31], though other work called the interpretation of the Clementine data into question [32]. More recently, the Mini-RF instrument of the Lunar Reconnaissance Orbiter, in concert with Arecibo Observatory's radio telescope acting as the transmitter, detected the opposition surge in certain areas of the lunar surface, again attributed to the presence of near-surface deposits of water ice [33].

In many of these experiments, observation of a backscatter enhancement peak at radio frequencies was interpreted as the CBOE. This interpretation was then used to infer the possible existence of water ice (presumably with a porous or disordered structure so as to elicit the effect) on the surface of the corresponding solar system bodies. Other works considered the CBOE in microwave scattering models of terrestrial snow [34] but could not analyze the peak shape of the CBOE. In this work we demonstrate that the existence of snow on the Earth can indeed cause a CBOE. We present a sampling of the peak shape at Ku- and X-band radio wavelengths with ground-based and spaceborne imaging radars.

4.2 METHODS

To characterize the angular peak of backscatter enhancement effects in the radio-frequency spectrum, we used two bistatic radar systems, the ground-based system KAPRI and the

spaceborne satellite formation TanDEM-X. For both systems, the transmitter and receiver are placed on independent platforms, and thus the bistatic angle can be varied. The bistatic angle β is defined as the angle between the transmitter, the observed location, and the bistatic receiver. In the exact direct return direction, the bistatic angle is zero and the scattering alignment is called the monostatic configuration.

4.2.1 *Ground-based observations – KAPRI*

The Ku-band Advanced Polarimetric Radar Interferometer (KAPRI) is a polarimetric radar system based on the GAMMA Portable Radar Interferometer (GPRI), developed by Gamma Remote Sensing [35, 36]. It is a ground-based Ku-band frequency-modulated continuous-wave (FMCW) real-aperture radar system, capable of performing fully polarimetric, bistatic measurements. In the bistatic configuration comprised of two synchronized radar instruments with different antenna configurations, the bistatic system offers coverage of areas hundreds of meters wide at a range of several kilometers. The instruments operate at a central frequency of 17.2 GHz ($\lambda = 1.74$ cm), with a 200 MHz bandwidth. The bistatic configuration and the processing pipeline to generate bistatic single-look complex (SLC) data are detailed in [37]. A description of the antenna configuration while using a cable synchronization setup can be found in [38, Fig. 2].

4.2.1.1 *Observation site – Rinerhorn, Davos*

For the ground-based experiment (map shown in Fig. 4.1), the observed region of interest (ROI) was located on the northwestern face of the Rinerhorn peak near Davos, Switzerland. Both devices were located on the valley side opposite the peak, at 46.763° N, 9.788° E (Fig. 4.1). The radar location features a straight and relatively flat segment of road approximately 200 m long with unobstructed view of Rinerhorn. The devices were placed at approximately 1620 m altitude, while the ROI altitude spans from 2050 to 2270 m. With this upward-looking observation geometry the vast majority of the ROI area is observed under a shallow local incidence angle larger than 70°. Problems with multipath interference arising from the upward-looking observation geometry while employing a fan-beam radar system [39] are avoided by placing the instruments on the opposing side of the valley.

We performed two experiments: in summer (5 August 2020), the ROI was covered by low grass. In winter (18 February 2021), the area was completely covered by approximately 1.5 m of seasonal snow. Each measurement began at approximately 08:00 local time, and the total duration of the observations was 3.5 h in summer and 5.5 h in winter. In winter,

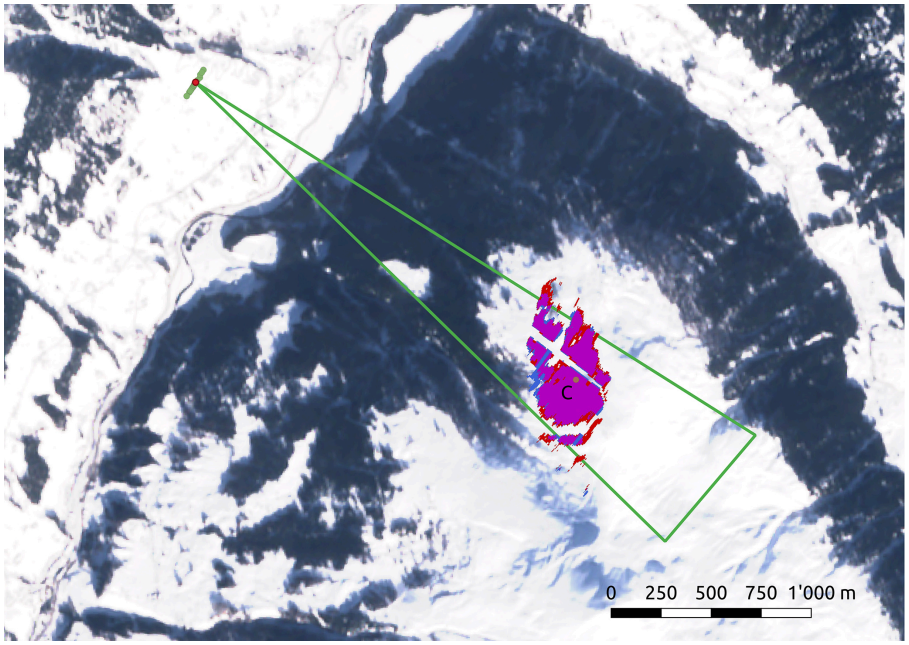

FIGURE 4.1: Map of the ground-based bistatic radar experiment. The position of the fixed transmitter (red dot) and the different receiver positions (green dots) are marked in the upper left corner and form the bistatic baseline b. The green triangle marks the -3 dB antenna beamwidth of 12° of the receiver device. The antennas are oriented towards the snow-covered northwest face of the mountain Rinerhorn, Switzerland. The region of interest (ROI) for the winter and summer seasons is shown in blue and red respectively. Their overlap is shown in purple. C is a reference point for the orientation of the bistatic receiver (see Fig. 4.4). The hollow line slicing through the ROI masks out metallic beams from a ski lift on the slope. Satellite imagery data: Sentinel-2 on 20 February 2021. Modified Copernicus Sentinel data 2021/Sentinel Hub.

a snow pit revealed snow temperatures of $-10\,°\mathrm{C}$ at the snow surface and $-0.2\,°\mathrm{C}$ at the bottom of the snowpack (Fig. 4.2, left). The traditional snow grain size, measured as the mean maximum extent of snow crystals [40], was $D_{\max} = 0.3\,\mathrm{mm}$ at the surface and $1.5\,\mathrm{mm}$ at the base (Fig. 4.2, right).

To select the ROI, a mask fulfilling the following three conditions was applied for each season: (1) include only terrain higher than the treeline at 2050 m altitude. (2) Exclude areas containing non-natural structures (metallic support beams, metal ropes, buildings, corner reflectors). (3) Exclude areas affected by radar shadow, and exclude areas outside of the main beam of the secondary antennas – these areas were detected by applying a threshold to the magnitude of the single-pass interferometric coherence γ of the secondary receiver in the VV channel. In every acquisition in the summer dataset, pixels with $\gamma < 0.85$ were masked out; in the winter dataset pixels with $\gamma < 0.80$ were masked out. A sliding window of 5×3 (range $\times$ azimuth) pixels was used for coherence estimation. The winter threshold is lower due to lower overall coherence in comparison to summer.

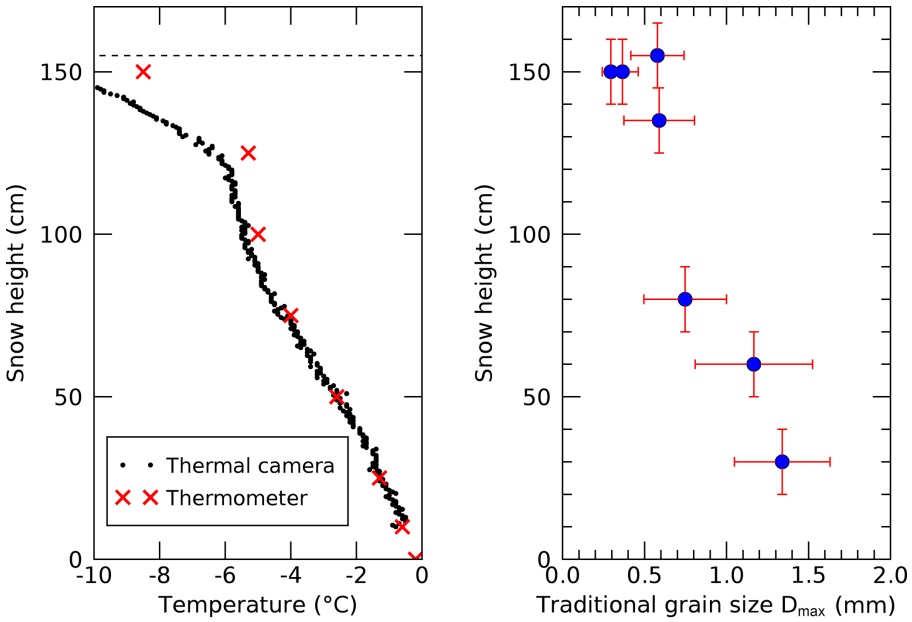

FIGURE 4.2: Snow temperature and grain size in the study area close to point C in Fig. 4.1 on 18 February 2021. Snow height is 1.55 m.

The masks defining the ROI for each season are shown in Fig. 4.1. They cover practically the same region of the hillside. The acquired calibrated SLC datasets were spatially multi-looked using a 5×3 window to obtain the intensity images and analyzed in the radar polar geometry (range $\times$ azimuth angle). The intensity value $\hat{I}(\beta)$ (the hat symbol $\hat{}$ indicates it is a measured quantity) was computed for every acquisition by averaging the measured intensities of all pixels within the ROI. We analyzed only acquisitions with VV and HH polarization as the cross-polarized signal was too close to the noise floor to provide reliable data.

4.2.1.2 *Device configuration and measurement procedure*

The primary (monostatic) transmitter–receiver remained stationary during the experiment (Fig. 4.3, top) and performed azimuthal sweep acquisitions of the observed area at a range of approximately 2.5 km. The secondary device (bistatic receiver) was moved stepwise to sample bistatic angles between 0.04 and 1.92°. In winter, the secondary device was mounted on a large sledge (*Hornschlitten*, Fig. 4.3, middle). In summer, a wheeled cart was used as a movable radar platform (Fig. 4.3, bottom). The trajectory of the secondary device is visualized in Fig. 4.4.

The bistatic angle β was calculated for each position of the secondary receiver S as

$$\beta = \arctan \frac{b}{d_{\mathrm{PC}}}. \tag{4.1}$$

The length of the bistatic baseline b is given by the length of the vector between the primary and secondary radar's positions, after projecting it into the plane orthogonal to the line of sight. The line of sight is the vector between the primary radar P and the reference point C in the ROI (see Fig. 4.4). Its length is $d_{PC} = 2500\,\text{m}$.

To ensure optimal overlap of the antenna patterns in the ROI, the secondary device was leveled and oriented manually in each position. The pitch and roll angles of the mobile platform with respect to the true vertical direction were measured with a digital spirit level at each measurement point and did not exceed 2° in either direction. In the azimuth direction, the device was oriented with a compass and optical viewfinder using a reference point in the center of the ROI (point C in Fig. 4.1). The estimated precision is 1°.

The transmit antennas on the primary KAPRI device have a physical horizontal length of 2 m (Fig. 4.3, top), and thus the bistatic angle at a 2.5 km range differs by $\sim 0.05°$ between the two edges of the transmit antenna. This imposes a practical limit on the resolution of the sampling of the intensity curve: any variation in intensity within bistatic angles of less than 0.05° will be smeared out by the non-zero size of the transmit antennas.

4.2.1.3 *KAPRI – radiometric precision*

Three main factors were identified which can affect the radiometric precision of the measurements: temporal drift of the scattering properties in the ROI, the radiometric stability of the bistatic KAPRI system, and the pointing precision of the secondary receiver's antennas.

The trajectory of the bistatic receiver (Fig. 4.4) was designed to repeatedly increase and decrease the absolute value of the bistatic baseline. This allows detection of any temporal drift of the scattering intensity over the course of the measurement (i.e., on the order of minutes to hours). Drifts would be detected by the different shape of the left and right wing of the intensity curve $\hat{I}(\beta)$.

The radiometric stability of KAPRI can be assessed by investigating the monostatic scattering intensity observed by the monostatic device from a reference target (a corner reflector). The maximal detected variation was observed in the HH channel in the winter season, with standard deviation of 16 % relative to the mean value.

For each individual measurement, the beam-pointing direction of the secondary receiver differed by less than 1° in the azimuth direction from the ideal central pointing direction towards point C. Due to the antenna pattern of the secondary receiver ([37], Fig. 7), an azimuthal misalignment of 1° can reduce the signal intensity by not more than $\sim 1\,\text{dB}$ (25 %) at the edge of the "ideal" antenna pattern footprint covering the ROI. However, when considering the total received backscatter from the ROI, this reduction is partially

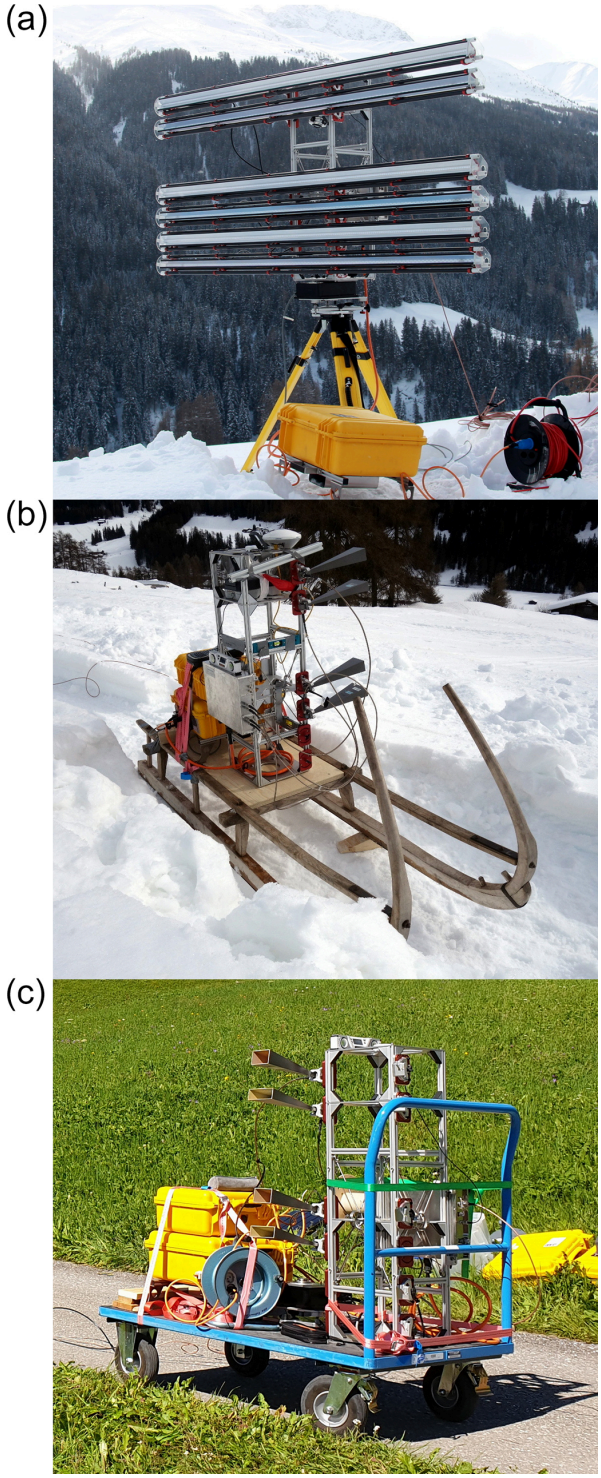

FIGURE 4.3: **(a)** Primary KAPRI radar tower (monostatic transmitter–receiver) during the ground-based experiment equipped with narrow-beam traveling-wave antennas. **(b)** Secondary KAPRI radar tower (bistatic receiver) equipped with horn antennas and deployed on a sledge (*Hornschlitten*) in winter. **(c)** Secondary KAPRI tower deployed on a wheeled cart in summer.

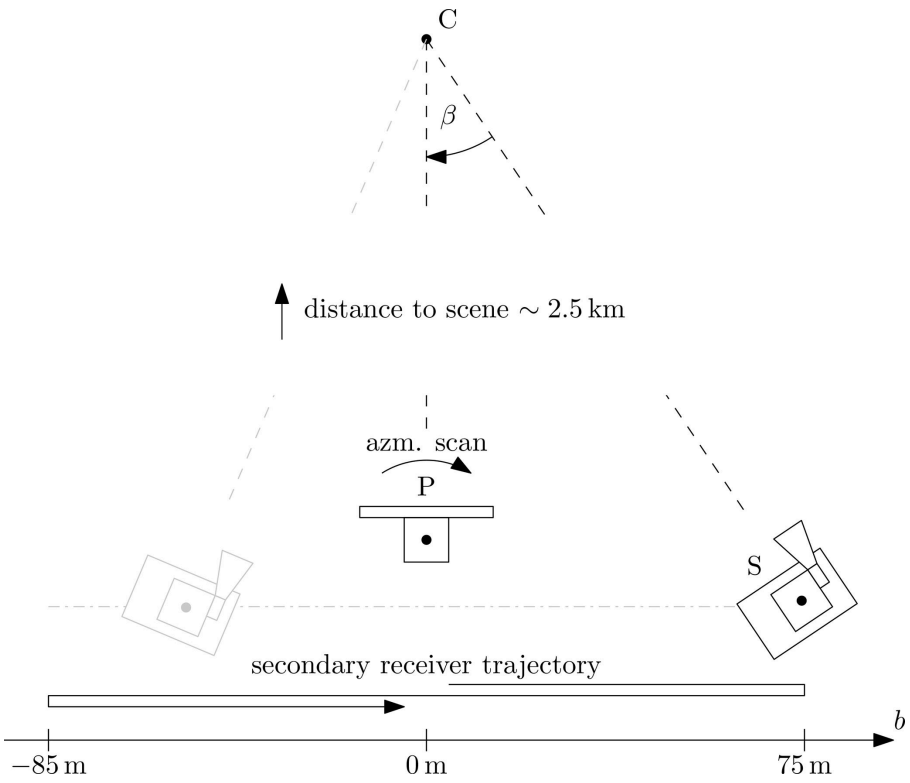

FIGURE 4.4: Diagram of the ground-based measurement procedure. The stationary, primary device P performs repeated azimuthal scans of the ROI around point C. To sample the scattering response of the ROI under a variety of bistatic angles β, the mobile secondary device S is repositioned in between acquisitions. For both winter and summer experiments, S was placed at bistatic baselines b varying between -85 and $+75$ m relative to P.

compensated for since the observed backscatter intensity from the other edge of the ROI would necessarily increase.

Due to the limited radiometric stability and the beam-pointing uncertainty, the observed backscatter intensity can thus be expected to vary stochastically with an estimated standard deviation of approximately 20 %, affecting each individual measurement by a significant amount. These effects are difficult to compensate for since there were no reference targets in the scene with a sufficiently high and stable bistatic radar cross-section. For this reason, no a posteriori radiometric calibration was applied to the data. However, the two effects are stochastic in nature and uncorrelated between individual receiver positions, and thus with a sufficiently high number of acquisitions, the enhancement peak should still be detectable, albeit with lower radiometric precision.

4.2.2 *Satellite observations – TanDEM-X*

The TanDEM-X satellite formation is the first spaceborne bistatic radar system with an adjustable bistatic baseline. The formation consists of two free-flying synthetic-aperture radar (SAR) satellites, TerraSAR-X and TanDEM-X, orbiting the Earth at about 514 km height in a helix-like formation [41]. The two radar instruments operate at the X-band at a central frequency of 9.65 GHz ($\lambda = 3.11$ cm). Depending on the acquisition mode, both satellites can act as either a transmitter or a receiver or both. In the bistatic mode, the transmit–receive satellite operates in a monostatic observation geometry and the receive-only satellite operates in a bistatic observation geometry.

Since the launch of TanDEM-X in June 2010, the distance between the two satellites has varied by several kilometers. The largest (and smallest) distances were obtained during the TanDEM-X science phase between October 2014 and February 2016 [42]. To find an area best suited for observation of the CBOE in the X-band, we searched the entire TanDEM-X archive for areas that are covered by deep snow and where long acquisition time series with large bistatic angles are available. Unfortunately, near the poles, bistatic angles are relatively small, making a sufficient sampling of the CBOE peak difficult. At the Equator, the largest bistatic angles of up to 0.35° are available but snow is naturally rare. As a best compromise, we not only selected the Jungfrau–Aletsch region in Switzerland but also analyzed the Teram Shehr and Rimo glaciers in the Karakorum (Supplement), where a considerably lower number of acquisitions were available.

4.2.2.1 *Jungfrau–Aletsch region*

The Jungfrau–Aletsch region was selected as a TanDEM-X super test site with the aim to acquire as many acquisitions as possible and to explore the scientific value of the bistatic radar mission. Between 2011 and 2019, 118 bistatic acquisitions at two polarizations (VV, HH) were acquired, most of them during winter (Fig. 4.5). At VH polarization no acquisitions at sufficiently large β values were available. For 104 acquisitions TerraSAR-X acted as the transmitter; for 14 acquisitions TanDEM-X acted as the transmitter. We removed the 14 TanDEM-X acquisitions because they showed slightly different antenna patterns that could not be compensated for through the calibration, especially at HH polarization, because of a too small number of acquisitions. For the remaining 104 acquisitions, bistatic baselines between 65 and 2100 m are available, corresponding to the range $\beta = 0.005$ to $\beta = 0.21°$. The incidence angle at the scene center is $\theta = 32°$ (orbit 154, descending). Time-averaged

backscatter images of the study area are provided in the Supplement Figs. S2 and S3. Interferometric and polarimetric properties of the dataset were analyzed by [43].

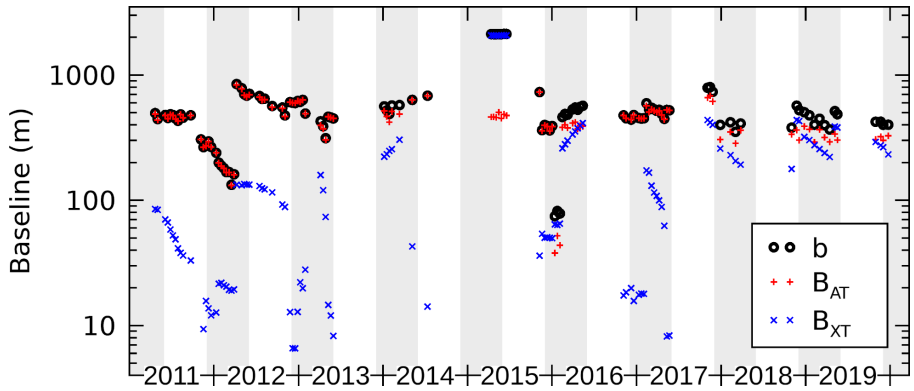

FIGURE 4.5: Time series of the bistatic baselines b according to Eq. (4.2) together with along- and across-track baselines B_{AT} and B_{XT} of the TanDEM-X satellite acquisitions of the Jungfrau–Aletsch region. Along-track baselines are adjusted by 30 m due to the satellite motion (see Sect. 4.2.2.2). Gray shading indicates the period from 1 December until 31 May for which we assume that the firn, present in the accumulation area > 3500 m, is completely frozen.

The Jungfrau–Aletsch region is highly glaciated with multiple peaks reaching above 4000 m. Cold firn, several tens of meters deep, is likely present throughout the year: depending on exposition, the transition to temperate firn is at 3400–4000 m, and the upper 15 m of firn experiences seasonal temperature cycles and can freeze in winter [44–46]. At the end of March 2021, snow temperatures of $-11 \pm 3\,^{\circ}$C in the upper 2 m and $-4 \pm 2\,^{\circ}$C at -8 m were measured by Jacqueline Bannwart (personal communication, 2021) at two sites, one at 3380 m altitude (46.5525° N, 8.0286° E) and one at 3350 m altitude (46.5483° N, 8.0323° E). At the beginning of March 2022, we measured snow temperatures of $-12 \pm 3\,^{\circ}$C in the upper 2 m and $-4 \pm 1\,^{\circ}$C at -5 m at 3640 m altitude (46.5515° N, 8.0062° E). Both Bannwart's firn cores as well as our snow pit measurements indicate the presence of an ice layer a few centimeters thick resulting from melt and refreeze during previous summers below the several-meters-thick seasonal snow cover.

The region contains the Great Aletsch Glacier (46.50° N, 8.03° E), the largest glacier in the European Alps. Its equilibrium line altitude, above which accumulation dominates, is at ~ 3000 m [47]. In the ablation area below, seasonal snow is present. Ice-free areas are dominated by rock and scree. Below 2500 m vegetation dominates with a treeline of 2000 m. For analysis of specific land cover types, we selected the following three regions of interest (ROIs) in the Jungfrau–Aletsch region (shown also in Fig. S8).

1. *The accumulation area of glaciers with altitudes above 3500 m.* These areas are at or above the temperate-to-cold firn transition, and we assume that firn conditions did not

change too drastically from winter to winter. To ensure refreezing of firn after summer and to avoid snowmelt in spring, we restricted the model parameter estimation to data acquired between 1 December and 31 May (gray shading in Fig. 4.5). The dry, deep firn acts as a thick medium with multiple scattering in the volume but low absorbance.

2. *The ablation area of the Great Aletsch Glacier with altitudes below 2700 m.* Field measurements indicate a seasonal snow cover of 0–3 m on the glacier tongue during winter [43]. The seasonal snow acts as a thin layer of volume scatterers with low absorption if the snow is dry ($T < 0\,^{\circ}\mathrm{C}$).

3. *Forested areas with at least 7 m height.* These areas are mainly conifer forest located in the Rhône Valley and the Grindelwald region. The forest acts as a medium where both volume scattering and absorption are significant.

4.2.2.2 *TanDEM-X – bistatic angle*

For TanDEM-X, the bistatic angle $\beta = b/R$ was determined from the average slant-range distance R to the scene center and from the bistatic baseline b, derived from the orbit coordinates. To compute b, the distance between the two satellites was decomposed into the along-track baseline B_{AT}; the across-track baseline B_{XT}; and the parallel, or line-of-sight, baseline B_{LOS}. The bistatic baseline b, perpendicular to the line-of-sight direction, is given by

$$b = \sqrt{B_{\mathrm{AT}}^2 + B_{\mathrm{XT}}^2}. \tag{4.2}$$

Figure 4.5 shows time series of b, B_{AT}, and B_{XT}. Because of the bistatic acquisition geometry, where the phase center of the bistatic receiver is located in the midpoint between the transmitter and the receiver [48], the across- and along-track baselines used in Eq. (4.2) are larger by a factor of 2 than the effective interferometric across- and along-track baselines given in the acquisition's meta-information ([43]; cf. their Fig. 2).

Even though we refer in the following to the monostatic acquisition, we note that the orbital velocity of $v = 7.6\,\mathrm{km\,s^{-1}}$ results in a small, velocity induced, bistatic angle of $\beta_{\mathrm{v}} = 0.003^{\circ}$ for the monostatic receiver because the satellite moves 30 m between transmission and reception of a radar pulse. The high orbital velocity also decreases (increases) the along-track baseline B_{AT} by 30 m when the bistatic receiver follows (is ahead of) the transmitter. We considered this in the analysis but found the effect to be negligible.

4.2.2.3 *TanDEM-X – radiometric calibration and computation of backscatter ratios*

Resolving the peak shape of the CBOE with a maximum expected peak height of 3 dB requires a precise radiometric calibration of the bistatic dataset.

To avoid any terrain-dependent or incidence-angle-dependent calibration, we analyzed the ratio between the backscatter intensity $\hat{I}_{\text{bist}}$ observed by the bistatic receiver and the intensity $\hat{I}_{\text{mono}}$ observed by the monostatic transmitter–receiver:

$$\hat{I}_{\text{r,0}} = \hat{I}_{\text{bist}} / \hat{I}_{\text{mono}} \, . \tag{4.3}$$

The index r, 0 indicates taking the ratio relative to $I(\beta = 0)$. Averaging ratios like $\hat{I}_{\text{r,0}}$ would result in a biased estimate. To estimate unbiased spatially or temporally averaged ratios, we first applied the averages to $\hat{I}_{\text{bist}}$ and $\hat{I}_{\text{mono}}$ and then computed the ratio $\hat{I}_{\text{r,0}}$. We use $\hat{I}$ to refer to the radar brightness commonly denoted by β_0 [49] to avoid confusion with the bistatic angle β.

For each polarization channel, we coregistered time series of the interferometric TanDEM-X CoSSC (Coregistered Single look Slant range Complex) acquisition pairs [48, 50]. To obtain the intensities $\hat{I}_{\text{mono}}$ and $\hat{I}^{\text{uncal.}}_{\text{bist}}$, we detected the temporally coregistered CoSSCs, applied 10×10 pixel multilooking and downsampled the data by a factor of 10.

Unlike the monostatic products, the bistatic TanDEM-X products are not radiometrically calibrated ([50], Sect. 4.3). The intensity ratio $\hat{I}^{\text{uncal.}}_{\text{r,0}} = \hat{I}^{\text{uncal.}}_{\text{bist}} / \hat{I}_{\text{mono}}$ showed, therefore, differences of 10 %–30 % between the bistatic and the monostatic receiver. While at VV polarization, $\hat{I}^{\text{uncal.}}_{\text{r,0,VV}}$ showed spatially relatively constant values at small bistatic angles and $\hat{I}^{\text{uncal.}}_{\text{r,0,HH}}$ showed terrain-independent trends of a few percent, presumably due to different antenna patterns (Figs. S4 and S5). To compensate for these patterns, we calibrated the intensity $\hat{I}^{\text{uncal.}}_{\text{bist}}$ at each polarization with the ratio of the pixel-wise temporal mean $\langle \cdot \rangle^{\text{temp.}}$ of 17 scenes with $\beta < 0.033°$. This threshold for β was chosen to be small enough to avoid any significant differences in backscatter enhancement between the monostatic and bistatic receiver. The bistatic intensity after antenna calibration is

$$\hat{I}^{\text{ant.cal.}}_{\text{bist}} = \hat{I}^{\text{uncal.}}_{\text{bist}} \frac{\langle \hat{I}_{\text{mono}} \rangle^{\text{temp.}}_{\beta<0.033°}}{\langle \hat{I}^{\text{uncal.}}_{\text{bist}} \rangle^{\text{temp.}}_{\beta<0.033°}}. \tag{4.4}$$

To obtain the calibrated intensity $\hat{I}_{\text{bist}}$, we compensated in each acquisition pair for the remaining spatially constant offset between the monostatic and bistatic data. For this we

multiplied $\hat{I}_{\text{bist}}^{\text{ant.cal.}}$ with the ratio of the monostatic and bistatic radar brightness, spatially averaged, as indicated by $\langle\cdot\rangle_{\text{cal.area}}^{\text{spat.}}$, over a pre-defined calibration area:

$$\hat{I}_{\text{bist}} = \hat{I}_{\text{bist}}^{\text{ant.cal.}} \frac{\langle \hat{I}_{\text{mono}} \rangle_{\text{cal.area}}^{\text{spat.}}}{\langle \hat{I}_{\text{bist}}^{\text{ant.cal.}} \rangle_{\text{cal.area}}^{\text{spat.}}}. \tag{4.5}$$

For calibration of the Jungfrau–Aletsch dataset we used areas that showed a temporally stable and baseline-independent backscatter ratio $\hat{I}_{\text{r},0}$. These areas were defined using two iterations. In a first iteration, we masked out very dark areas, possibly affected by noise, such as shadow ($\hat{I}_{\text{mono}} < -14\,\text{dB}$) and also very bright areas such as layover and strong local scatterers ($\hat{I}_{\text{mono}} > +1\,\text{dB}$) through thresholding the temporal mean of the backscatter intensity. We also masked out the ROIs later analyzed by masking elevations above 3000 m where multi-year firn occurs and regions covered by forest, as well as the ablation area of the Great Aletsch Glacier. After using the remaining pixels for calibration, in the second iteration we additionally masked out areas showing possible artifacts where $\hat{I}_{\text{r},0}$, computed pixel-wise using the temporal means of $\hat{I}_{\text{mono}}$ and $\hat{I}_{\text{bist}}$ from 43 acquisitions with bistatic angles smaller than 0.04° (Eq. 4.4), deviated more than 5 % from unity. Such deviations appeared in areas of low radar backscatter and areas not directly affected by layover but next to layover in the far-range direction. The deviations might partially originate from bright azimuth ambiguities. We also believe that double-reflections occurring within layover, with a reflection on each side of a north–south-oriented valley and an additional propagation path between the two reflections, cause further radar echoes appearing beyond the layover area. These artifacts appear stronger at HH than at VV (due to reflections close to the Brewster angle) and are also stronger with wet snow due to more specular reflection compared to dry snow or summer with more diffuse reflections (the artifacts are well visible in Supplement figures when comparing Fig. S2 with Fig. S3 and Fig. S4 with Fig. S5). We also removed areas where the pre-calibrated backscatter ratio $\hat{I}_{\text{r},0}$ showed a temporal standard deviation larger than 0.08 (Figs. S6 and S7). Finally, to avoid the CBOE or possibly the SHOE affecting the calibration, we masked out areas that showed more than 5 % enhanced scattering in the direct return direction in the large-baseline acquisitions $B_{\perp} > 2\,\text{km}$. In total, we masked out approximately 50 % of pixels from the scene (Fig. S8) and used the remaining pixels, mainly grassland, rock, and the ablation areas of glaciers, for calibration in Eq. (4.5). In this data-driven calibration we assume that the regions selected for calibration show an equal backscatter intensity for the monostatic and bistatic receiver.

To determine the backscatter ratio for the ROIs, we used Eq. (4.3) with $\hat{I}_{\text{bist}}$ and $\hat{I}_{\text{mono}}$ averaged over the ROI. To differentiate between dry and wet snow for snow-covered areas, we used the mean backscatter intensity $\hat{I}_{\text{mono}}$ as a proxy.

To display imagery of $I_{\text{r},0}$ with sufficient radiometric resolution, we applied additional 4×4 pixel multilooking to the downsampled backscatter imagery, corresponding to an effective multilooking operation of 41×41 pixels. This value was chosen to keep the standard deviation $\sigma = I/\sqrt{N}$ of the multilooked intensity I sufficiently low [51]. N is the number of looks. Given that adjacent pixels are statistically not completely independent (the SLC data are oversampled by a factor of 1.3 in the slant range direction and 2.9 in the azimuth direction, resulting in 3.73 pixels per look), we obtain a value of $N = 41^2/3.73 = 450$ looks, which corresponds to a radiometric accuracy (standard deviation) of 0.2 dB (5 %) at an intensity of $I = -5$ dB.

4.2.3 *Backscatter model for the CBOE*

Coherent backscatter enhancement was first explained through time-reverse propagation in double and multiple-scattering paths between scatterers with a low volume fraction in free space using second-order multiple-scattering theory and expansion in Feynman diagrams [3, 6, 52]; [15] added particle-independent absorption through the background medium. For a review see [4] and [1]. To our knowledge, no complete theory for the CBOE in densely packed media of particles that are small compared to the wavelength exists. Furthermore, in snow, scattering can occur at various length scales (i.e., ice grains, density fluctuations, inter-layer boundaries, and ice layers; [53]), and no CBOE model for multi-layer structures is currently available. In order to describe the complex snow structure in the context of existing models, we consider snow an effective scattering medium occupying a semi-infinite space with homogeneous scattering and absorption properties and follow the description from [1] for interpretation and modeling of our results. In chap. 9, Eqs. (9.40) and (9.44) [1], as well as in [4, 14] and [54], the peak shape of the coherent backscatter enhancement is described for non-absorbing and absorbing media by the following equation:

$$B_{\text{C}}(\beta) = \frac{1}{[1 + 1.42K]\,[1 + \xi(\beta)\,]^2} \left[1 + \frac{1 - e^{-1.42K\xi(\beta)}}{\xi(\beta)}\right], \tag{4.6}$$

where $B_C(\beta)$ is the magnitude of the coherent backscatter intensity enhancement relative to the incoherent background I_0 at small bistatic angles $\beta \approx \sin\beta$. For notational simplicity and in accordance with [1], Eq. (9.44), and [15], we defined the following:

$$\xi(\beta) = \sqrt{\left(\frac{2\pi\Lambda_T\beta}{\lambda}\right)^2 + \frac{3\Lambda_T}{\Lambda_A}}. \tag{4.7}$$

In this equation λ is the free-space wavelength, $\Lambda_T \propto S^{-1}$ is the transport mean free path which is proportional to the inverse of the scattering coefficient S of the medium, and $\Lambda_A = A^{-1}$ is the absorption mean free path in the medium with absorption coefficient A. Assuming that the snow depth is much larger than Λ_T, i.e., that snow can be considered an optically thick medium, the scattering and absorption coefficients that parametrize Eq. (4.7) can be linked to snow properties derived from density and the microstructure [53] as discussed in Sect. 4.4.4. The factor K is a correction factor, described in [1], pp. 164–167, as the "porosity coefficient". The factor K increases the extinction coefficient $E = S + A$ in densely packed media where inter-particle effects of particles that are large relative to λ occur. As ice grains are much smaller than the wavelength, we assume $K = 1$.

The incoherent background intensity I_0 is determined by the single- and multiple-scattered background intensity from the medium for which no time-reverse counterparts exist (i.e., no coherent enhancement), so

$$I(\beta) = I_0[1 + B_C(\beta)] \tag{4.8}$$

describes the total backscatter intensity $I(\beta)$ in the proximity of several degrees from the direct backscatter direction.

The peak shape, as drawn in Fig. 4.6, is determined by the ratio of the scattering mean free path Λ_T to the wavelength λ, as already indicated by [3], and by the probability distribution of scattering path lengths in the medium. A (monostatic) scattering path begins at the first scattering event in the medium, travels along multiple scatter events with a mean distance Λ_T, and ends when the radiation is scattered back out of the medium in the direct return direction ([1], chap. 9.3). In the monostatic configuration, radiation traveling along such a path interferes constructively with radiation propagating along the time-reversed counterpart, thus causing the backscatter intensity enhancement. Long scattering paths, consisting of multiple scattering events, have a longer distance between the path's start and end point and cause a narrow peak, while short scattering paths cause a broad peak. The final peak shape is determined by the sum of all occurring peak shapes of different widths [52], weighted according to their occurrence probabilities. An increase in absorption causes

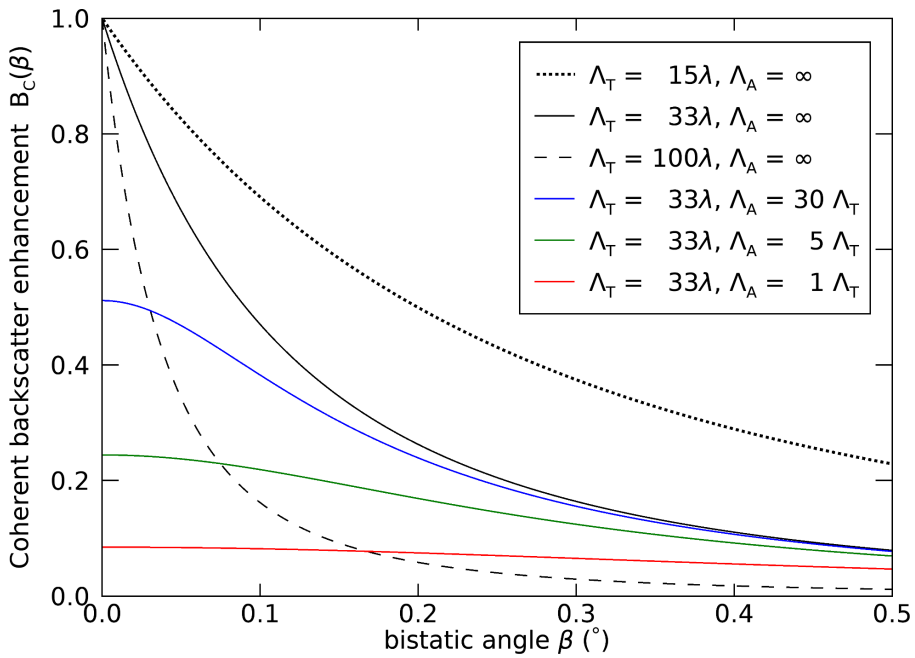

FIGURE 4.6: Modeled peak shape of the CBOE for different scattering mean free paths Λ_T given in multiples of the wavelength λ and for different absorption mean free paths Λ_A (in multiples of Λ_T) in a medium with small scattering particles (porosity coefficient $K = 1$). For a non-absorbing medium ($\Lambda_A = \infty$) a very sharp peak can be observed. Already with a weak absorption $\Lambda_A = 30\Lambda_T$ (blue) the peak height is reduced to 50 % and the peak becomes much rounder. For comparable scattering and absorption lengths the peak is not noticeable (red).

shortening of the scattering paths that can contribute to the coherent peak and reduction of the occurrence probability of higher-order scattering; hence the peak becomes rounder and wider ([4], their Fig. 7, and [15]). Long scattering paths can also be limited by a finite sample (snowpack) thickness, which also causes a rounding of the peak and an increase in its width ([6], their Fig. 20, and [16]).

Figure 4.6 shows the shape of the CBOE peak for a range of values of Λ_T and Λ_A given in multiples of λ. For non-absorbing media ($\Lambda_A = \infty$, black curves), longer scattering lengths Λ_T cause a narrower peak with a HWHM of $0.36\lambda/(2\pi\Lambda_T)$ [6, 55]. This peak width holds for sparsely packed media; for densely packed media of hard spheres, [56] suggests a significantly reduced HWHM.

With increasing absorption, the peak height decreases, its width increases, and the peak becomes rounder. To characterize the peak height and width for absorbing media, we found that Eq. (4.6), with $K = 1$, can be well approximated by

$$B_C(\beta) \approx \frac{1}{[1 + 1.3\,\xi(\beta)\,]^2}, \tag{4.9}$$

where the factor 1.3 corrects deviation resulting from neglecting first- and second-order terms of $\xi(\beta)$ in the numerator. Equation (4.9) provides an analytical form to link the ratio Λ_T/Λ_A to the peak height:

$$B_C(0) = \frac{1}{\left(1 + 1.3\sqrt{3\frac{\Lambda_T}{\Lambda_A}}\right)^2}. \tag{4.10}$$

A slightly more complicated equation can be obtained for the peak width for finite Λ_A. Hence, when characterizing the full peak shape or at least its height and width, the parameters Λ_T and Λ_A can be determined.

Most CBOE models are based on scalar waves which do not consider the vector character of electromagnetic waves, i.e., their polarization. However, experimental and theoretical works show that the CBOE occurs predominantly for co-polarized transmitted and received waves (VV and HH) where the model matches well experimental observation. They also show that the CBOE for cross-polarized (VH) observations is significantly weaker and decreases with increasing sample thickness [12, 55, 57, 58].

4.2.3.1 *Application to KAPRI data*

With the two ground-based KAPRI instruments, the benefit of the flexible configuration allows us to sample the intensity peak up to relatively high values of bistatic angle β, and thus the flat region of the intensity curve ($I(\beta \to \infty) \to I_0$) should be observable. However, the very top of the peak is difficult to sample due to the non-negligible size of the primary device's antennas, as well as the possibility of the devices obstructing each other's view when placed very close together. Because of this, for analysis of KAPRI data, we use the intensity ratio $I_{r,\infty}(\beta)$, which is normalized to the incoherent background intensity $I(\infty)$ and can be expressed with the aid of Eq. (4.8) as

$$I_{r,\infty}(\beta) = \frac{I(\beta)}{I(\infty)} = \frac{I_0(1 + B_C(\beta))}{I_0(1 + B_C(\infty))} = 1 + B_C(\beta). \tag{4.11}$$

To calculate the intensity ratio of Eq. (4.11) from the actual observed mean ROI intensity $\hat{I}(\beta)$, we approximate $I(\infty)$ as the mean value of $\hat{I}(\beta)$ from all acquisitions within the corresponding dataset where $\beta > 1^\circ$ (i.e., values well within the flat region of the intensity curve):

$$\hat{I}_{r,\infty}(\beta) \approx \frac{\hat{I}(\beta)}{\langle \hat{I}(\beta) \rangle_{\beta > 1^\circ}}. \tag{4.12}$$

Because the model $B_C = B_C(\beta, \Lambda_T, \Lambda_A)$ depends on the transport mean free path Λ_T and absorption length Λ_A through Eqs. (4.6) and (4.7), we can use Eq. (4.11) to fit different values

of Λ_T and Λ_A to the observed intensity curve $\hat{I}_{r,\infty}(\beta)$ by nonlinear least-squares minimization. For the fitting procedure, we used the TRF (trust region reflective) optimization method implemented via the `curve_fit` function of the `scipy.optimize` library [59]. The initial parameter values of the (Λ_T, Λ_A) pair were set to (1 m, 100 m), and both parameters were restricted to the non-negative real-number domain.

4.2.3.2 *Application to TanDEM-X data*

With TanDEM-X we measured the intensity ratio $\hat{I}_{r,0}(\beta)$ between the bistatic receiver $\hat{I}_{bist} = \hat{I}(\beta > 0)$ and the monostatic receiver $\hat{I}_{mono}(\beta_v = 0.003°) \approx I(0)$ (Sect. 4.2.2.2). This approximation is well justified considering that the expected width of the peak is at least 1 order of magnitude larger than the small bistatic angle of the monostatic receiver (see Fig. 4.6) and that rounding of the peak tip due to weak absorption can be expected. The TanDEM-X measurement can, therefore, be described by Eq. (4.8) as

$$I_{r,0}(\beta) = \frac{I(\beta)}{I(0)} = \frac{I_0(1 + B_C(\beta))}{I_0(1 + B_C(0))} = \frac{1 + B_C(\beta)}{1 + B_C(0)}. \tag{4.13}$$

The intensity ratio $I_{r,0}(\beta)$ is 1.0 for $\beta = 0$ and reaches its minimum of 0.5 at $\beta \to \infty$ when absorption is negligible. With increasing absorption the ratio $I(\beta)/I(0)$ lowers and $I_{r,0}(\beta \to \infty)$ increases from 0.5 to eventually 1.0 when the CBOE is negligible.

A lower limit for the enhancement $B_C(\beta = 0)$ can be quickly estimated: because $B_C(\beta_{max}) > B_C(\infty) = 0$, it follows from Eq. (4.13) that

$$B_C > I_{r,0}^{-1}(\beta_{max}) - 1 = \frac{\hat{I}_{mono}}{\hat{I}_{bist}(\beta_{max})} - 1; \tag{4.14}$$

i.e., the enhancement B_C is at least as large as the relative difference between the monostatic and the bistatic backscatter, $\hat{I}_{mono}$ and $\hat{I}_{bist}$, at the largest available bistatic angle β_{max}.

To fit the model, we used winter data from the accumulation area (Sect. 4.2.2.1). To determine the optimal value of the parameter pair (Λ_T, Λ_A) and the 95 % confidence intervals, we used the TRF method (Sect. 4.2.3.1) and set the starting parameter of (Λ_T, Λ_A) to (2 m, 20 m). However, a sampling of the RMSE $[\hat{I}_{r,0}(\beta) - I_{r,0}(\beta)]$ in the parameter space of Λ_T, Λ_A around the optimal value revealed that the global minimum is weakly constrained, and solutions across a large span of values of Λ_A provide an acceptably low RMSE value. Thus, to explore multiple parameter pair values, we sampled a range of values of Λ_A and used a downhill simplex method implemented in the `amoeba` IDL function [60] to determine the corresponding Λ_T.

4.3 RESULTS

4.3.1 *Ground-based observations – KAPRI*

Figure 4.7 shows the observed intensity ratio $\hat{I}_{r,\infty}(\beta)$ defined by Eq. (4.12) at HH and VV polarization and the least-squares best fit of the model defined by Eqs. (4.6), (4.7), and (4.11).

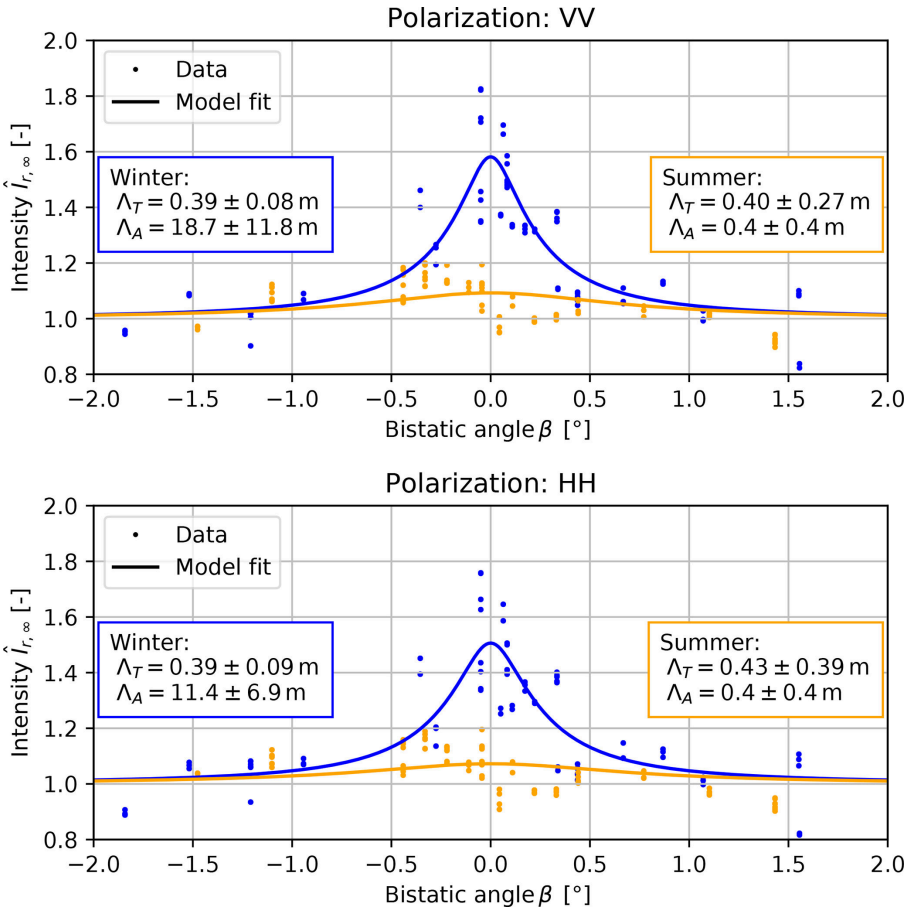

FIGURE 4.7: Intensity ratio $\hat{I}_{r,\infty}(\beta)$ observed during the ground-based experiment (KAPRI), showing backscatter enhancement in the winter dataset (blue). For the summer dataset (orange), the comparable values of the Λ_T and Λ_A estimates, as well as their relatively large confidence intervals, indicate that the CBOE peak was not detectable. The observed intensities $\hat{I}(\beta)$ were averaged over the whole region of interest for both polarizations, VV and HH. The blue and orange lines describe the least-squares fit model defined by Eqs. (4.6), (4.7), and (4.11) for winter and summer respectively. The colored boxes for each dataset show the best-fit value and the 95 % confidence interval for the model parameters Λ_T and Λ_A describing the scattering and absorption mean free paths.

For the winter dataset a clear intensity peak is detected, with a HWHM of approx. 0.25° and amplitude $B_C(0) \approx 0.5$ (1.8 dB), corresponding to $\Lambda_T \approx (0.4 \pm 0.1)$ m for the HH and VV polarization. The derived absorption lengths Λ_A are much longer than the scattering lengths with $\Lambda_A \approx (11 \pm 7)$ m for the HH polarization and $\Lambda_A \approx (19 \pm 12)$ m for the

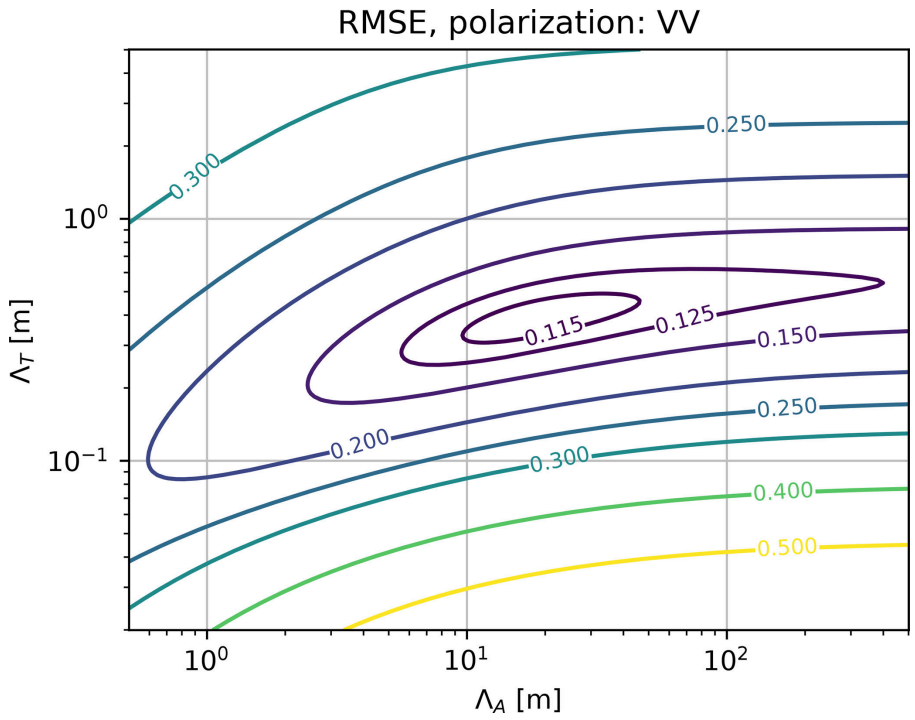

FIGURE 4.8: Contour plot of root mean square error (RMSE) between measured and modeled winter data in the Ku-band (Fig. 4.7) for different parameter pairs of Λ_A and Λ_T. The plot indicates a clear global minimum because the CBOE peak height and hence Λ_A can be well estimated due to the availability of ground-based KAPRI measurements at large bistatic angles of $\beta > 1°$.

VV polarization. For the summer dataset, the flat profile of the observed intensity curve indicates that very little or no backscatter enhancement is present – this is reflected in the model fit in the low value and large confidence interval (relative to the value) of the absorption length $\Lambda_A \approx (0.4 \pm 0.4)$ m. The estimates of the scattering length in the summer dataset ($\Lambda_T \approx (0.40 \pm 0.27)$ m and $\Lambda_T \approx (0.43 \pm 0.39)$ m for the VV and HH polarization respectively) have comparable value to the winter estimates; however the much larger confidence intervals indicate that the value of Λ_T could not be determined more precisely for the summer dataset due to the absence of a clear enhancement peak. The uncertainty in the value estimates corresponds to the 95 % confidence interval.

Figure 4.8 shows the RMSE of the model fit to the dataset with VV polarization, depending on values of the fit parameters Λ_T and Λ_A. A clear global minimum can be found in the 2-dimensional parameter space at the best-fit parameter values mentioned above, with RMSE of approximately 0.11. Residuals of the model fits for selected values of parameters Λ_T and Λ_A are shown in Fig. S1.

4.3.2 *Satellite observations – TanDEM-X*

4.3.2.1 *Jungfrau–Aletsch region*

The large number and wide coverage of the TanDEM-X scenes allow an analysis of the dependency of $\hat{I}_{r,0}$ on β for different land cover types. In Fig. 4.9, where the color of data points refers to I_{mono} (Fig. 4.10) to distinguish between dry and wet snow, only $\hat{I}_{r,0}$ in the accumulation area $> 3500\,m$ (Fig. 4.9a, b) shows a significant dependence on β: the ratio $\hat{I}_{r,0}(\beta)$ forms a clear peak that shows some rounding between $\beta = 0$ and $0.05°$, characteristic of weak absorption. At both polarizations, VV and HH, and only in dry-snow conditions, at the largest available bistatic angles $\beta_{max} = 0.2°$ the bistatic backscatter intensity $\hat{I}_{bist}$ is reduced by approximately 20 % compared to $\hat{I}_{mono}$. For wet snow (dark dots) no reduction in $\hat{I}_{r,0}$ is observed at β_{max}. In contrast, neither the ablation area of the Great Aletsch Glacier, Fig. 4.9c, nor areas covered by conifer forest, Fig. 4.9d, show any significant dependence of $\hat{I}_{r,0}$ on β.

To investigate the spatial distribution of areas that show enhanced backscattering, Fig. 4.11 shows imagery of the monostatic-to-bistatic backscatter ratio $\hat{I}_{r,0}^{-1}$ together with the radar brightness I_{mono} for a series of three acquisitions with $\beta = \beta_{max}$ at the onset of snowmelt in April and May 2015: on 24 April (Fig. 4.11a, d), backscatter enhancement is visible for a considerable amount of the area, corresponding to glaciers at high altitude ($> 3000\,m$). On 5 May (Fig. 4.11b, e), the backscatter enhancement is limited to high altitudes because snowmelt is occurring up to an altitude of approximately 3300 m. On 7 June (Fig. 4.11c, f), snowmelt reaches the peaks of the highest mountains (4274 m) and no enhanced backscattering is detectable at any place.

To estimate the scattering and absorption parameters Λ_T and Λ_A, as well as the peak width and the backscatter enhancement, we fitted the model, Eq. (4.13), to the dry firn data of the accumulation area, constrained to winter acquisitions (the selection is specified in Sect. 4.2.3.2 and indicated by gray shading in Fig. 4.10a). Figure 4.12a and b show the selected dataset at two different scales of β. The solution with the minimal RMSE value is indicated by the dashed black line. This solution corresponds to $\Lambda_T = 2.13 \pm 0.36\,m$ and $\Lambda_A = 21.77 \pm 2.72\,m$ (95 % confidence interval, VV polarization), an enhancement of $B_C = 35\,\%$ (+1.3 dB), and a HWHM of the peak of $0.12°$. From the HH polarized data (not shown), we obtained $\Lambda_T = 1.62 \pm 0.35\,m$ and $\Lambda_A = 25.88 \pm 5.27\,m$, corresponding to $B_C = 41\,\%$ (+1.5 dB) and a HWHM of $0.14°$.

Figure 4.12a also illustrates that the available data, sampled with a limited range of bistatic angles, allow multiple model solutions with similar RMSE values (colored lines).

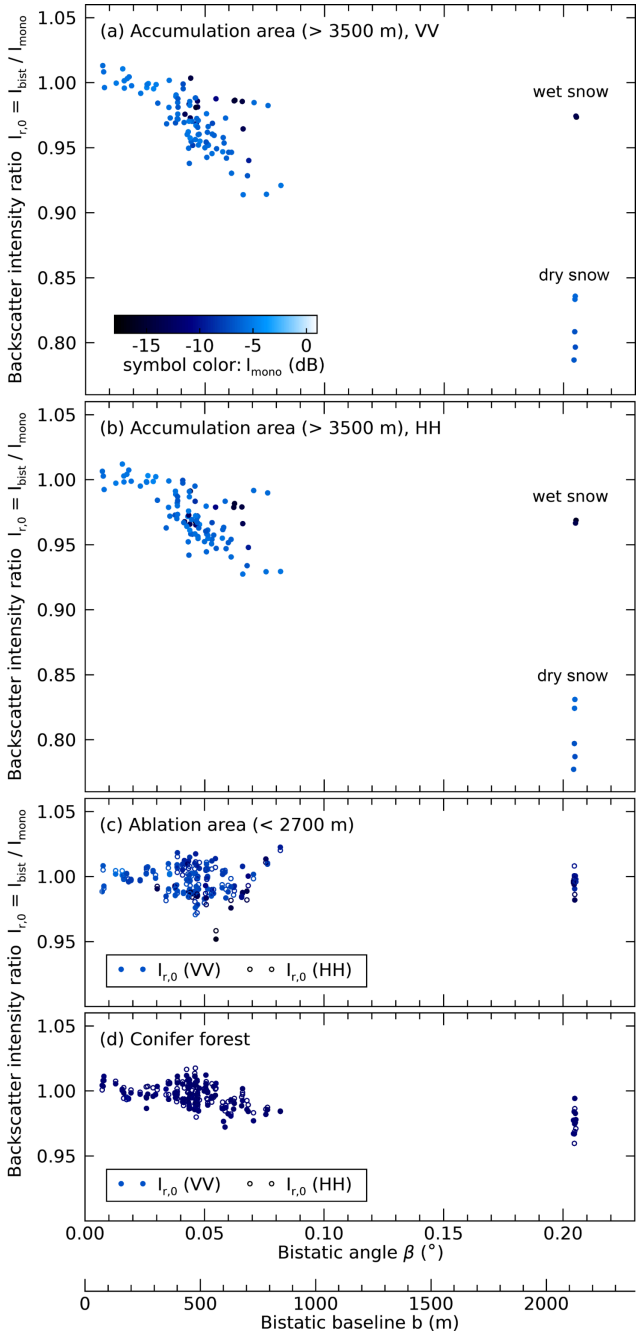

FIGURE 4.9: **(a, b)** The intensity ratio $\hat{I}_{r,0}$ observed by the satellite TanDEM-X in the accumulation area. Backscatter enhancement is indicated by the significant dependence of $\hat{I}_{r,0}$ on the bistatic angle β for dry-snow observations at both polarizations (VV, HH). The symbol color indicates the monostatically measured radar brightness I_{mono} and helps to differentiate between wet snow (dark blue) and dry snow (light blue); see Fig. 4.10a. **(c)** The ablation area of the Great Aletsch Glacier, located below 2700 m, is covered by 0–3 m of snow in winter but does not show any dependence of $\hat{I}_{r,0}$ on β. **(d)** Areas covered by conifer forest show no significant dependence on β.

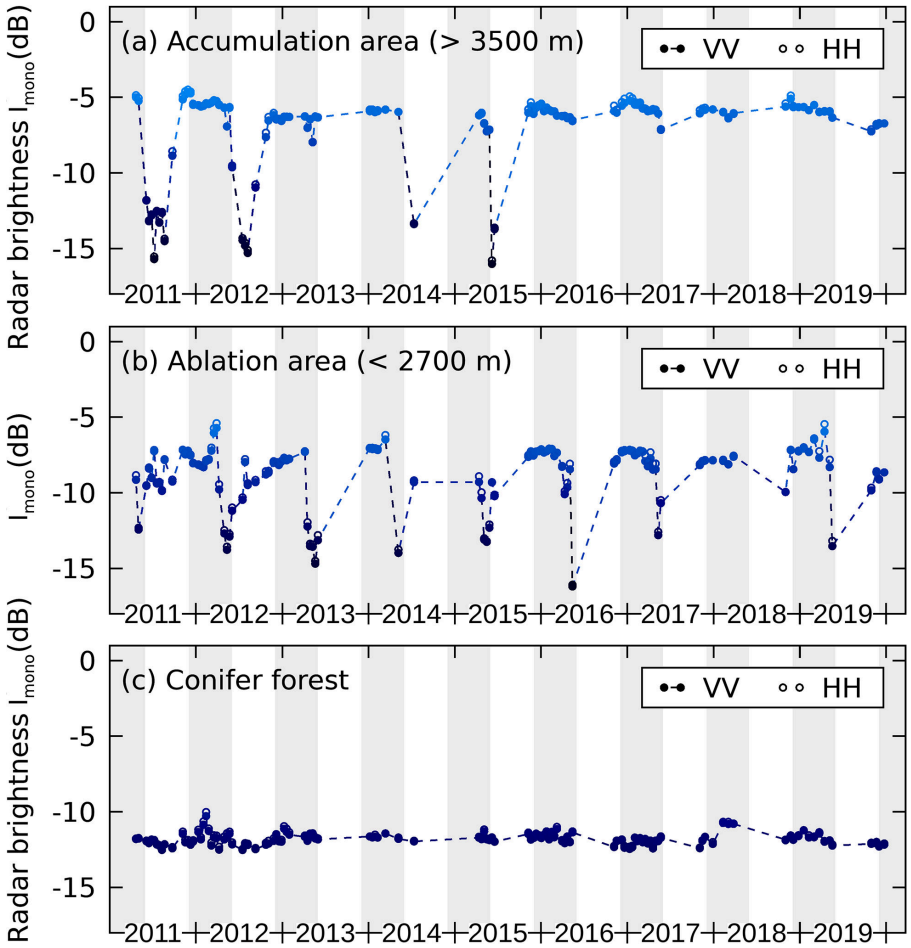

FIGURE 4.10: Time series of the monostatically measured radar brightness $\hat{I}_{\text{mono}}$ observed by the satellite TanDEM-X for three different land cover types: **(a)** deep firn in accumulation areas above 3500 m and **(b)** the tongue of the Great Aletsch Glacier which is covered by 0–3 m of snow in winter. In **(a)** and **(b)** seasonal variations in I_{mono} provide a good indicator for distinguishing between dry and wet snow. Gray shading indicates the period 1 December–31 May when dry firn is most likely present in the accumulation zone. This period was selected for estimation of the absorption and scattering lengths Λ_{A} and Λ_{T}. A backscatter difference between the VV and HH polarized data is hardly visible. **(c)** Compared to snow, forest (mainly conifer forest) shows only small variations in the radar brightness when summer and winter acquisitions are available (2011–2013).

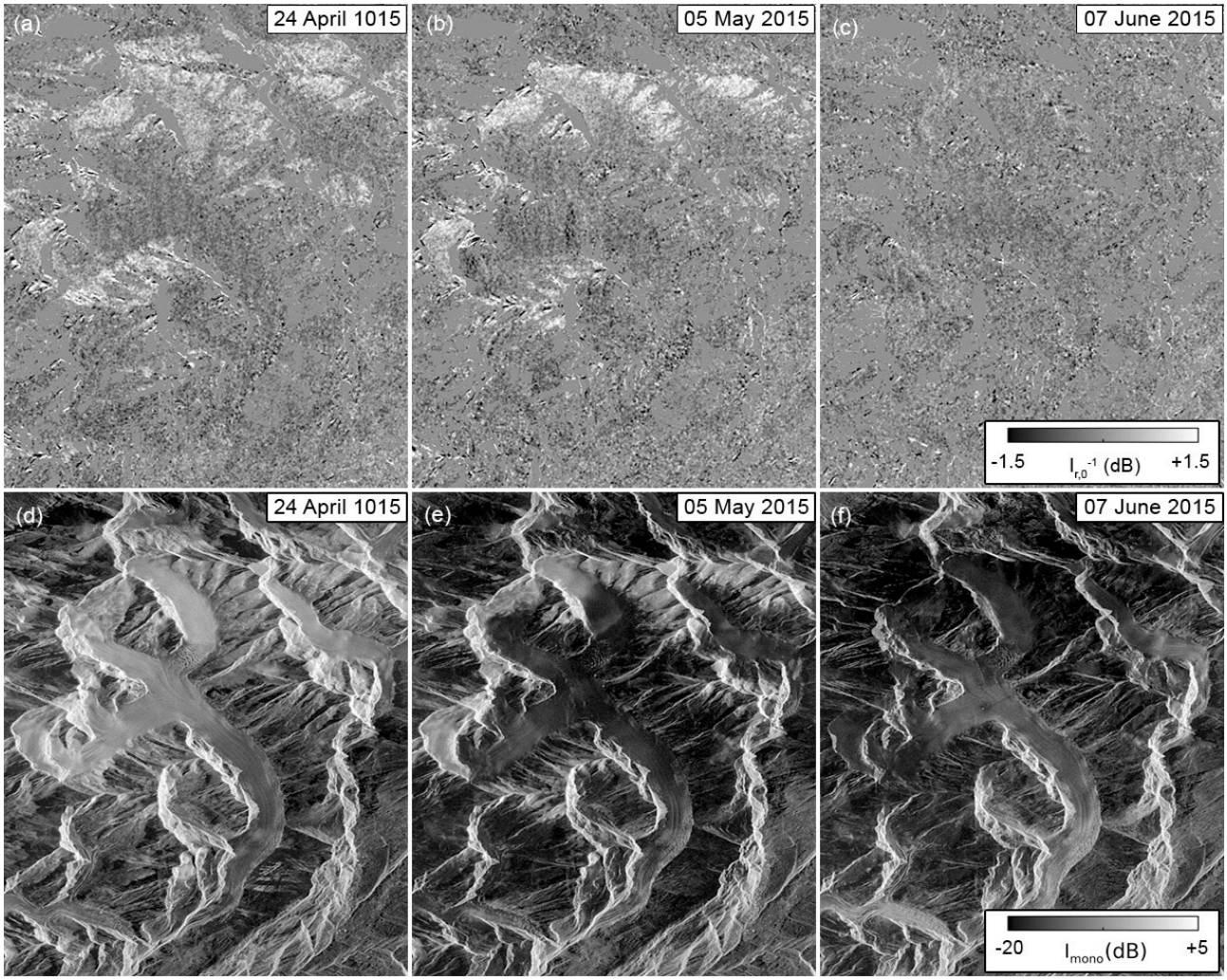

FIGURE 4.11: **(a–c)** Monostatic-to-bistatic backscatter ratio $\hat{I}_{r,0}^{-1}$, observed by TanDEM-X at the largest available bistatic angles $\beta_{\max} = 0.2°$ before **(a)** and during **(b, c)** snowmelt. **(d–f)** Radar brightness for the same dates (**d**: before snowmelt; **e, f**: during snowmelt). Areas covered by wet snow appear dark. The Great Aletsch Glacier flows clockwise from top to bottom. In **(a)** and **(b)**, high-altitude areas (above 3000 and above 3400 m) show backscatter enhancement. In **(c)** wet snow is present in the entire scene and absorption prevents the CBOE. In **(f)** an increase in the backscatter intensity becomes visible on the tongue of the Great Aletsch Glacier and on nearby vegetation-covered slopes, indicating that in these areas all snow has melted. Images are shown in slant-range and azimuth coordinates.

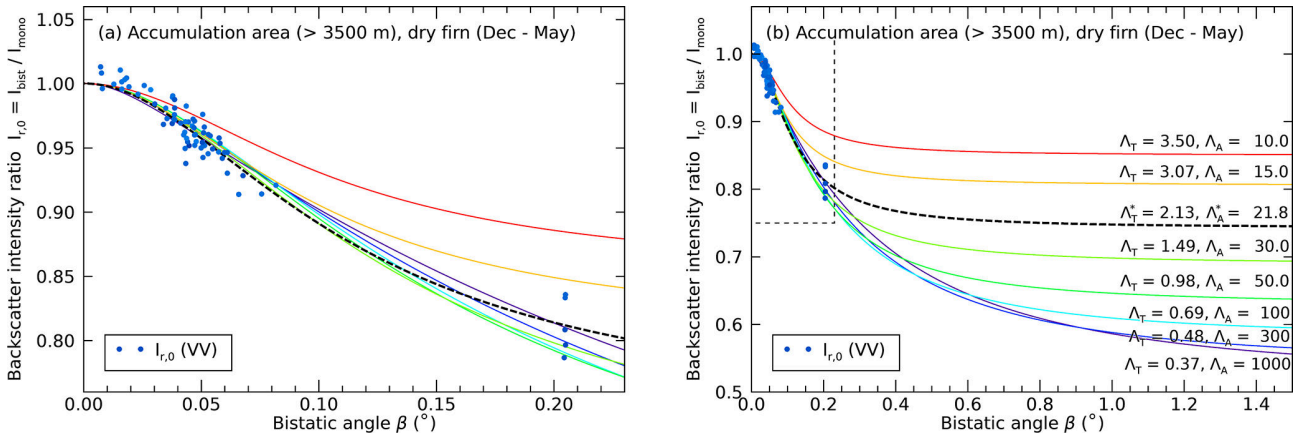

FIGURE 4.12: **(a)** Backscatter ratios $\hat{I}_{r,0}(\beta)$ (dots) restricted to dry firn observations in winter (1 December–31 May; $I_{\text{mono}} > -8\,\text{dB}$) in the accumulation areas of the Jungfrau–Aletsch region from TanDEM-X at VV polarization. Colored lines indicate different CBOE model curves, Eq. (4.13), parametrized by a range of scattering and absorption parameter combinations (Λ_T, Λ_A) that can describe the data to different degrees. **(b)** Same as **(a)** (in dashed box) but zoomed out to visualize at which β values the different model fits converge to the flat region of the intensity curve $I_{r,0}(\beta \to \infty)$ where coherent backscatter enhancement is negligible. Measurements at larger bistatic angles of $\beta > 0.5°$ could substantially better constrain the total peak height (and thereby Λ_A), but such large angles are currently not available.

The solutions are parametrized by different pairs of scattering and absorption mean free paths Λ_T and Λ_A and were determined by finding Λ_T for a fixed Λ_A. Table 4.1 summarizes these parameter pairs and lists for each solution the modeled peak characteristics and the RMSE with respect to the measured data.

Figure 4.12b illustrates how the different model solutions asymptotically reach the incoherent background $I_{r,0}(\beta \to \infty)$ at large bistatic angles. The sampling of larger bistatic angles would reveal whether significantly lower values of $I_{r,0}(\beta)$ than those observed exist and would, therefore, allow a better constraint on the model parameters.

A contour map of the RMSE between the measured and the modeled values (VV) is shown in Fig. 4.13. While the shallow global minimum (RMSE = 0.0106) is located at the optimal solution $\Lambda_T = 2.13\,\text{m}$ and $\Lambda_A = 21.8\,\text{m}$, multiple other solutions exist that show only slightly higher RMSE values between 0.011 and 0.015 (see also Table 4.1). This set of possible parameter pairs (Λ_A, Λ_T) forms a nonlinear curve (1-dimensional manifold) in the 2-dimensional parameter space (red "+" symbols in Fig. 4.13).

TABLE 4.1: Scattering length Λ_T, peak height $B_C(0)$, and peak width (HWHM) for a set of chosen absorption lengths Λ_A determined from the TanDEM-X dataset (VV) of dry firn in the high-altitude accumulation area. The bold-formatted rows indicate the optimal parameter pair at VV and HH polarization. RMSE is the root mean square error between the measured and the modeled value of $I_{r,0}$.

Λ_A (m)	Λ_T (m)	$B_C(0)$	HWHM (deg)	RMSE
1000	0.37	0.92	0.28	0.0111
300	0.48	0.85	0.25	0.0117
100	0.69	0.72	0.21	0.0129
50	0.98	0.59	0.17	0.0129
30	1.49	0.45	0.14	0.0116
25.9	**1.63**	**0.41**	**0.14**	**0.0103** (HH)
21.8	**2.13**	**0.35**	**0.12**	**0.0106** (VV)
15	3.08	0.24	0.10	0.0145
10	3.50	0.18	0.11	0.0257

4.4 DISCUSSION

4.4.1 *Cause of enhancement – CBOE vs. SHOE*

In both Ku-band and X-band observations of terrestrial snow, we observed narrow intensity peaks with an angular width of a fraction of 1°. These peaks are clearly attributable to the CBOE as opposed to the SHOE, which follows from a comparison of the effects' properties as described by [1, chap. 9].

Firstly, the SHOE requires that the scatterers are much larger than the wavelength of the incident radiation so that they can cast sharp shadows. This requirement can hardly be fulfilled at radar wavelengths of several centimeters since ice particles in snow have average diameters on the order of millimeters [61]. A grain size of 0.3–1.5 mm was observed in the seasonal snowpack studied by the KAPRI experiment (Fig. 4.2). The snowpack did not show any centimeter-sized ice structures that could have been caused by strong melt events. Furthermore, the narrow peak width is in agreement with characteristics of the CBOE, while a SHOE peak usually has a width of several degrees or tens of degrees, depending on particle size distribution. Finally, the SHOE is only present in media where single scattering is dominant. Multiple-scattering processes decrease the amplitude of the SHOE and increase the amplitude of the CBOE. Since dry snow is a weakly absorbing medium for microwaves

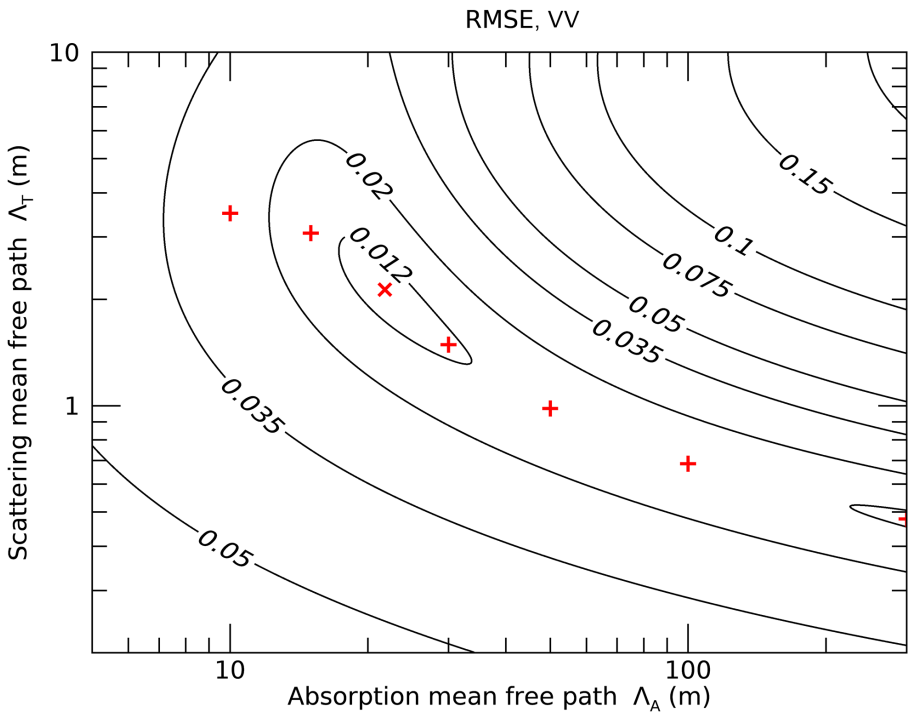

FIGURE 4.13: Contour map of root mean square error (RMSE) between measured and modeled data for TanDEM-X (Fig. 4.12) for different pairs of Λ_A and Λ_T. The plot shows a weak global minimum because acquisitions at sufficiently large β values that could better constrain Λ_A were not currently available. The model parameters and RMSE values for the red "+" symbols are given in Table 4.1. For these points, the parameter value of Λ_T was estimated by nonlinear least-squares minimization for different choices of Λ_A.

where multiple (i.e., volume) scattering is considerable [61], the CBOE is expected to be the dominant effect.

4.4.2 *Observations of CBOE*

4.4.2.1 *Ground-based observations – KAPRI*

Figure 4.7 shows a statistically significant enhancement peak for the winter acquisition and a lack of such a peak for the summer dataset, which was acquired using an identical target region of interest, identical acquisition procedure (except platform substitution to allow movement on snow/the road), and identical processing pipeline. The summer dataset thus serves as a useful control which ensures that the detected enhancement peak is not an erroneous artifact of the bistatic data processing pipeline, and it also indicates that the enhancement peak is indeed caused by the snow layer present on the hillside. In the summer scenario (i.e., absence of a clear backscatter enhancement peak), the model, described in Sect. 4.2.3 and visualized in Fig. 4.6, predicts that the absorption length is shorter than or

equal to the scattering length ($\Lambda_A \leq \Lambda_T$). An interpretation of this scenario is that higher-order scattering paths are suppressed due to absorption, and thus the summer scenario is dominated by a single-scattering process. In the summer scenario the model becomes much less sensitive to the precise value of Λ_T (which is a measure of the width of the peak), and thus estimates of this value have much higher uncertainty as opposed to the case of a clearly detectable enhancement peak in winter.

The best-fit values of model parameters in Fig. 4.7 indicate a scattering mean free path value Λ_T between 30 and 50 cm and an absorption length Λ_A between 6 and 24 m at both polarizations, which matches well the observations by [62]. No statistically significant difference in the parameter estimates is observed between the HH and VV polarized data. This is well aligned with the theoretical model of [57], in which there is only a very small difference between the co-polarized backscatter enhancement factors at these two polarizations. The HWHM of the angular peak of $\approx 0.25°$ is sufficiently wide so that KAPRI's transmit antennas' non-zero size, which limits the angular resolution to 0.05° (Sect. 4.2.1.2), has only a very limited effect on the precision with which the width and height of the peak can be determined.

The snow depth during the winter acquisitions was measured on-site as approximately 1.5 m (Fig. 4.2), and thus the estimate of Λ_A is several times higher than the snow depth. The extremely shallow local incidence angle (above 70° for the vast majority of the ROI area) and short transport mean free path Λ_T would likely lead to longer trajectories of the radiation through the snow medium before reaching the ground. Nevertheless, the optical thickness $\tau_d = E\,d \approx d/\Lambda_T$ of the snow depth d of only three to four scattering mean free paths Λ_T could limit higher-order scattering. While [52] conclude that already at $\tau_d = 4$, models approximate well the half-space solution (where $\tau_d = \infty$), [6] (Figs. 9, 12) show that the peak height and width, at least for very weakly absorbing media ($\Lambda_A \gg \Lambda_T$), might be affected up to $\tau_d \approx 30$. Missing higher-order scattering, in turn, is an explanation for a rounding of the peak shape ([4], Fig. 7). During the field experiment, a corner reflector lowered to the bottom of a 1.55 m deep snow pit with vertical walls was still visible, indicating that at least a fraction of microwaves reached the ground, thereby limiting higher-order scattering.

4.4.2.2 *Satellite observations – TanDEM-X*

A significant dependence of the backscatter intensity on the bistatic angle, $\hat{I}_{r,0}(\beta)$, is only visible in the accumulation zones of the Jungfrau–Aletsch region with altitude $H > 3500$ m (Fig. 4.9a, b). Above this altitude, a firn layer with below-freezing snow temperatures is present to a depth of several tens of meters ([63]; [44]). This thick and cold firn layer

represents a disordered medium where multiple scattering is possible and at the same time microwave absorption is weak because liquid water is absent. The existence of the CBOE in dry firn is further supported by the spatial and temporal distribution of an enhanced brightness ratio $\hat{I}_{r,0}$. Spatially, the enhancement matches the accumulation area of high-altitude glaciers in the Jungfrau–Aletsch region (Fig. 4.11). Temporally, the backscatter enhancement vanishes in these areas when snowmelt sets in, and thus the scattering predominantly takes place at the snow surface. These observations were confirmed by additional data from the Teram Shehr and Rimo glaciers in the Karakorum (see Supplement).

The rounding of the peak shape in Fig. 4.12a indicates that either absorption or a limited thickness of firn is present in the accumulation area. Field measurements indicate cold firn in at least the upper 8 m (Jacqueline Bannwart, personal communication, 2021), and literature data indicate that temperate firn might be present at around 15 m below the surface [44]. The global minimum at $\Lambda_T = 2.1\,\mathrm{m}$ and $\Lambda_A = 21.8\,\mathrm{m}$ in Fig. 4.13 might therefore provide a realistic estimate for Λ_A as larger absorption lengths are difficult to conform to field measurements. Our observed values for absorption and scattering lengths also agree with the measurements by [62].

On the tongue of the Great Aletsch Glacier, where a seasonal snowpack is present during winter, no backscatter enhancement was observed in the X-band (Fig. 4.9c). As seasonal snow is younger than multi-year firn, smaller snow grain sizes are expected, resulting in scattering lengths larger than the value $\Lambda_T = 2.1\,\mathrm{m}$ determined for the accumulation area. The thickness of the seasonal snowpack of 0–3 m corresponds therefore to an optical thickness of $\tau_d \approx 1$ or less, which considerably affects the peak intensity ([6], Fig. 9). In consequence, the single scattering at the (possibly rough) snow–ice interface at the bottom of the snowpack can remain the dominant scattering process. The low average number of scattering events in the seasonal snow volume is, therefore, not sufficient for the CBOE to occur on the ablation area of the Great Aletsch Glacier.

In forest-covered areas, no significant dependency of $\hat{I}_{r,0}$ on β is visible. We think the reason for this is that, compared to dry snow, multiple scattering at the X-band is reduced in forest due to absorption of microwaves; hence the CBOE is prevented.

We also did not observe coherent backscatter enhancement in any area other than the high-accumulation area, even though the tongue of the Great Aletsch Glacier is highly crevassed and valley slopes are covered by rock debris. From this we conclude that in the X-band, rough surfaces do not elicit the CBOE.

4.4.2.3 *Comparison of bistatic measurement geometries*

The KAPRI experiment sampled a larger range of bistatic angles (up to 1.92°) so that the flat incoherent intensity background I_0 could be sampled. Therefore, both the width and the height of the enhancement peak in winter can be constrained much better than with the TanDEM-X observations where $\beta_{\text{max}} \approx 0.2°$. This, in turn, translates to better-constrained estimates of parameters Λ_T and Λ_A as illustrated by the clearly visible global minimum in the plot of the RMSE value in Fig. 4.8 as compared to Fig. 4.13.

Compared to the KAPRI experiment, the bistatic angles sampled by TanDEM-X are relatively small, making it possible that not the entire peak of the CBOE was sampled. In consequence, the bistatic data at $\beta_{\text{max}} = 0.2°$ might still be affected by the CBOE. Missing measurements at larger bistatic angles result in a weak constraint of the parameter pair (Λ_T, Λ_A), permitting a range of value pairs that each can fit the data (Table 4.1 and Figs. 4.12 and 4.13). To better constrain the observed values of Λ_T and Λ_A, bistatic angles of at least $\beta = 0.5°$ would need to be sampled by TanDEM-X. However, such larger angles are currently not available.

4.4.3 *Impact of the CBOE on backscatter observations*

Generally, the existence of a narrow backscatter enhancement peak around the monostatic direction needs to be kept in mind when performing backscatter measurements of snow, regardless of whether the sensors used are considered monostatic or bistatic. On one hand, for truly monostatic sensors the CBOE is strongest. On the other hand, some radar sensors are considered monostatic even though they have a small but non-zero spatial separation between the transmitting and receiving antennas. Due to this bistatic baseline, the detected backscatter intensity value could be significantly reduced compared to the value that would have been detected by a truly monostatic sensor. When prior estimates of Λ_T and Λ_A over a particular medium are available, Eq. (4.6) could be used to roughly estimate the width and height of the peak, which can subsequently be used to estimate bistatic angle values where the CBOE might affect the measurements (see also Sect. 4.4.4).

As an example of the necessity to precisely align the measurement geometry to the expected width of the peak, [34] compared modeled results to active and passive microwave measurements at the X- to Ka-band performed in Sodankylä, Finland, as part of the NoSREx field experiment [64]. The active measurements were performed with the SnowScat instrument [65]. The model, which includes backscatter enhancement into the dense-media

radiative transfer (DMRT) theory, might provide a significant step forwards for modeling of the radar backscatter signal from snow. However, if the peak width of the CBOE in the NoSREx experiment were comparable to the narrow observed peak widths in our study (HWHM $\approx 0.2 \pm 0.1°$), the bistatic angles of the SnowScat measurements would actually be 1 order of magnitude too large to observe the CBOE. This follows from the instrument height of 9.6 m, the incidence angle range of 30–60° [64], and the antenna separation of 72 cm [65, 66], resulting in bistatic angle values of $\beta = 1.8$ to $\beta = 3.7°$.

Except for possible extreme cases of a medium causing an extremely narrow enhancement peak (with width on the order of thousandths of a degree), the velocity-induced bistatic angle β_v of moving radar platforms is negligible in the context of the CBOE. For the side-looking geometry, the bistatic angle β_v caused by platform motion with velocity v can be calculated as $\beta_\mathrm{v} = 2v/c$, where c is the speed of light. Thus, for all conventional sensors – even for satellite platforms in low Earth orbit moving at speeds of 6–8 $\mathrm{km\,h^{-1}}$ – the resulting value of β_v is on the order of thousandths of a degree or less.

4.4.4 *Link to the microstructure of snow*

In the model outlined in Sect. 4.2.3, which assumes an optically thick medium, the two parameters Λ_T and Λ_A, defining the peak shape, can be linked to the snow microstructure and to the density of snow. The transport mean free path $\Lambda_\mathrm{T} \geq \Lambda_S$ is a measure of the medium's scattering properties and corresponds to the scattering mean free path $\Lambda_S = S^{-1}$ for particles that scatter EM radiation symmetrically in the forward and backward direction ([1], Eq. 7.24b and Sect. 5.2.7); see also [6, Sect. IV-A]. For negligible absorption, Λ_T describes the one-way penetration depth where the incident radiation is reduced to $1/e$ by sideways scattering. While in the context of CBOE modeling, the (volume-averaged) scattering coefficient S is derived from the scattering cross-section of individual particles in sparse media ([1], chap. 5; [67], chap. 2; and [6]), for snow the scattering coefficient needs to be estimated with dense-media radiative transfer theories like DMRT (e.g., [68]) or the improved Born approximation (IBA) [69] as shown in Picard, Sandells & Löwe (2018, Sect. 3.1) and as already indicated by [56]. The description of the SMRT model [53] provides a direct relation between the scattering coefficient S and the phase function and links these to the autocorrelation function of the medium indicator function that represents the spatial 3D microstructure of the snow–ice matrix [70]. Still, both theories, DMRT and IBA, are not yet sufficiently parametrized by field-measurable quantities [53]. An empirical relation to link the microstructure to S is given in [71].

The absorption mean free path $\Lambda_A = A^{-1}$ is a measure of the medium's absorbing properties given by the volume-averaged absorption coefficient A ([1], Eq. 7.18a). For negligible scattering, Λ_A describes the absorption length where the incident radiation intensity is reduced to $1/e$; for continuous media (without scatterers) A would be equivalent to the absorption coefficient $\alpha = 4\pi/\lambda n_i$ with n_i being the imaginary part of the refractive index. For snow, [53] recommend computation of n_i from the Polder–van Santen formula, e.g., in [72], [69], and [71]; the refractive index of pure ice is given by [19].

The absorption and scattering coefficient sum to the extinction coefficient $E = S + A$, which corresponds in the sparse-media models from [3, 52] and Van Der Mark, van Albada & Lagendijk (1988, below Eq. 26b) by $E = 2K''$ to the effective propagation constant K'' that is related to particle absorption and scattering properties described by the scattering amplitude f.

4.4.5 *Limitations of the model*

The CBOE model used in this work can accurately predict the peak shapes observed in various volume fractions of colloidal suspensions where the particle sizes are within the order of magnitude of the wavelength [4, 6]. The parameters of the model, in particular the scattering coefficient $S \propto \Lambda_T^{-1}$ and absorption coefficient $A = \Lambda_A^{-1}$ that determine the shape of the CBOE peak, can, in theory, be estimated from the microstructure and density of the snowpack when considering dense-media scattering theories [53]; see also [56], who addresses a snow-like structure. However, the often complex (multi-layer) snow structure (e.g., [73]) together with current limitations in accurately predicting the scattering coefficients from the snow microstructure [74] might prevent a precise estimate of the peak shape even though a rough estimate of the peak width is feasible. An additional limitation for an accurate estimation of Λ_A, as well as possibly Λ_T, results from the assumption that the scattering medium fills a semi-infinite space, whereas the snowpack has a limited optical thickness τ_d. Hence, Λ_A might be underestimated due to limited layer thickness [6, 16].

Our observations of the CBOE peak shape originate from natural (non-homogeneous) snow cover, and currently no laboratory experiments of the CBOE at microwave frequencies, including a precise characterization of the microstructure, are available. Such experiments could validate the model used and might indicate whether adaption of the model or introduction of additional correction factors could be required in order to precisely link the microstructure to the CBOE peak shape. Nevertheless, we clearly observed the CBOE

peak in natural snow, which can lead to development of new methods for snow and ice monitoring.

4.4.6 *Applications based on the CBOE*

In TanDEM-X data we have observed a backscatter enhancement of at least 1.3 dB for firn-covered areas of the European Alps and in the Karakorum, while for firn-free areas no backscatter enhancement could be observed. This suggests that detection of deep firn with the X-band is possible when large enough bistatic angles, $\beta > 0.2^\circ$, are available.

For seasonal snow, we observed a clear CBOE peak ($\sim$ 1.8 dB of backscatter enhancement) at the Ku-band using KAPRI, whereas in the X-band we were not able to observe an enhancement. The higher sensitivity of high-frequency systems (Ku- or possibly Ka-band) for detecting the CBOE in seasonal snow results from the shorter scattering length since sufficiently high-order scattering events can occur within the snow layer of limited thickness. Furthermore, the difference between KAPRI observations in summer (no CBOE from vegetation) and winter (snow-induced CBOE) demonstrates how Ku-band bistatic observations could potentially provide a means to discriminate dry snow from vegetation and therefore provide a means to map snow cover extent. Beyond that, the frequency dependency of the scattering lengths makes a characterization of the intensity of the CBOE at multiple frequencies possible, which, in turn, could allow a quantitative characterization of the height or water equivalent of seasonal snow. The area covered by snow, the snow depth, and the snow water equivalent are considered key data products for the snow essential climate variable [75]. Bistatic missions characterizing the CBOE occurring in snow can thus be an asset in mapping these data products.

In terms of polarimetric measurements, the results of this study, as well as experimental work and theoretical models [12, 55, 57, 58], indicate that the effect is present predominantly in co-polarized channels and the effect is equally strong at both horizontal and vertical polarizations. Nevertheless, in further studies the use of full-polarimetric radar systems can still be advantageous, e.g., to decisively differentiate the CBOE and the SHOE based on their different impact on linear and circular polarization ratios ([1, 26], Sect. 9.4).

Existing bistatic ground-based SAR sensors [76, 77] and to a certain extent also airborne bistatic SAR sensors [78, 79] could be employed to study the effect locally with a high temporal resolution and to observe temporal variations in the effect as well as its dependence on layer thickness and snow structure. Spaceborne platforms, while limited by orbital mechanics and repeat intervals, can provide a means to sample and to characterize the

CBOE on the global scale. Finally, our characterization of the CBOE at the X- and Ku-band in terrestrial snow could inspire future inter-planetary missions aiming to search for water ice and possibly other types of snow to employ bistatic radar measurements.

4.5 CONCLUSIONS

In this work we presented the first observations of the coherent backscatter opposition effect (CBOE) and the sampling of its angular peak shape at radio wavelengths within the Earth's cryosphere. The existence of the peak was confirmed in seasonal dry snow cover at Ku-band wavelengths by the ground-based bistatic radar system KAPRI. With the bistatic satellite formation TanDEM-X, the effect was also confirmed at the X-band within the accumulation zone of high-altitude glaciers in the European Alps and the Karakorum.

The observability of the CBOE in bistatic radar measurements of snow presents an opportunity for future satellite missions aiming to derive snow properties from synthetic-aperture radar data on the global scale. The radiometric precision requirement for such a spaceborne radar system is demanding since the theoretical maximal amplitude of the effect is 3 dB – in this study, we were able to characterize the peak using TanDEM-X and data-driven radiometric calibration. Deployment of such bistatic systems – at bistatic angles up to 1 or 2° and covering the entire CBOE peak including the incoherent background – would open up a new pathway to characterize snow through microwave scattering.

The Ku-band observations presented in this paper suggest that the CBOE can be used as an indicator for presence of seasonal snow cover. At the X-band, the CBOE could be applied to detect dry snow thicker than several meters, e.g., multi-year firn in accumulation areas of glaciers. Furthermore, through analysis of the angular width and height of the enhancement peak, scattering and absorption mean free paths within the snowpack can be estimated. Knowledge of the scattering mean free path and the discrimination between single (surface) and higher-order (volume) scattering in areas where the CBOE is present could help to better constrain the radar penetration depth, which, in turn, is crucial for precise surface height estimation by means of radar altimetry and interferometry.

The CBOE thus provides a pathway towards better characterization of areas covered by snow and possibly also snow depth and snow water equivalent, which are the three key data products for snow as an essential climate variable. Furthermore, the detection and characterization of the CBOE in terrestrial snow also are an encouraging sign for applying this measurement concept to space missions which aim to confirm the presence of water ice on surfaces of other solar system bodies.

ACKNOWLEDGEMENTS

The authors would like to thank Henning Löwe and the anonymous reviewer for their in-depth peer reviews and for constructive comments and suggestions on how to improve the paper. Furthermore, the authors would like to thank Tingting Li, Yuta Izumi, Simone Jola, and Michael Arnold for their support during fieldwork in Davos; Christian Mätzler and Rosemary Willatt for valuable feedback and discussion; Emmanuel Trouvé for proofreading the manuscript; Laurane Charrier for valuable input regarding applications of the CBOE; and Thomas Busche for support with the TanDEM-X acquisitions. The authors would also like to thank Reto Müller for access to his property during acquisitions and the staff of Bergbahnen Rinerhorn AG for assistance with equipment transportation. The TanDEM-X data were provided by the German Aerospace Center (DLR) via proposal XTI_GLAC6780.

Financial statement: Silvan Leinss was supported by the French Ministry for Europe and Foreign Affairs, within the framework of the third "Make Our Planet Great Again" (MOPGA) program (mopga-postdoc-3) for postdoctoral researchers. The MOPGA grant has been issued by Campus France under grant no. 0821369222.

Data availability: TanDEM-X data are available from DLR at `https://tandemx-science.dlr.de/`and were provided by the proposal leinss_XTI_GLAC6870. KAPRI SLC data, as well as data values for plots, are published in the ETH Research Collection with the DOI 10.3929/ethz-b-000516171.

Supplement. The supplement related to this article is available on-line at:
https://doi.org/10.5194/tc-16-2859-2022-supplement

Author contributions: SL conceptualized the study of coherent backscatter enhancement in snow with bistatic radar. MS and SL designed the Davos field experiment and wrote the manuscript together. MS processed and analyzed the ground-based data and SL the spaceborne data. IH suggested exploration of bistatic radar signals with KAPRI. All authors reviewed, edited, and approved the submitted version of the manuscript.

Review statement: This paper was edited by Carrie Vuyovich and reviewed by Henning Löwe and one anonymous referee.

REFERENCES

1. Hapke, B. *Theory of reflectance and emittance spectroscopy, second edition* 1. doi:`10.1017/CBO9781139025683` (Cambridge University Press, Cambridge, 2012).

2. Kuga, Y. & Ishimaru, A. Retroreflectance from a dense distribution of spherical particles. *Journal of the Optical Society of America A* **1**, 831. doi:10.1364/josaa.1.000831 (1984).

3. Tsang, L. & Ishimaru, A. Backscattering enhancement of random discrete scatterers. *Journal of the Optical Society of America A* **1**, 836. doi:10.1364/josaa.1.000836 (1984).

4. Akkermans, E., Wolf, P. E., Maynard, R. & Maret, G. Theoretical study of the coherent backscattering of light by disordered media. *Journal de Physique* **49**, 77. doi:10.1051/jphys:0198800490107700 (1988).

5. Aegerter, C. M. & Maret, G. in *Progress in Optics* 1 (Elsevier, 2009). doi:10.1016/S0079-6638(08)00003-6.

6. Van Der Mark, M. B., van Albada, M. P. & Lagendijk, A. Light scattering in strongly scattering media: multiple scattering and weak localization. *Physical Review B* **37**, 3575. doi:10.1103/PhysRevB.37.3575 (1988).

7. Hapke, B. Bidirectional reflectance spectroscopy: 4. The extinction coefficient and the opposition effect. *Icarus* **67**, 264. doi:10.1016/0019-1035(86)90108-9 (1986).

8. Hapke, B., DiMucci, D., Nelson, R. & Smythe, W. The cause of the hot spot in vegetation canopies and soils: Shadow-hiding versus coherent backscatter. *Remote Sensing of Environment* **58**, 63. doi:10.1016/0034-4257(95)00257-X (1996).

9. Hapke, B., Nelson, R. & Smythe, W. The Opposition Effect of the Moon: Coherent Backscatter and Shadow Hiding. *Icarus* **133**, 89. doi:10.1006/icar.1998.5907 (1998).

10. Montgomery, W. W. & Kohl, R. H. Opposition-effect experimentation. *Optics Letters* **5**, 546. doi:10.1364/OL.5.000546 (1980).

11. Mishchenko, M. I., Luck, J.-M. & Nieuwenhuizen, T. M. Full angular profile of the coherent polarization opposition effect. *Journal of the Optical Society of America A* **17**, 888. doi:10.1364/JOSAA.17.000888 (2000).

12. Wolf, P. E. & Maret, G. Weak localization and coherent backscattering of photons in disordered media. *Physical Review Letters* **55**, 2696. doi:10.1103/PhysRevLett.55.2696 (1985).

13. Van Albada, M. P. & Lagendijk, A. Observation of weak localization of light in a random medium. *Physical Review Letters* **55**, 2692. doi:10.1103/PhysRevLett.55.2692 (1985).

14. Akkermans, E., Wolf, P. E. & Maynard, R. Coherent backscattering of light by disordered media: Analysis of the peak line shape. *Physical review letters* **56**, 1471. doi:10.1103/PhysRevLett.56.1471 (1986).

15. Wolf, P. E., Maret, G., Akkermans, E. & Maynard, R. Optical coherent backscattering by random media : an experimental study. *Journal de Physique* **49**, 63. doi:10.1051/jphys:0198800490106300 (1988).

16. Van Albada, M. P., Van Der Mark, M. B. & Lagendijk, A. Polarisation effects in weak localisation of light. *Journal of Physics D: Applied Physics* **21**, S28. doi:10.1088/0022-3727/21/10S/009 (1988).

17. Van Albada, M. P., Van der Mark, M. B. & Lagendijk, A. in *Scattering and Localization of Classical Waves in Random Media* 97 (World Scientific, 1990). doi:10.1142/9789814340687_0002.

18. Kaasalainen, S., Kaasalainen, M., Mielonen, T., Suomalainen, J., Peltoniemi, J. I. & Näränen, J. Optical properties of snow in backscatter. *Journal of Glaciology* **52**, 574. doi:10.3189/172756506781828421 (2006).

19. Warren, S. G. & Brandt, R. E. Optical constants of ice from the ultraviolet to the microwave: A revised compilation. *Journal of Geophysical Research: Atmospheres* **113**, 1. doi:10.1029/2007JD009744 (2008).

20. Mätzler, C. & Wegmüller, U. Dielectric properties of freshwater ice at microwave frequencies. *J. Phys. D: Appl. Phys.* **20**, 1623. doi:http://dx.doi.org/10.1088/0022-3727/20/12/013 (1987).

21. Mätzler, C. & Wegmüller, U. Dielectric properties of freshwater ice at microwave frequencies - Errata. *J. Phys. D: Appl. Phys.* **20**, 1623 (1987).

22. Muhleman, D. O., Butler, B. J., Grossman, A. W. & Slade, M. A. Radar images of mars. *Science* **253**, 1508. doi:10.1126/science.253.5027.1508 (1991).

23. Black, G. J., Campbell, D. B. & Nicholson, P. D. Icy Galilean Satellites: Modeling Radar Reflectivities as a Coherent Backscatter Effect. *Icarus* **151**, 167. doi:10.1006/icar.2001.6616 (2001).

24. Hapke, B. W., Nelson, R. M. & Smythe, W. D. The Opposition Effect of the Moon: The Contribution of Coherent Backscatter. *Science* **260**, 509. doi:10.1126/science.260.5107.509 (1993).

25. Rignot, E. J., Ostro, S. J., van Zyl, J. J. & Jezek, K. C. Unusual Radar Echoes from the Greenland Ice Sheet. *Science* **261**, 1710. doi:10.1126/science.261.5129.1710 (1993).

26. Rignot, E. J. Backscatter model for the unusual radar properties of the Greenland ice sheet. *Journal of Geophysical Research* **100**, 9389. doi:10.1029/95JE00485 (1995).

27. Hapke, B. Coherent backscatter and the radar characteristics of outer planet satellites. *Icarus* **88**, 407. doi:10.1016/0019-1035(90)90091-M (1990).

28. Simpson, R. A. Spacecraft Studies of Planetary Surfaces Using Bistatic Radar. *IEEE Transactions on Geoscience and Remote Sensing* **31**, 465. doi:10.1109/36.214923 (1993).

29. Palmer, E. M., Heggy, E. & Kofman, W. Orbital bistatic radar observations of asteroid Vesta by the Dawn mission. *Nature Communications* **8**. doi:10.1038/s41467-017-00434-6 (2017).

30. Yushkova, O. V., Gavrik, A. L., Marchuk, V. N., Yushkov, V. V., Smirnov, V. M., Laptev, M. A., Chernyshev, B. V., Dutyshev, I. N., Lebedev, V. P., Medvedev, A. V. & Petrukovich, A. A. Bistatic Radar Detection in the Luna-Resurs Mission. *Solar System Research* **52**, 287. doi:10.1134/S0038094618040081 (2018).

31. Nozette, S., Lichtenberg, C. L., Spudis, P., Bonner, R., Ort, W., Malaret, E., Robinson, M. & Shoemaker, E. M. The Clementine bistatic radar experiment. *Science* **274**, 1495. doi:10.1126/science.274.5292.1495 (1996).

32. Simpson, R. A. & Tyler, G. L. Reanalysis of Clementine bistatic radar data from the lunar South Pole. *Journal of Geophysical Research: Planets* **104**, 3845. doi:10.1029/1998JE900038 (1999).

33. Patterson, G. W., Stickle, A. M., Turner, F. S., Jensen, J. R., Bussey, D. B. J., Spudis, P., Espiritu, R. C., Schulze, R. C., Yocky, D. A., Wahl, D. E., Zimmerman, M., Cahill, J. T. S., Nolan, M., Carter, L., Neish, C. D., Raney, R. K., Thomson, B. J., Kirk, R., Thompson, T. W., Tise, B. L., Erteza, I. A. & Jakowatz, C. V. Bistatic radar observations of the Moon using Mini-RF on LRO and the Arecibo Observatory. *Icarus* **283**, 2. doi:10.1016/j.icarus.2016.05.017 (2017).

34. Tan, S., Chang, W., Tsang, L., Lemmetyinen, J. & Proksch, M. Modeling Both Active and Passive Microwave Remote Sensing of Snow Using Dense Media Radiative Transfer (DMRT) Theory with Multiple Scattering and Backscattering Enhancement. *IEEE Journal of Selected Topics in Applied Earth Observations and Remote Sensing* **8**, 4418. doi:10.1109/JSTARS.2015.2469290 (2015).

35. Werner, C., Wiesmann, A., Strozzi, T., Kos, A., Caduff, R. & Wegmiüler, U. *The GPRI multi-mode differential interferometric radar for ground-based observations* in *EUSAR 2012; 9th European Conference on Synthetic Aperture Radar* (2012), 304.

36. Baffelli, S., Frey, O., Werner, C. & Hajnsek, I. Polarimetric Calibration of the Ku-Band Advanced Polarimetric Radar Interferometer. *IEEE Transactions on Geoscience and Remote Sensing* **56**, 2295. doi:10.1109/TGRS.2017.2778049 (4 2018).

37. Stefko, M., Frey, O., Werner, C. & Hajnsek, I. Calibration and Operation of a Bistatic Real-Aperture Polarimetric-Interferometric Ku-Band Radar. *IEEE Transactions on Geoscience and Remote Sensing* **60**, 1. doi:10.1109/TGRS.2021.3121466 (2022).

38. Stefko, M., Frey, O., Werner, C. & Hajnsek, I. *KAPRI: A Bistatic Full-Polarimetric Interferometric Real-Aperture Radar System for Monitoring of Natural Environments* in *2021 IEEE International Geoscience and Remote Sensing Symposium IGARSS* (IEEE, 2021), 1950. doi:10.1109/IGARSS47720.2021.9553427.

39. Lucas, C., Leinss, S., Bühler, Y., Marino, A. & Hajnsek, I. Multipath interferences in ground-based radar data: A case study. *Remote Sensing* **9**, 1. doi:10.3390/rs9121260 (2017).

40. Fierz, C., Armstrong, R. L., Durand, Y., Etchevers, P., Greene, E., McClung, D. M., Nishimura, K., Satyawali, P. K. & Sokratov, S. A. *The International Classification for Seasonal Snow on the Ground* 2009.

41. Krieger, G., Moreira, A., Fiedler, H., Hajnsek, I., Werner, M., Younis, M. & Zink, M. TanDEM-X: A satellite formation for high-resolution SAR interferometry. *IEEE Transactions on Geoscience and Remote Sensing* **45**, 3317. doi:10.1109/TGRS.2007.900693 (2007).

42. Hajnsek, I., Busche, T., Krieger, G., Zink, M., Schulze, D. & Moreira, A. *Announcement of opportunity: TanDEM-X science phase* tech. rep. TD-PD-PL-0032 (Microwave and Radar Institute (DLR-HR), 2014).

43. Leinss, S. & Bernhard, P. TanDEM-X:Deriving InSAR Height Changes and Velocity Dynamics of Great Aletsch Glacier. *IEEE Journal of Selected Topics in Applied Earth Observations and Remote Sensing* **14**, 4798. doi:10.1109/JSTARS.2021.3078084 (2021).

44. Suter, S., Laternser, M., Haeberli, W., Frauenfelder, R. & Hoelzle, M. Cold firn and ice of high-altitude glaciers in the Alps: measurements and distribution modelling. *Journal of Glaciology* **47**, 85. doi:10.3189/172756501781832566 (2001).

45. Suter, S. & Hoelzle, M. Cold firn in the Mont Blanc and Monte Rosa areas, European Alps: spatial distribution and statistical models. *Annals of Glaciology* **35**, 9. doi:10.3189/172756402781817059 (2002).

46. Jun, L., Wang, W. & Zwally, H. J. Interannual variations of shallow firn temperature at Greenland summit. *Annals of Glaciology* **35**, 368. doi:10.3189/172756402781816933 (2002).

47. Zemp, M., Hoelzle, M. & Haeberli, W. Distributed modelling of the regional climatic equilibrium line altitude of glaciers in the European Alps. *Global and Planetary Change* **56**, 83. doi:https://doi.org/10.1016/j.gloplacha.2006.07.002 (2007).

48. Duque, S., Balss, U., Rossi, S., Fritz, T. & Balzer, W. *TanDEM-X Payload Ground Segment CoSSC Generation and Interferometric Considerations, TD-PGS-TN-3129, issue 1.0* Remote Sensing Technology Institute, DLR (2012).

49. Raney, R. K., Freeman, T., Hawkins, R. W. & Bamler, R. *A plea for radar brightness* in *Proceedings of IGARSS '94 - 1994 IEEE International Geoscience and Remote Sensing Symposium* **2** (1994), 1090. doi:10.1109/IGARSS.1994.399352.

50. Fritz, T., Brautigam, B., Krieger, G. & Zink, M. *TanDEM-X Ground Segment - TanDEM-X Experimental Product Description, TD-GS-PS-3028, issue 1.2* 1.2. DLR (2012).

51. Oliver, C. & Quegan, S. *Understanding synthetic aperture radar images* (Scitech Publishing, Raleigh, NC, 2004).

52. Tsang, L. & Ishimaru, A. Theory of backscattering enhancement of random discrete isotropic scatterers based on the summation of all ladder and cyclical terms. *Journal of the Optical Society of America A* **2**, 1331. doi:10.1364/JOSAA.2.001331 (1985).

53. Picard, G., Sandells, M. & Löwe, H. SMRT: An active-passive microwave radiative transfer model for snow with multiple microstructure and scattering formulations (v1.0). *Geoscientific Model Development* **11**, 2763. doi:10.5194/gmd-11-2763-2018 (2018).

54. Akkermans, E. & Montambaux, G. Mesoscopic physics of photons. *J. Opt. Soc. Am. B* **21**, 101. doi:10.1364/JOSAB.21.000101 (2004).

55. Van Albada, M. P., van der Mark, M. B. & Lagendijk, A. Observation of weak localization of light in a finite slab: Anisotropy effects and light path classification. *Phys. Rev. Lett.* **58**, 361. doi:10.1103/PhysRevLett.58.361 (1987).

56. Mishchenko, M. I. The angular width of the coherent back-scatter opposition effect: an application to icy outer planet satellites. *Astrophysics and space science* **194**, 327. doi:10.1007/BF00644001 (1992).

57. Mishchenko, M. I. Polarization characteristics of the coherent backscatter opposition effect. *Earth, Moon and Planets* **58**, 127. doi:10.1007/BF00054650 (1992).

58. Mishchenko, M. I. Enhanced backscattering of polarized light from discrete random media: calculations in exactly the backscattering direction. *J. Opt. Soc. Am. A* **9**, 978. doi:10.1364/JOSAA.9.000978 (1992).

59. Virtanen, P., Gommers, R., Oliphant, T. E., Haberland, M., Reddy, T., Cournapeau, D., Burovski, E., Peterson, P., Weckesser, W., Bright, J., van der Walt, S. J., Brett, M., Wilson, J., Millman, K. J., Mayorov, N., Nelson, A. R. J., Jones, E., Kern, R., Larson, E., Carey, C. J., Polat, İ., Feng, Y., Moore, E. W., VanderPlas, J., Laxalde, D., Perktold, J., Cimrman, R., Henriksen, I., Quintero, E. A., Harris, C. R., Archibald, A. M., Ribeiro, A. H., Pedregosa, F., van Mulbregt, P. & SciPy 1.0 Contributors. SciPy 1.0: Fundamental Algorithms for Scientific Computing in Python. *Nature Methods* **17**, 261. doi:10.1038/s41592-019-0686-2 (2020).

60. Nelder, J. A. & Mead, R. A simplex method for function minimization. *The computer journal* **7**, 308. doi:10.1093/comjnl/7.4.308 (1965).

61. Kuga, Y., Ulaby, F. T., Haddock, T. F. & DeRoo, R. D. Millimeter-wave radar scattering from snow 1. Radiative transfer model. *Radio Science* **26**, 329. doi:10.1029/90RS02560 (1991).

62. Wiesmann, A., Mätzler, C. & Weise, T. Radiometric and structural measurements of snow samples. *Radio Science* **33**, 273. doi:10.1029/97RS02746 (1998).

63. Haeberli, W. & Alean, J. Temperature and Accumulation of High Altitude Firn in the Alps. *Annals of Glaciology* **6**, 161. doi:10.3189/1985AoG6-1-161-163 (1985).

64. Lemmetyinen, J., Kontu, A., Pulliainen, J., Vehviläinen, J., Rautiainen, K., Wiesmann, A., Mätzler, C., Werner, C., Rott, H., Nagler, T., Schneebeli, M., Proksch, M., Schüttemeyer, D., Kern, M. & Davidson, M. W. J. Nordic Snow Radar Experiment. *Geoscientific Instrumentation, Methods and Data Systems* **5**, 403. doi:10.5194/gi-5-403-2016 (2016).

65. Wiesmann, A., Werner, C., Strozzi, T., Mätzler, C., Nagler, T., Rott, H., Schneebeli, M. & Wegmuller, U. *SnowScat, X-to Ku-band scatterometer development* in *ESA Living Planet Symposium* **686** (2010), 160.

66. Wiesmann, A. & Werner, C. *SnowScat, X- to Ku-Band Scatterometer Development: D13 SnowScat User Manual* tech. rep. ESTEC/AO1-5311/06/NL/EL (ESA ESTEC / GAMMA, 2010).

67. Ishimaru, A. *Wave propagation and scattering in random media* (Academic press New York, 1978).

68. Tsang, L., Pan, J., Liang, D., Li, Z., Cline, D. W. & Tan, Y. Modeling Active Microwave Remote Sensing of Snow Using Dense Media Radiative Transfer (DMRT) Theory With Multiple-Scattering Effects. *IEEE Trans. Geosci. Remote Sens.* **45**, 990. doi:10.1109/TGRS.2006.888854 (2007).

69. Mätzler, C. Improved Born approximation for scattering of radiation in a granular medium. *J. Appl. Phys.* **83**, 6111. doi:http://dx.doi.org/10.1063/1.367496 (1998).

70. Löwe, H. & Picard, G. Microwave scattering coefficient of snow in MEMLS and DMRT-ML revisited: the relevance of sticky hard spheres and tomography-based estimates of stickiness. *The Cryosphere* **9**, 2101. doi:10.5194/tc-9-2101-2015 (2015).

71. Wiesmann, A. & Mätzler, C. Microwave emission model of layered snowpacks. *Remote sensing of environment* **70**, 307. doi:10.1016/S0034-4257(99)00046-2 (1999).

72. Sihvola, A. Mixing rules with complex dielectric coefficients. *Subsurface Sensing Technologies and Applications* **1**, 393. doi:10.1023/A:1026511515005 (2000).

73. Proksch, M., Löwe, H. & Schneebeli, M. Density, specific surface area, and correlation length of snow measured by high-resolution penetrometry. *Journal of Geophysical Research: Earth Surface* **120**, 346. doi:https://doi.org/10.1002/2014JF003266 (2015).

74. Vargel, C., Royer, A., St-Jean-Rondeau, O., Picard, G., Roy, A., Sasseville, V. & Langlois, A. Arctic and subarctic snow microstructure analysis for microwave brightness temperature simulations. *Remote Sensing of Environment* **242**, 111754. doi:https://doi.org/10.1016/j.rse.2020.111754 (2020).

75. Et al. Belward, A. *The global observing system for climate: implementation needs* tech. rep. GCOS-200 (World Meteorological Organization, 2016).

76. Pieraccini, M. & Miccinesi, L. *Bistatic GBSAR for detecting target elevation* in *2017 IEEE International Conference on Microwaves, Antennas, Communications and Electronic Systems (COMCAS)* (2017), 1. doi:10.1109/COMCAS.2017.8244728.

77. Wang, S., Feng, W., Kikuta, K., Chernyak, G. & Sato, M. *Ground-Based Bistatic Polarimetric Interferometric Synthetic Aperture Radar System* in *IGARSS 2019 - 2019 IEEE International Geoscience and Remote Sensing Symposium* (IEEE, 2019), 8558. doi:10.1109/IGARSS.2019.8900455.

78. Dubois-Fernandez, P., Cantalloube, H., Vaizan, B., Krieger, G., Horn, R., Wendler, M. & Giroux, V. ONERA-DLR bistatic SAR campaign: Planning, data acquisition, and first analysis of bistatic scattering behavior of natural and urban targets. *Radar, Sonar and Navigation, IEE Proceedings* - **153**, 214. doi:10.1049/ip-rsn:20045117 (2006).

79. Meta, A., Trampuz, C., Coccia, A., Placidi, S., Hendriks, L. C. I., Davidson, M. & Schuettemeyer, D. *Bistatic Airborne SAR Acquisitions at L-Band by MetaSensing: First Results* in *EUSAR 2018; 12th European Conference on Synthetic Aperture Radar* (2018), 1.

80. Agarwal, V., Bolch, T., Syes, T. H., Pieczonka, T., Strozzi, T. & Nagaich, R. Area and mass changes of Siachen Glacier (East Karakoram). *Journal of Glaciology* **63**, 148. doi:10.1017/jog.2016.127 (2017).

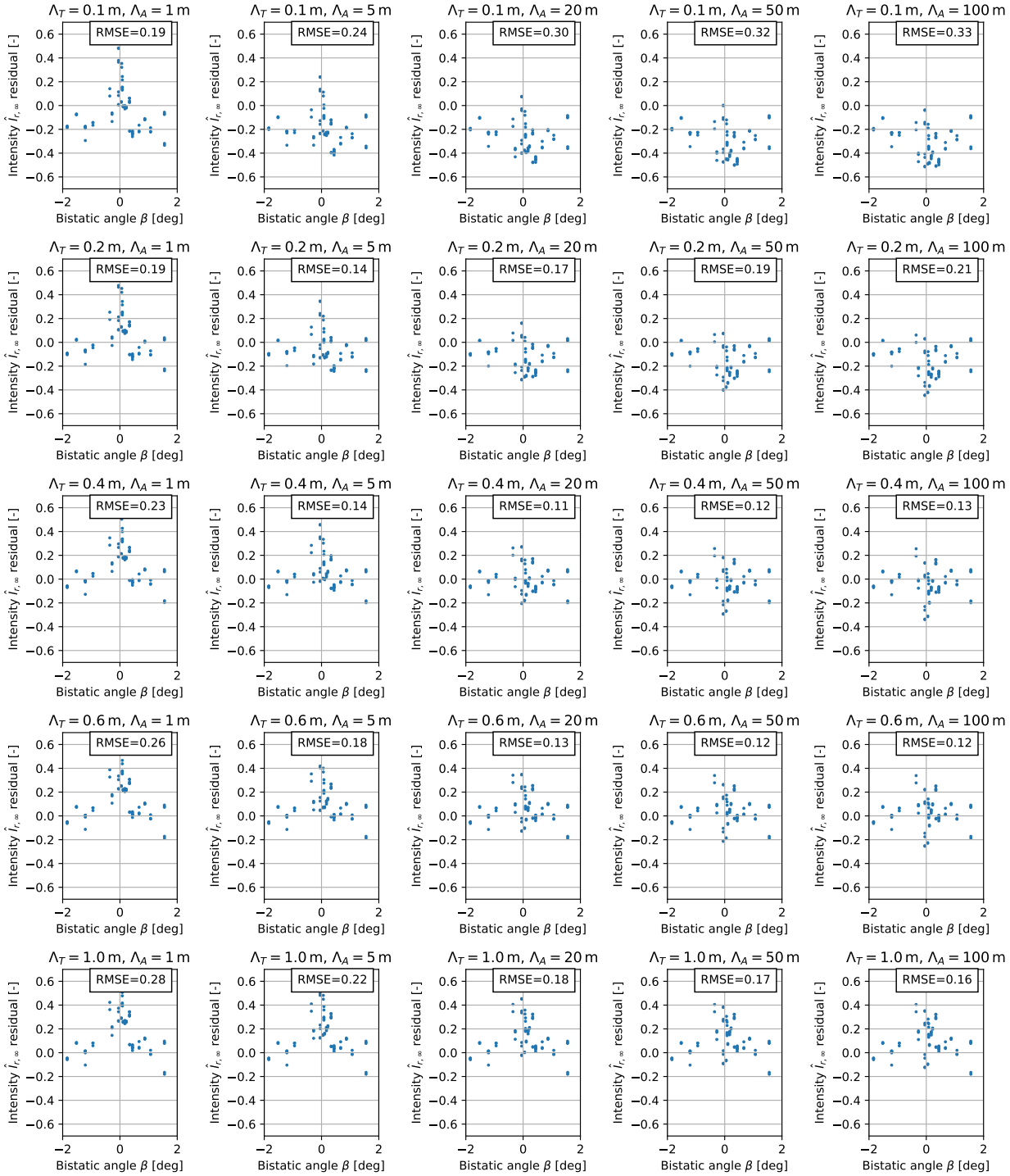

FIGURE S4.1: Plots of residuals of winter KAPRI measurements at Davos, Rinerhorn, in the VV polarimetric channel, with varying values of model parameters Λ_T (constant along rows) and Λ_A (constant along columns). The residual was computed as the difference between observed value of $\hat{I}_{r,\infty}$ and value predicted by the model $I_{r,\infty}$ defined by parameters Λ_T, Λ_A, at the corresponding bistatic angle β.

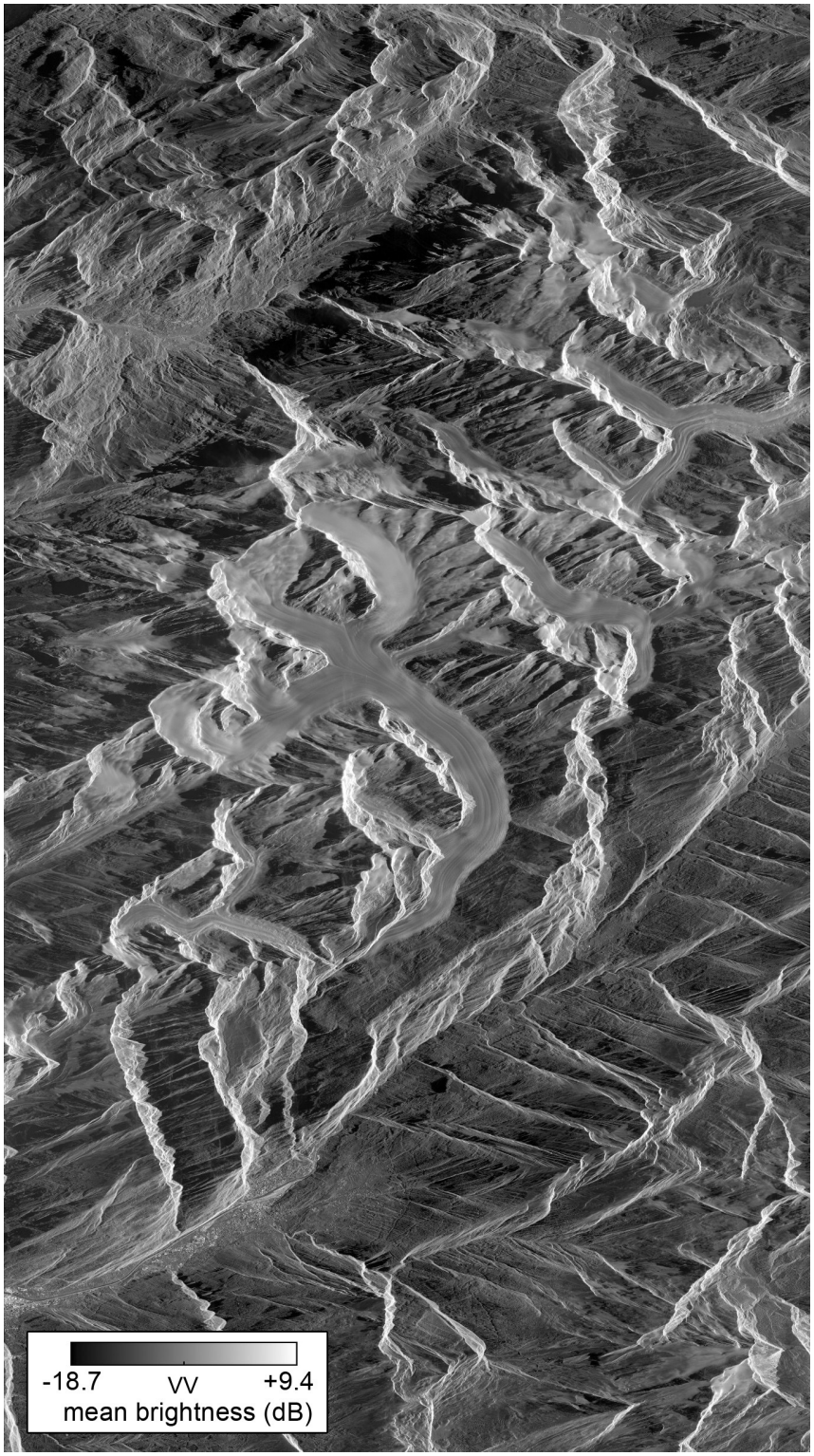

FIGURE S4.2: Intensity average of 118 TanDEM-X acquisitions of the Jungfrau-Aletsch region (VV polarization). The image has been flipped/rotated to align approximately with the north-direction. The slant-range direction is from right to left; azimuth from top to bottom.

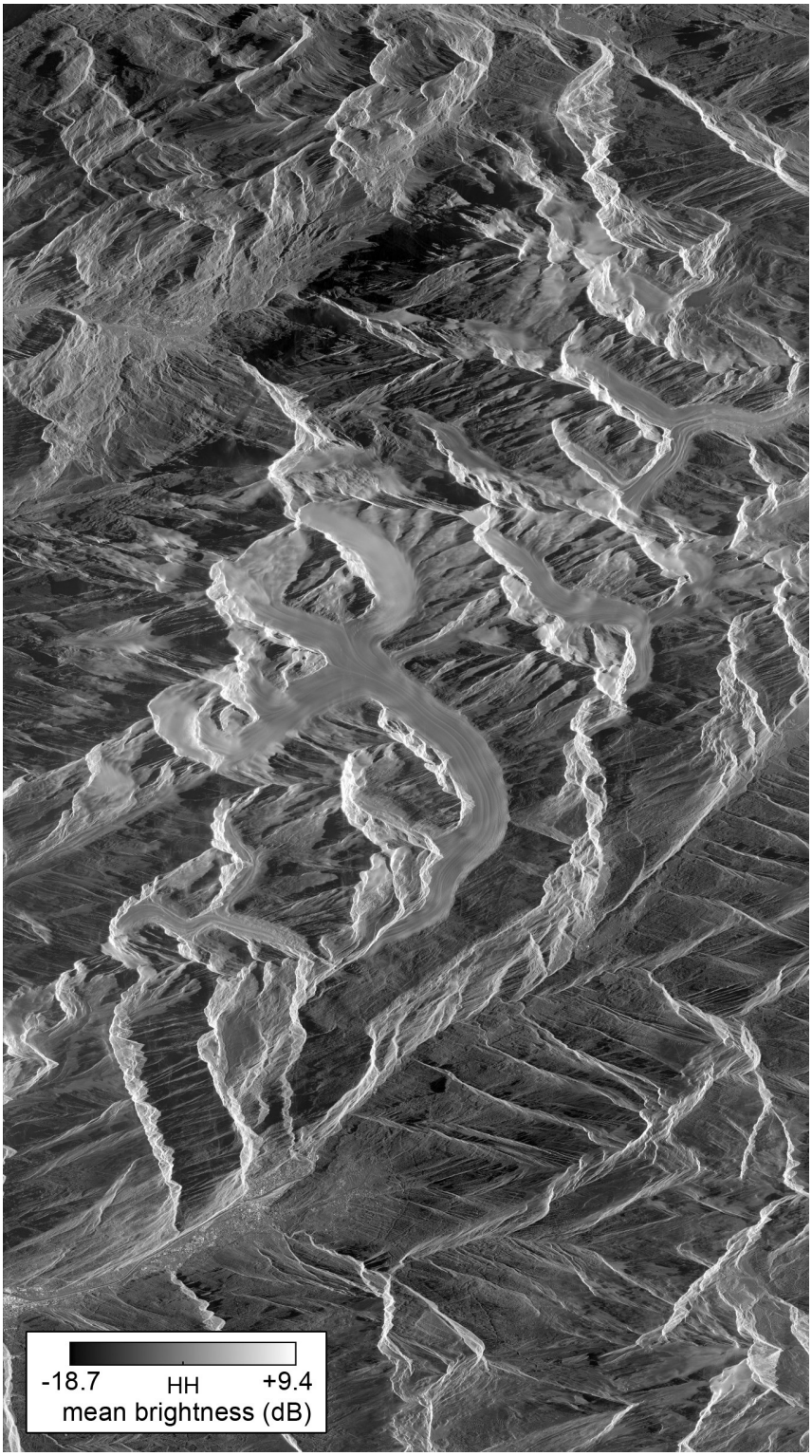

FIGURE S4.3: Intensity average of 118 TanDEM-X acquisitions of the Jungfrau-Aletsch region (HH polarization). The image has been flipped/rotated to align approximately with the north-direction. The slant-range direction is from right to left; azimuth from top to bottom.

FIGURE S4.4: Backscatter ratio $\hat{I}^{uncal.}_{r,0,VV}$ of the mean of 17 scenes (VV) with a baseline $b < 300\,m$. Narrow areas behind layover with ratios deviating more than 5% from unity might partially result from double-reflections within layover. Some of the dark areas are azimuth ambiguities.

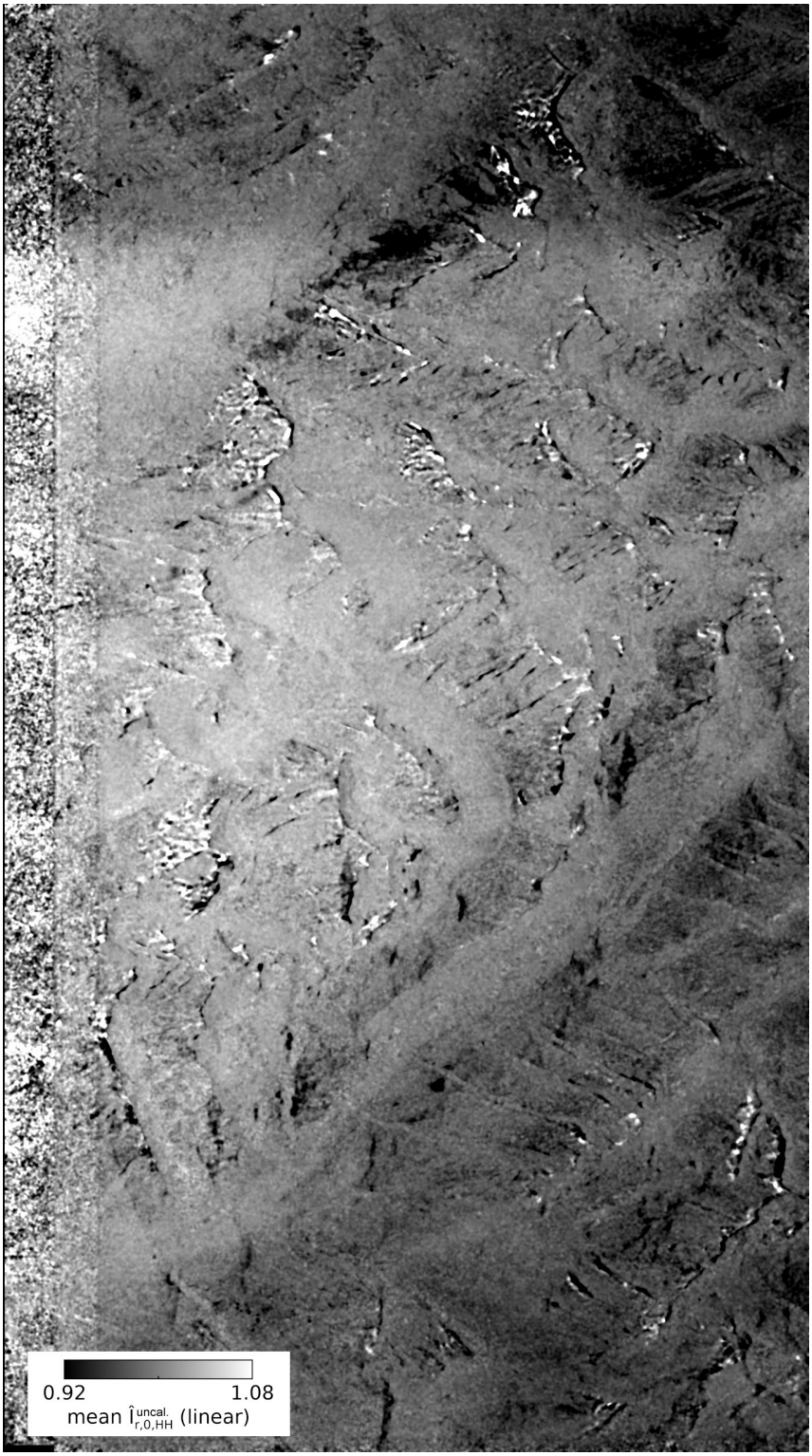

FIGURE S4.5: Backscatter ratio $\hat{I}^{\text{uncal.}}_{\text{r,0,HH}}$ of the mean of 17 scenes (HH) with $b < 300\,\text{m}$. The large-scale spatial variations might originate from an uncompensated antenna pattern or different gains. Narrow areas behind layover show values deviating more than 5% from unity (cf. Fig. S4.4).

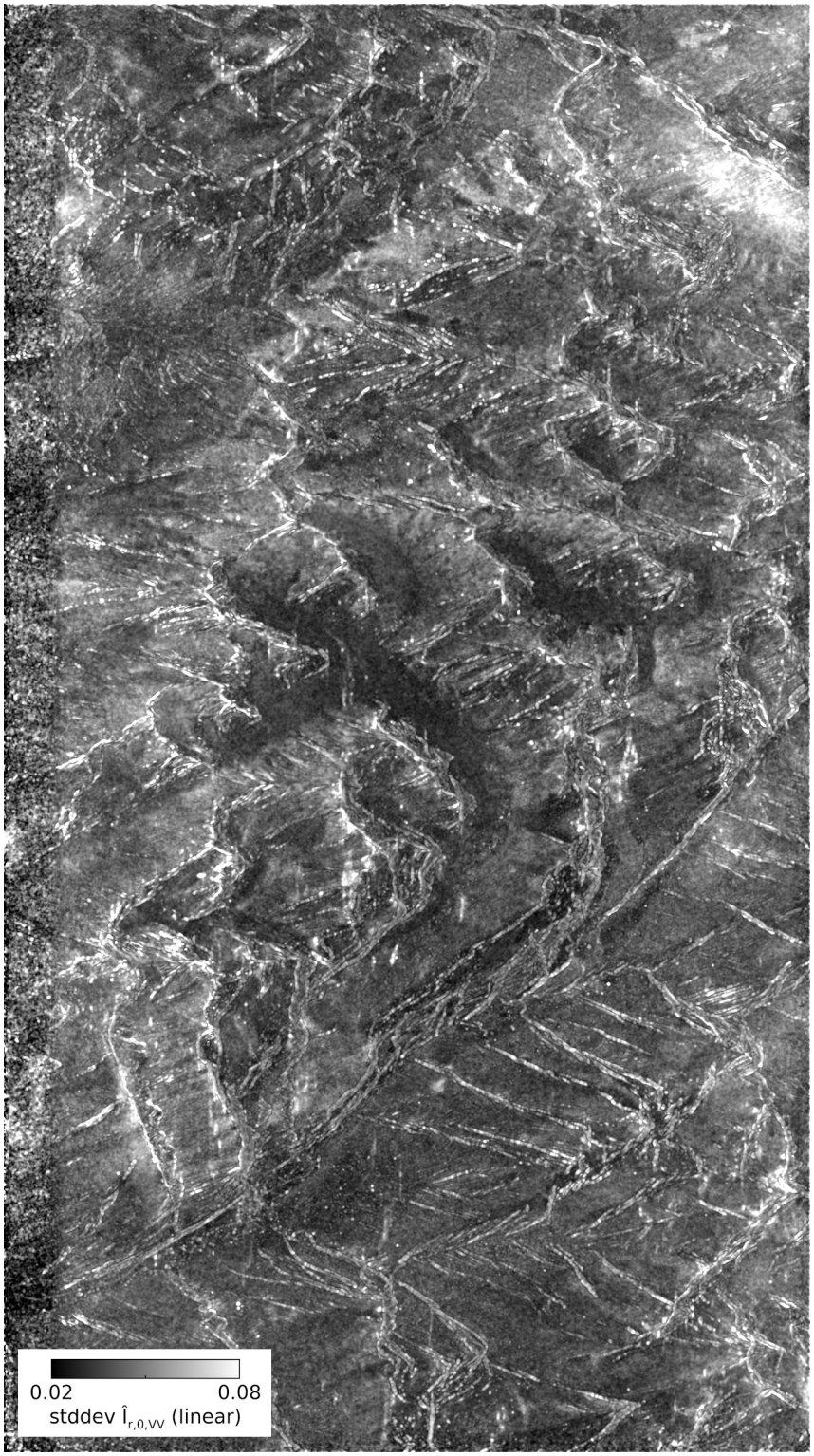

FIGURE S4.6: Temporal standard deviation of the backscatter ratio $\hat{I}_{r,o}$ (VV) of all 118 acquisitions after correction for atenna pattern.

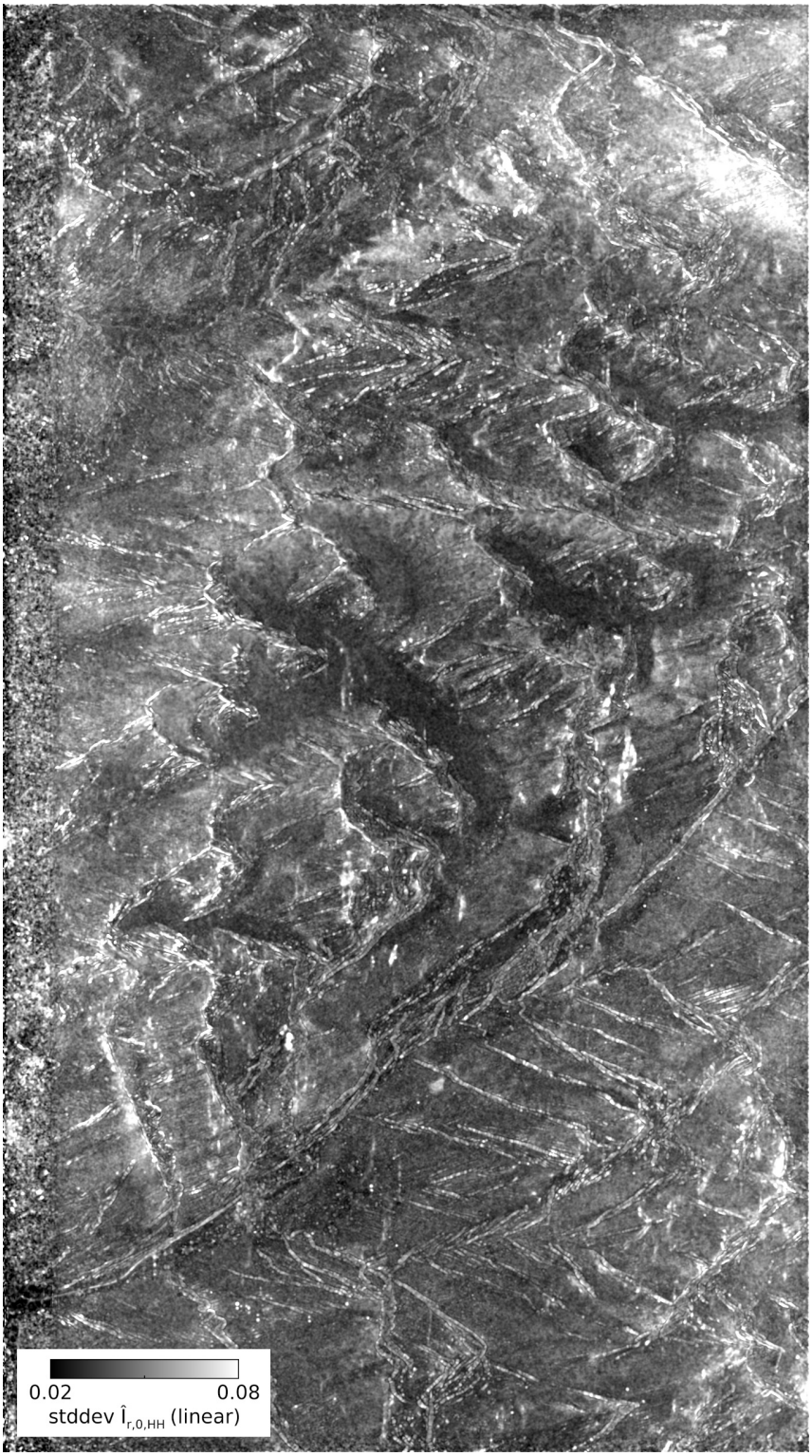

FIGURE S4.7: Temporal standard deviation of the backscatter ratio $\hat{I}_{r,o}$ (HH) of all 118 acquisitions after correction for atenna pattern.

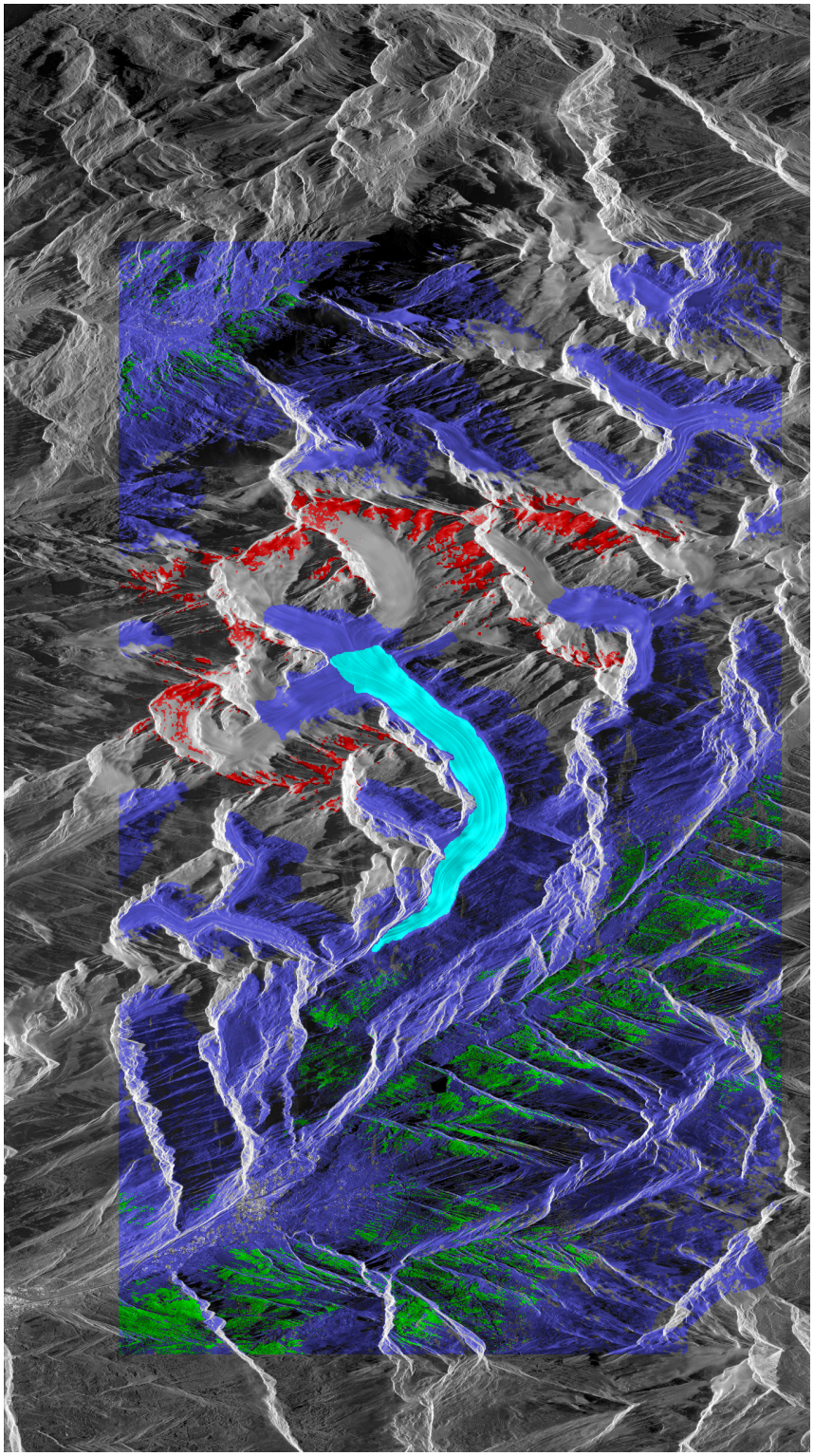

FIGURE S4.8: Mask used for the VV polarization indicating the three ROIs, the high accumulation area > 3500 m (red), the ablation area of Great Aletsch Glacier (cyan), and conifer forest (green), together with the mask used for calibration (blue). The masks in HH are very similar.

Additional observation site: Teram-Shehr/Rimo Glacier

On the plateau between Teram-Shehr and Rimo Glacier (35.47°N, 77.30°E), we selected the accumulation area above 6100 m where we expect dry snow that could cause the CBOE. The equilibrium line altitude of Teram-Shehr glacier, an eastern tributary of Siachen glacier in the Karakorum, is at approximately 5250 m [80]. Compared to the Jungfrau-Aletsch dataset, considerably fewer acquisitions are available and, even though the site is closer to the equator, bistatic angles are not significantly larger: for orbit 98 ($\beta = 0.04$–$0.23°$, $\theta = 39°$, asc.) nine acquisitions with high backscatter indicate dry snow and 17 acquisitions with low backscatter indicate wet or partially wet snow. For orbit 75 ($\beta = 0.04$–$0.19°$, $\theta = 43°$, desc.) we found 18 acquisitions indicating dry snow and 25 indicating wet snow. Both datasets are acquired at HH polarization only. To ensure refreezing of snow and firn after summer, we restricted the analysis of the baseline-dependent bistatic-to-monostatic backscatter intensity ratio to data between 01 December and 30 June.

The Teram-Shehr dataset did not provide enough suitable acquisitions for antenna calibration according to Eq. (4) in the main paper. For calibration with Eq. (5), we used the glacier tongue (ablation area, below 5000 m).

Due to the limited amount of acquisitions we only briefly summarize here some observations. In the accumulation area, above 6100 m, we observed backscatter ratios $\hat{I}_{\mathrm{r,o}}(\beta)$ between 0.72 and 0.77 in five large-baseline acquisitions with $\beta = 0.193°$ from orbit 75 between 11 May and 24 June 2015 (Fig. S4.9,top). For orbit 98 with $\beta = 0.231°$, we observed ratios $\hat{I}_{\mathrm{r,o}}(\beta)$ between 0.74 and 0.81 between 01 May and 03 June 2015 (Fig. S4.9,bottom). With Eq. (14) these values allow estimating an lower limit for the backscatter enhancement B_C and correspond to an enhancement of at least 23–39% (+0.9 to +1.4 dB). In comparison, for the Jungfrau-Aletsch region, we obtain a lower limit of 19–27% (+0.8 to +1.0dB). Due to weak model constraints in the Teram-Shehr dataset, we do not provide parameters estimated by model fits.

Figures S4.10 and S4.11 snow that spatially, the enhancement matches to the accumulation area of the Teram-Shehr/Rimo glacier. The periodic variations of visible in the backscatter ratio is already visible on the delivered TanDEM-X CoSSC data and islikely an artifact from the interpolation during coregistration of the bistatic dataset to the monoscatic one.

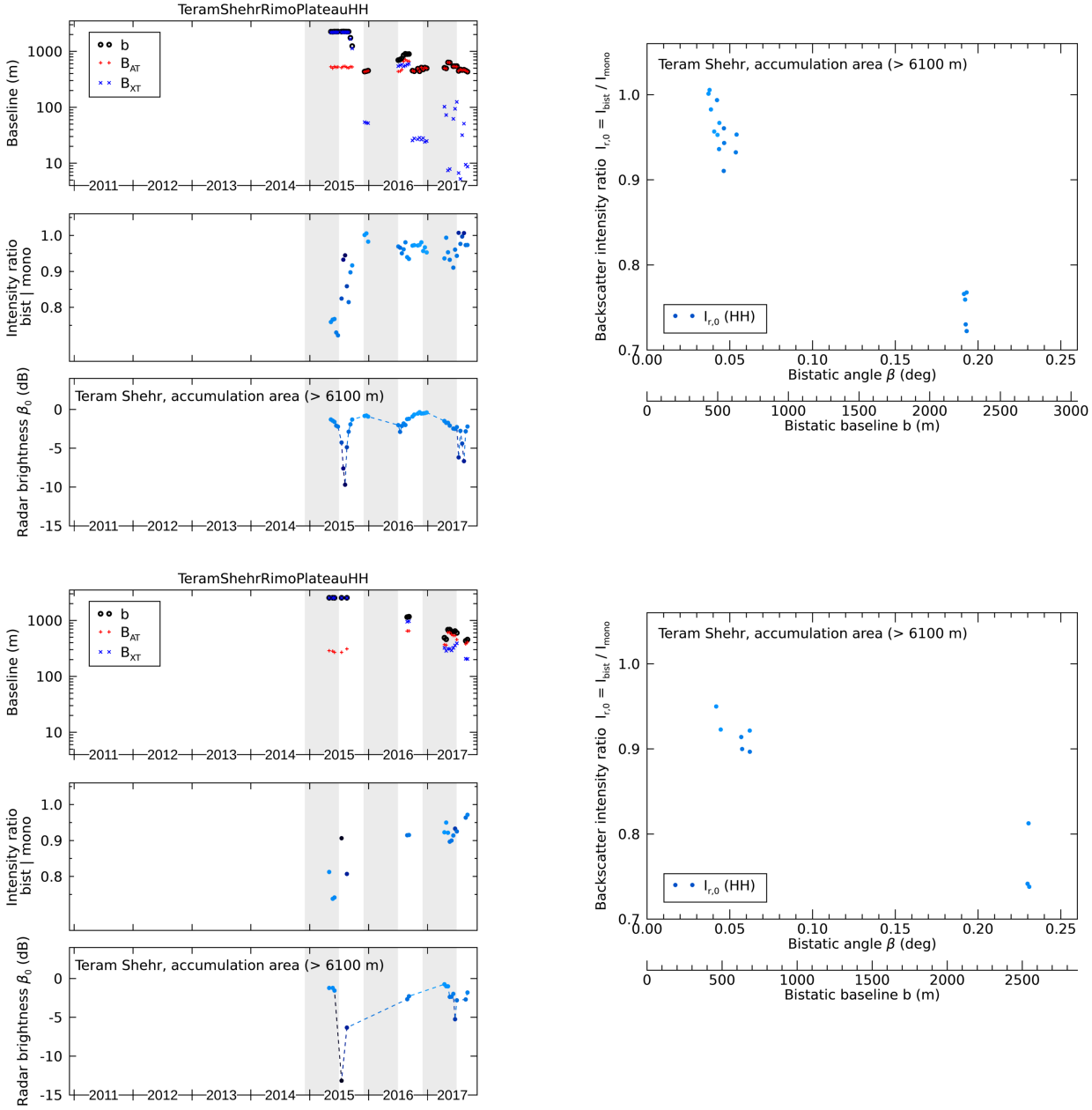

FIGURE S4.9: Time series of baselines b, B_{XT}, B_{AT}, bistatic-to-monostatic backscatter ratios $I_{r,0}$, and radar brightness $I_{\mathrm{mono}} \equiv \beta_0$ for the accumulation area of Teram-Shehr glacier in the Karakorum. Top: orbit 075 (descending), bottom: orbit 098 (ascending). The right hand side shows $I_{r,0}$ for dry snow conditions plotted over the bistatic angle β (data only from 01 December - 30 June as indicated by the gray shading in the time-series figures on the left).

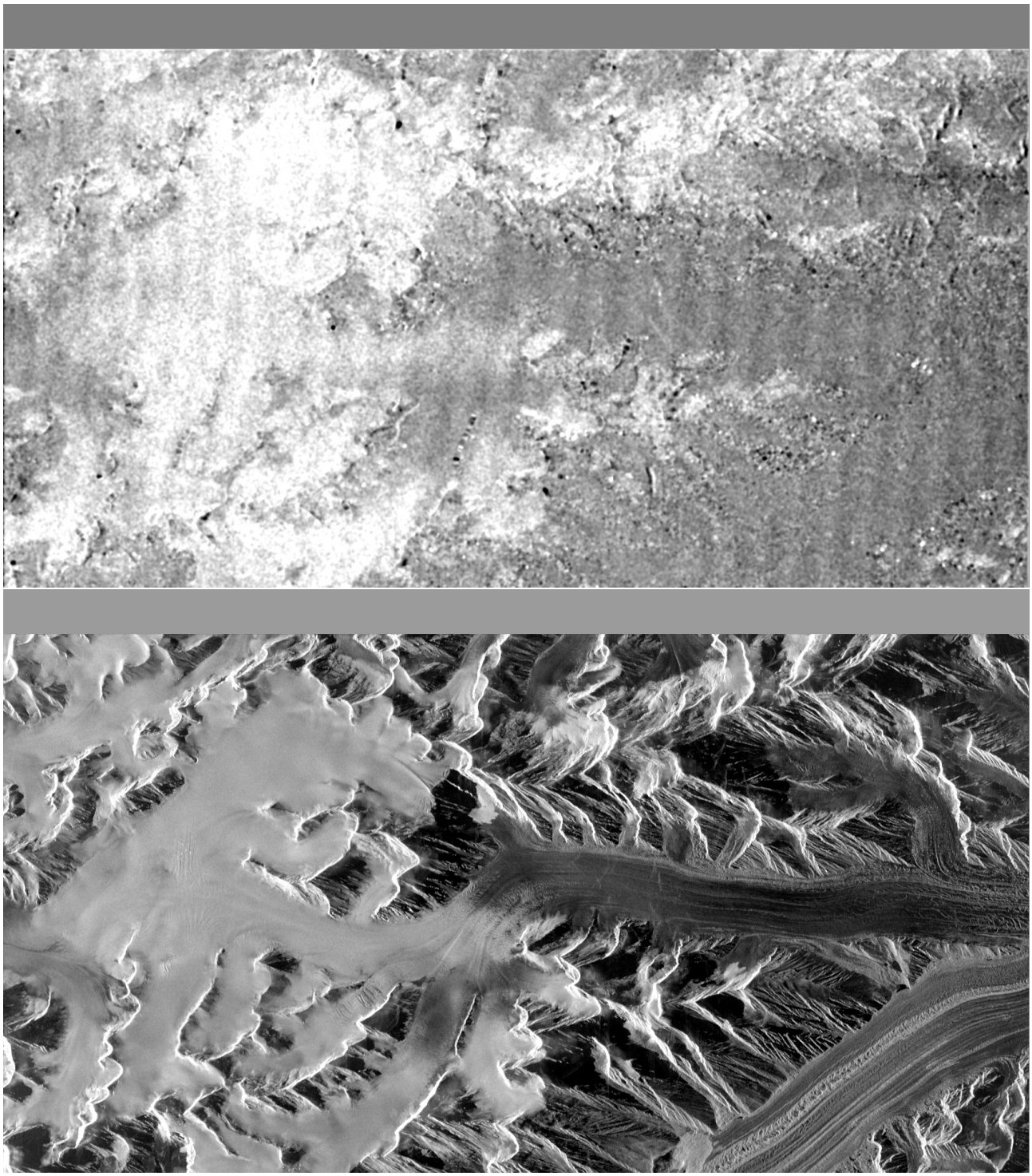

FIGURE S4.10: Top: A high monostatic-to-bistatic backscatter ratio $\hat{I}_{r,0}^{-1}$, observed by TanDEM-X on 2015-06-24 (orbit 075, descending) with $\beta = 0.19°$ indicates CBOE in the dry-snow areas. Gray color scale: [-1.5...+1.5 dB]. Bottom: Radar backscatter intensity for the same date. Color scale: [-20..+5 dB]. Bright backscatter indicates dry snow in the accumulation area and dark snow indicates wet snow on the glacier tongue. Images shown in radar coordinates.

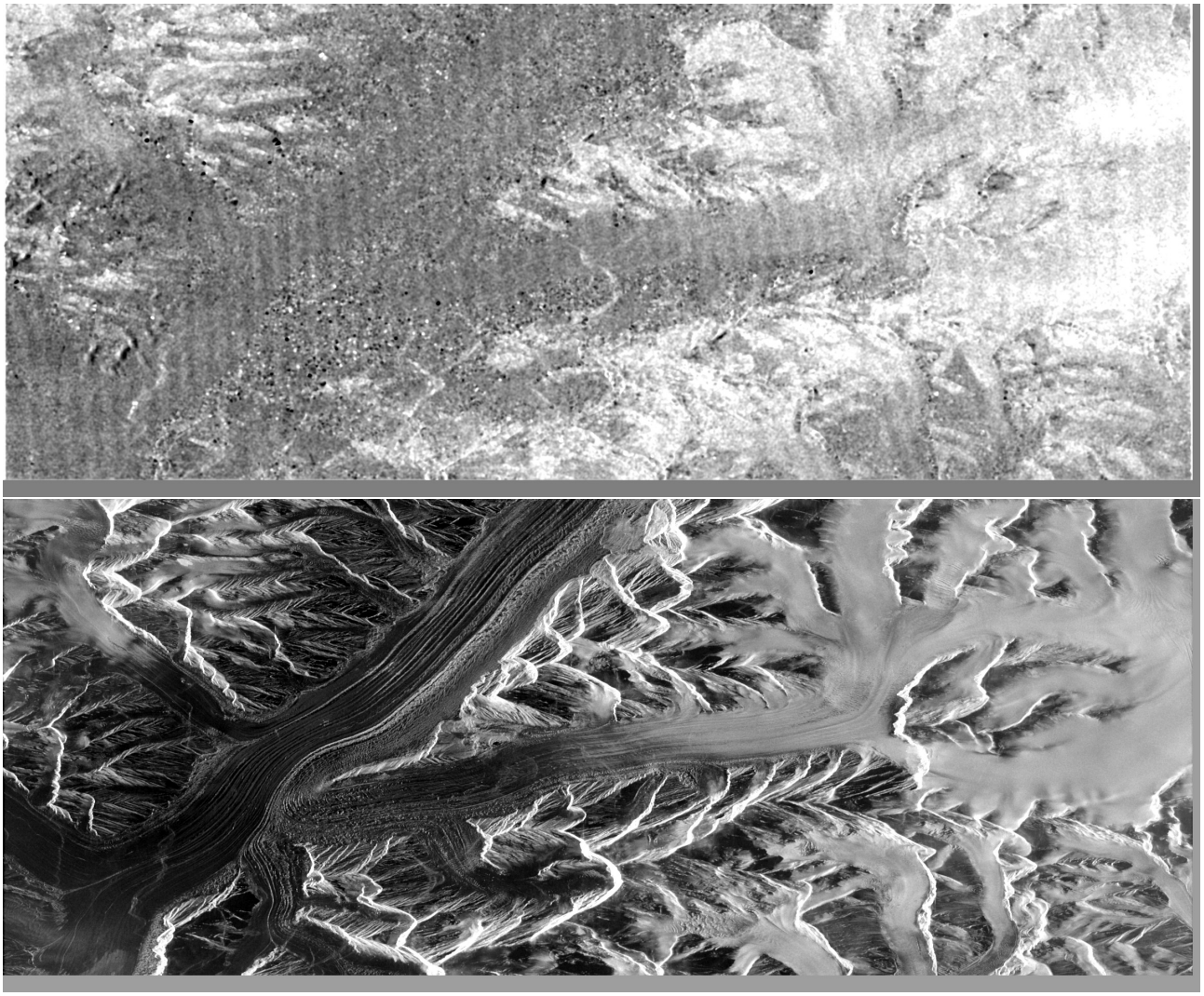

FIGURE S4.11: Top: A high monostatic-to-bistatic backscatter ratio $\hat{I}_{r,0}^{-1}$, observed by TanDEM-X on 2015-05-23 (orbit 098, ascending) with $\beta = 0.23^{\circ}$ indicates CBOE in the dry-snow areas. Gray color scale: [-1.5...+1.5 dB]. Bottom: Radar backscatter intensity for the same date. Colorscale: [-20..+5 dB]. Bright backscatter indicates dry snow in the accumulation area and dark snow indicates wet snow on the glacier tongue. Images shown in radar coordinates.

5

CONCLUSION

This chapter summarizes the main findings of the presented investigations by providing answers to the research questions (RQ) stated in Section 1.3. For quick reference, the relevant questions are reiterated at the beginning of each subsection. This is followed up by an outlook where possible future research directions for bistatic KAPRI applications are outlined.

5.1 MAIN FINDINGS

5.1.1 *Chapter 2: Calibration and operation of a bistatic real-aperture polarimetric-interferometric Ku-band radar*

RQ1.1 *How to model and compensate the offset between the transmitter's and the receiver's internal oscillators in a bistatic frequency-modulated continuous-wave radar system, so that accurate range and phase information can still be retrieved?*

RQ1.2 *How to modify the polarimetric processing pipeline of a monostatic real-aperture fan-beam radar system in order to enable processing of acquisitions in an arbitrary bistatic geometry?*

RQ1.3 *How can one efficiently estimate the polarimetric calibration parameters of KAPRI in the bistatic regime, which precludes the application of the reciprocity principle and use of trihedral corner reflectors?*

This chapter developed the tools necessary for bistatic operation of KAPRI and its application for monitoring of natural environments. Specifically, the synchronization, operation, calibration, and data processing procedures were defined in order to allow production of coregistered and calibrated monostatic and bistatic polarimetric datasets. These procedures enabled the use of bistatic KAPRI for the investigations described in the latter two chapters.

The first challenge of synchronization of the two devices' oscillators (RQ1.1) was resolved through transmission of a reference chirp directly between the two devices, without scattering off objects in the scene. This reference chirp is sampled together with the scene signal, but owing to its direct path and high intensity it can be easily identified in the data, isolated, and used for a-posteriori correction of the phase and range offsets caused by oscillator mismatch. To ensure correct path length determination, this compensated signal afterwards needed to be multiplied by a "synthetic" beat signal corresponding to the path delay caused by the bistatic baseline.

While use of this reference chirp did eliminate the range mismatch caused by oscillator offsets, additional steps were needed to process the bistatic signal (RQ1.2), specifically to remove range,

intensity and phase distortions arising from the bistatic elliptical geometry. These distortions were compensated through analysis of the acquisition geometry and establishment of an unified "bistatic-north" coordinate system between the two devices. By performing a range shift from elliptical to polar geometry and intensity scaling, the bistatic data is effectively coregistered with monostatic data, which enables the application of previously-developed geocoding and analysis algorithms which assume a monostatic polar geometry. Special care however needs to be applied especially when applying the topographic phase compensation algorithm, as the topographic phase varies differently for the transmit and the receive segment of the signal's path. Furthermore, in case of a non-horizontal bistatic baseline, proper care needs to be taken to correctly establish the bistatic-north coordinate system, which can vary for individual targets within the primary device's fan beam.

Bistatic polarimetric calibration (RQ1.3) required development of a new approach, as the approach chosen for monostatic calibration makes use of concepts which are only applicable in monostatic observations (namely the use of trihedral corner reflectors for calibration of co-polarized channels, and the assumption of reciprocity for calibration of cross-polarized channels). Similarly to other bistatic calibration efforts, an active calibration device was identified as the most suitable choice, due to the relative ease of configuration for a particular bistatic geometry, and flexibility in terms of polarimetric signature. These benefits are considered to outweigh the drawbacks of lower robustness and the necessity of active operation. The developed active calibration device VSPARC and the associated calibration method are an effective and relatively low-cost approach towards calibration of bistatic polarimetric systems with good polarization isolation. Comparative tests between the monostatic corner-reflector-based method and the VSPARC method showed a good match of the retrieved calibration coefficients – within 20° and 5% for phase and amplitude imbalances, respectively – thus validating the VSPARC method for bistatic use. It should be noted that the VSPARC concept is not KAPRI-specific, and could be used for calibration of also other bistatic systems with good polarization isolation.

5.1.2 *Chapter 3: Polarimetric analysis of multi-seasonal monostatic and bistatic radar observations of a glacier accumulation zone at Ku-band*

RQ2.1 *What is the timescale on which snow cover on top of a glacier maintains/loses its interferometric coherence at Ku-band in summer and in winter?*

RQ2.2 *What are the similarities and the differences of polarimetric scattering characteristics of snow cover between the monostatic and the bistatic regime, and between summer and winter observations?*

RQ2.3 *Does the reciprocity principle remain valid, or do non-reciprocal scattering processes arise in the bistatic regime in snow at Ku-band?*

This publication applied the developed bistatic operation mode to monitor and analyze the snow cover on top of the Great Aletsch Glacier in Switzerland. Through use of a combined monostatic/bistatic acquisition mode and full-polarimetric time series acquisition, the dataset provided a lot of information about spatial and temporal behaviour of the scattering characteristics of snow cover at Ku-band, both in the monostatic and bistatic regime.

The first investigated phenomenon was the temporal decorrelation rate of the snow cover at Ku-band (RQ2.1). The decorrelation rate is an important parameter for repeat-pass methods, since it sets an upped bound on the maximal possible value of the revisit time that still makes applications of repeat-pass methods viable. Since the observations were carried out on snow cover on top of a relatively fast-moving glacier, we applied a decimation-based approach to mitigate the coherence loss caused by glacier drift. The observations revealed that the snow cover at Ku-band decorrelates in the span of 4-12 hours, depending on particular area and time of year. This value can be a critical constraint on applications of repeat-pass methods in the Ku-band using spaceborne sensors, since these have a revisit time usually on the order of days, which is prohibitively long. The use of single-pass InSAR sensors can thus be greatly advantageous for observation of these environments at Ku-band.

Using the multi-modal capabilities of KAPRI, we characterized the behavior of a large number of polarimetric parameters (RQ2.2). Analysis of the scattering entropy and alpha angle showed that while in summer the scattering is dominated by snow melt and surface scattering processes, in winter the deep penetration into the fresh snow cover exhibits a much higher diversity of scattering processes. Analysis of the co-polar phase difference $\phi_{\mathrm{HH-VV}}$ (CPD) also supports this interpretation, since it showed a well-behaved, smooth, incidence-angle dependent profile in summer, while in winter it varied rapidly on short spatial scales and showed to be very susceptible to phase-wrapping. This indicates that parameter inversion based on CPD measurements of fresh snow cover is difficult at Ku-band in case of layer thicknesses larger than several tens of centimeters, since the phase wrapping precludes the existence of a bijective function between CPD and input model parameters. The summer observations of CPD showed differences of its spatial behaviour when compared to other observations in literature, although this divergence could be attributed to different observation conditions (i.e. presence of repeatedly melted and refrozen snow cover, and possible presence of liquid water), as well as different observation setup (Ku-band frequency and high incidence angles). We proposed one possible explanation of the observed spatial trend of CPD (strong negative value at steep incidence, and a transition to a slight positive value at shallow incidence), specifically an incidence-angle-dependent variation of dihedral scattering contribution.

The presence of non-reciprocal scattering in the bistatic regime (RQ2.3) was investigated through analysis of the relative value of the fourth eigenvalue λ_4 of the coherency matrix, and analysis of the cross-polar phase difference $\phi_{\mathrm{HV-VH}}$ (XPD). Its presence was confirmed, as indicated by the relatively large value of λ_4 and the non-zero value of XPD in the bistatic dataset. The proposed interpretation of the cause of this non-zero XPD value in summer is a combination of birefringence

of the snow pack and different geometries (specifically incidence angles) of the transmission and reception segments of the signal's path. In winter, akin to the CPD, a large variation of the HV and VH phase center positions combined with phase-wrapping was identified as the likely cause.

The acquired dataset thus provided insights into temporal behaviours and polarimetric characteristics of snow cover, including the quantification of parameters such as scattering entropy H, mean alpha angle $\bar{\alpha}$, and the polarization phase differences $\phi_{\mathrm{HH-VV}}$ and $\phi_{\mathrm{HV-VH}}$. This information is useful for future investigations of snow cover at Ku-band, as it can provide estimates for the expected values of these parameters and thus help guide the observation design and timing. The acquired data also revealed several phenomena of interest for future observations with KAPRI, such as observation of CPD evolution during fresh snow accumulation periods, or the evolution of polarimetric parameters over the course of the months-long transition of snowpack from the fresh, volume-like structure in winter to the aged, layered and firn-like structure in summer. Finally, the precise interpretation of the observed CPD and XPD behaviour remains an open question and further investigation is needed in order to confirm the proposed interpretations or find alternatives.

5.1.3 *Chapter 4: Coherent backscatter enhancement in bistatic Ku- and X-band radar observations of dry snow*

RQ3.1 *Does the coherent backscatter opposition effect (CBOE) occur in terrestrial snow cover at radio frequencies?*

RQ3.2 *What are the characteristics of the CBOE enhancement peak in snow cover at X-/Ku-band, and where does it occur?*

RQ3.3 *Can bistatic radar observations of the CBOE enhancement peak be used to infer properties of the scattering medium?*

In this investigation, we designed an experiment which used bistatic KAPRI to investigate the presence of the coherent backscatter opposition effect (CBOE) in seasonal snow at radio frequencies (RQ3.1). The experiment confirmed the presence of the CBOE in a layer of seasonal snow on top of the peak Rinerhorn near Davos, Switzerland. To the best of our knowledge, this is the first and so far only full bistatic characterization of the effect in the Earth's cryosphere using a terrestrial radar sensor. This publication also presented the detection of the same effect in deep firn regions of the Great Aletsch Glacier using the spaceborne X-band bistatic system TanDEM-X. To the best of our knowledge this is also the first known bistatic characterization of the effect in terrestrial snow using a spaceborne sensor.

Characterization of the peak behaviour was carried out, using both datasets (RQ3.2). At Ku-band, the peak was detected in both co-polarized channels, HH and VV, and did not show detectable differences in behaviour between these channels. The effect was detected with an amplitude of

$1.8 - 2.0\,\mathrm{dB}$ and angular half-width-at-half-maximum (HWHM) of 0.25°, in agreement with the theory-predicted property ranges of the effect. At X-band, only the VV polarization was investigated, where the CBOE peak showed to have at least 1.3 dB amplitude and 0.12° HWHM. However, the limited sampling of the bistatic angle values in the TanDEM-X dataset did not allow tightly constraining the peak parameters.

The acquired data showed that a very fine control over the bistatic angle of the acquisition is needed for precise characterization of the effect, since the peak's angular width showed to be less than one degree. In order to precisely sample the peak's width and height, the bistatic angle needs to be sampled with sufficient density to reveal the peak shape, while it also needs to be sampled with sufficient span so as to correctly quantify the background, non-enhanced intensity level. Due to the relative invariance of the effect's angular width with respect to wavelengths and scattering medium, the general recommendation to characterize the effect can be given to sample the bistatic angle range between 0° and at least 1.5°, with sampling density on the order of several hundredths of a degree. This would allow sufficient sampling range to identify the "flat" part of the intensity curve, while providing sufficient sampling density to precisely identify the peak shape. While the effect should be symmetrical with respect to positive/negative bistatic angles, two-sided sampling of the curve (i.e. from $-1.5°$ to 1.5°) would further eliminate suspicions of possible biases in terms of the experimental setup, and provide more independent samples for model fitting.

We also investigated the possibility of snow parameter inversion from radar CBOE observations (RQ3.3). Through application of a CBOE scattering model originally developed in the domain of optics, we were able to retrieve the scattering and absorption mean free paths Λ_T, Λ_A of the radio waves within the snow layer from the peak's observed angular shape. We observed $\Lambda_\mathrm{T} = 0.4 \pm 0.1\,\mathrm{m}$ and $\Lambda_\mathrm{A} = 19 \pm 12\,\mathrm{m}$ at the Ku-band and $\Lambda_\mathrm{T} = 2.1 \pm 0.4\,\mathrm{m}$ and $\Lambda_\mathrm{A} = 21.8 \pm 2.7\,\mathrm{m}$ at the X-band, assuming an optically thick medium.

This publication shows a pathway towards applications of CBOE observations in methods which aim to retrieve snow parameters from radar observations. Furthermore, knowledge of the scattering and absorption lengths can help independently quantify the penetration bias, which can improve the accuracy of DEM generation methods from single-pass interferometric data. Models of the CBOE have already been used to provide insights into structural properties of water ice on surfaces of various Solar System bodies, even when only very limited data was available. A higher availability and quality of bistatic backscatter data in the Earth's cryosphere, combined with the much greater ease of performing in-situ validation measurements, can lead towards development of new and improved snow parameter inversion methods based on radar remote sensing observations.

5.2 OUTLOOK

Over the course of this work on bistatic radar and its applications to snow-covered environments, several interesting pathways for further investigation were identified.

In terms of hardware development, the most innovative contribution of this work is arguably the VSPARC active calibrator concept. While the concept of active calibration of bistatic systems is – as mentioned in the introduction – not new, the VSPARC construction which uses independent pointing and rotation of the two antennas allows for a very flexible configuration which enables full polarimetric calibration in virtually arbitrary bistatic geometries. The current VSPARC prototype is sufficient for calibration at relatively short ranges, however further steps could be taken in order to boost the signal amplification and prevent unwanted passive backscatter from the device's metallic components, thus increasing the maximal range distance limit between the calibrator and the radar devices. Currently a delay line is in place to separate in range the calibrator's signal response from the unwanted scattering from its body – if the body is sufficiently shielded, the delay line can be removed from the signal chain, further boosting the signal-to-clutter ratio. The mounting adapters were constructed using off-the-shelf camera mounts and 3D-printed adapters, which proved to be extremely effective for rapid prototyping, however for long-term usage it is recommended to substitute the components for more robust and specialized variants. Furthermore, the operation of VSPARC is currently completely manual, which limits its long-term deployment use cases, since operator presence is required. Development of a motorized, remotely-controlled alternative could remove this bottleneck, though sufficient care needs to be taken to keep the device sufficiently robust for deployment in remote, inhospitable environments, where KAPRI is likely to be further used.

While the polarimetric characteristics of the multistatic Ku-band dataset acquired in the Jungfraufirn region were analyzed in Chapter 3, the dataset certainly deserves a more in-depth interferometric analysis. The combined differential interferometric information from the two devices could be used in order to directly construct a 3-dimensional displacement vector field, unlike usual monostatic differential interferometry approaches which can only detect the along-range component and need to resort to additional assumptions in order to determine total displacement. Due to the high repetition frequency of the measurements, development of a temporal multilooking algorithm would also be of interest in order to boost the signal-to-noise ratio (SNR), especially for the bistatic dataset which suffers from poor SNR at high ranges. This algorithm would need to correctly compensate for rapid glacier drift which can cause phase-wrapping already on the time scales of tens of minutes, and to avoid biasing the noise characteristics of individual polarimetric channels, since this could bias the estimates of parameters such as scattering entropy, interferometric coherence, or polarization phase differences.

The Jungfraujoch dataset also revealed certain phenomena for which carrying out further acquisition campaigns would be desirable. The observed behaviour of the co-polar phase difference raises

questions about how it behaves both on short timescales of minutes during events such as fresh snowfall, and on long timescales of months (i.e. transition of snow cover from fresh snow to firn). Furthermore, the interesting spatial behaviour of the co-polar and cross-polar phase differences in both the monostatic and the bistatic regimes certainly deserves more study both from the experimental, as well as the theoretical approach.

Finally, the confirmation and preliminary characterization of the coherent backscatter opposition effect (CBOE) at Ku-band and X-band in snow (Chapter 4) opens up a completely new pathway towards possible retrieval of snow parameters from radar observations. While extensive CBOE modeling research had been carried out in the past decades, most of these analyses were focusing on optical-frequency domains or on analysis of purely monostatic observations, in part due to unavailability of bistatic data. A long-term ground-based radar measurement campaign can fill this research gap through a thorough bistatic characterization of CBOE at radio frequencies, possibly combining radar observations with in-situ measurements of snow properties. Such a campaign would enable validation of scattering models, and open up the possibility to search for a connecting link between CBOE peak characteristics, and parameters of the snow medium. Parameters of interest include layer thickness, snow grain size, snow density, or the snow water equivalent. The TanDEM-X observations indicate that the characterization of CBOE is also feasible using spaceborne sensors, which provides an opportunity for worldwide monitoring of snow cover properties, should the aforementioned connecting link be identified. It is not likely (though not currently disproven) that CBOE observations by themselves could provide direct access to the parameters of interest. However, combining CBOE observations with conventional monostatic approaches – through use of, e.g., a bistatic receive-only attachment – could provide additional input information to inversion methods aiming to retrieve snow parameters from radar observations, thus improving their accuracy. Further study, both experimental and theoretical, is thus certainly desirable to assess the potential of snow characterization using bistatic radar observations of the CBOE.

PUBLICATIONS

Articles published in peer-reviewed journals:

1. Štefko, M., Ottino, B., Douglass, K. M. & Manley, S. Autonomous illumination control for localization microscopy. *Optics Express* **26**, 30882. doi:10.1364/OE.26.030882 (2018).
2. Annex, A. M., Pearson, B., Seignovert, B., Carcich, B. T., Eichhorn, H., Mapel, J. A., von Forstner, J. L. F., McAuliffe, J., del Rio, J. D., Berry, K. L., Aye, K.-M., Stefko, M., de Val-Borro, M., Kulumani, S. & Murakami, S.-y. SpiceyPy: a Pythonic Wrapper for the SPICE Toolkit. *Journal of Open Source Software* **5**, 2050. doi:10.21105/joss.02050 (2020).
3. Stefko, M., Frey, O., Werner, C. & Hajnsek, I. Calibration and Operation of a Bistatic Real-Aperture Polarimetric-Interferometric Ku-Band Radar. *IEEE Transactions on Geoscience and Remote Sensing* **60**, 1. doi:10.1109/TGRS.2021.3121466 (2022).
4. Stefko, M., Leinss, S., Frey, O. & Hajnsek, I. Coherent backscatter enhancement in bistatic Ku- and X-band radar observations of dry snow. *Cryosphere* **16**, 2859. doi:10.5194/tc-16-2859-2022 (2022).

Articles currently submitted for publication:

1. Stefko, M., Berhnard, P., Frey, O. & Hajnsek, I. Polarimetric analysis of multi-seasonal monostatic and bistatic radar observations of a glacier accumulation zone at Ku-band. *IEEE Journal of Selected Topics in Applied Earth Observations and Remote Sensing*. submitted (2023).

Selected conference contributions:

1. Stefko, M., Leinss, S. & Hajnsek, I. *Bistatic radar observations of the coherent backscatter opposition effect in dry snow* in *EGU General Assembly Conference Abstracts* (2021), EGU21.
2. Stefko, M., Frey, O., Werner, C. & Hajnsek, I. *KAPRI: A Bistatic Full-Polarimetric Interferometric Real-Aperture Radar System for Monitoring of Natural Environments* in *2021 IEEE International Geoscience and Remote Sensing Symposium IGARSS* (IEEE, 2021), 1950. doi:10.1109/IGARSS47720.2021.9553427.
3. Stefko, M., Frey, O. & Hajnsek, I. *Snow Characterization at Ku-Band with a Bistatic Polarimetric Ground-Based Radar* in *IGARSS 2022 - 2022 IEEE International Geoscience and Remote Sensing Symposium* (IEEE, 2022), 4256. doi:10.1109/IGARSS46834.2022.9884442.

4. Stefko, M., Shiyi, L., Luck, M. & Hajnsek, I. *SAR² - An augmented-reality App for exploration of principles of synthetic aperture radar* in *4th Symposium on Space Educational Activities* (Universitat Politècnica de Catalunya, 2022), 2. doi:10.5821/conference-9788419184405.031.